On the Processing and the Tarnishing Mechanism of Gold-based Bulk Metallic Glasses

Dissertation
zur Erlangung des Grades des

Doktors der Ingenieurwissenschaften (Dr.-Ing.)

der Naturwissenschaftlich-Technischen Fakultäten
Chemie, Pharmazie, Bio- und Werkstoffwissenschaften
der Universität des Saarlandes

vorgelegt von

Dipl.-Ing. Miriam Eisenbart

Saarbrücken, 2015

Tag des Kolloquiums: 28. April 2016

Dekan: Prof. Dr.-Ing. Dirk Bähre

1. Gutachter: Prof. Dr. rer. nat. Ralf Busch

2. Gutachter: Prof. Dr.-Ing. Frank Mücklich

Vorsitz: Prof. Dr. mont. Christian Motz

Akad. Mitarbeiter: Dr.-Ing. Dr. rer. nat. Anne Jung

Abstract

In 2005, an amorphous gold alloy with 760 mass-‰ gold, i.e. 18 karat (k), with the composition $Au_{49}Ag_{5.5}Pd_{2.3}Cu_{26.9}Si_{16.3}$ at.% was developed by Schroers et al. [1].

In the years following the alloy's discovery, a fast introduction into industrial production was anticipated due to several promising factors: i.e. Ni-free white-gold color, outstanding mechanical properties, excellent formability and processability and minimal casting shrinkage [2]. However, the alloy shows an exceptionally fast tarnishing behavior resulting in a significant color change.

The scope of the present work was on the one hand to investigate possible processing routines for the industrial production of small amorphous parts for jewelry, watch making or technical applications. On the other hand, the understanding of the mechanism of the tarnishing behavior was an ultimate goal aiming at tarnishing rate reduction [3, 4].

The present work involves the production of a semi-finished product, the investigation of various casting routines and a study on thermoplastic forming. All applied processing techniques are typical industrial processing techniques or very similar. In addition, a new casting technique was developed that combines traditional investment casting with electroforming [5]. A comprehensive investigation of the tarnishing process was done based on which a first approach towards the development of a tarnish resistant alloy was accomplished and recommendations for future work are given.

Kurzfassung

2005 wurde von Schroers et al. eine amorphe 18 Karat (kt) Goldlegierung mit 760 Masse-‰ Gold bzw. der Zusammensetzung $Au_{49}Ag_{5.5}Pd_{2.3}Cu_{26.9}Si_{16.3}$ Atom-% entwickelt [1].

In den Jahren nach der Entdeckung dieser Legierung wurde aufgrund mehrerer vielversprechender Faktoren wie z.B. Ni-freie Weißgoldfarbe, herausragende mechanische Eigenschaften, exzellente Formbarkeit sowie minimale Gussporosität eine baldige industrielle Anwendung erwartet [2]. Allerdings zeigt die Legierung ein außerordentlich rasantes Anlaufverhalten, das in einer signifikanten Farbänderung resultiert.

Das Ziel dieser Arbeit war zum einen die Untersuchung der Verarbeitbarkeit in industriellen Fertigungsprozessen bei der Produktion von Schmuck- und Uhrenteilen sowie von technischen Bauteilen. Zum anderen wurde der Anlaufmechanismus in einer systematischen Korrosionsstudie analysiert [3, 4].

Diese Arbeit beinhaltet die Herstellung eines Halbzeuges, die Untersuchung verschiedener Gießtechniken sowie eine Studie zur thermoplastischen Verformbarkeit. Bei der Auswahl der Prozesstechniken wurde ein Fokus auf industrienahe Prozesse gelegt. Darüber hinaus wurde ein neues Gießverfahren entwickelt, das herkömmlichen Feinguss mit Galvanoformen verknüpft und somit den Guss in verlorene Metallformen ermöglicht [5].

Basierend auf dem Verständnis des Anlaufmechanismus konnten bereits erste Versuche zur Neuentwicklung einer anlaufbeständigen Legierung durchgeführt und Empfehlungen für weiterführende Arbeiten gegeben werden.

Contributions and Publications
Publications by the author related to the content of this thesis:

- M. Eisenbart, U. E. Klotz, R. Busch, I. Gallino, On the abnormal room temperature tarnishing of an 18 karat gold bulk metallic glass alloy, Journal of Alloys and Compounds, 615, Supplement 1 2014, pp. S118 - S122
- M. Eisenbart, U. E. Klotz, R. Busch I. Gallino A colourimetric study of the tarnishing of gold-based bulk metallic glasses, Corrosion Science, 2014, 85, 258-269
- U. E. Klotz, M. Eisenbart Gold-Based Bulk Metallic Glasses: Hard Like Steel, Moldable Like Plastics, Proceedings of the Jewelry Technology Forum, 2014
- U. E. Klotz, M. Eisenbart Gold-Based Bulk Metallic Glasses: Hard Like Steel, Moldable Like Plastics, Proceedings of the Twenty-Seventh Santa Fe Symposium in Albuquerque, New Mexico, 2013, pp. 221-236
- M. Eisenbart, Herstellungs- und Anwendungsmöglichkeiten massiver metallischer Gläser auf Edelmetallbasis, Pforzheimer Werkstofftag, 2013, pp. 101-115
- Patent filed internationally on casting with lost metal molds under No. PCT/EP 2014/001418 / WO2014198380A1 "Verfahren zum Gießen eines Gegenstandes aus metallischem Glas"

Oral Conference and Symposium Presentations:

- M. Eisenbart, U. E. Klotz, R. Busch I. Gallino ISMANAM 2013, 01. July 2013: Casting and tarnishing studies of the $Au_{49}Ag_{5.5}Pd_{2.3}Cu_{26.9}Si_{16.3}$ at% bulk metallic glass for jewelry technology
- M. Eisenbart, U. E. Klotz, R. Busch, I. Gallino, EUROMAT 2013, 09. September 2013: Casting and tarnishing studies of bulk metallic glass based on noble metal for jewelry technology
- M. Eisenbart, Herstellungs- und Anwendungsmöglichkeiten massiver metallischer Gläser auf Edelmetallbasis, Pforzheimer Werkstofftag, 2013
- M. Eisenbart, U. E. Klotz: Freitagsseminar 07. Dezember 2012, Schwäbisch Gmünd: Herstellungs- und Anwendungsmöglichkeiten von massiven metallischen Gläsern auf Edelmetallbasis
- M. Eisenbart, U. E. Klotz, I. Gallino, R. Busch. Gold Conference Tokyo, 08. September 2012: Processing and Properties of 18 karat Au-based Bulk Metallic Glasses for Jewelry Technology

Poster presentation:

- M. Eisenbart, U.E. Klotz, Kupfersymposium Berlin, 04. und 05. November 2015: Massive Metallische Gläser: Vorstellung der Materialklasse und Überblick über MMG auf Cu-Basis
- M. Eisenbart, U. E. Klotz, O. Gross, R. Busch, I. Gallino, ISMANAM 2015 Paris, 13.-17. Juli 2015: Tarnishing Studies on the $Au_{49}Ag_{5.5}Pd_{2.3}Cu_{26.9}Si_{16.3}$ at% Bulk Metallic Glass
- M. Eisenbart, U. E. Klotz, R. Busch, I. Gallino, Doktorandentag Universität des Saarlandes, 13. November 2013: Tarnishing Mechanism of an 18K Amorphous White Gold Alloy (A Microstructure Investigation of the Corrosion Process)
- M. Eisenbart, S. Mozgovoy, J. Heinrich, U. E. Klotz, R. Busch, ISMANAM 2010 Zürich, 05. Juli 2010: Properties of Amorphous 18k Gold Based Alloys

I want to thank Dr. Isabella Gallino for giving me a lot of input about the corrosion behavior of bulk metallic glasses and for the constant support of my research work in general. I am very grateful towards Professor Dr. Ralf Busch for the discussion of my results, the opportunity to do the present work in cooperation with the Saarland University and for the support in improving this thesis. I want to thank Professor Dr. Frank Mücklich for his work as my second advisor.

I would also like to express my great thankfulness towards Dr. Ulrich E. Klotz for the opportunity to use the results created at **fem** research institute in this thesis and the support and freedom to pursue this scientific topic in detail while giving me the extra push towards some interesting topics that I may have overlooked otherwise. I am very grateful towards Dr. Zielonka for the opportunity to work with the outstanding facilities at **fem** research institute. There are a lot more people at **fem** to thank for the support and help with the setup of the experiments and the performance of the investigations: Franz Held for numerous casting trials, metallographic investigations and tarnishing experiments, Britta Schöne, Rita Bretzler and Wolf-Alexander Heiss for the SEM, STEM and FIB investigations, Patricia Guther, Marianne Stoll, Marcel Widmann, Karin Pfeffer and Ulrike Schindler for the metallographic preparation, Kerstin Petrikowski, Andreas Richter, Herbert Kappl, Martin Balzer and Lilia Schmalz for XRD measurements and colorimetric analyzes. I would also like to thank Patrick Wais for the design of the chart in Figure 5.3 and Dario Tiberto for performing the casting simulation.

I thank Lisa-Yvonn Schmitt for her work on the gold alloy; especially for the experiments on repeated cast cycles for $Au_{49}Ag_{5.5}Pd_{2.3}Cu_{26.9}Si_{16.3}$ and the opportunity to show some of her work in this thesis. I want to empathize my thankfulness towards Oliver Gross and Zach Evenson, who performed the DSC scans on my sample material and Dipl.-Ing. Jörg Schmauch of the Saarland University for the performance of the TEM investigation, Mr. Watzal from Heraeus for AES spectroscopy and Dr. Kovacz from Limedion for the XPS analysis.

Thank you Moritz, Will, Sanja, Shuai and Jochen for helping out with the experiments performed at the Chair of Metallic Materials, Saarland University and for being awesome colleagues.

Thank you Sebastian, Boris and Svenja for proof reading and George, Chrissa, BaumbaRt, Linda, Diana, tChörch, Edna, Haraaaaaald and Martina for the distraction that is sometimes essential when you're stuck ;)

Imke, Chrissa, Tank, Com and all the numerous brothers of A.V. Hütte: you're the best motivators.

Thanks to my parents, who always were convinced, my work is the best in the world.

For Angus

Contents

1 Introduction

Conventional crystalline solidifying precious metal alloys have a comparatively low hardness and are prone to be scratched and deformed during usage. This is detrimental to technical as well as decorative applications. Hence, the development of new alloys is often driven by the necessity to improve the mechanical properties. Depending on the application for which they are intended, additional properties can be of interest, such as electric conductivity for contact materials or scratch resistance and an attractive color for jewelry applications. Independent of the final application, a good and cost-efficient processability is desirable.

High hardness and high abrasion resistance are not easy to achieve in precious metals and their alloys, as can be seen for example in gold and conventional gold alloys. Pure gold is extremely soft even in a drastically cold worked state and can easily be scratched and deformed. Gold-based bulk metallic glasses (BMG) on the other hand have an exceptionally high as-cast hardness, such as for example 360 HV1 for the amorphous solidifying alloy $Au_{49}Ag_{5.5}Pd_{2.3}Cu_{26.9}Si_{16.3}$ at.%, short Au-BMG1. Alloy compositions are always given in at.% in this thesis, if not declared otherwise.

Recently, several new Au-based bulk metallic glasses have been introduced [2, 6, 7, 8], some of which can be cast amorphously into geometries of up to 5 mm at cooling rates that are easily achieved in common casting devices using partable copper molds. Their as-cast hardness exceeds the as-cast hardness of conventional crystalline solidifying jewelry alloys significantly.

These exceptionally high as-cast hardness and strength values have led to an enhanced interest in industrial applications of gold-based bulk metallic glasses. Especially in investment casting and micro casting, where cold working as a measure to improve the hardness is typically not applied, the precious-metals-based amorphous alloys seem to be the ideal material.

The liquidus temperature T_l of Au-BMG1 was reported by Schroers et al. [1] to be 644 K (371 °C). The low T_l allows a low casting temperature of 873 - 1073 K (600 to 800 °C) [9], and the amorphous solidification minimizes shrinking porosity, and near net shape casting is possible. Once it is produced amorphously, the bulk metallic glass can be further processed by thermoplastic forming (TPF) similar to the thermoplastic forming of plastics or the blow molding of conventional silica glasses [10] opening new possibilities for shaping.

The Au-based amorphous alloy investigated and documented best to date is $Au_{49}Ag_{5.5}Pd_{2.3}Cu_{26.9}Si_{16.3}$. Its color is described in [11] as "standard White" or "off-White", with an average Yellowness Index YI of 25.3 according to standard test ASTMD 1925. The Yellowness Index is determined from color values that are measured under standard testing procedures. It is usually referred to when white gold colors are classified [12]. The lower

the YI, the "whiter" the color and, hence, the more desirable for white gold applications. More recent testing at **fem** *Forschungsinstitut Edelmetalle + Metallchemie*, Schwäbisch Gmünd, Germany, shows Yellowness Index values of 15-17 for $Au_{49}Ag_{5.5}Pd_{2.3}Cu_{26.9}Si_{16.3}$ in a freshly polished state. This YI corresponds even to a premium white color, a very desirable white color for jewelry products.

Thus, color, processability, and mechanical properties meet the expectations of jewelry producers. However, the amorphous gold-based alloy compositions in the Au-Cu-Ag-(Pd)-Si system show a fast and distinct color change often described as "tarnishing". An example of the tarnishing effect is shown for an amorphous ring of composition $Au_{49}Ag_{5.5}Pd_{2.3}Cu_{26.9}Si_{16.3}$ in Figure 1.1. After a 52 days wear test under real-life conditions, the ring shows a severe discoloring that does not wear off. This color change is the main obstacle for a widespread application of gold-based amorphous metals for decorative products.

(a) As-polished ring (b) Ring after 52 days wear test

Figure 1.1: Amorphous ring with alloy composition $Au_{49}Ag_{5.5}Pd_{2.3}Cu_{26.9}Si_{16.3}$ prior to and after a wear test of 52 days, previously published in [13, 14, 15].

The present work presents studies on different processing routines for the production of amorphous products, a newly inducted casting process developed throughout the present work, the results of a systematic micro-structural and colorimetric study on the tarnishing behavior and it proposes a theory on the underlying tarnishing mechanism.

2 Literature Review and Theory

2.1 Introduction to Bulk Metallic Glasses

A so called "metallic glass", also referred to as "amorphous metal", is formed, if the crystallization during cooling from the liquid state is avoided. Although there are several other sorts of amorphous metallic materials, e.g. electroless nickel coatings, the term *metallic glass* only refers to amorphous metals formed during fast quenching from the liquid state [16, 17].

The formation of a crystalline phase during cooling is inhibited as soon as the cooling rate R_{cool} is sufficiently high to bypass crystallization. The minimum cooling rate at which still no crystallization takes place is called the critical cooling rate R_c. It depends on the alloy composition. In Figure 2.1, a schematic time temperature transformation diagram (TTT-diagram) is plotted. It shows the time-dependent crystallization event, the so called-crystallization "nose". It is called nose due to its c-shape. If the applied cooling rate during casting is high enough for the material to bypass the crystallization nose, an amorphous metal is formed. Exemplary cooling rates for an amorphous and a crystalline solidification are sketched in Figure 2.1.

A *bulk* metallic glass is formed, if the critical cooling rate R_c is sufficiently low to cast geometries of at least several millimeters and up to several centimeters in thickness. The maximum casting thickness that can be achieved for a certain bulk metallic glass is called the critical casting thickness d_c [18].

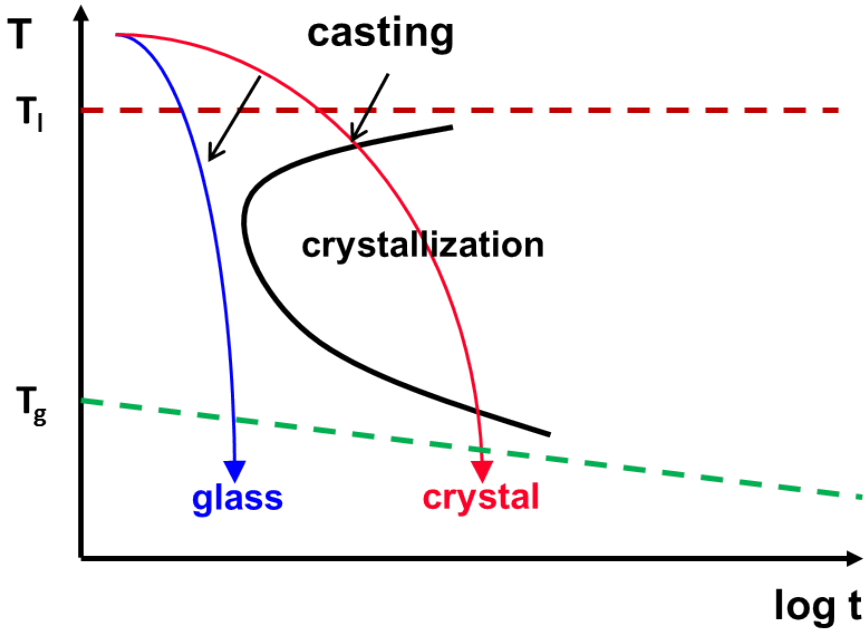

Figure 2.1: Schematic TTT-diagram for amorphous solidification; published in an earlier version in [13, 14, 15].

In 1960, the first metallic glass, near eutectic $Au_{75}Si_{25}$ at.%, was accidentally produced during an experiment [19]. The experimental setup by P. Duwez and his group was initially designed to obtain a solid solution in binary alloys of copper and silver by the use of rapid quenching from the melt [17]. After the group indeed succeeded to fabricate a small foil with a single-phase, face-centered solid solution, they were curious what would happen, if the rapid quenching technique was applied to a system in which a solid solution cannot exist. From preliminary experiments with binary silver-germanium alloys, the formation of a non-equilibrium hexagonal close-packed phase was expected to form during rapid quenching of gold-silicon alloys. "Instead the x-ray diffraction pattern of the quenched Au-20 at.% Si alloy indicated the absence of crystallinity." as P. Duwez later stated in [17].

With the alloys known at that time, comparatively high critical cooling rates of approx. 10^6 to 10^8 K/s were necessary to form an amorphous metal. Due to this high R_c, only very thin foils or ribbons of 20-30 μm thickness could be produced for example by splat cooling or melt spinning [17, 20]. Since 1960, alloys of more and more complex compositions have been developed in many different research groups worldwide. Today there are alloys available with the crystallization retarded to a degree at which cooling rates of less than 1 K/s can be applied and bulk amorphous products can still be cast. With critical cooling rates of this order of magnitude, bulk metallic glasses can be produced by simple casting into copper molds. The copper of the mold provides a sufficiently high thermal conduction for fast cooling.

The bulk metallic glass with the highest d_c known today is a Pd-based bulk metallic glass with the composition $Pd_{42.5}Cu_{30}Ni_{7.5}P_{20}$. It was reported to be castable fully amorphous

in diameters of up to 80 mm [21]. Due to these high critical casting thicknesses, metallic glasses have evolved from scientific curiosities to engineering materials. Applications in the production of bulk parts are now not only possible, they are in fact very desirable considering their exceptional properties.

2.2 Properties

Due to their amorphous structure, some of the properties of bulk metallic glasses differ from those of crystalline metals. The lack of any crystalline structure results in the absence of typical crystallographic defects or imperfections such as dislocations and grain boundaries. Since the plastic deformation of crystals is mainly determined by the behavior of such crystal imperfections, e.g. the movement of dislocations through a crystal structure and their accumulation at grain boundaries, the mechanical properties of amorphous metals are very different in nature.

An amorphous metal does not yield to mechanical loads by the movement of dislocations but by the formation of one or several shear bands, hence its yield strength is almost as high as the theoretical limit [22]. Whether single or multiple shear bands are formed depends on the bulk metallic glass at hand. There are no mechanisms for strain hardening during yielding available in an amorphous structure. In fact, the amorphous metals rather show strain softening [23]. The plastic deformation of BMGs does not simultaneously take place over the complete sample until necking occurs as it is the case for crystalline metals, but rather only within the shear bands, leading to a high elastic strain limit and a macroscopically brittle behavior.

A very high quality polishing of amorphous casting goods is possible due to the lack of grain boundaries and the very homogenous distribution of the alloying elements. Additionally, the high hardness of the cast products in as-cast condition is beneficial to the surface finishing as plastic deformation during grinding and polishing is avoided.

2.2.1 Elastic Deformation

Bulk metallic glasses can reach elastic strains ϵ_{el} of up to more than 2% [22], while crystalline metals usually yield at an elastic strain of about 0.5% or less [23]. BMG usually have a macroscopically comparatively low Young's modulus (E) [22].

The very high elastic strain limits result in high resiliance values for the metallic glasses. The resiliance is a measure for the elastic energy that can be stored in a material. The elastic energy E_{el} is defined as:

$$E_{el} = \frac{1}{2} * \sigma * \epsilon_{el} = \frac{1}{2} * E * \epsilon_{el}^2 \tag{2.1}$$

With a Young's modulus of 74.6 10^9 $\frac{N}{m^2}$ [24] and a maximum elastic strain ϵ_{el} of around 1.5% [25], an elastic energy E_{el} of around 8.4 10^6 $\frac{N}{m^2}$. can be calculated for the alloy $Au_{49}Ag_{5.5}$ $Pd_{2.3}Cu_{26.9}Si_{16.3}$.

Figure 2.2 schematically illustrates the strength as a function of elastic strain for different material classes and the corresponding elastic energies as the area beneath the stress-strain curves. The capability to store such a high amount of elastic energy in comparison to crystalline metals and polymers makes BMGs excellent spring materials, especially as the amorphous structure leads to a low internal friction and, hence, a low damping. Thus, the elastic energy is stored and released with a low loss. As a result, the first applications of BMGs so far have been as spring materials in sporting equipment such as tennis rackets and golf clubs. Other applications are casings due to their high hardness and scratch resistance [26], micro-electro-mechanical systems (MEMS) and nano-electro-mechanical systems (NEMS) [27, 28, 29] due their accurate net shape formability even in small dimensions.

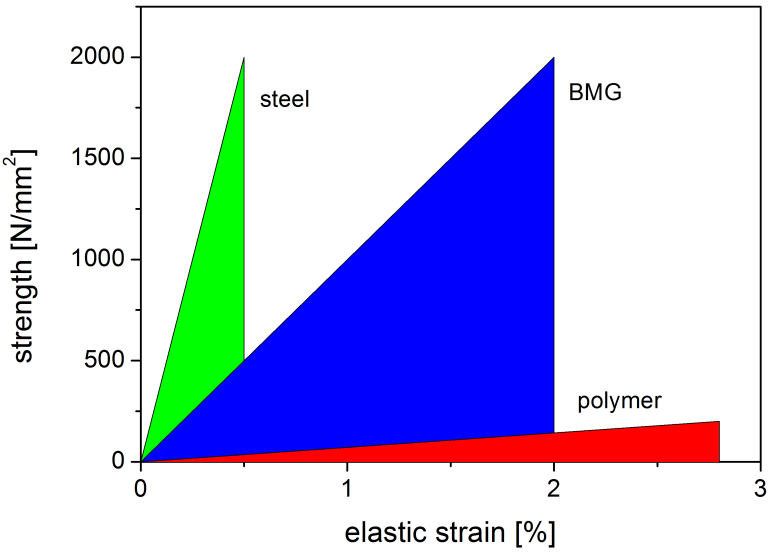

Figure 2.2: Schematic resilience of different material classes; published in an earlier version in [13, 14].

Figure 2.3 shows the ratio of strength to elastic strain for several different material classes according to [30]. The metallic glasses combine the high elastic strains usually found in polymers with the high strength typically found in some steel alloys. This unique combination of mechanical properties is the main reason why an industrial application of amorphous metals as engineering materials is highly desirable.

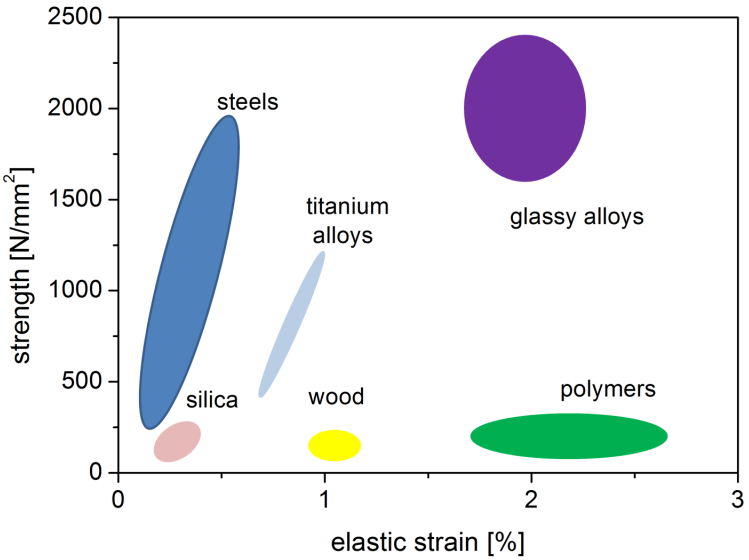

Figure 2.3: Comparison of the strength and the maximum elastic strain for different material classes after [30].

2.2.2 Plastic Deformation below T_g

One of the less desirable properties of BMG is their exceptionally low macroscopic plastic deformability **below** T_g. Most BMG fail at plastic deformations below 1% [31] or 2% [32], showing no macroscopic necking or any other sign of failure before they suddenly fracture. This is seen as a main disadvantage for applications as engineering materials [33]. The underlying failure mechanisms are still not entirely understood [32, 34, 35], but the failure occurs under static load in most cases along a single shear band under 45° to the principal normal stress, at the maximum shear stress. While BMG show no global plasticity, the fracture surface still shows a vein pattern indicating a high and highly located plasticity within the shear band [36, 37].

Some investigations of plasticity enhancement are carried out by various scientific researchers. One approach to enhance ductility is the development of composite materials with an amorphous matrix reinforced by a crystalline phase for example by melt infiltration. [38] for instance describes a method of casting a composite material with copper wires in a BMG matrix, combining the exceptional electric conductivity and ductility of crystalline copper with the high strength of the BMG, thereby having a high conductivity in the direction of the crystalline copper wires and a low conductivity within the BMG matrix orthogonal to the wire orientation. Another approach is the introduction of nano-crystals into the amorphous metal matrix by controlling the cooling conditions. The cooling rate is slowed in order to start crystallization, but it is still high enough to prevent the completion of the crystallization process. [39, 40]. The same effect can be achieved by a controlled annealing of an amorphous sample within the super cooled liquid region ΔT beyond the time

until onset of crystallization $t_{x,start}$. Controlled amounts of nano-crystals can be introduced into the BMG matrix by these methods. The presence of nano-crystals in the matrix is not always beneficial, as the introduction of brittle phases can lead to a severe embrittlement of the entire sample [40, 41], and partially crystalline samples are thermodynamically unstable compared to their fully amorphous counterparts. Some BMG alloys posses an intrinsic ductility [31, 42] which is attributed to the formation of nano-crystals in the crack tip by some researchers [23].

Recently, some exceptionally ductile BMGs that also show an extraordinary high fracture toughness K_{Ic} have been reported [43, 44]. The toughness of a BMG can range between 1 and $100MPa\sqrt{m}$, with some having fracture toughness values that can be compared to those of ceramics and some having fracture toughness values that can be compared to those of steels [20]. These values give rise to the expectation that amorphous metals may be able to reach a high damage tolerance after all.

2.2.3 Thermoplastic Forming

During heating above their glass transition temperature T_g, glassy alloys relax into the so called "supercooled" or "undercooled" liquid accompanied by a severe drop of the viscosity [45]. At T_g it reaches a value of 10^{12} Pa·s and drops further during subsequent heating [46]. Continued heating will cause primary crystallization at the crystallization temperature T_x. As a result of the low viscosity within the temperature range $\Delta T = T_x - T_g$, the material can be shaped by applying plastic deformations of up to several hundred percent at relatively low forces [47, 48]. This processing route is called "thermoplastic forming" (TPF) and can be compared to the deformation of thermoplasts or the blow molding of silica-glasses. The amorphous structure can be preserved during this shaping process, as long as the material is cooled below T_g before crystallization takes place. The time range from start until crystallization depends on the applied temperature. Time-temperature-transformation diagrams (TTT-diagrams) show the crystallization onset depending on time and temperature for a distinct alloy at isothermal conditions. Crystallization (also called devitrification) has to be avoided, since the crystalline counterparts of bulk metallic glasses are usually extremely brittle [49]. Once the BMG crystallizes, it can no longer be thermoplastically formed and has to be remelted and rapidly quenched in order to restore the amorphous structure.

An exemplary processing routine for thermoplastic forming (TPF) is shown in Figure 2.4 as an isothermal processing routine together with the continuous-cooling transformation during casting. Within ΔT, filigree surface patterning with high aspect ratios in the micro and nanometer range, joining of amorphous metal parts as well as the deformation of massive samples can be obtained [50, 51]. For the shaping of massive products either a massive amorphous semi-finished product, like e.g. a pellet, can be thermoplastically deformed or smaller fractions of a semi-finished product, e.g. granules, can be joined to produce a massive product, forming a stable bonding between the formerly separated material fractions [10]. Thermoplastic forming processes range from surface patterning techniques like embossing at the micro scale [52] to blow molding of vast hollow shapes [53]. The massive

deformation in the supercooled liquid state can reduce residual casting porosity. Thermoplastic forming can augment the shaping possibilities for amorphous metals that are limited during casting due to the need for a high cooling rate and the typically high viscosities of bulk metallic glass melts. Both properties are detrimental to a good form filling.

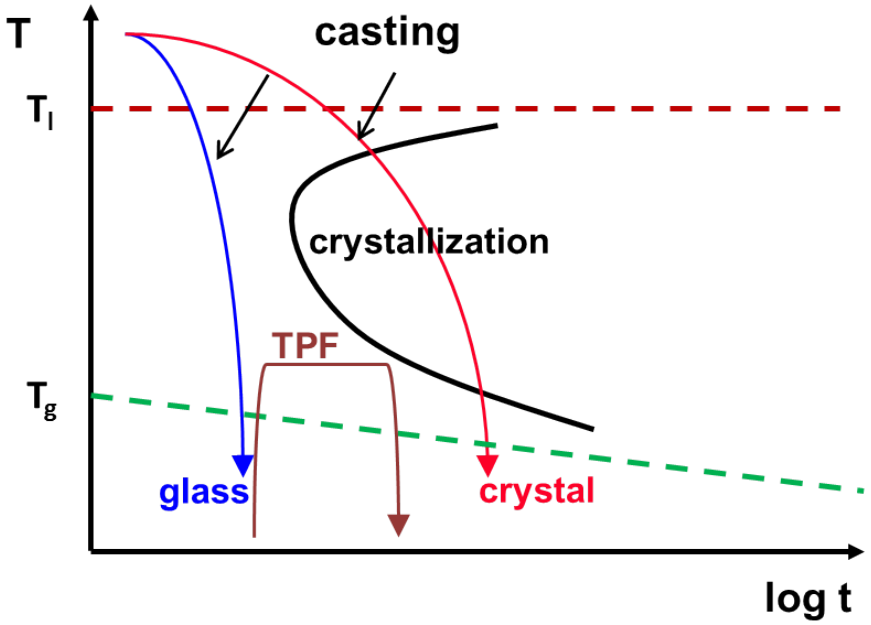

Figure 2.4: Schematic TTT-diagram for amorphous solidification with an isothermal processing routine for TPF; published in an earlier version in [13, 14, 15].

The viscosity of a supercooled liquid decreases with a rising processing temperature. At a given load, the deformation velocity depends on the viscosity. The lower the viscosity becomes, the higher the deformation velocity at a distinct load can become. Due to the need for a higher temperature, a smaller time frame for the deformation is available in that case as can be seen at the crystallization nose in the TTT-diagram in Figure 2.4. In [10] the author quantifies the deformability using the Hagen-Poiseuille equation, which describes the flow of a liquid through a canal with diameter d and length L. Figure 2.5 shows the velocity gradient of a liquid that flows through a canal.

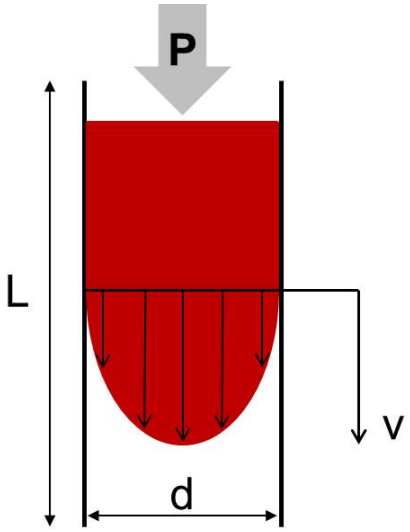

Figure 2.5: Velocity profile of a liquid that flows through a canal with diameter d and length L after [54].

The required pressure P can be calculated as:

$$P = 32v * \eta * \frac{L}{d^2} \tag{2.2}$$

with v being the velocity of the liquid and η the viscosity at the processing temperature. If the time until the onset of crystallization is taken into account v can be replaced by the term L/t_{onset} and equation 2.2 becomes:

$$P = \frac{32\eta L^2}{td^2} \tag{2.3}$$

The length of a canal L that can be filled at a certain processing temperature before crystallization sets in can be calculated as:

$$L = \sqrt{P * t_{x,onset} * \frac{d^2}{32\eta}} \tag{2.4}$$

With these relations, it was shown that the formfilling for the amorphous $Zr_{44}Ti_{11}Cu_{10}Ni_{10}B_{25}$ with the temperature-dependent crystallization time t_{onset} and the viscosity η (Figure 2.6) is constantly enhancing with increasing temperature.

The reason for this behavior is the much higher temperature dependency of the viscosity η compared to that of t_{onset}. It is therefore preferable to choose as high a processing temperature as possible within the range $\Delta T(T_x - T_g)$ to achieve maximum thermoplastic deformation.

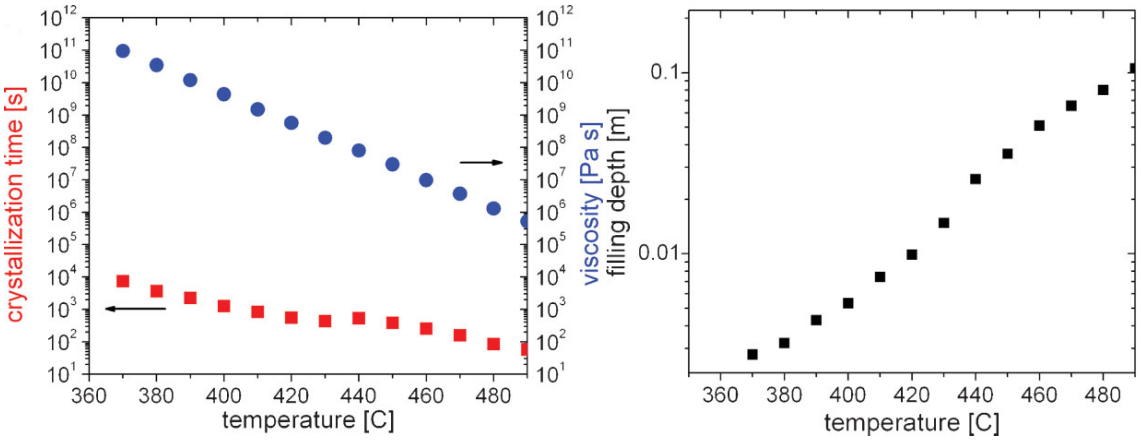

(a) TTT / viscosity (b) filling depth

Figure 2.6: left: TTT-diagram with $T_{x,onst}$ and temperature-dependent viscosity for the BMG $Zr_{44}Ti_{11}Cu_{10}Ni_{10}B_{25}$; right: filling depth calculated according to equation 2.2 (Diagrams reprinted from [10, 55]).

For the gold-based BMG $Au_{49}Ag_{5.5}Pd_{2.3}Cu_{26.9}Si_{16.3}$, a systematic study of time, temperature and pressure related deformability in the supercooled liquid region was carried out by Wang et al., showing best results at temperatures just below T_x [56].

Fiore et al. published a TTT-diagram of $Au_{49}Ag_{5.5}Pd_{2.3}Cu_{26.9}Si_{16.3}$ in 2011 [57]. This TTT-diagram is reprinted in figure 2.7. According to this TTT diagram, the time to crystallization onset at an isothermal processing temperature of 423 K (150 °C) is ≈ 32 min, at 433 K (160 °C) it is ≈ 8 min and at 443 K (170 °C) ≈ 3.5 min.

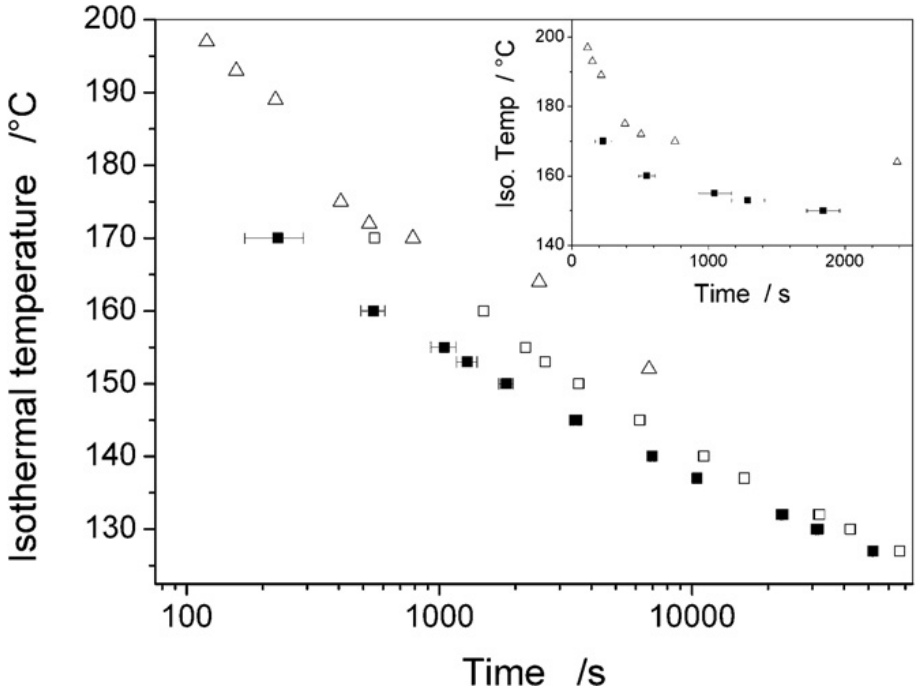

Figure 2.7: The TTT Diagram for $Au_{49}Ag_{5.5}Pd_{2.3}Cu_{26.9}Si_{16.3}$ reprinted from [57]

2.2.4 Shrinkage During Solidification

Bypassing crystallization during quenching of the melt not only means that an amorphous phase is formed, it also means that shrinkage due to crystallization does not take place as shown in Figure 2.8. The lack of crystallization shrinkage leads to a significant reduction of shrinkage-related casting defects like shrinkage porosity. The shrinkage in volume of amorphous metals is as low as $\approx$ 0.5 to 1 %, compared to $\approx$ 5 % in crystalline alloys [58]. For platinum-based crystalline solidifying alloys, a volume shrinkage of even 10% is reported [59], leading to a high amount of casting defects. This is particularly harmful in the processing of high-value precious metals.

The reduced shrinkage of BMG results in minimal dimensional discrepancies between casting products and mold geometries. Even nanometric features present on a mold surface are accurately reproduced on the surface of the amorphous cast product. Hence, near netshape casting can be achieved.

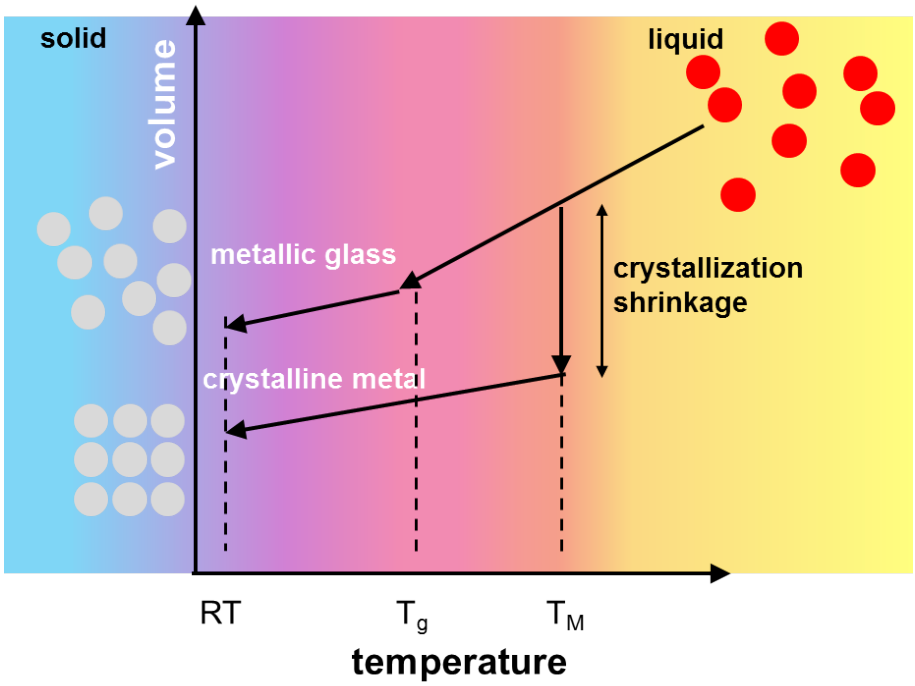

Figure 2.8: Schematic diagram for the volume reduction during solidification of a crystalline material in comparison to an amorphous metal; previously published in an earlier version in [13, 14, 15].

2.3 Glass-forming Ability (GFA) and Alloy Development

To date no comprehensive theory has been established on how to develop a glass-forming alloy with a good glass-forming ability. There are some empirical rules, though, on how to identify promising chemical compositions.

Bulk metallic glass-formers are usually found at eutectic or near eutectic compositions [60] in alloy systems with three or more components. A metallic melt is very stable against crystallization at its eutectic composition c_{eu}, this is reflected in its significantly low T_l [16]. Hence, most known BMG have a composition at or near to a deep eutectic. The driving forces for crystallization due to undercooling below the eutectic temperature T_{eu} at c_{eu} are lower than at compositions far from c_{eu} [16]. Having compositions at or near c_{eu}, the liquidus temperatures T_l of bulk metallic glasses are lower than the interpolation of the respective T_l of its components.

The lower the liquidus temperature of an alloy is, the more likely an amorphous solidification becomes. A high temperature in the melt causes a high atom mobility promoting the rearrangement of atoms and thus crystallization during cooling. Casting at low temperatures, as can be accomplished with eutectic or near eutectic alloy compositions, is therefore beneficial.

As a guideline for alloy development, Inoue et al. formulated three empiric rules for the identification of bulk metallic glass-forming compositions [61, 62].

1. The alloy should consist of more than three components
2. The three main alloy components should have atom radii that differ at least 12 %
3. The alloy constituents should have negative enthalpies of mixing

These empiric rules and their success in anticipating good glass-forming alloy combinations can be explained to some degree.

To have more than three components in a bulk metallic glass alloy is beneficial for the glass-forming ability (GFA), because crystallization is hindered by a topological and chemical diversity on atomic scale [63], and careful selection of the alloying elements can further lower the liquidus temperature. In complex alloys, a variety of complicated crystalline phases compete during nucleation. A vast reorganization by diffusion of several different atoms has to take place to form a nucleus. Hence, crystallization is also kinetically slowed down. This applies especially for complex eutectic systems, when several complex phases form at the same time and temperature.

To thermodynamically stabilize the amorphous phase against crystallization, the Gibbs free energy G_{glass} of the amorphous phase has to be below that of the crystalline phase $G_{crystal}$. The Gibbs free energy G is given by the following equation:

$$G = H - TS \tag{2.5}$$

The term $\Delta G = G_{glass} - G_{crystal}$ has to be negative, if the amorphous phase should be more stable than the crystal. Δ means the difference between the final and the initial state. ΔG can be expressed as:

$$\Delta G = \Delta H_f - T\Delta S_f \tag{2.6}$$

with H_f and S_f being enthalpy and entropy of fusion, respectively [16].

This means according to equation 2.6 either the difference in entropy of fusion ΔS_f has to be increased, or the value of ΔH_f has to be reduced (or both) [16] in order to have a negative value of ΔG. Increasing the amount of alloying components increases the entropy significantly, thereby leading to a dense atomic packing and meanwhile to a reduction of ΔH_f.

The atom radii of the alloy constituents should differ 12% or more in total. The atomic packing density is increased by a large variety of atom sizes, and the free volume for diffusion is reduced, resulting in a comparatively high viscosity of the melt and, hence, a retarded crystallization process [64]. From the kinetic point of view, melts with a high viscosity and a low amount of free volume favor the suppression of nucleation and crystal growth [65]. This is why bulk metallic glasses with exceptional glass-forming abilities are usually alloys with a large amount of constituents, which have large differences in the atom radii.

A negative heat of mixing also reduces atomic mobility by hindering the rearrangement towards a crystalline structure [64].

Another approach towards predicting good glass-forming ability can be made with the so called "Efficient Cluster Packing Model" or short ECP-model. According to this model, potentially successful alloys can be calculated [66] using theories about atomic structuring of multicomponent melts and dividing the alloying elements into solute and solvent species. In the case of the bulk metallic glass $Au_{49}Ag_{5.5}Pd_{2.3}Cu_{26.9}Si_{16.3}$, the solvent species is represented by gold, silver and palladium. The solvent species encircles the solute species, in this case copper and silicon, and forms so called clusters. The amount of atoms that are necessary to encircle a solvent is defined by the ratio of the atom radii.

Those clusters inhabit the lattice sites of an fcc, bcc or sc lattice and can overlap each other. Residual vacancies are occupied by the solved atoms. Thus the element concentration for the formation of the respective structure can be calculated from the atom radii. The calculated composition for an fcc-crystal-structure in the Au-Ag-Pd-Cu-Si system is as follows: $(AuAgPd)_{60}Cu_{20}Si_{20}$. The actual composition of Au-BMG1 $(AuAgPd)_{56,8}Cu_{26,9}Si_{16,3}$ is very close to the calculated value. For other precious metal alloys that have almost the same radii-ratios, $Pt_{60}(CuCo)_{18}P_{22}$ [2] and $Pd_{40}(CuNi)_{40}P_{20}$, and therefore the same results for an fcc-lattice, the compositions lie within the calculated values, as well. Deviations from the calculated values result from different cluster overlaps in contrast to the assumption from the model or from possible false occupancies.

In general, this model is an opportunity to identify concentration ranges with high probabilities for the existence of bulk metallic glass-forming compositions. Nevertheless, it is the interrelation of several different factors that contributes to the glass-forming ability of an alloy. The interaction of these different factors cannot be foreseen or simulated yet and can only be assessed alloy system by alloy system in trial and error testing.

The bulk metallic glass-forming systems either have only metals as their constituents, or one or several metalloids are alloyed to the metal alloys. In metal-metalloid BMGs, the content of metalloids was found to be ideally between 15 and 25 at.%. Pure metals alloys can already form metallic glasses with a content of 9 at.% additional alloying elements. This empiric rule is not yet understood theoretically [16].

These general criteria can be used as guidelines for the development of new bulk glassy alloys. For the development of a new gold-based BMG for jewelry applications, some additional constraints exist that limit the possibilities in alloy development. Jewelry alloys should not contain any elements that can be harmful to the health of the owner. Thus allergenic elements such as nickel are usually avoided. The usage of poisonous alloying elements such as cadmium is also restricted in jewelry applications. These restrictions rule some alloying elements for jewelry applications out. Another limitation for jewelry alloy development is the gold content, which should fit a certain caratage. Table 2.3 gives an overview over the most common gold contents. Potential BMG alloys on gold base should have a gold content that is at least as high but not much higher than either of these caratages. A gold content somewhere between two caratages is disadvantageous, as no intermediate caratage can be hallmarked and, hence, the lower of the two caratages would be hallmarked. The difference between the nominal caratage and the actual gold content

would be lost to the value of the alloy.

Table 2.1: Overview of the most common caratages in Germany

caratage	gold content [mass ‰]
22k	916
18k	750
14k	585
9k	375

2.4 Precious-Metals-Based Bulk Metallic Glasses

The exceptional properties of bulk metallic glasses suggest industrial applications for products that require properties such as high strength, high resilience or a high-quality surface finishing. In recent years gold- and platinum-based bulk metallic glasses that meet the specifications for jewelry alloys have been introduced [1, 2]. In the case of gold-based alloys, a minimum gold content of 75 wt% is necessary for the alloy to be hallmarked as a 18k gold alloy. Amorphous alloys with low gold content (e.g. 9k) are not attractive, as amorphous alloys are expected to be more expensive than their crystalline counterparts as long as their industrial production is not established yet. 18k alloys are usually applied in a more high-priced sector where high performance is regarded more important than low cost production. The amorphous platinum-based alloys introduced in 2007 have a platinum content of more than 85 wt%. In 2011 Pt-based BMG with a Pt content of 95 wt% were reported [67]. However, their critical casting thickness only reaches a maximum of 2 mm. But as 95 wt% alloys are more accepted in the market, those latter alloys can still be interesting for an introduction in industrial jewelry production.

Precious-metals-based bulk metallic glasses can exceed the properties of conventional crystalline jewelry alloys. For instance, typical drawbacks of precious metals and their alloys are their usually very low hardness and wear resistance, which render them prone to scratches or even deformation during usage. A crystalline 18k gold alloy usually has an as-cast hardness between 100 and 150 HV1 and up to 250 HV1 [9] or 300 HV1 [68] if thermomechanically treated. Amorphous $Au_{49}Ag_{5.5}Pd_{2.3}Cu_{26.9}Si_{16.3}$, on the other hand, possesses a hardness of 360 HV1 already in as-cast condition, with no need for further thermomechanical processing. For amorphous Pt-based alloys, as-cast hardness values of 400 HV1 are reported [2]. Comparable crystalline alloys possess an as-cast hardness of 37-136 HV1 and can reach up to 280 HV1 when hardened. Crystalline $Pt(CuCo)_{4.8}$ Ma-% is an exception. It possesses an as-cast hardness of 175-185 HV1, and after cold working and subsequent annealing it achieves hardness values of 420-430 HV1 [69].

To improve its strength, pure gold is usually alloyed for example with copper, silver, and other elements, and is additionally cold-worked. Figure 2.9 plots hardness values depending

on the amount of cold-working for different alloys, and Figure 2.10 shows tensile strength values depending on the alloying elements concentration.

Still, only a maximum hardness of 240 HV can be achieved by cold-working, and in this peak hardness case, the gold content already drops to 70 wt.%, which corresponds to a caratage below 18k (Figure 2.9). For high-performance and high-value applications, gold contents below 18k are not well accepted in the jewelry market.

The as-cast hardness of the BMG $Au_{49}Ag_{5.5}Pd_{2.3}Cu_{26.9}$ $Si_{16.3}$ at.% is shown in this plot along with the conventional crystalline alloys for comparative reasons. The as-cast hardness of $Au_{49}Ag_{5.5}Pd_{2.3}Cu_{26.9}Si_{16.3}$ has been reported by [2, 70, 25] to be 360 HV1, which was confirmed by hardness measurements performed during the present work. This high hardness in *as-cast* condition is unmatched by any crystalline gold alloy known today.

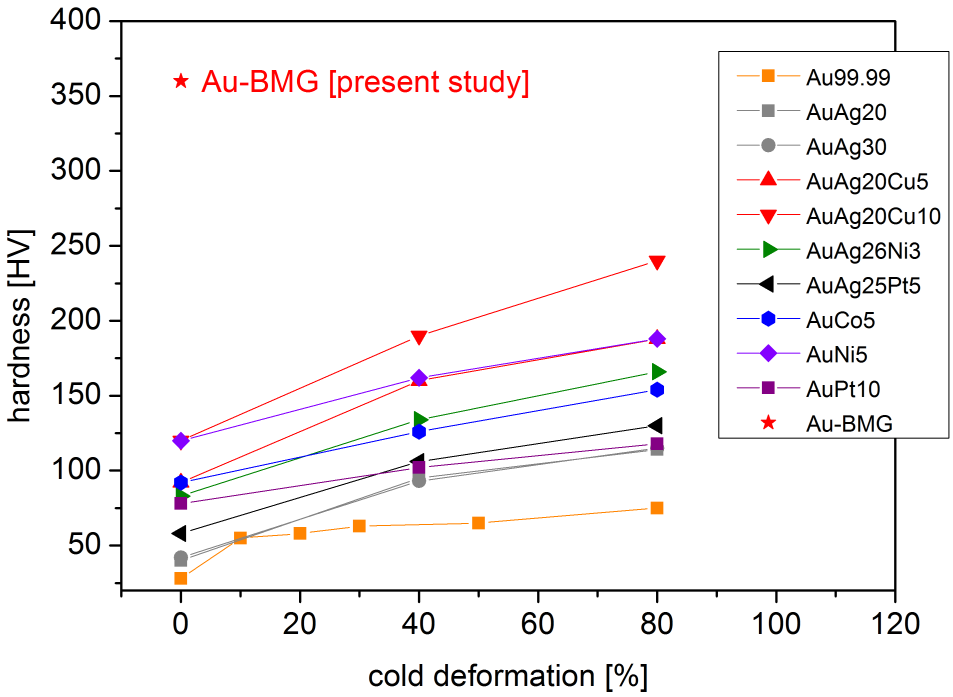

Figure 2.9: Hardness of gold (99.99% Au) and different gold-alloys depending on the level of work hardening after [59].

The influence of alloy elements on the tensile strength of conventional gold alloys is illustrated in Figure 2.10. The tensile strength can be considerably enhanced by adding nickel to the alloy. As many people are allergic to nickel, the alloying of nickel is detrimental for applications in the jewelry and watchmaking sector. Nickel can therefore only be used in alloys for technical applications. The compressive and tensile strengths of the gold-based BMG Au-BMG1 $Au_{49}Ag_{5.5}Pd_{2.3}Cu_{26.9}Si_{16.3}$ in comparison are also shown in Figure 2.10 [70, 25, 71].

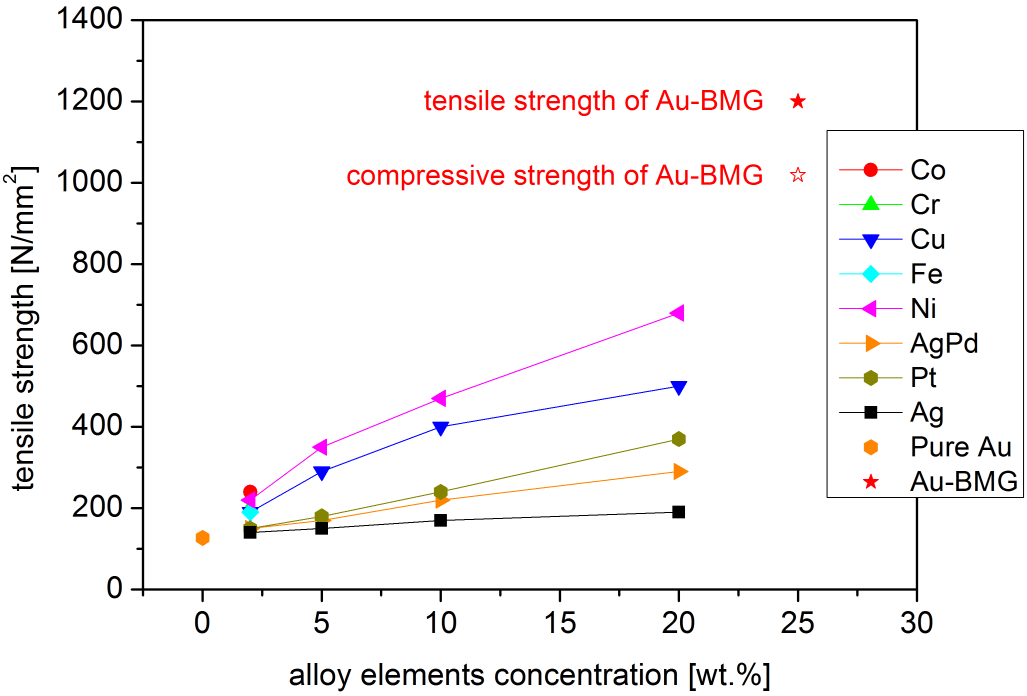

Figure 2.10: Tensile strength R_m of binary and ternary gold alloys depending on the content of alloying elements after [59], tensile strength value of Au-BMG after [9], compressive strength value after [70].

More recent studies report hardness values for crystalline 18k Au-Cu-Ag alloys in annealed and age-hardened condition plotted against the silver content in Figure 2.11 [72]. Hardness values of 300 HV can be achieved under laboratory conditions, but in industrial production, values of around 220 to 240 HV are more common [73, 74].

Another beneficial characteristic of BMG from the jewelry production point of view is their lower thermal conductivity with respect to comparable crystalline alloys. The thermal conductivity is reduced by one to two orders of magnitude [38, 75]. For jewelry products made from bulk metallic glass, this means that they feel "warmer" during cold temperatures in winter and "cooler" with respect to crystalline alloys if worn at hot temperatures as e.g. in a sauna, because the heat transfer is minimized.

Functional parts such as latches, chains or springs for watches are typical products that require high strength and high resilience. Crystalline precious metal alloys usually do not have sufficient material properties for those applications and hence, these parts are often made of steel or other not noble materials. This reduces the merit of the product and is not very desirable in the high price jewelry or watch sector. Amorphous metals possess the strength and resilience to replace those not noble parts, thereby enhancing the value of the product.

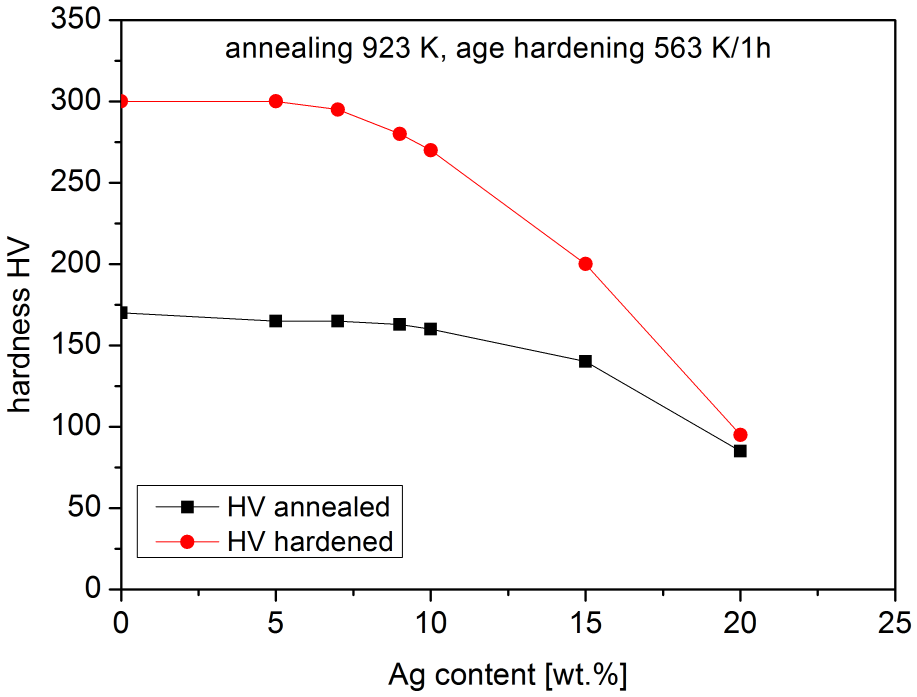

Figure 2.11: Vickers hardness of 18k Au-Cu-Ag alloys in annealed and age hardened condition depending on the silver content after [72]; previously published in an earlier version in [13, 14].

To date, the majority of industrial applications of BMG use zirconium-, cobalt- and iron-based alloys. Those alloys show considerable reactions with oxygen or the crucible material during the casting process. The resulting contamination of the melt with the products of these reactions often reduces the maximum casting thickness dramatically [16].The precious metal melts are much less prone to those reactions and are less complicated to handle in industrial casting devices, where contamination with oxygen cannot be completely avoided.

The gold-based alloy with the best properties is $Au_{49}Ag_{5.5}Pd_{2.3}Cu_{26.9}Si_{16.3}$. It has a ΔT of 58 °C [1] for thermoplastic forming and a critical casting thickness of 6 mm [76]. The platinum-based alloy with the best properties is $Pt_{57.5}Cu_{14.7}Ni_{5.3}P_{22.5}$. As it contains nickel, it may release nickel during usage as jewelry material. This can cause a nickel allergy, if the nickel release is too high. An alternative is the composition $Pt_{60}Cu_{16}Co_2P_{22}$, which does not contain any nickel. Its glass-forming ability is still very good. It can be thermoplastically formed in a temperature range ΔT of 63 K and has a critical casting thickness of 16 mm.

Usually, crystalline platinum-based alloys require a casting temperature of 1973 K to 2273 K (1700 °C to 2000 °C). Those high casting temperatures favor reactions between melt and crucible or investment material, if investment casting is applied. Amorphous platinum-based alloys only require casting temperatures between 873 K and 1173 K (600 °C to 900 °C). This dramatic reduction of the casting temperature reduces detrimental

reactions with crucible and investment. For gold-based alloys, the casting temperature is also reduced, albeit for gold-based alloys, this problem is not as pronounced as for platinum alloys. For an 18k crystalline solidifying gold-palladium white-gold, still a casting temperature of approximately 1673 K (1400 °C) is required [77], and only ≈ 873 K (600 °C) for the amorphous $Au_{49}Ag_{5.5}Pd_{2.3}Cu_{26.9}Si_{16.3}$ [9].

Table 2.2 lists the amorphous solidifying gold- and platinum-based alloys and their characteristic temperatures as they are reported in literature to date.

Table 2.2: Precious-metals-(PM)-based bulk metallic glasses and some of their properties according to [2, 6, 7, 67, 78, 79, 8]

Composition [at.%]	PM [wt.%]	T_g [K]	T_x [K]	ΔT[K]	T_l [K]	d_c [mm]
$Au_{49}Ag_{5.5}Pd_{2.3}Cu_{26.9}Si_{16.3}$	76	401	459	58	644	5
$Au_{40}Ag_7Pd_5Cu_{28}Si_{20}$	68.47	N/A	N/A	N/A	N/A	N/A
$Au_{52}Pd_{2.3}Cu_{29.2}Si_{16.5}$	79.98	393	427	34	651	2
$Au_{46}Ag_5Cu_{29}Si_{20}$	75.48	395	420	25	664	1
$Au_{55}Cu_{25}Si_{20}$	83.44	348	383	35	654	0.5
$Au_{50}Cu_{33}Si_{17}$	79.28	383	405	22	679	<1
$Au_{50}Cu_{25.5}Ag_{7.5}Si_{17}$	77.21	377	419	42	652	5
$Au_{60}Cu_{15.5}Ag_{7.5}Si_{17}$	83.88	359	403	44	670	5
$Au_{65}Cu_{10.5}Ag_{7.5}Si_{17}$	86.76	342	392	50	678	4
$Au_{70}Cu_{5.5}Ag_{7.5}Si_{17}$	89.39	339	375	36	680	3
$Au_{44}Cu_{37}Ti_1Si_{18}$	74.9	N/A	N/A	N/A	N/A	N/A
$Au_{44}Cu_{36}Ti_2Si_{18}$	75	N/A	N/A	N/A	N/A	N/A
$Au_{44}Cu_{31}Ti_4Si_{21}$	75.9	N/A	N/A	N/A	N/A	N/A
$Au_{42}Cu_{29}Ti_8Si_{21}$	74.61	393	413	20	1168	N/A
$Au_{50}Cu_{26}Sn_6Si_{18}$	77.43	355	386	31	603	1
$Pt_{57.5}Cu_{14.7}Ni_{5.3}P_{22.5}$	85.24	508	606	98	795	16
$Pt_{42.5}Cu_{27}Ni_{9.5}P_{21}$	73.93	515	589	74	873	20
$Pt_{60}Cu_{16}Co_2P_{22}$	86.75	506	569	63	881	16
$Pt_{76.5}P_{18}B_4Si_{1.5}$	95.87	474	511	37	859	0.5
$Pt_{74.4}Ni_{2.1}P_{18}B_4Si_{1.5}$	94.99	473	521	48	855	0.7
$Pt_{74.5}Cu_2P_{18}B_4Si_{1.5}$	94.97	480	528	48	865	0.9
$Pt_{74.5}Cu_{1.2}Ni_{0.8}P_{18}B_4Si_{1.5}$	94.99	476	522	46	857	1.3
$Pt_{74.7}Cu_{1.5}Ag_{0.3}P_{18}B_4Si_{1.5}$	94.98	479	529	50	862	2

2.5 Oxidation of Bulk Metallic Glasses

2.5.1 Rate Equations

The kinetic rate equations for the description of time-depending corrosion processes at a certain constant temperature are logarithmic, parabolic, cubic and linear equations according to [80].

2.5.1.1 Logarithmic Rate Equation

For low temperature oxidation, most metals show a rapid reaction at the beginning of the exposure of an unprotected active surface. The reaction then quickly slows down to almost unobservable rates or even ceases to take place. For example, this is the case when a passivating surface scale forms as a protective layer that prevents further oxidation. The kinetics of the reaction can often be quantified by the observation of a weight gain, the growth of a corrosion scale or the detection of a color change. The analyzed data can then usually be described by a logarithmic rate equation of the type:

$$Y = k_{log} log(t) + A \tag{2.7}$$

Y is the observed parameter that quantifies the progress of the oxidation. t is the time, k_{log} the rate constant and A a constant.

2.5.1.2 Parabolic Rate Equation

Parabolic rate equations can often describe data for oxidation at higher temperatures, where solid state diffusion is fast. Unlike the logarithmic behavior, parabolic rates do not approximate a point at which the reaction seemingly stops completely. However, compared to the initial oxidation rate, the reaction is slowed down at prolonged times. Parabolic rates can be described using either the differential or the integral form:

$$\frac{dY}{dt} = \frac{\widetilde{k_p}}{Y} \tag{2.8}$$

$$Y^2 = 2\widetilde{k_p}t + C = k_p t + C \tag{2.9}$$

k_p is the parabolic rate constant (and $\widetilde{k_p}$ is $\frac{1}{2}k_p$), while C is an integration constant. Parabolic behavior at high temperature oxidation applies as soon as thermal diffusion is the rate-determining process. The oxidation process is characterized by the diffusion of the respective reactants through a growing oxide scale, e.g. out-diffusion of the metal and in-diffusion of oxygen. A schematic drawing of this diffusion process is shown in Figure 2.12.

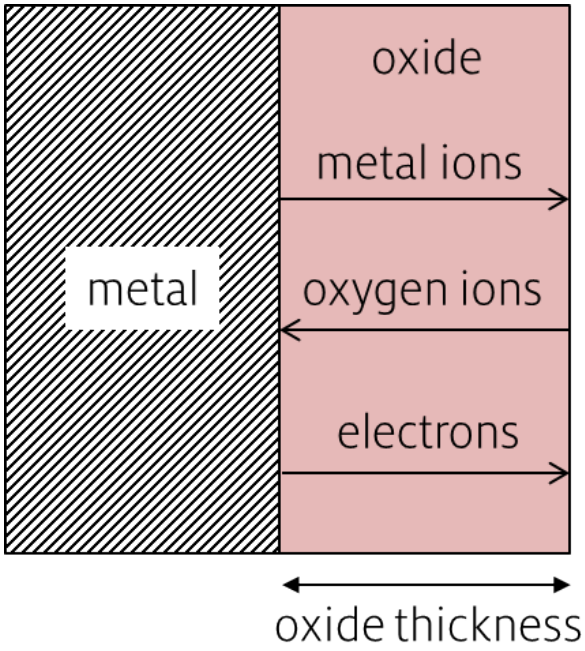

Figure 2.12: Schematic of the ion diffusion through an oxide scale typical for high temperature oxidation and a parabolic oxidation rate after [80].

2.5.1.3 Linear Rate Equation

Linear rate equations apply as soon as the oxidation process is not slowed down with progressing time but continues constantly. This may be the case if a steady state reaction that is limited by the absorption at the surface takes place or if the diffusion through a surface layer of a constant thickness is rate determining. The rate can then be described by the following equations:

$$\frac{dY}{dt} = k_l t \tag{2.10}$$

$$Y = k_l t + C \tag{2.11}$$

where Y is the observed parameter for the progress of oxidation, k_l is the linear rate constant, t the reaction time and C the integration constant.

Figure 2.13 shows the schematic behavior for ideal logarithmic, parabolic and linear behavior after [80].

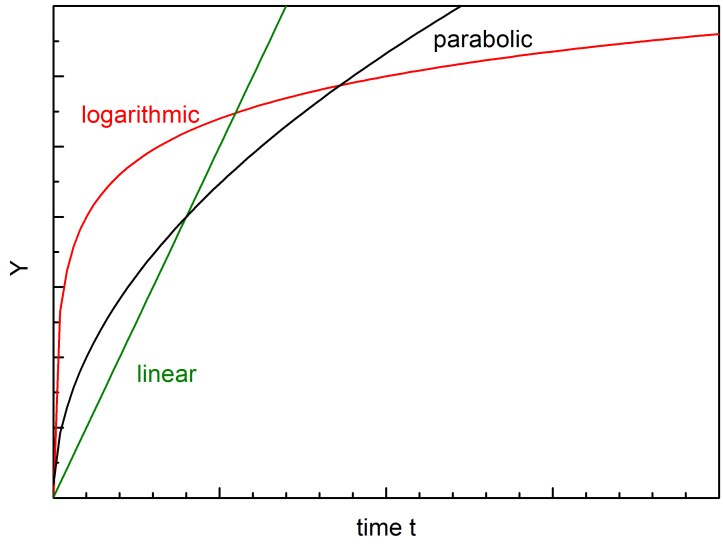

Figure 2.13: Schematic of the development of the observed oxidation coordinate following logarithmic, parabolic, and linear rates with respect to the isothermal time of oxidation after [80]. The oxidation coordinate can be any physical effect caused by corrosion attack including weight gain or weight loss, oxide scale thickness, or color change.

2.6 Dendritic Growth versus Dense Branching Morphology

During non-equilibrium crystalline solidification, dendritic growth of the solidifying phase is usually observed. This is a result of a distinct anisotropy caused by the developing crystalline phase and the predominant growth of a needle into the residual melt. For cubic metals, the direction of growth follows the preferred (100) direction [81]. In the presence of surface tension and the absence of "sufficient" anisotropy in either the surface tension or the growth kinetics, a different morphology can be observed: the dense branching morphology (DBM) [82, 83, 84]. The dense branching morphology is characterized by multiple tip splittings during the growth of branches of the new phase. During dendritic growth of needle-shaped dendrites no tip splitting occurs, though secondary needle-shaped branches can evolve starting from the main needle. The development of these two different morphologies can best be observed in 2D experiments in so-called Hele-Shaw cells, two transparent plexi-glass plates oriented parallel to each other and with little space between them which is filled with a viscous fluid. In figure 2.14, dyed glycerine was employed as the viscous fluid between the plexi glass plates [83]. In the center of the top plate, a less viscous fluid or gas (for example water or air) can be injected with a certain pressure to enforce

the replacement of glycerine by the injected phase, and the pattern of replacement can be observed. Employing flat (non-patterned) Plexi-glass plates, the authors always found the DBM pattern in their experiments. Employing patterned plexi-glass plates, meaning plexi-glass with distinct groove patterns, faceted growth or dendritic growth was observed, depending largely on the pattern geometry and the applied pressure on the less viscous liquid.

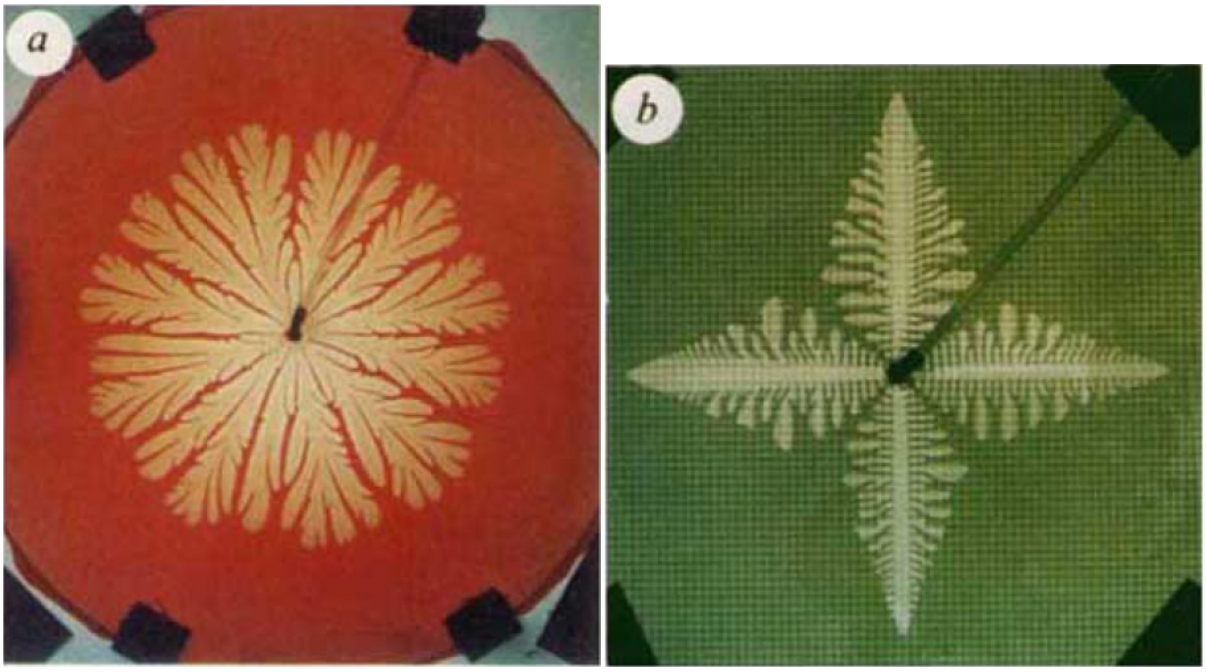

(a) Dense branching morphology (b) Dendritic growth

Figure 2.14: DBM and dendritic growth in Hele-Shaw cells for 2D observation of the differences in the morphologies reprinted from [83]

For the development of dendrites as well as tip splitting (namely dense branching morphology), the formation of stable protrusions on the interface between the growing phase and the surrounding phase is imperative. For the development of dendrites during *solidification* of alloys, the appearance of protrusions at the interface may occur statistically. In order for them to grow in needle shape into the liquid, this growth has to be favored in comparison to the uniform propagation of the solidification front. According to [81], a constitutional supercooling occurs in the liquid where protrusions are formed. This arises from the concentration gradient in the liquid from the rejected solvent elements during solidification of the primary phase which usually leads to a reduction of the local T_L of the liquid in the vicinity of the interface and rises first rapidly, then, farther away from the interface, it will slowly level to the overall T_L of the liquid. The temperature gradient in the melt however will rise linearly into the melt, resulting in the constitutional undercooling of the melt in the vicinity of the solid/liquid interface. The undercooling is highest at the protrusions, leading to a preferential solidification at the tip of the protrusion [85].

Dendrites grow in preferred growth directions. For example fcc crystals grow in ⟨100⟩ crystallographic direction [85], resulting in the typical needles during dendritic solidification. The reason why the initial needles are followed by the formation of secondary and tertiary arms is not fully understood.

2.7 Tarnishing and Corrosion of the Amorphous Au-Cu-Si System

The color change of gold-based amorphous alloys due to a tarnishing effect in artificial sweat has been reported and described for melt spun ribbons of $Au_{49}Ag_{5.5}Pd_{2.3}Cu_{26.9}Si_{16.3}$ and Ti-alloyed Au-Cu-Si alloys by P. Rizzi et al. [86, 87, 78, 79]. Of all alloys investigated in those studies, $Au_{49}Ag_{5.5}Pd_{2.3}Cu_{26.9}Si_{16.3}$ shows the worst behavior in terms of tarnishing. The ribbons surfaces were distinguished in wheel side, as the side of the ribbon that was in contact to the copper wheel during rapid solidification, and air side, the side facing away from the copper wheel. X-ray photoelectron spectroscopy (XPS) profiles were taken on both sides of the ribbons prior to and after the incubation in artificial sweat.

On melt-spun ribbons in as-quenched state, the formation of a 1 to 3 nm thick SiO_2 layer on the air side due to residual air trapped in the solidification chamber was observed, while the wheel side was found to be enriched in both silicon and copper. The preferential oxidation of silicon on the air side may be explained by its high tendency to oxidize with respect to the other alloying elements, copper, gold, palladium and silver. Silicon has also been reported to diffuse to the surface in liquid Au-Si due to its higher surface tension [88], which probably contributes to the formation of a dense SiO_2 layer during solidification.

After the test in artificial sweat, copper was found to be depleted in a surface layer on the wheel side and dissolved in the test solution, as was shown by inductively coupled plasma optical emission spectroscopy (ICP-OES) of the artificial sweat solution after the test. In comparison to the crystalline feedstock material, the melt-spun ribbons showed a better corrosion resistance quantified by the release of metal ions into the test solution.

Gold nano-particles were found to form on the surface as a consequence of the free corrosion in the test solution. The observed color change after incubation in artificial sweat was attributed to the formation of nanoporous gold on the surface [87]. The formation of nano-crystals is a result of the selective corrosion of the less noble alloying elements copper and silicon. The remaining matrix deviates from the initial composition resulting in non-glass-forming composition and hence allowing nano-crystallization. This effect can be used to intentionally form nanoporous gold surfaces, which was shown in [78] and [79] for $Au_{44}Cu_{31}Ti_4Si_{21}$, $Au_{42}Cu_{29}Ti_8Si_{21}$ and $Au_{40}Ag_7Pd_5Cu_{28}Si_{20}$.

Ketov et al. [89] report a discoloring towards yellow for $Au_{49}Ag_{5.5}Pd_{2.3}Cu_{26.9}Si_{16.3}$, as well. The yellow color was observed immediately after casting of rod-shaped samples into a copper mold. This initial yellow color was attributed to a crystalline surface layer of up to $80\mu m$ thickness that forms during casting probably due to heterogeneous nucleation in contact with the copper mold and not because of a corrosion reaction, namely tarnishing.

The underlying mechanisms of the tarnishing have been understood as a result of the work presented in this thesis and are discussed in Section 5.2.

2.8 Investment Casting of Small Metal Parts

Investment casting is a lost mold casting procedure. It is the most common casting procedure in jewelry production as it provides high flexibility in the geometry of the cast product, a good form filling and allows the fabrication of small parts with thin walls and high complexity. The typical steps are:

1. Fabrication of a wax or plastic model of the desired cast product
2. Positioning of the model on a cast tree (Figure 2.15 (a))
3. Installation of the wax tree in a flask for the casting (Figure 2.15 (b))
4. Filling of the flask with the liquid investment material (Figure 2.15 (c))
5. Hardening of the investment inside a furnace and removal of the wax (or plastic) parts by melting (Figure 2.15 (d))
6. Casting of the molten alloy into the cavity left by the removed wax model (Figure 2.15 (e))
7. Removal of the investment to retrieve the metal tree (Figure 2.15 (f))
8. Removal of the cast products from the sprue and finishing of the parts

The wax or plastic models can be individually shaped. Commercial rapid manufacturing and prototyping devices for the fabrication of the models are available. The easy access to individual shapes directly from computer-aided designs (CAD) creates the possibility to produce prototypes and small-sized batches within short time frames. On the other hand also mass production of jewelry items and other cast products is applied in investment casting today [90, 91, 92].

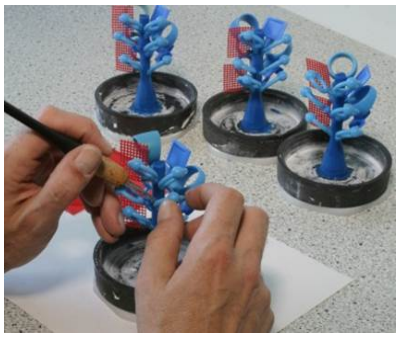

(a) Wax models on a tree

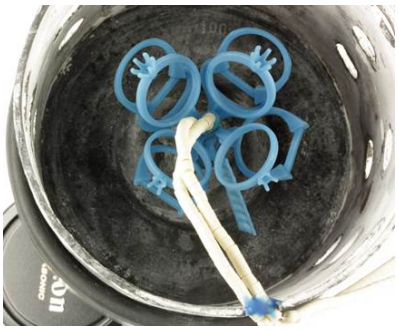

(b) Tree inside the flask

(c) Flask with investment

(d) Removal of the wax (melting)

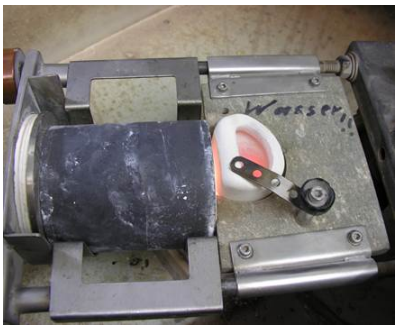

(e) Casting into the flask cavity

(f) metal tree after removal of investment

Figure 2.15: Investment casting of jewelry items.

The investment is usually optimized to withstand high temperatures and to have a low driving force for a reaction with the liquid metal in contact during the casting. Often the investment is heated prior to casting in order to prolong the time span in which the metal stays liquid within the mold. This promotes a high form filling and reduces cast pores caused by premature solidification (shrinkage cavities or sinkholes). Hence for the application of investment casting with bulk metallic glasses, the usual investment material is not suitable. Peker et al. [93] state in paragraph [0030] of their 2006 US patent regarding the investment casting of bulk-solidifying amorphous alloys: "The investment casting process has not yet been successfully applied to the production of these bulk-solidifying amorphous alloys." As one of the main obstacles for the application of investment casting on BMG alloys the patent authors name the difficulty to apply sufficient cooling rates in the paragraph [0030].

As a result of the present work, a solution to this problem has been found, see Section 4.1.4.

2.9 Electroforming of Copper Molds on Wax Models

Electroforming is a well established technique to build massive structures through electrochemical precipitation of metal from an electrolyte on an electric conductive substrate [94]. On wax models that are inherently not conductive, the surface has to be coated with a thin electric conductive layer such as silver conductive paste or graphite powder. The thickness of the electroformed metal layer can easily reach several centimeters, if the eloctrolyte is monitored during the procedure.

For copper galvanoforming, cyanidic as well as acidic electrolytes can be applied. However, acidic electrolytes with copper sulfate $CuSO_4$ are more common. Copper electrolytes usually contain 80-250 g/l $CuSO_4 \cdot 5H_2O$, 40-200 g/l sulfuric acid H_2SO_4 and 30-150 mg/l chloride. The precipitation of elemental copper follows the equation [95, 96]:

$$Cu^{2+} + 2e^- \rightarrow Cu \tag{2.12}$$

3 Methods

3.1 Processing

In this section, the experimental setup and the general parameters for the sample production are described. In particular, the descriptions of the casting, thermoplastic forming, preparation of crystalline sample material and grinding and polishing are given.

3.1.1 Casting

The castings were performed employing commercially available casting devices, namely an Indutherm MC50 tilt casting machine and a Topcast TCE10 centrifugal casting device.

3.1.1.1 Tilt Casting

The tilt casting experiments were conducted in a commercial Indutherm MC50 tilt casting device. The chamber was evacuated and subsequently purged with argon in three so called washing cycles. Following the three washing cycles, the chamber was evacuated one final time, and the feedstock material was melted in an inductively heated graphite crucible and brought to a casting temperature of 1423 K (1150 °C). As feedstock either the raw elements were directly alloyed in the casting device and then cast into the desired sample shape or pre-alloyed granules were remelted and cast. This is shown in Figure 3.1 (a) and (b). As soon as the melt reached the casting temperature, the chamber was tilted in order to let the melt flow into the mold using gravity as the only acceleration force. This is illustrated in Figure 3.1 (c). At a tilting angle of 75°, argon was pumped into the chamber building an overpressure of 1.5 bar to force the residual melt into the mold cavity for a better formfilling.

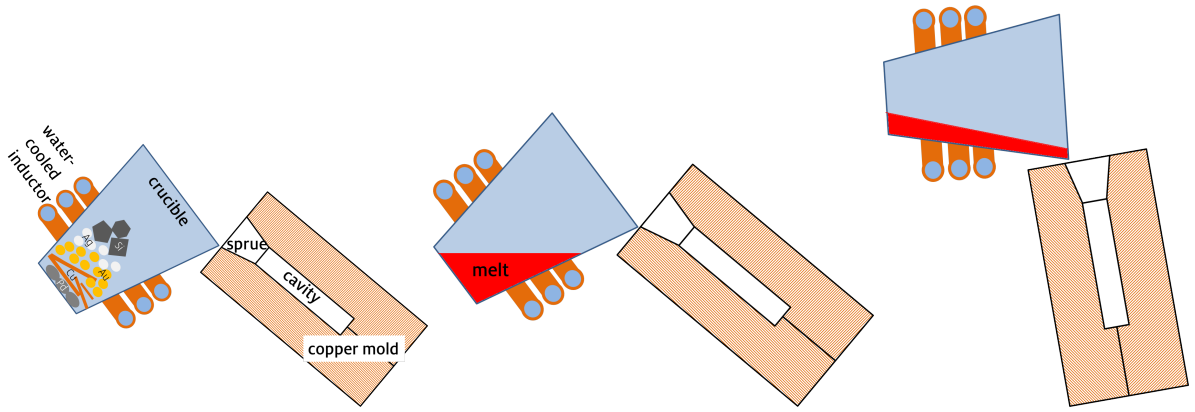

(a) set up before heating (b) melting the ingredients (c) pouring the melt into the crucible

Figure 3.1: Tilt casting: (a) crucible with raw material inside the spool; (b) heating and alloying of the raw material; (c) tilting of the casting chamber and gravity casting.

Figure 3.2 (a) shows the setup of the casting chamber with the inductor, a typical graphite crucible and a massive copper mold that was installed inside a graphite cylinder to ensure a secure fixture for the mold during tilt casting. Figure 3.2 (b) shows a massive copper mold with an as-cast sample of $Au_{49}Ag_{5.5}Pd_{2.3}Cu_{26.9}Si_{16.3}$ after the tilt casting procedure. This particular mold allowed casting of samples with a rectangular shape of 2x12x47 mm, the standard sample shape for most experiments conducted in the present work.

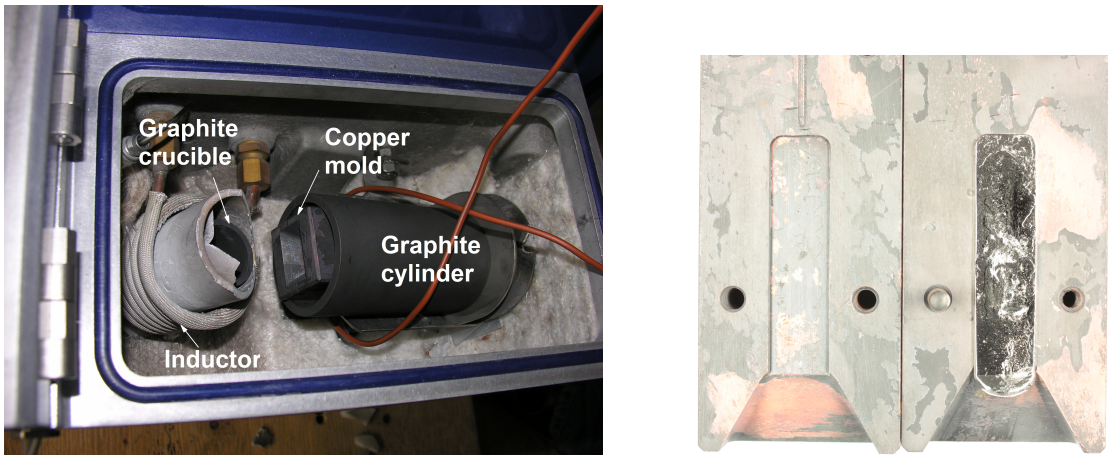

(a) casting chamber of MC50 (b) Copper mold with an as-cast sample

Figure 3.2: Tilt casting: (a) photograph of the casting chamber with graphite crucible inside the induction heating device, copper mold and graphite cylinder for mold fixture; (b) Copper mold for the casting of amorphous samples with a tilt-cast sample still inside the mold. The temperature during casting was measured at the tip position of the cavity.

3.1.1.2 Centrifugal Casting

The majority of the specimens processed in the present work was cast employing a centrifugal casting process in a Topcast TCE10 (10 kW) casting device. The centrifugal forces guarantee a high accelaration towards the mold and hence a better formfilling in comparison to gravity or tilt casting. The centrifugal arm was accelerated to its final velocity of 440 rpm (rounds per minute) within 0.73 seconds. Figure 3.3 illustrates the centrifugal casting process. After the feedstock material was heated to its casting temperature the induction spool was lowered and the arm accelerated. The acceleration shifted the crucible towards the mold, and the melt rose inside the cone-shaped crucible until it left the crucible through a small opening and flowed into the sprue and the cavity of the copper mold as illustrated in Figure 3.3 (b).

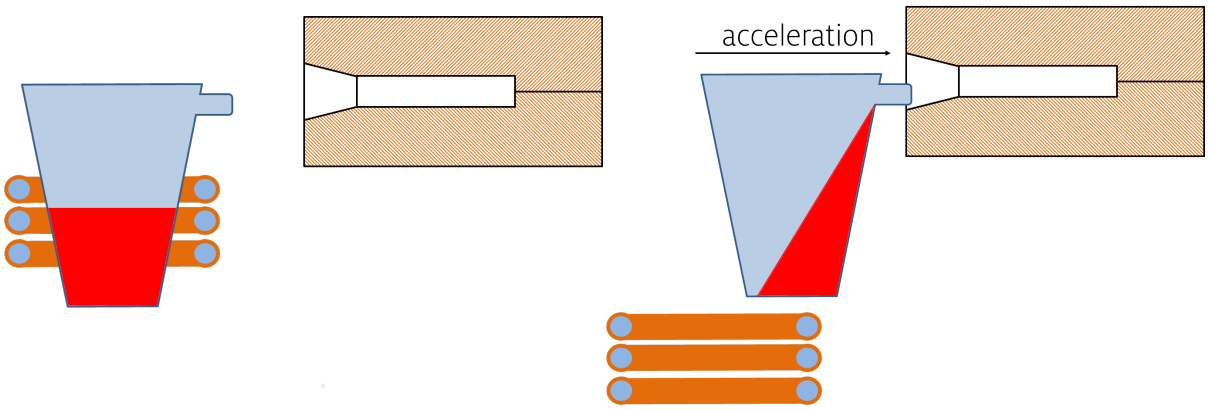

(a) setup during heating (b) acceleration during casting

Figure 3.3: Centrifugal casting: (a) the crucible and the melt inside the induction spool during heating; (b) acceleration of the crucible and the melt towards the mold during centrifugal casting.

The temperature of the mold was monitored during the entire casting procedure. Under ideal casting conditions, the temperature of the mold rose only 3 to 5 K above the initial mold temperature, which usually was room temperature of 293 - 297 K (20 - 24 °C). The setup within the casting chamber is shown in Figure 3.4. The counter weight balances the weight of the crucible including the alloy material and the copper mold with a fixture to prevent vibrations due to imbalance while casting. The temperature of the melt was monitored with a Maurer pyrometer type QKTRD1085-1 through an observation window. Temperatures that can be observed by the pyrometer range between 1023 and 2773 K (750 - 2500 °C). Typical casting temperatures of 1423 - 1473 K (1150 - 1200 °C) were applied for castings into massive copper molds. For castings with the new casting technique (lost metal mold casting), the casting temperatures were reduced to 1023 - 1073 K (750 - 800 °C) to decrease the thermal energy of the melt and hence the equilibrium temperature of mold and sample. This is described in more detail in section 4.1.4.

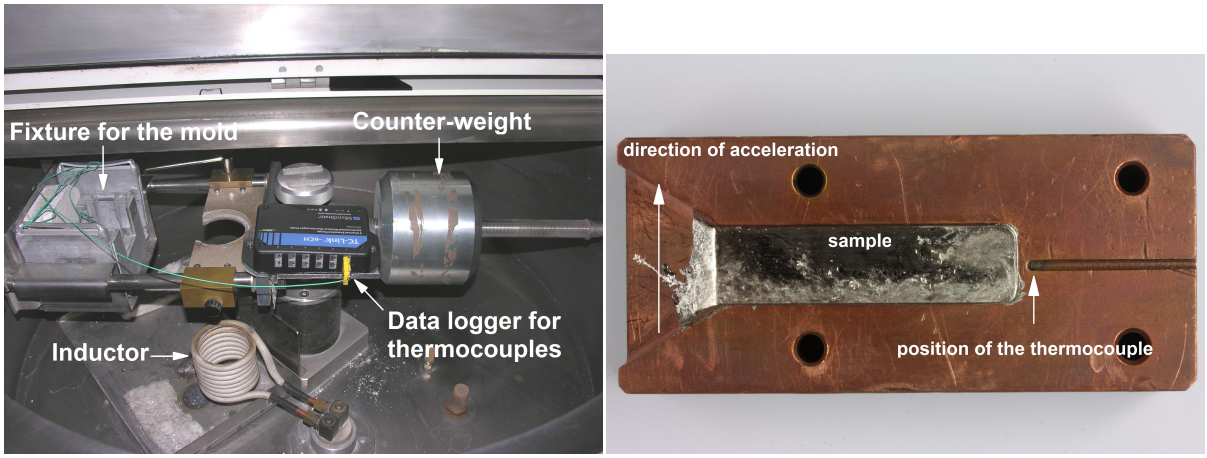

(a) casting chamber of TCE10 (b) Copper mold with an as cast sample

Figure 3.4: Centrifugal casting; (a) photograph of the casting chamber with the rotatable casting arm, fixture for the mold, inductor, counter weight, and data logger for temperature monitoring with thermocouples; (b) copper mold for the casting of an amorphous sample with a centrifugal cast sample still inside the mold; previously published in [13, 14, 15].

3.1.1.3 Casting Simulation

The Software FLOW3D uses the Finite Difference Model, a method that discretizes the spatial domain into small cells to form a volume mesh or grid. The software has its own internal multi-block meshing system, which allows to increase the detail on specified areas of the geometry, and it then adopts a "control volume" approach to solve the Navier-Stokes equations: for the conducted simulations a grid with 200.000 - 250.000 cubic cells was adopted, with a cell size of approximately 0.001 mm. To simulate the tilting and centrifugal processes, the corresponding physical models were activated (GMO - Moving and deforming objects). Density was set to 14.7 kg/m^3, and viscosity was set to 0.004 Pa·s.

3.1.2 Thermoplastic Forming with Granules as Feedstock Material

The granules were positioned inside a partable metal molding device to form cup-shaped samples and then heated above T_g as shown in the sketch of Figure 3.5. With a deformation force of up to 5 kN, the granules were then pressed between the two metal parts. The formability of the amorphous $Au_{49}Ag_{5.5}Pd_{2.3}Cu_{26.9}Si_{16.3}$ within the supercooled liquid region then results in a bonding between the granules.

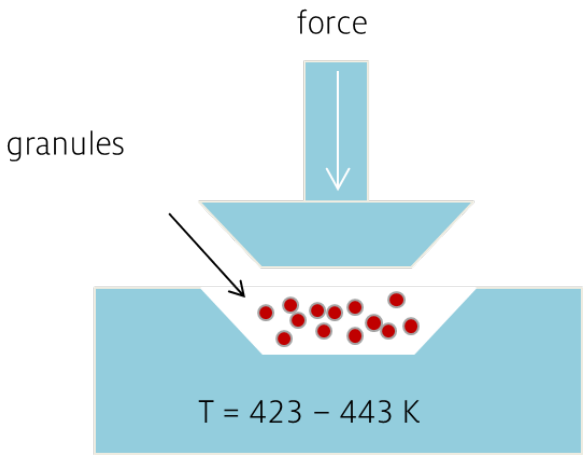

Figure 3.5: Thermoplastic forming of bulk samples using amorphous granules.

The sample material shown in the present work was thermoplastically formed at Saarland University.

3.1.3 Preparation of Crystalline Sample Material

Bulk metallic glass alloys show a sluggish crystallization behavior and often do not crystallize completely even when cast in much higher thicknesses than the critical casting thickness. To cast fully crystalline samples, a significantly slow cooling rate has to be applied to allow the equilibrium crystal phases to form. As an alternative to this procedure, amorphous samples can be isothermally annealed above the glass transition, allowing the crystallization to start and finish according to the TTT-diagram, or amorphous sample material can be heated above the crystallization temperature, causing immediate crystallization when passing T_x.

For this study, crystalline samples were prepared by:

1. Slow cooling from the melt inside the furnace: equilibrium-cooled
2. Isothermal heat treatment for 1 h at 423 K (150 °C) and additional 3 h at 428 K (155 °C), both temperatures are between T_g and T_x
3. Isothermal heat treatment for 1 h at 523 K (250 °C), which is above T_x

The first and the second crystallization treatment was performed at Saarland University. The schematic isothermal time-temperature profiles for each heat treatment are shown in Figure 3.6. Heat treatment number 2 was at first carried out for 1 hour at 423 K (150 °C) but this resulted in an only partially crystalline sample according to XRD analysis. Hence, a second heat treatment for another 3 hrs at the even higher temperature of 428 K (155 °C) was carried out.

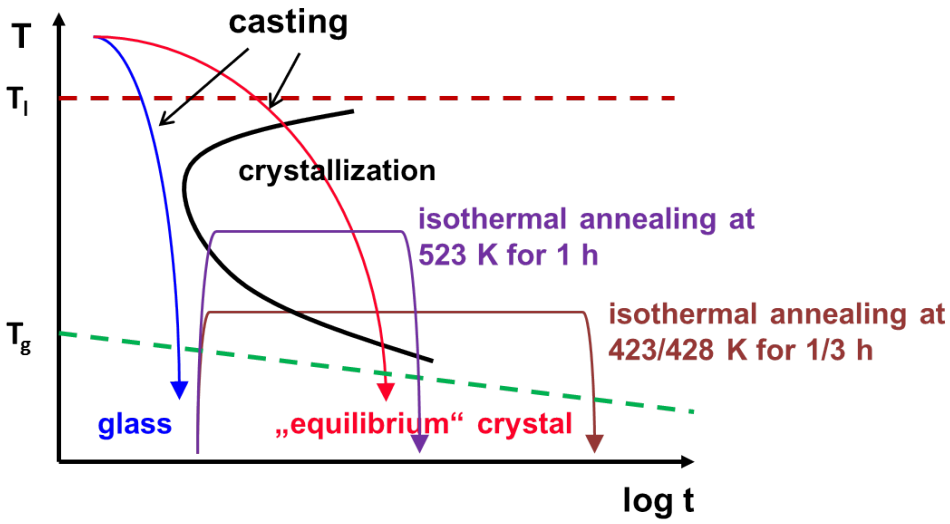

Figure 3.6: Time-temperature profiles for the preparation of crystalline samples for this study.

3.1.4 Standard Grinding and Polishing Procedure

Grinding was done by successively employing coarse to fine grain-sized sand paper from 500 grains per inch to 1200 grain per inch according to the "Federation of European Producers of Abrasives" (FEPA) European standard. Subsequent polishing was carried out with diamond particles dispersions, successively applying coarse particle sizes to finer particle sizes from a diameter of 6 μm to 3 μm to 1 μm.

3.1.5 Ion Milling

During mechanical polishing as described in the preceding section, plastic deformation of the polished surface cannot be avoided in the majority of cases. Residual plastic deformations in the surface after the polishing can alter the observed microstructure. The extent of residual plastic deformation depends on the applied forces during sample preparation and on the material parameters. Soft materials tend to be deformed to a larger extent than hard materials, with the effect that soft phases can smear over harder phases or the entire microstructure is deformed in one direction, giving the erroneous impression of a textured microstructure.

The plastic deformation is a superficial effect and can be removed by ion milling. For SEM investigation, the BMG samples were argon-ion milled in a BAL-TEC rapid etching system (RES) 101. To avoid heating of the sample during ion milling, a special routine was applied with alternating 2 min ion milling sequences and 15 min pauses. The acceleration voltage was 6 V, and the current 2.2 mA. Canon I and II were oriented at an angle of 3°.

3.2 Corrosion Experiments

A systematic study was set up to investigate the corrosion behavior in various different controlled environmental conditions. The conditions involve different atmospheres and liquid environments as well as different temperatures. The following sections describe the different experimental setups for the corrosion experiments.

3.2.1 Heat Treatment Experiments

Heat treatment experiments were conducted at different temperatures and different atmospheres. Amorphous samples in the shape of 2 x 12 x 47 mm were prepared using copper mold casting. These long plates were subsequently cut into smaller pieces of approximately 12 x 10 mm rectangular shape. To guarantee a reproducible surface condition and to remove possible residual oxides and other cast contaminates, all samples were ground and polished on one side according to the standard grinding and polishing procedure of Section 3.1.4.

The samples were cleaned in ethanol using an ultrasonic standard cleaning device and subsequently handled with great care using tweezers and gloves to avoid the contact with sweat from bare fingers.

For the aging experiments, four temperatures were chosen. An elevated temperature of 348 K (75 °C), which is approximately 50 K below the glass transition of $Au_{49}Ag_{5.5}Pd_{2.3}Cu_{26.9}Si_{16.3}$ (T_g = 401 K), 310 K (37 °C), because the intended application as a jewelry alloy requires stability at body temperature, 297 K (24 °C) as reference for storage at room temperature (RT) and 255 K (-18 °C), which is almost another 50 K below room temperature. Table 3.1 gives an overview on the applied conditions. At RT and at 348 K (75 °C), in addition to the treatment in laboratory air, the influence of vacuum and dry air[1] and argon flux treatment was investigated, respectively.

Temperature [K]	Air	Dry air[1]	Ar	Vacuum
255	x			
297	x	x		x
310	x			
348	x		x	

Table 3.1: Aging experiments

The samples were stored in different sample holders for different test runs. Figure 3.7 gives an overview on the different storage conditions applied in this study. The storage in glass tubes resulted in significantly reduced tarnishing rates in comparison to the storage in small ceramic cups or samples that were situated in the furnace on a plate without a sample holder. Different test runs are therefore difficult to compare with each other,

[1]Dry air means sample storage in a desiccator.

especially if different alloy compositions are compared with each other. Thus, in each test run, the alloy $Au_{49}Ag_{5.5}Pd_{2.3}Cu_{26.9}Si_{16.3}$ was always included as a benchmark material, and the corrosion performance of other compositions was evaluated in comparison to the benchmark material. In a test run with 2 individual samples of $Au_{49}Ag_{5.5}Pd_{2.3}Cu_{26.9}Si_{16.3}$ from different casts stored under identical storage conditions, the color development showed a high reproducibility.

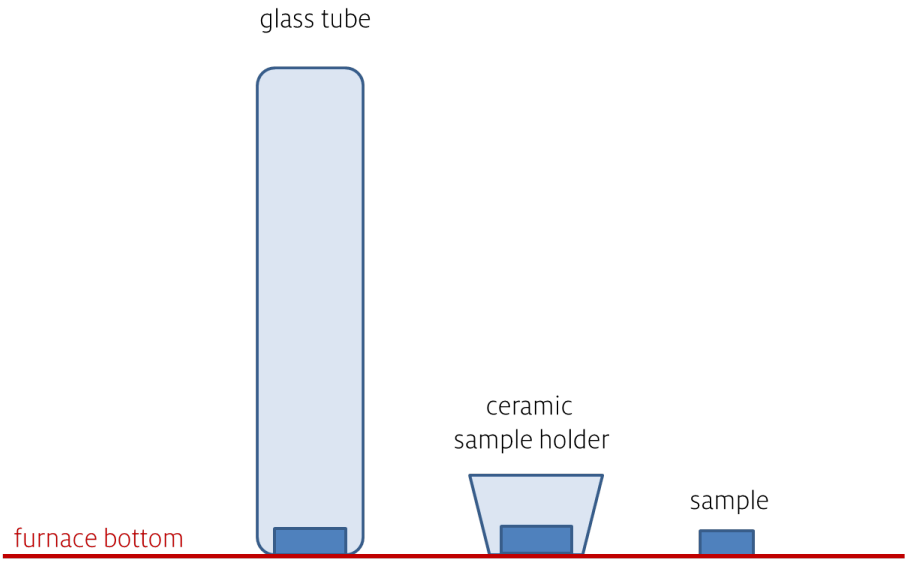

Figure 3.7: Sample storage conditions for the tarnishing test at elevated temperatures in air. For different test runs, different sample holders were used. The test of samples in glass tubes produced significantly lower tarnishing rates due to the limited oxygen flux in the tube.

3.2.2 Test in Simulated Body Fluids

The test in simulated body fluids was carried out on ground amorphous samples of 2 mm thickness. The grinding procedure is described in section 3.1.4. Each sample surface area, i.e. the interface between sample and test solution, was measured prior to the test, and the samples were subsequently immersed into the respective test solution, i.e. artificial sweat or saliva at body temperature of 310 K (37 °C). After a test period of 7 days, the test solution was analyzed for the alloying elements, in order to determine which elements went into solution as a result of the corrosion attack of the respective artificial body fluid. The element concentration was then determined as dissolved element concentration per cm^2 sample surface.

3.2.2.1 Artificial Saliva Standard Test DIN EN 10271

The test solution was created by dissolving 10.0 ± 0.1 g lactatic acid $C_3H_6O_3$ of 90% analytic cleanliness and 5.85 ± 0.005g NaCl with analytic cleanliness into approximately

300 ml water (quality 2 according to ISO 3585). Once the solvents were dissolved, the solution was further diluted with water to 1000 ± 10 ml. The pH-value was tested. If it was within 2.3 ± 0.1, the fluid was taken for the test, otherwise, it was discarded.

3.2.2.2 Artificial Sweat Standard Test DIN EN 1811

The test solution was prepared by dissolving 5.00 ± 0.01 g NaCl, 1.00± 0.01 g urea $CO(NH_2)_2$ and 1.00± 0.01 g lactatic acid $C_3H_6O_3$ in 900 ml de-ionized water.

3.2.3 Sulfide Immersion Standard Test EN ISO 1562

Amorphous sample material was prepared by casting plates of 2 mm thickness. The sample material for the sulfide immersion test was prepared in a metallographic cross section embedded in resin material. For this study, "EpoFix Resin" and "EpoFix Hardener" from "Struers" were employed as resin material. The cross sections were ground and polished in subsequent steps until a polish with 1 μm diamond solution was applied according to the standard polishing procedure of section 3.1.4.

The test solution for the sulfide immersion standard test was an aqueous solution of 0.1 mol/l sodium sulfide. 22.3 ± 0.1 g sodium sulfide hydrate (Na_2S x H_2O approx. 35% Na_2S) were dissolved in water of quality 2 according to ISO 3696:1987 and diluted to 1000 ± 3 ml water.

The samples were then installed in the test setup shown in Figure 3.8. The test is usually carried out for 72 h, and the test solution is exchanged with a freshly prepared solution every 24 hours. During this short interruption of the immersion test, the samples were cleaned with ethanol C_2H_5OH to remove any non-adhesive pollution on the samples surface that could influence the contact between sample surface and test solution. During the immersion sequences, the samples were dipped into the test solution in a cycle of one immersion per minute. During these 60 second cycles, the entire sample surface was covered by the test solution for 10 to 15s. The temperature was kept at 296 ± 2 K (23 ± 2 °C). For the first 72 h, the test was carried out according to the Standard EN ISO 1562. Subsequently, the test was run for another 4 days under the same conditions, but without an exchange of the test solution.

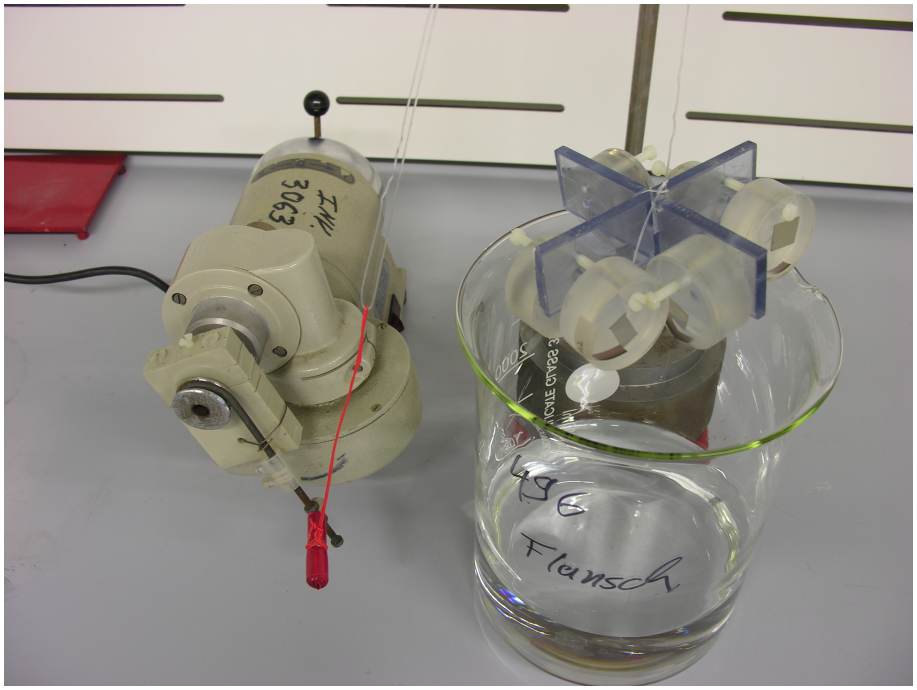

Figure 3.8: Test apparatus for the sulfide immersion test with samples embedded in transparent resin material.

3.3 Analysis

In the following subsections, the analyzes that were employed to characterize the samples are described. This includes colorimetric analysis, DSC measurement, XRD analysis as well as SEM, STEM and TEM investigation and chemical analyzes.

3.3.1 Colorimetric Analysis According to Standard Tests DIN 5033, ASTM D1925 and DIN 6174

To quantify the color of metallic samples, a standard test according to DIN 5033 part 4 was carried out. A standardized quantification of the color is of great interest for jewelry products, as different viewers evaluate colors differently, especially under different lighting conditions. For the present work, the observer was 10 °, the light applied was D65 "Daylight" and the analysis geometry was d/8 according to the standard test. The colorimetric analysis data were also used to quantify the change in color ΔE due to the tarnishing effects, and the Yellowness Index YI was determined according to standard ASTM D1925.

The samples are required to have a flat and polished surface to guarantee best light reflection conditions. As the surface roughness can have an influence on the L^*-value, all samples were ground and subsequently polished according to the standard polishing procedure of Section 3.1.4. This procedure also removes residual oxides originating from the casting process and provides a homogeneous surface condition.

Applying standard test procedure DIN 5033, the color is given by three coordinates: L^* for the luminescence, $+a^*$ and $-a^*$ for colors that tend to a reddish or greenish appearance, respectively, and $+b^*$ or $-b^*$ for colors that tend to have a yellowish or blueish appearance, respectively. Figure 3.9 shows the color distribution, as it can be described by the $L^*a^*b^*$ coordinates.

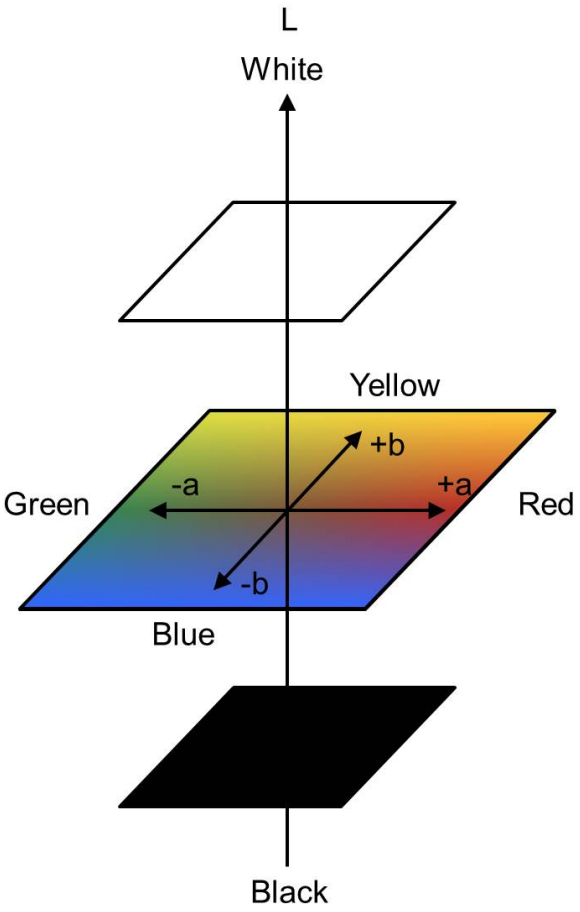

Figure 3.9: $L^*a^*b^*$ Color coordinates according to DIN 5033 and [97].

The $L^*a^*b^*$ coordinates are derived from the standard color values X, Y and Z and are calculated according to the following equations:

$$L^* = 116\sqrt[3]{Y/Y_n} - 16 \tag{3.1}$$

$$a^* = 500[\sqrt[3]{X/X_n} - \sqrt[3]{Y/Y_n}] \tag{3.2}$$

$$b^* = 200[\sqrt[3]{Y/Y_n} - \sqrt[3]{Z/Z_n}] \tag{3.3}$$

X_n, Y_n and Z_n are the standard color values of a perfect dull white body at the respective measurement parameters (DIN 5033, part 7).

Using these color coordinates, according to DIN 6174 a color change ΔE can be determined by applying the following equation:

$$\Delta E = \sqrt{(\Delta L^*)^2 + (\Delta a^*)^2 + (\Delta b^*)^2} \tag{3.4}$$

ΔE describes the distance between the coordinates of two colors. Plotting ΔE values at different times during exposure to corroding environments can describe and quantify the effects of the tarnishing procedure on the sample's color.

Another approach towards the quantification of the color change during tarnishing tests is to plot the Yellowness Index YI for different times of exposure. The YI is calculated according to equation 3.5

$$YI = 100\frac{1.28X - 1.06Z}{Y} \tag{3.5}$$

The Yellowness Index is often used to describe the aberration from a perfect white towards a yellowish color. It is very useful for the quantification of the quality of white gold alloys, as white gold tends to have a yellow component in its color originating from the characteristic yellow color of pure gold.

For white gold alloys, a so called "premium white" color is most desirable. A Yellowness Index between 0 and 19 is attributed to a premium white color [12]. Table 3.2 gives an overview on the YI values and the attributed color grades.

Table 3.2: Classification of white gold alloy colors with the Yellowness Index

Yellowness Index YI	Classification
<19	Premium White
19-24.5	Standard White
24.5-32	Off-White
>32	Non-White

As the gold-based bulk metallic glasses are reported to attain a yellow color during tarnishing in air, the development of the YI can describe the tarnishing dynamics and quantify the parameters at which the premium white color regime is left and an undesirable standard, off-white or even non-white color is present.

A very detailed summary on color detection methods for precious metal alloys can also be found in references [98, 12].

3.3.2 X-Ray Diffraction Analysis (XRD)

Qualitative X-ray diffraction patterns of surfaces and cross sections were usually measured with Cu Kα radiation on a Bruker D8 Discover equipped with 1 mm collimator, parallel

beam optics and a Bruker Vantec-500 detector system. The detection was carried out with a two-dimensional detector "Vantec-500" at 300 s per frame. The detected diffraction patterns were integrated to a one-dimensional diffractogram using the softwares "GADDS" and "MERGE".

Some spectra were detected using the D8 Discover and CuKα X-ray with a divergent aperture of 0.6 ° in the primary beam. In the secondary beam, parallel beam optics were employed. Detection was done with a one-dimensional LynxEye detector and a step distance of 0.01 ° and a measure time per step of 0.1 s. The latter spectra typically have a larger scattering in the data collection.

3.3.3 Scanning Electron Microscopy (SEM) and Scanning Transmission Electron Microscopy (STEM)

SEM investigations for the present work were performed using the following SEM instruments: Zeiss Auriga 60 Cross Beam, Zeiss Supra 55VP, and Zeiss EVO. The Zeiss Auriga 60 is equipped with a field emission cathode that can achieve a resolution of up to 1 nm at an acceleration voltage of 15 kV. Secondary electron (SE) detection can be performed within the chamber using the SE detector or using the InLens detector in the column. For the backscattered electron (BSE) detection inside the chamber a backscattered electron detector (BSD) detector can be used, or an energy-selective backscatter (EsB) detector can be used that is located above the Inlens detector in the column. For BSE detection in the Zeiss supra, the BSD is called RE-detector (Rückstreuelektronendetektor) in the respective image captions. The Zeiss Auriga is also equipped with a STEM detector for scanning transmission microscopy, with a silicon drift detector (SDD) for energy dispersive x-ray spectroscopy (EDX), and with an electron backscatter diffraction (EBSD) detector.

3.3.3.1 Interaction between Electron Beam and Sample, Material Contrast

A sample in the SEM is mapped by a scanning electron beam. The primary electrons (PE) enter the sample and interact with its atoms. If they interact elastically, they nearly don't lose any energy but can be diverted by the interaction with the sample's atoms. The scattering inside the sample can lead to a random path through the sample and to an exit point up to several μm away from the point where it entered the sample. These electrons are called backscattered electrons (BSE). The ratio between the number of BSE (N_{BSE}) and PE (N_{PE}) is called backscatter coefficient η.

$$\eta = \frac{N_{BSE}}{N_{PE}} \tag{3.6}$$

If the electron interacts with the atoms inelastically the energy of the electron is reduced and the interaction can lead to an ionization of the atom at hand when valence electrons are released. The latter electrons usually have an energy below 50 eV and are called secondary electrons (SE). Due to their low energy level, they can only leave the sample if their origin is somewhere near the surface, i.e. in a surface layer of 5-50 nm thickness [99]. Elastically

back scattered BSE have still approximately the energy of the primary electron (PE) beam, inelastic BSE have energies somewhere between 50 eV and the PE energy level.

In SEM investigations, either the SE or the BSE are detected to display the sample surface. As the SE originate from a very thin surface layer, the topography of the sample surface can be displayed much more accurately with SE detection than with BSE detection. BSE on the other hand can map a so called material contrast by displaying materials with a larger atomic number (Z) in a brighter shade than material with lower Z. The reason for this material contrast lies is the backscatter coefficient η, which is larger for higher Z. This behavior is most useful in analyzes of multi-phase material.

Figure 3.10 shows a schematic drawing of the sample volume that interacts with the electron beam. The influencing factors on volume and shape of the interacting material region are the acceleration voltage of the electron beam and the atomic number of the sample material. The larger the acceleration voltage, the larger the sample volume in interaction. And the higher Z becomes, the more the shape of the interacting volume flattens. The larger the atoms in the material become, the more likely a scattering of the incoming electron becomes. Hence, the electrons are sooner diverted from their original moving direction.

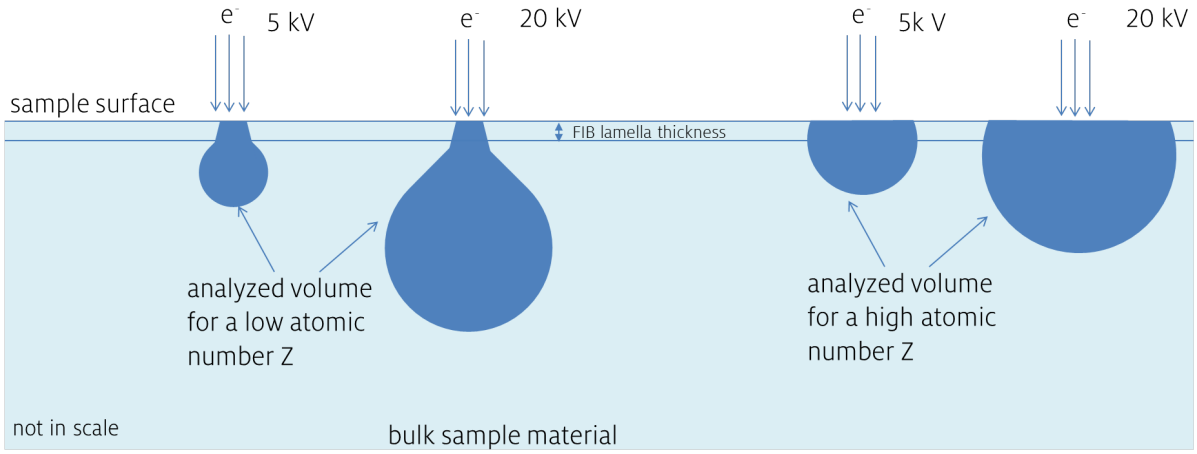

Figure 3.10: Schematic drawing of the volume that interacts with the incoming electron beam during an EDX analysis. Shape and volume strongly depend on the acceleration voltage of the electron beam and the atomic number Z of the analyzed sample material. Higher voltage results in the interaction with larger sample volumes, and a higher atomic number flattens the pear-shaped volume; after [99].

A Monte-Carlo simulation of the interacting volume was run for the composition $Au_{49}Cu_{27}Pd_2Ag_6Si_{16}$, which is close to the bulk metallic glass composition $Au_{49}Ag_{5.5}Pd_{2.3}Cu_{26.9}Si_{16.3}$, since only positive integers for the element concentration can be run in the simulation software. Figure 3.11 shows the respective sample volume that interacts with the primary electron beam for acceleration voltages of 20 kV and 5 kV. This sample volume in

interaction with the primary electron beam gives the information for image construction and chemical analysis when Au-BMG1 is investigated in the SEM. This has to be considered especially for localized EDX analysis at high magnifications. The chemical analysis often shows a mixture of the composition of a phase that was intended to be analyzed and the surrounding matrix material.

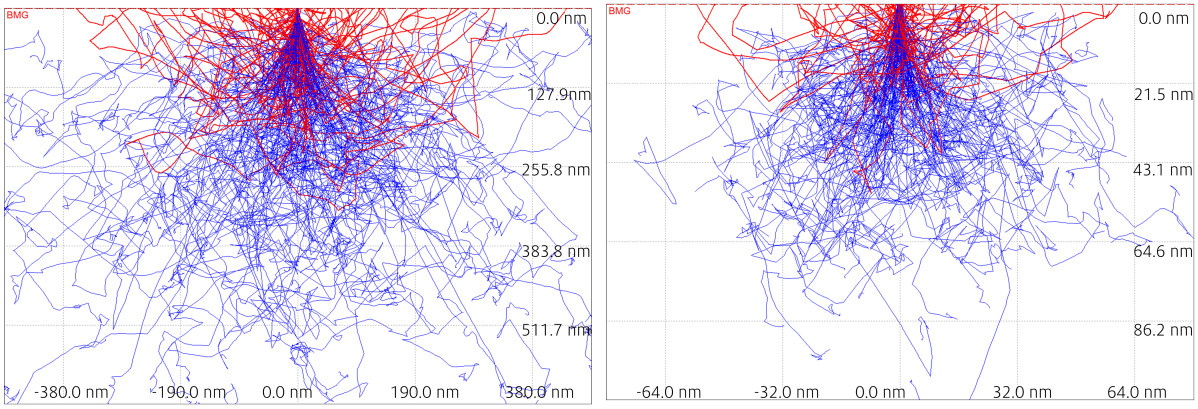

(a) Acceleration voltage = 20kV (b) Acceleration voltage = 5kV

Figure 3.11: Monte-Carlo simulation of the material volume that is analyzed during a typical EDX measurement depending on the acceleration voltage of the electron beam calculated for $Au_{49}Cu_{27}Pd_2Ag_6Si_{16}$ at.% for the present work.

Electrons that are not backscattered can lead to a charging of the sample, if the sample current is not discharged. If the sample thickness is in the range of several ten nanometers, depending on the sample material, the electrons can pass through the sample and can be detected from the backside in transmission electron microscopy (TEM) or scanning transmission electron microscopy (STEM) analysis. In this case, the volume interaction due to diverted electrons is largely reduced, leading to a higher resolution for imaging and EDX analysis.

3.3.3.2 Energy Dispersive X-Ray Micro-Analysis (EDX)

EDX analysis was carried out using either SiLi-detectors, if they were carried out in the Zeiss Supra or EVO and with an SDD detector, if they were carried out in the Zeiss Auriga. All SEMs were equipped with analysis systems from Oxford Instruments.

EDX allows the analysis of the chemical composition of an investigated material inside the SEM. Although the accuracy of the analysis is strongly dependent on the surface structure and condition of the sample material, among other factors, and gives therefore usually only qualitative results, it can be very useful to identify localized sample compositions in sample volumes of only few μm lateral circumference.

3.3.4 Focused Ion Beam Preparation (FIB)

The Zeiss Auriga 60 Cross Beam has an additional focused gallium ion beam column with a maximum acceleration voltage of 30 kV. Using the focused ion beam, abrasive sample preparation with up to 10 nm accuracy can be carried out. It is possible to mill away very thin slices of sample material perpendicular to the surface and thereby prepare exact cross sections of very small volume fractions, to extract lamellae of few nanometer thickness or even produce a tomography of the local phase distribution by adding up an image stack of FIB milled slices to a 3D image.

Figure 3.12 shows an example for the preparation of a lamella. To protect the surface that will become the top of the lamella from scattered abrasive gallium ions, first a protective platinum coating is applied on the location of the FIB section as shown in Figure 3.12 (a). The platinum is condensed on the surface employing first electron beam induced deposition (EBID) followed by ion beam induced deposition (IBID).

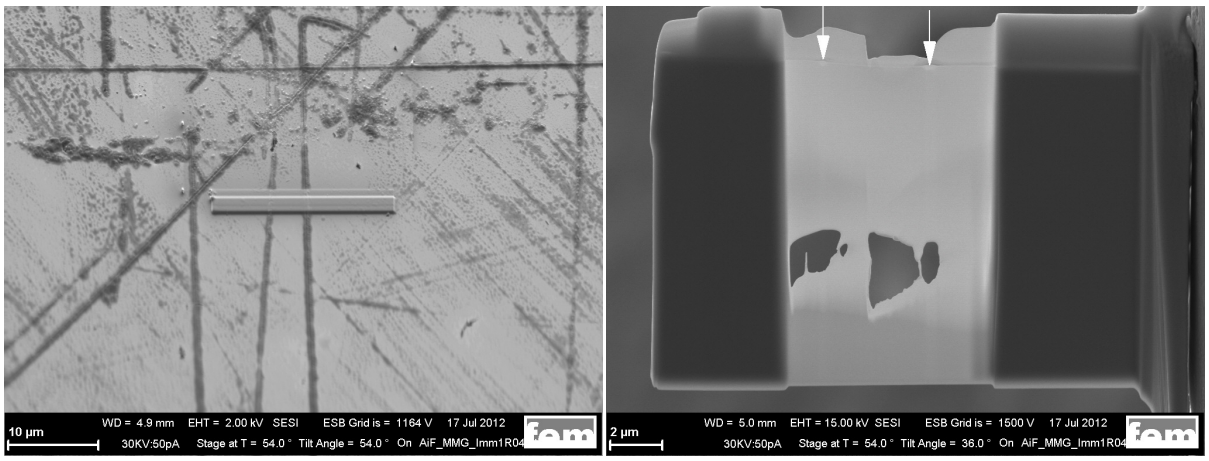

(a) SEM image of the location of the FIB cut (b) STEM image of the FIB cross section

Figure 3.12: FIB cut through two superficial scratches in an as-cast surface of Au-BMG1. (a) One of the scratches is a simple single scratch; the other scratch consists actually of two close and very fine parallel scratches. (b) The scratches are indicated with arrows in the STEM image.

In amorphous samples, FIB investigations may cause localized nano-crystallization [100] due to the bombardment with gallium ions. This has to be taken into account in STEM and TEM investigations of amorphous metals.

3.3.5 TEM-Investigation

The TEM investigation was carried out with a Jeol JEM 2010 at Saarland University.

3.3.6 Auger Spectroscopy

Auger spectroscopy was carried out with a Physical Electronics PHI 5800 ESCA system with 5 KV acceleration voltage and a current of 10 nA. The sputter rate was calibrated on Ta_2O_5 coatings.

3.3.7 X-Ray Photoelectron Spectroscopy (XPS)

X-ray photoemission spectra (XPS) were derived using a Thermo Fisher Scentific 1 XPS system equipped with a hemispherical Alpha 110 Analyser. The analysis was carried out using Al Kα excitation with a resolution of 1 eV. The energy of the Ar+ ion beam has been set to 2.0 keV and the sample current density was 0.2 A/m^2. The sputtering rate was estimated to be approximately 4.56 nm/min in Si-rich regions and 18 nm/min in Au-rich regions.

3.3.8 Differential Scanning Calorimetry (DSC)

DSC analyzes were carried out in a power-compensated Perkin Elmer Diamond DSC (DSC8500 or DSC800) at a heating rate of 20 K/min. For samples that were heated above the melting temperature, Al_2O_3 pans were chosen and the model DSC8000 was used. For samples that were only heated until crystallization was completed and that were not melted during the analysis, high purity aluminum pans were employed, and the tests were carried out in the model DSC8500. The samples were portioned to a weight between 10 and 100 mg.

3.3.9 Inductively Coupled Plasma Optical Emission Spectroscopy ICP-OES

The ICP-OES was performed in a Viste Pro radial, Varian. For the sample preparation, dissolution of $\approx$ 100 mg of the alloyed sample material was done in 10 ml aqua regia with an addition of hydrofluoric acid (HF) to dissolve the silicon. After dissolution 40 ml hydrochloric acid (HCl) were added, and the sample was transferred into a volumetric flask. The solution was diluted with water until 100 ml sample volume and 6 mol/l HCL concentration were reached.

3.3.10 Glow-Discharge Optical Emission Spectroscopy (GDOES)

The GDOES analysis was carried out with a glow discharge spectrometer Spectruma GDA 750. The sample material was ground prior to the analysis to produce a flat and smooth surface condition. The analysis was carried out similar to the test standard ISO 14707.

3.3.11 Energy-dispersive X-ray fluorescence (EDXRF)

EDXRF analyzes were performed either with the Fisherscope X-Ray XDVM or the X-Ray XDAL according to DIN EN ISO 3497.

3.4 Tabular Overview of Samples and Experiments

Table 3.3 gives an overview of all samples and the corresponding aging treatment or experiment, respectively, which is described in chapter 4. The samples are numerated in the order in which they are mentioned in the text.

Table 3.3: Tabular overview for the samples used in the experiments conducted in the present work, sample composition in mass-% according to Table 4.3.

No.	Shape	Alloy	Treatment
1	granules	$Au_{49}Ag_{5.5}Pd_{2.3}Cu_{26.9}Si_{16.3}$	RT, as-cast
2	granules	$Au_{49}Ag_{5.5}Pd_{2.3}Cu_{26.9}Si_{16.3}$	348 K, as-cast
3	granules	$Au_{49}Ag_{5.5}Pd_{2.3}Cu_{26.9}Si_{16.3}$	348 K, HF etched
4	plate	$Au_{49}Ag_{5.5}Pd_{2.3}Cu_{26.9}Si_{16.3}$	30 months, lab air, not cleaned
5	plate	$Au_{49}Ag_{5.5}Pd_{2.3}Cu_{26.9}Si_{16.3}$	131 days, 348 K, air
6	plate	$Au_{49}Ag_{5.5}Pd_{2.3}Cu_{26.9}Si_{16.3}$	327 days, 348 K, air
7	plate	$Au_{49}Ag_{5.5}Pd_{2.3}Cu_{26.9}Si_{16.3}$	365 days, 348 K, air
8	plate	$Au_{49}Ag_{5.5}Pd_{2.3}Cu_{26.9}Si_{16.3}$	23 days, 348 K, air
9	plate	$Au_{49}Ag_{5.5}Pd_{2.3}Cu_{26.9}Si_{16.3}$	593 days at RT, dry air
10	plate	$Au_{49}Ag_{5.5}Pd_{2.3}Cu_{26.9}Si_{16.3}$	RT, air-conditioned laboratory
11	plate	$Au_{49}Ag_{5.5}Pd_{2.3}Cu_{26.9}Si_{16.3}$	RT, vacuum
12	plate	$Au_{49}Ag_{5.5}Pd_{2.3}Cu_{26.9}Si_{16.3}$	255 K, air
13	plate	$Au_{49}Ag_{5.5}Pd_{2.3}Cu_{26.9}Si_{16.3}$	310 K, dry air
14	plate	$Au_{49}Ag_{5.5}Pd_{2.3}Cu_{26.9}Si_{16.3}$	310 K, humid air
15	plate	$Au_{49}Ag_{5.5}Pd_{2.3}Cu_{26.9}Si_{16.3}$	348 K, Ar
16	plate	$Au_{49}Ag_{5.5}Pd_{2.3}Cu_{26.9}Si_{16.3}$	artificial sweat test 7 days, 310 K
17	plate	$Au_{49}Ag_{5.5}Pd_{2.3}Cu_{26.9}Si_{16.3}$	artificial saliva test 7 days, 310 K
18	plate	$Au_{49}Ag_{5.5}Pd_{2.3}Cu_{25.9}Si_{16.3}Al_1$	327 days, 348 K, air
19	plate	$Au_{60}Ag_{5.5}Pd_2Cu_{15.5}Si_{17}$	327 days, 348 K, air
20	plate	$Au_{50}Ag_{7.5}Cu_{25.5}Si_{17}$	327 days, 348 K, air
21	plate	$Au_{49}Ag_{5.5}Pd_{2.3}Cu_{25.9}Sn_1Si_{16.3}$	348 K, air, long glass tube
22	plate	$Au_{49}Ag_{5.5}Pd_{2.3}Cu_{25.9}Ga_1Si_{16.3}$	348 K, air, long glass tube
23	plate	$Au_{49}Ag_{5.5}Pd_{2.3}Cu_{25.9}Fe_1Si_{16.3}$	348 K, air, long glass tube
24	plate	$Au_{49}Ag_{5.5}Pd_{2.3}Cu_{25.9}Cr_1Si_{16.3}$	348 K, air, long glass tube
25	plate	$Au_{49}Ag_{5.5}Pd_{2.3}Cu_{26.9}Ge_1Si_{15.3}$	348 K, air, long glass tube

Continued on next page

Table 3.3 – continued from previous page

No.	Shape	Alloy	Treatment
26	plate	$Au_{49}Ag_{5.5}Pd_{2.3}Cu_{26.9}Ge_3Si_{13.3}$	348 K, air, long glass tube
27	plate	$Au_{49}Ag_{5.5}Pd_{2.3}Cu_{26.9}Si_{16.3}$	348 K, air, long glass tube
28	section	$Au_{65}Ag_{5.5}Pd_2Cu_{10.5}Si_{17}$	sulfide dip test
29	section	$Au_{49}Ag_{5.5}Pd_{2.3}Cu_{24.9}Si_{16.3}Al_2$	sulfide dip test
30	section	$Au_{60}Ag_{5.5}Pd_2Cu_{15.5}Si_{17}$	sulfide dip test
31	section	$Au_{49}Ag_{5.5}Pd_{2.3}Cu_{25.9}Si_{16.3}Al_1$	sulfide dip test
32	section	$Au_{49}Ag_{5.5}Pd_{2.3}Cu_{26.9}Si_{16.3}$	sulfide dip test
33	section	$Au_{49}Ag_{5.5}Pd_{2.3}Cu_{26.9}Si_{16.3}$	sulfide dip test
34	section	$Au_{65}Ag_{7.5}Cu_{10.5}Si_{17}$	sulfide dip test
35	section	$Au_{60A}g_{7.5}Cu_{15.5}Si_{17}$	sulfide dip test
36	section	$Au_{50}Ag_{7.5}Cu_{25.5}Si_{17}$	sulfide dip test
37	plate	$Au_{49}Ag_{5.5}Pd_{2.3}Cu_{26.9}Si_{16.3}$	crystalline, 327 days, 348 K, air
38	plate	$Au_{49}Ag_{5.5}Pd_{2.3}Cu_{26.9}Si_{16.3}$	crystalline, 327 days, 348 K, air
39	plate	$Au_{49}Ag_{5.5}Pd_{2.3}Cu_{26.9}Si_{16.3}$	artificial saliva test 7 days, 310 K
40	plate	$Au_{49}Ag_{5.5}Pd_{2.3}Cu_{26.9}Si_{16.3}$	artificial saliva test 7 days, 310 K
41	plate	$Au_{49}Ag_{5.5}Pd_{2.3}Cu_{26.9}Si_{16.3}$	crystalline, art. sal. test 7 days, 310 K
42	plate	$Au_{56.88}Pd_{22.43}Cu_{13.85}Zn_{6.84}$	crystalline, art. sal. test 7 days, 310 K
43	plate	$Au_{43.56}Ag_{25.15}Pd_{22.05}Cu_{9.23}$	crystalline, art. sal. test 7 days, 310 K
44	plate	$Pt_{88.66}Cu_{11.34}$	crystalline, art. sal. test 7 days, 310 K
45	plate	$Ag_{87.9}Cu_{12.1}$	crystalline, art. sal. test 7 days, 310 K
46	plate	$Ag_{89.45}Cu_{10.55}$	crystalline, art. sal. test 7 days, 310 K

4 Results

Parts of the results that are presented here have been published in an earlier version by the author of this thesis and co-workers [4, 13, 14, 15, 3, 76].

4.1 Processing of Bulk Metallic Glasses and Development of New Processing Techniques

The following subsections introduce the results on casting and thermoplastic forming that were found in the present work. Commercially available casting devices that are often used in jewelry casting were used for the casting experiments to mirror industrial processing techniques. The aim of this part of the work was to investigate the suitability of the Au-Ag-(Pd)-Cu-Si bulk metallic glass system for jewelry, watch making and technical applications. The focus of this part of the work is on the well known alloy composition $Au_{49}Ag_{5.5}Pd_{2.3}Cu_{26.9}Si_{16.3}$. Along with the investigation of established casting techniques, a new casting technique, tailored for the application of bulk metallic glasses in jewelry production was developed and is introduced here for the first time.

4.1.1 Melting

For alloys that have both palladium and silicon as alloying elements, it is necessary to avoid the formation of palladium silicide precipitates during the melting and subsequent casting procedure. Once palladium silicide precipitates are formed, they are difficult to dissolve or melt due to their high melting temperatures. They can trigger crystallization because they act as nucleation sites for heterogeneous nucleation and because the residual melt is depleted in palladium and silicon. The altered composition of the residual melt possibly has an inferior glass forming ability. Figure 4.1 shows the binary phase diagram of the Pd-Si system with the silicides Pd_3Si, Pd_2Si, PdSi and possibly Pd_9Si_4 [101].

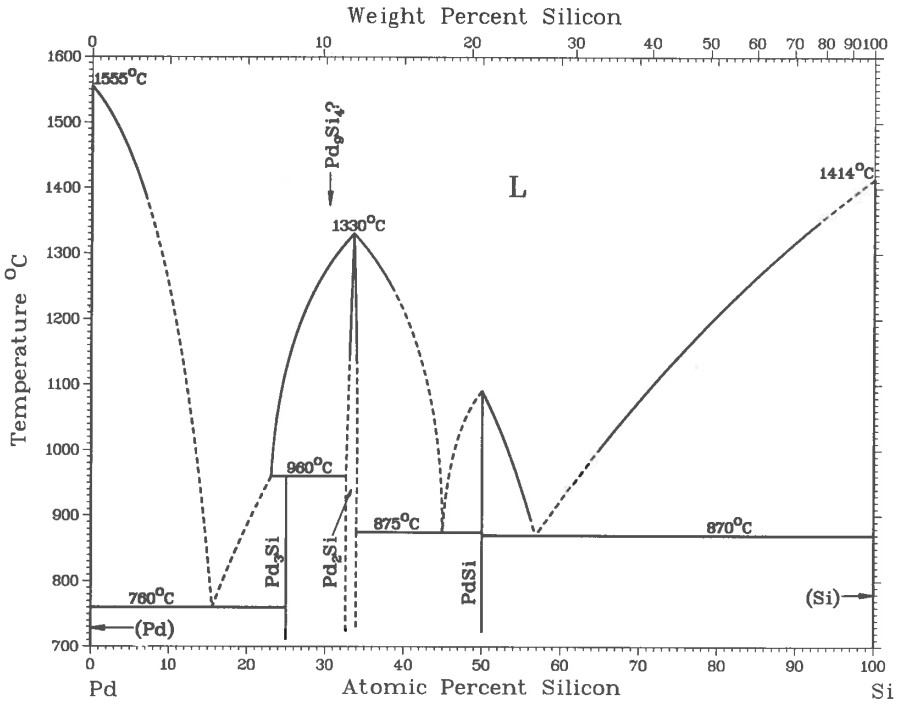

Figure 4.1: Binary phase diagram of the Pd-Si system. Several palladium silicides exist that can form during solidification and have high liquidus temperatures; reprinted from [101].

Figure 4.2 shows palladium silicide precipitates such as Pd_3Si, Pd_5Si_2 or Pd_2Si that are expected according to [11]. The silicide crystals can be observed as dark particles in the backscatter image due to their high silicon content in comparison to the brighter surrounding phases with a high gold content.

The formation of these precipitates can be avoided by pre-alloying palladium and silicon independently from each other. In the present work, pre-alloying was investigated using two variations according to Table 4.1. Each variation was found to be appropriate to avoid the formation of palladium silicide precipitates and for casting fully amorphous samples in the consecutive alloying and casting steps.

Table 4.1: Variations of pre-alloying

variation	pre-alloy 1	pre-alloy 2
variation 1	Au-Si	Pd-Cu-Ag
variation 2	Au-Pd-Cu-Ag	Si

Further experiments showed a pre-alloying step is not necessary, if the elements in the crucible are stacked as is suggested in Figure 4.3. Stacking the palladium as far away as possible from the silicon guarantees that the silicon is at first dissolved into to the molten

gold, and a direct reaction with palladium at the bottom is avoided. Using this stacking sequence, casting of amorphous samples and granules without pre-alloying was possible.

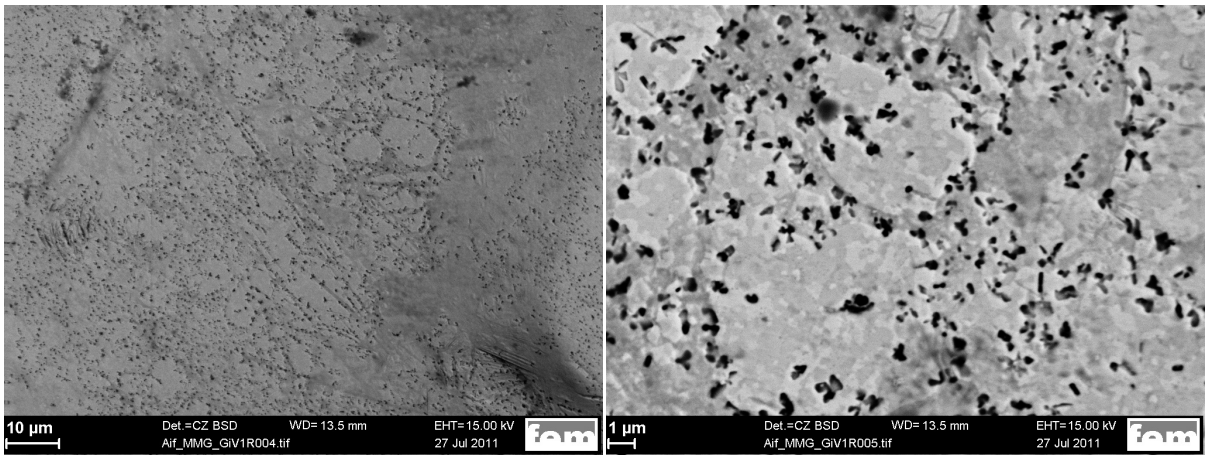

(a) Overview (b) Detail

Figure 4.2: SEM images of a sample of $Au_{49}Ag_{5.5}Pd_{2.3}Cu_{26.9}Si_{16.3}$ with a high amount of palladium silicide precipitates that are shown in a dark contrast in the BS-image (a) overview (b) magnification of the precipitates.

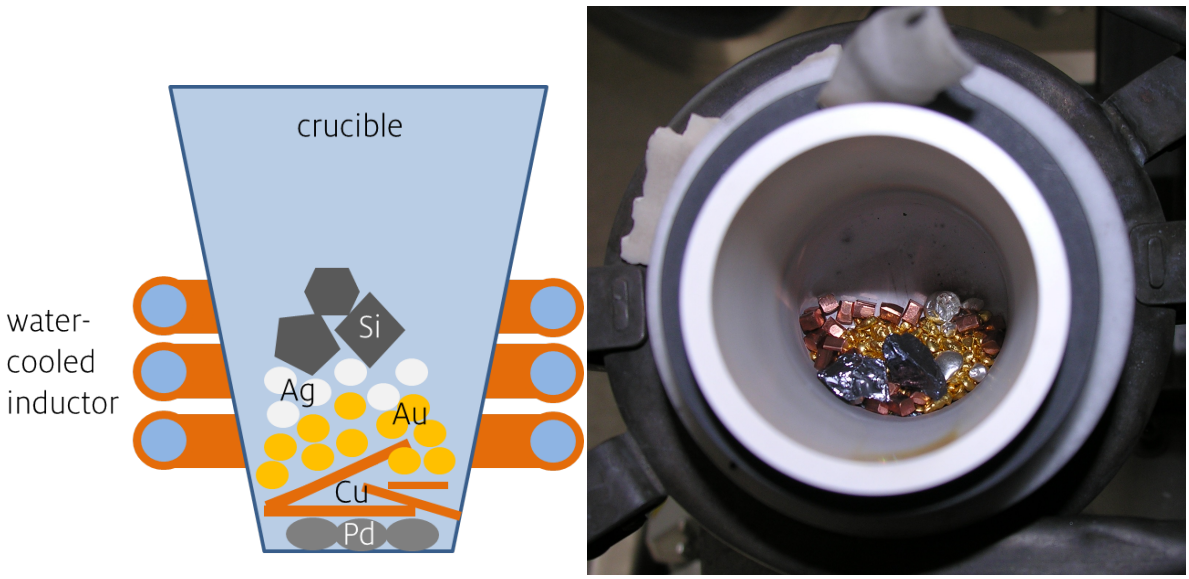

(a) sketch (b) photograph

Figure 4.3: Ideal distribution of the raw elements in the crucible

To evaluate the use of graphite crucibles for $Au_{49}Ag_{5.5}Pd_{2.3}Cu_{26.9}Si_{16.3}$, a sample of the alloy was molten inside a graphite crucible to investigate possible crucible reactions.

There was almost no observable wetting of the BMG melt on the graphite substrate. The melt was kept liquid inside the graphite crucible for more than ten minutes, longer than any granulation or casting procedure would require. The sample was then analyzed for its carbon content in comparison to a sample that was melted in a boron nitride (BN) crucible. BN typically shows no reaction with metallic melts and is therefore used as reference. Table 4.2 gives the results of the analysis. Gold, silver, palladium and copper were analyzed using energy dispersive X-ray fluorescence (EDXRF) while silicon, carbon, and sulfur were analyzed by glow discharge optical emission spectroscopy (GDOES). The carbon content in the samples was below the detection limit in both cases. Hence, graphite crucibles are suitable for casting BMG in the Cu-(Pd)-Ag-Cu-Si system.

Table 4.2: Chemical analysis of two samples of $Au_{49}Ag_{5.5}Pd_{2.3}Cu_{26.9}Si_{16.3}$ molten inside a BN crucible and a graphite (C) crucible, respectively.

	C crucible [wt.%]	BN crucible [wt.%]	nominal composition [wt.%]
Au	76.2	76.0	76.0
Ag	4.9	5.1	4.7
Pd	1.92	1.87	1.9
Cu	13.4	13.4	13.5
Si	3.5	3.5	3.6
C	<0,005	<0,005	
S	<0,005	<0,005	

4.1.2 Production of Semi-finished Products

The fabrication of a semi-finished product in large batch sizes has the advantage that large amounts of the alloy are produced from the raw elements in one step. This means that the accurate weighing of 5 components has to be performed only one time for a large batch, and subsequently the semi-finished product with the final alloy composition can be further processed. Direct casting from the pure elements on the other hand requires an accurate weighing of the alloying elements for each cast.

A typical example of a semi-finished product is a pellet with a defined geometry, cast into a copper mold. In that case, a distinct pre-alloyed volume is received and can be thermoplastically formed or re-melted and cast into a final geometry. The pellet size can be designed to fit the required alloy volume for a certain product as an ideal feedstock for mass production.

In the present work a granulation process has been developed for the production of a semi-finished product with a small and undefined geometry: small spherical granules. The small spheres can be easily portioned in variable fractions and are therefore a more flexible feedstock material, ideal for individual castings and small batch series.

To assess proper processing parameters for the granulation, at first an experimental setup was tested in which the metallic glass melt was processed inside a graphite crucible positioned in an induction coil. The crucible was placed in an open environment. However it

was purged with argon during the entire process. Once the feedstock material was melted, the argon-pressure in the chamber above the melt was increased, accelerating the melt through a small nozzle at the bottom of the crucible. Throughout the present work, the gold based BMG forming liquids were observed to behave differently to conventional metal melts, due to significantly higher viscosity values. It has been reported that BMG-forming liquids have viscosity values that are several orders of magnitude higher than those of pure metal melts [61]. Hence, in order to form spherical granules, a higher argon pressure and a smaller nozzle size were required to account for this difference.

Figure 4.4 (a) shows the experimental setup during the granulation procedure. Figure 4.4 (b) shows the granulation procedure applied for pure silver. This setup was used for granulation of the bulk metallic glass $Au_{49}Ag_{5.5}Pd_{2.3}Cu_{26.9}Si_{16.3}$. Beneath the nozzle, the formation of spherical shaped granules from the liquid melt stream can be observed. The spheres fall into a water/ethanol mixture with 50/50 volume-% where they are rapidly quenched. The water/ethanol mixture was chosen because ethanol reduces the surface tension of the quenching liquid significantly [102]. Gas bubbles forming on the melt droplets during immersion into the quenching liquid can therefore detach faster from the droplets and the surface can sooner be wetted by the quenching liquid.

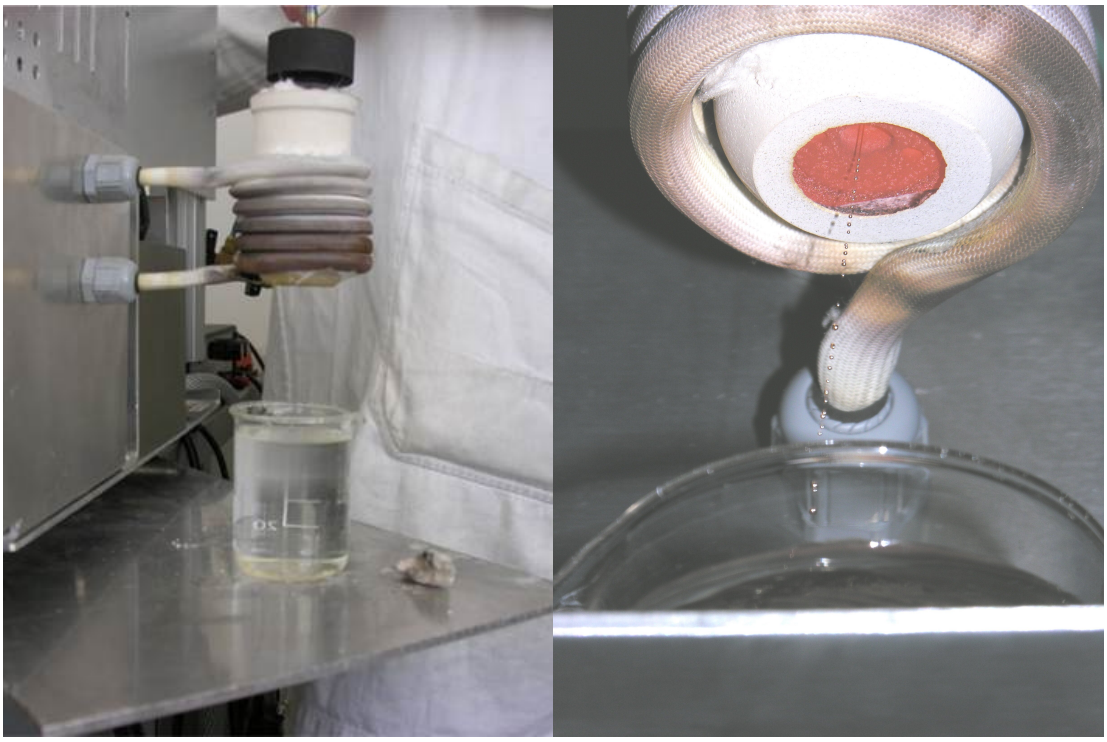

(a) Experimental test setup (b) Detail of droplets during granulation

Figure 4.4: Granulation in the test setup: (a) Experimental setup; (b) Formation of spherical silver granules from a liquid melt stream a few millimeters beneath the crucibles nozzle. ((b) was previously published in [13, 14, 15])

For the production of larger batch sizes the process was transferred to an Indutherm VC500 casting device with a bigger graphite crucible. Figure 4.5 shows a schematic drawing of the crucible. It can be evacuated and purged with an inert processing gas. In this case argon was used. The graphite crucible was heated inductively, and the temperature was monitored with a thermocouple inside the graphite crucible. The nozzle on the bottom of the crucible was closed by a graphite shank that could be lifted and lowered from outside the crucible chamber. Once the desired granulation temperature was reached, the shank was lifted, and the melt was accelerated through the circular nozzle by an argon over-pressure in the crucible.

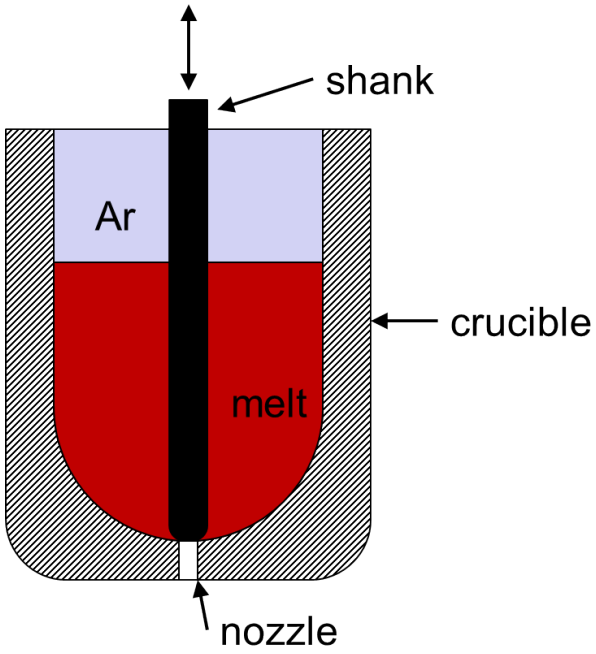

Figure 4.5: Sketch of the graphite crucible in the VC500 casting device. The shank closes the nozzle during melting and homogenization and can be lifted by an external control setup.

In contrast to the crucible chamber, the area beneath the crucible was in open air and could therefore not be evacuated. Figure 4.6 (a) shows the setup of the quenching liquid beneath the encapsulated graphite crucible. For the quenching, 4 liters of a water/ethanol mixture with the ratio 50:50 was employed. To reduce the contamination of the liquid melt droplets with oxygen from laboratory air, the distance between the nozzle and the surface of the quenching liquid was minimized to 5 cm and the gas volume above was purged with a constant argon flux as is shown in Figure 4.6 (b).

(a) Indutherm VC500 with quenching tank (b) Detail of the Ar flux above the quenching liquid

Figure 4.6: Granulation with the indutherm VC500 casting device with a water/ethanol mixture as a quenching liquid. (a) Granulation chamber, which can be evacuated and purged with an inert gas (b) Position of the quenching tank beneath the granulation chamber and Ar-purge supply.

The granulation process parameters such as temperature, argon pressure and nozzle diameter were systematically varied until the majority of the granules were produced within a diameter range of 0.7 mm to 2 mm. The most homogeneous granulate was achieved at a granulation temperature of $\approx$ 1223 K (950°C), an Ar pressure of $\approx$ 3-4 bar and a nozzle size of $\approx$ 500 μm. Figure 4.7 shows the as cast granules (a) in an overview and (b) in a detailed SEM image.

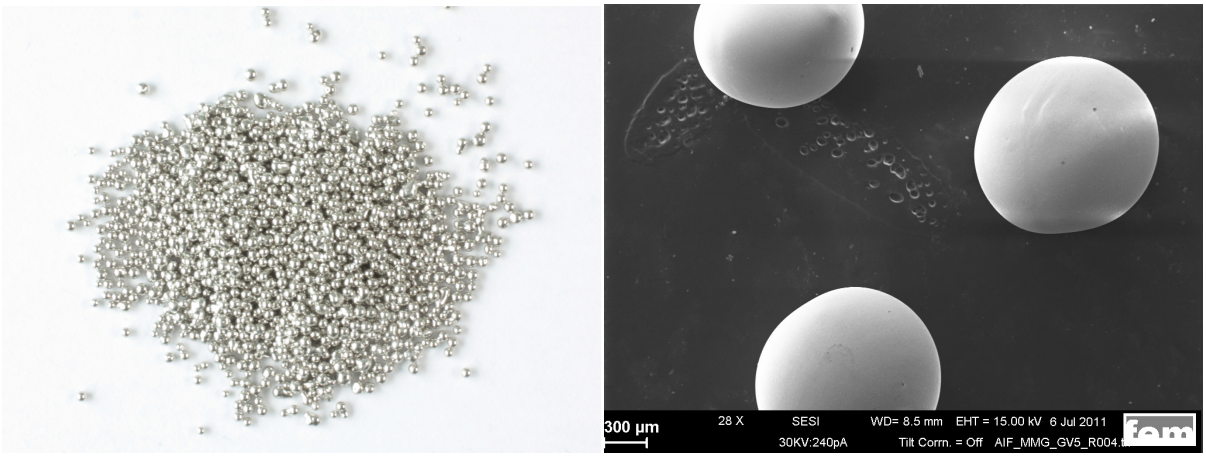

(a) As-cast granules dia. 0.7-2mm (b) SEM image of as cast granules

Figure 4.7: (a) As-cast granules of $Au_{49}Ag_{5.5}Pd_{2.3}Cu_{26.9}Si_{16.3}$ (b) SEM image of the granules in as-cast state (previously published in [13, 14, 15]).

The granules are covered with a SiO_2 film of irregular thickness. On granules that were produced under argon flux, this layer is extremely thin for almost the entire granules surface area and cannot be detected by an EDX measurement from the top-view (Figure 4.7 (b)) because the matrix volume that interacts with the electron beam for the EDX analysis is too large in comparison to the thin oxide layer (see Section 3.3.3.2).

Only in some locations the oxide layer is thicker and forms stripes or larger areas that can easily be detected in the SEM via EDX analysis and can be observed as dark superficial areas like e.g. in Figure 4.8 (a). A cross-section through such an oxide island perpendicular to the sample surface was carried out using a FIB. The oxide layer can be identified as the dark, irregular layer in Figure 4.8 (b). It was determined to be up to 100 nm thick in this location.

The XRD spectrum of the granules in the diameter range between 0.7 mm and 2 mm shows two broad maxima without any sharp reflections indicating crystallinity, proving the X-ray-amorphous state of the granules and the surface film.

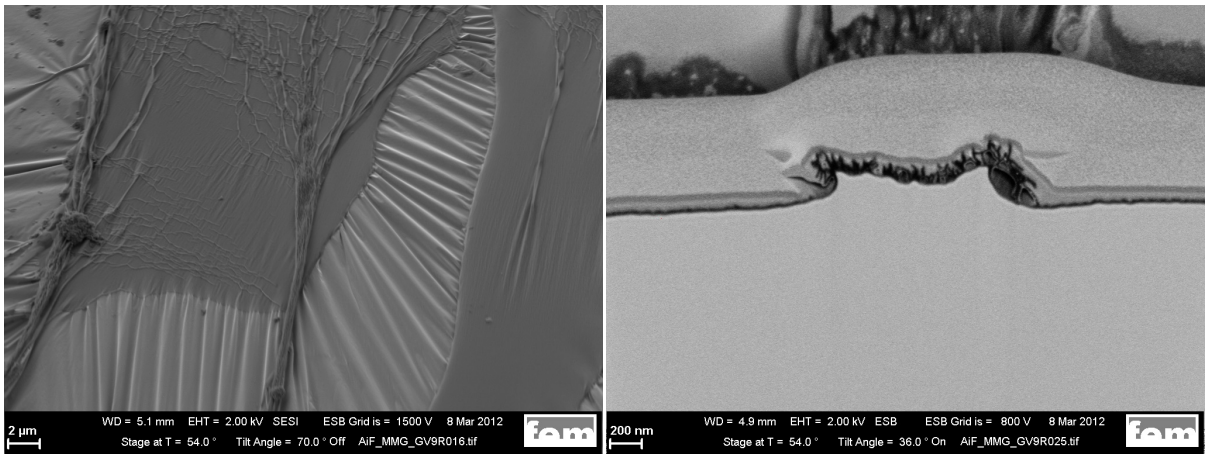

(a) Top view (b) FIB cross-section of (a)

Figure 4.8: SEM images of a granule surface with a particularly thick SiO_2 layer. The oxide layer is up to 100 nm thick.

4.1.3 Evaluation of Different Casting Routines

On freshly produced plate-shaped samples produced as described in Section 3.1.1, usually a superficial layer with a small fraction of nano-crystals was found. The existence of a thin superficial layer enriched in nano-crystals in the range of 10 to 80 μm has been described before by Ketov et al. [89].

As this nano-cyrstallization is only found in thin superficial scales that can easily be removed by polishing, for further investigations only polished sample surfaces were analyzed by XRD.

The application of different casting routines was evaluated by casting $Au_{49}Ag_{5.5}Pd_{2.3}Cu_{26.9}Si_{16.3}$ into the same simple plate-shaped cavity with the dimensions 2 x 12 x 47 mm using tilt casting and centrifugal casting procedures. At first, casting directly from the pure elements was applied for both casting techniques. Then the same casting parameters were applied using the granules as feedstock. The casting products proved to be XRD-amorphous independent from the respective casting routine and feedstock material. For each routine several casts (at least 3 repetitions) were performed to prove the reproducibility of the casting of amorphous samples. As an example, Figure 4.9 shows XRD-spectra for $Au_{49}Ag_{5.5}Pd_{2.3}Cu_{26.9}Si_{16.3}$ cast in plates of 2 x 12 x 47 mm produced with tilt and centrifugal casting using granules as feedstock.

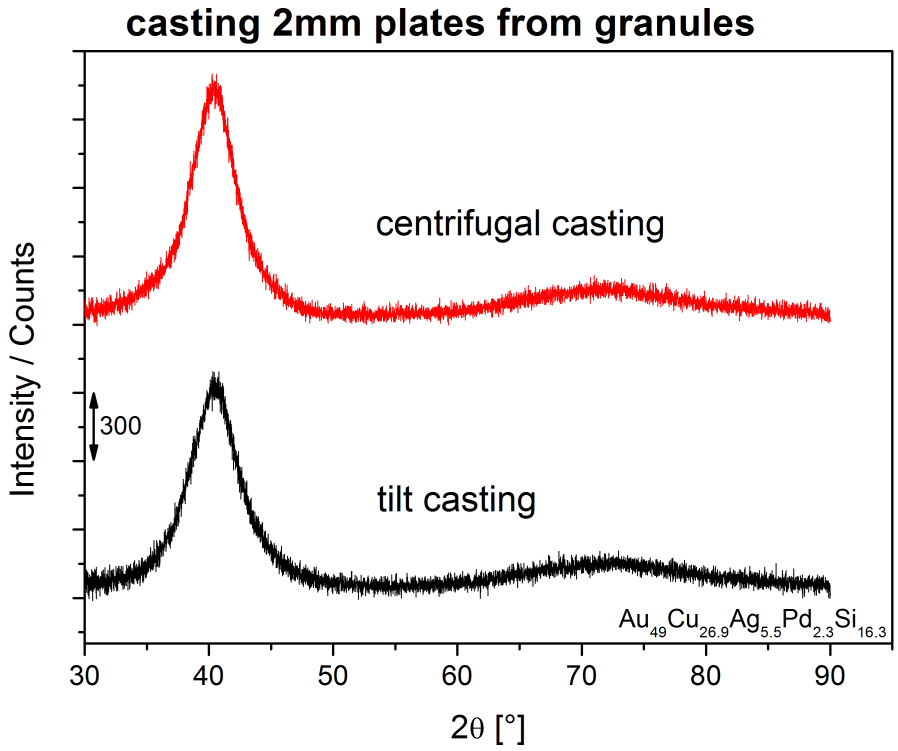

Figure 4.9: XRD diffractograms obtained from a tilt cast and a centrifugal cast polished plate (2 x 12 x 47 mm) of $Au_{49}Ag_{5.5}Pd_{2.3}Cu_{26.9}Si_{16.3}$ using granules as feedstock, previously published in an earlier version in [13, 14, 15].

Repeated casts into a copper mold with a rod-shaped cavity with a length of 34 mm and a diameter of 5 mm of the same batch with composition $Au_{49}Ag_{5.5}Pd_{2.3}Cu_{26.9}Si_{16.3}$ were applied by subsequent melting and re-casting [76]. This was done in order to find the maximum number of successful fully amorphous subsequent casts without recycling of the material. The first casting was carried out using raw elements and all castings were performed in a tilt casting machine Indutherm MC50. After the 12th repetition, the material was still X-ray-amorphous, suggesting that the alloy can be re-used for castings at least 10 times in industrial casting. Figure 4.10 shows the XRD spectra of the last 4 repetitions [76]. The same work shows that the critical casting thickness of $Au_{49}Ag_{5.5}Pd_{2.3}Cu_{26.9}Si_{16.3}$ is at least 6 mm. It has been reported before to be at least 5 mm in reference [1].

When identical casting parameters in centrifugal casting were applied on other compositions like, for example, $Au_{60}Ag_{7.5}Cu_{15.5}Si_{17}$, nano-crystallization was observed in some cases. Figure 4.11 shows a cross-section of $Au_{60}Ag_{7.5}Cu_{15.5}Si_{17}$ cast in 2 mm thickness applying centrifugal casting. According to [6], this alloy has a critical casting thickness of 5 mm, which is the same d_c as reported for $Au_{49}Ag_{5.5}Pd_{2.3}Cu_{26.9}Si_{16.3}$ in [2]. In the case of centrifugal casting the d_c of alloy $Au_{60}Ag_{7.5}Cu_{15.5}Si_{17}$ seems to be even lower than 2 mm.

The nano-crystals are concentrated in near-surface regions of the cast representing material that was close to the copper mold during solidification and the center of the cast

product shown in the microscope image in Figure 4.11.

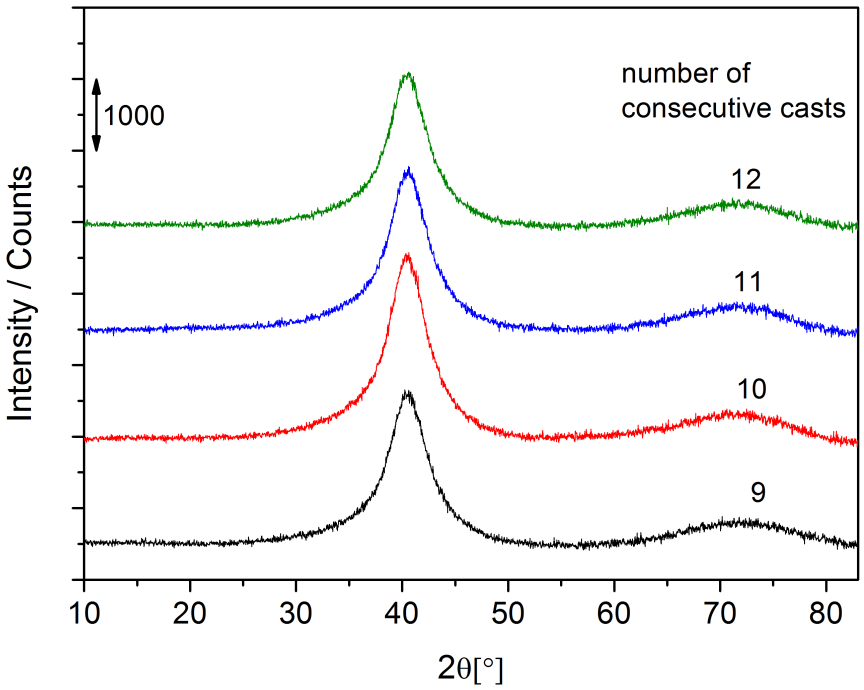

Figure 4.10: XRD diffractograms obtained from the cross sections of tilt cast rods with a diameter of 5 mm of $Au_{49}Ag_{5.5}Pd_{2.3}Cu_{26.9}Si_{16.3}$. The same material was cast, molten, and recast 12 times, unfailingly resulting in amorphous sample material. Figure reprinted slightly modified with permission from Schmitt [76].

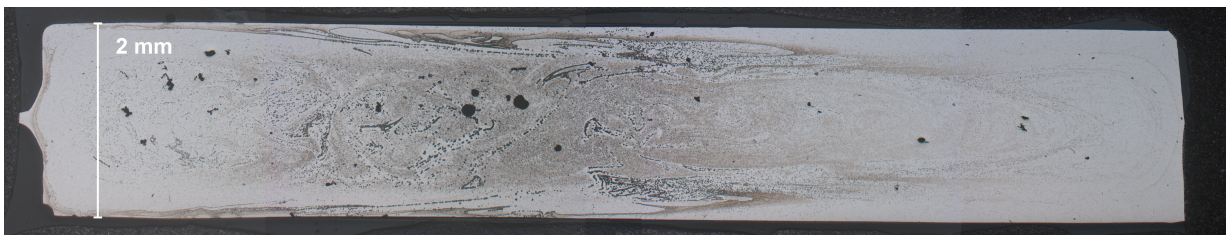

Figure 4.11: Cross-section of a plate of $Au_{60}Ag_{7.5}Cu_{15.5}Si_{17}$ etched with ion beams. The etching effect is more evident at the center of the cross-section. Despite the fact that the cast was below the critical casting thickness d_c of 5 mm for this alloy, shear-rate-induced nano-crystallization is clearly visible; previously published in another version [13, 14].

To evaluate the form filling behavior and the strain in the melt during form filling and solidification, a simulation of the tilt and centrifugal casting process was set up. Figure

4.12 shows screen-shots of the simulation of the tilt casting process. The simulation shows a distinctly higher strain rate $\dot{\epsilon}$ for the centrifugal casting procedure as in Figure 4.13. In some locations strain rates almost 3 times higher than the maximum strain rates of the tilt casting process of 570 1/s are reached, resulting in strain rates up to 1600 1/s for centrifugal casting.

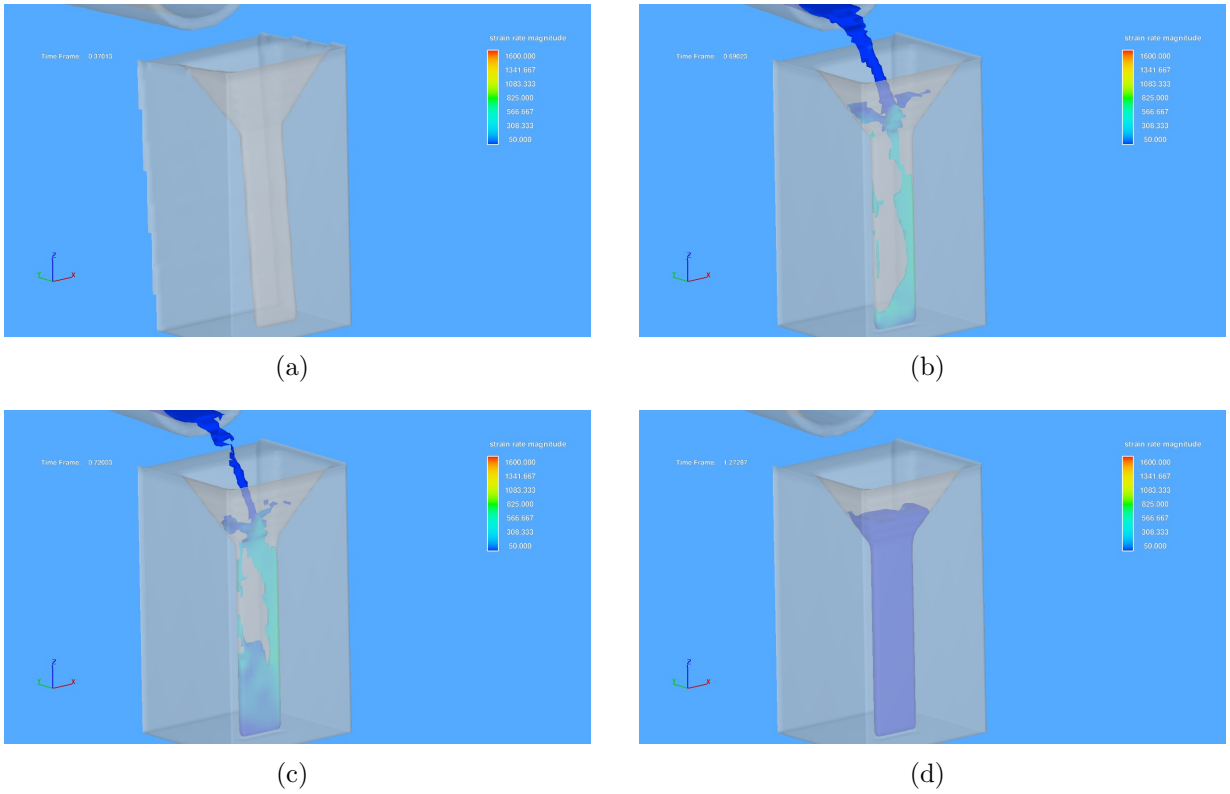

(a) (b)

(c) (d)

Figure 4.12: Simulation of the tilt casting process. Strain rates $\dot{\epsilon}$ of up to 570 1/s are reached during form filling at some locations in the melt (b) and (c). Previously published in [13, 14].

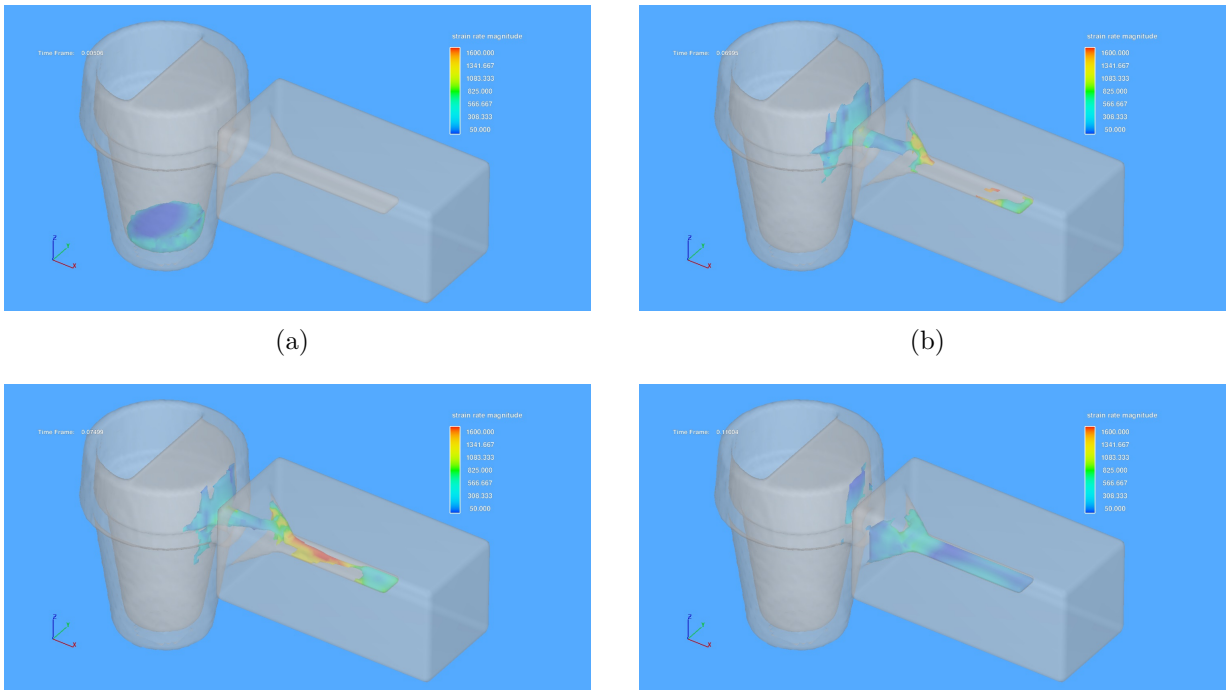

(a) (b)

(c) (d)

Figure 4.13: Simulation of the tilt casting process. Strain rates $\dot{\epsilon}$ of up to 1600 1/s are reached during form filling at some locations in the melt (c). This is almost three times as much as the maximum strain that is observed in tilt casting for this geometry. Previously published in [13, 14].

4.1.4 A New Casting Method in Lost Metal Molds

The majority of jewelry products are produced using the investment casting technique, a lost mold casting technique that employs wax or plastic models (see also Section 2.8). As typical investment material cannot provide a sufficient cooling rate for an amorphous solidification, today most bulk metallic glasses are produced using massive metal molds. They usually consist of copper and are sometimes additionally cooled to ensure a constant mold temperature during form filling. The molds are typically designed as separable molds for an easy removal of the cast product and repeated usage. Due to the need for mold manufacturing techniques based on cutting, like milling and turning, and the need to remove the final cast product from the mold without damaging the mold or the cast product, the possible shapes of the final products are limited. This is a big disadvantage as soon as complex shapes are desired, for example in jewelry production.

During the conduction of the present work, a combination of the lost wax technique with casting into metal molds was developed by electroforming of copper directly on the wax-model surface, thereby reproducing the surface accurately. The electroforming procedure was perfomed in an acidic copper sulfate electrolyte. The wax was removed from the mold

by melting in a furnace. After removal of the wax, a hollow copper mold was obtained in which the liquid alloy could be cast. The production steps for casting in lost metal molds are:

1. manufacturing or rapid prototyping of a wax or plastic model of the desired item and adding a sprue system
2. application of a conductive coating such as graphite powder, graphite conductive paste or silver conductive paste, preferably very thin and smooth for an accurate replication of the surface
3. electroforming of copper onto the electric conductive surface
4. removal of the wax or plastic either by melting or chemical decomposition
5. casting into the cavity left by the wax or plastic model
6. removal of the copper mold by etching; the mold is lost but the copper can be reintroduced into the process cycle as anodic material and deposited on the next model

A sketch of the copper mold fabrication is illustrated in Figure 4.14.

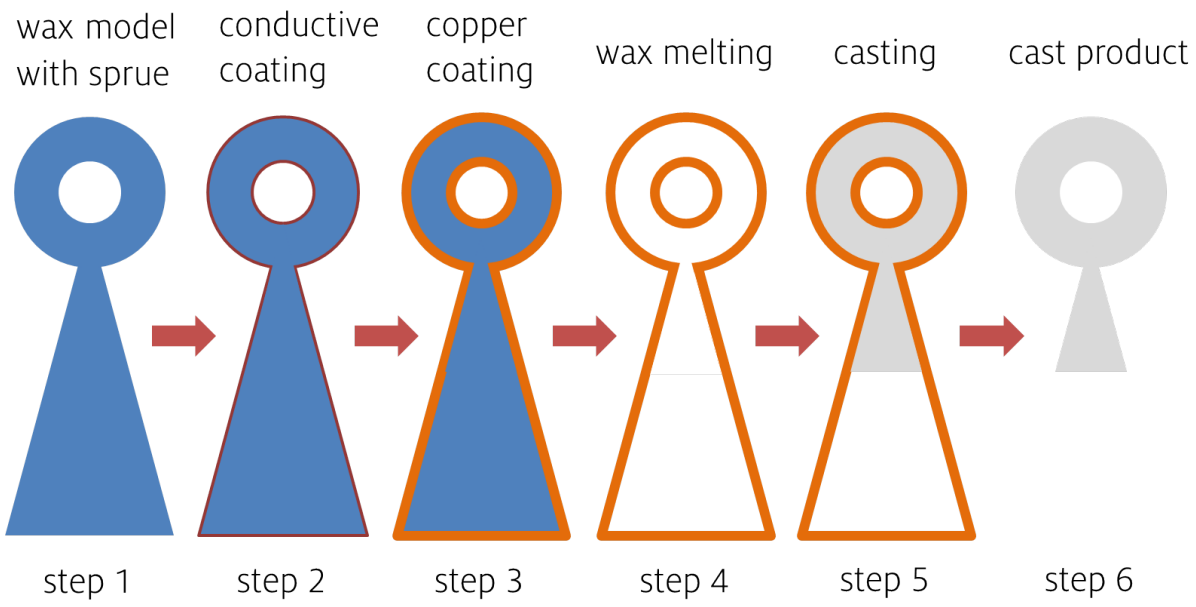

Figure 4.14: Electroforming of a lost copper mold: step 1: forming a wax model with sprue system; step 2: application of a conductive coating; step 3: electroforming of copper coating; step 4: removal of the wax; step 5: casting into the hollow copper shape; step 6: removal of the copper (etching).

Figure 4.15 shows photopraphs of the wax model, in this case it was a ring, including the sprue prior to and after the application of an electric conductive coating. In this case silver conductive paste was applied as electric conductive coating.

Figure 4.15: Wax models with hand-made sprue: (a) original wax surface; (b) wax model covered with silver conductive paste.

In molds that are not equipped with a cooling system, the required quenching for amorphous solidification is achieved solely by the heat transfer from the melt to the copper mold. In order to determine which copper mold thickness provides sufficient cooling to cast amorphous products, an estimation of the minimum copper mass can be made. The amount of heat that is transferred from the melt during casting ΔQ_{melt} is equal to the amount of heat that is received by the copper mold ΔQ_{Cu}, if a loss-free process, i.e. adiabatic conditions, is assumed (equation 4.1):

$$\Delta Q_{melt} = \Delta Q_{Cu} \tag{4.1}$$

Depending on the heat conductivity of the copper mold and on the heat conductivity of the bulk metallic glass and also on the temperature depending specific heat capacity c_p of both materials and the heat transfer coefficient, a time-dependent cooling rate can be calculated. Unfortunately, the heat conductivity and the heat transfer coefficient are often not known yet for bulk metallic glasses. However, after some time, an equilibrium temperature T_{end} is reached, which can be calculated independently of those unknown values. Equation 4.1 can then be written as:

$$\Delta Q_{melt} = m_{melt} * c_{melt}(T_{cast} - T_{end}) = \Delta Q_{Cu} = m_{Cu} * c_{Cu}(T_{end} - T_{Cu}) \tag{4.2}$$

Thus the mass of the copper mold can be calculated as:

$$m_{Cu} = m_{melt} * \frac{c_{melt}(T_{cast} - T_{end})}{c_{Cu}(T_{end} - T_{Cu})} \tag{4.3}$$

The specific heat at a given atmospheric pressure c_p is a temperature-dependent value. In first approximation the minimum required copper mass can be calculated using the

value of c_p at the casting temperature for the bulk metallic glass melt $c_{p,cast}$ and the value at room temperature for c_p of the copper mold. Equation 4.3 can then be written as:

$$m_{Cu} = m_{melt} * \frac{c_{p,cast}(T_{cast} - T_{end})}{c_{p,CuRT}(T_{end} - RT)} \tag{4.4}$$

To guarantee an amorphous solidification, T_{end} should be below T_g. For the gold-based bulk metallic glass $Au_{49}Ag_{5.5}Pd_{2.3}Cu_{26.9}Si_{16.3}$, this means that T_{end} should be below 401 K (128 °C).

$c_{p,cast}$ at T_{cast} is 39.488 $\frac{J}{g-atom*K}$ [103]. The specific heat capacity of copper is approx. 385 $\frac{J}{kg*K}$ or 24.467 $\frac{J}{g-atom*K}$. At a casting temperature of 723 K (450 °C), according to equation 4.4 the copper mold should weigh at least 5 times as much as the melt. For a more conservative calculation at a casting temperature of 1073 K (800 °C), the copper mold should outweigh the melt 10 times.

Figure 4.16 (a) shows a typical copper mold for the new casting procedure electroformed directly on a wax model of a ring with a cone-shaped sprue. Figure 4.16 (b) shows a CT image of the copper mold of a complicatedly shaped ring called "cage-ring" after the casting process was completed. The form filling is almost 100%.

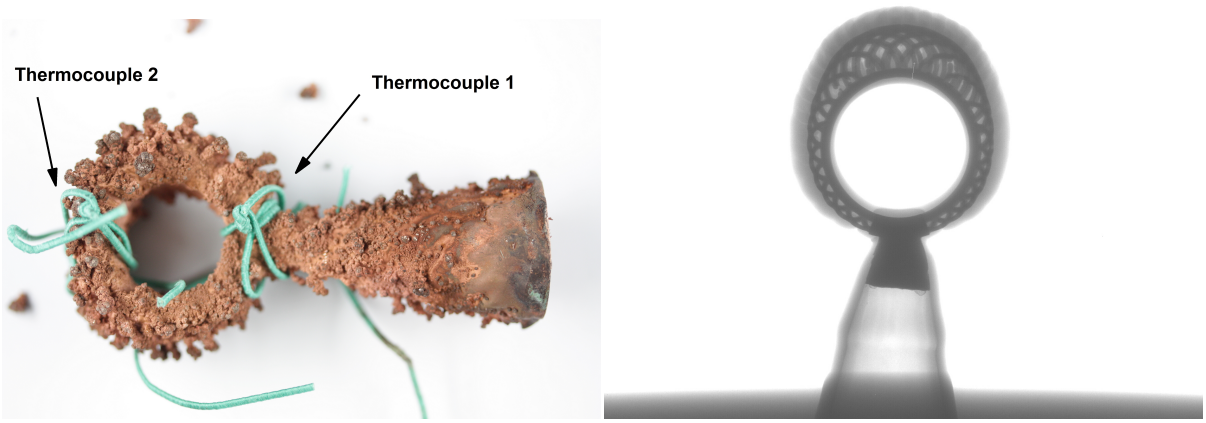

(a) Electroformed copper mold (b) CT image of filled mold

Figure 4.16: Casting into lost metal molds: electroformed copper molds CT image previously published in [13].

Figure 4.17 shows the cooling curves as monitored during centrifugal casting for 3 different castings of a simple ring shape as e.g. shown in Figure 4.18 (a). Each casting was carried out for a metal melt mass m_{melt} of 16 g with the composition $Au_{49}Ag_{5.5}Pd_{2.3}Cu_{26.9}Si_{16.3}$ at a casting temperature of 1073 K (800 °C). The copper molds had different mold masses, resulting from different electroforming times. The mass of each copper mold used in the casting trials of to ring 1, 2 or 3 are given in Figure 4.17.

During the first casting (ring 1), the temperature stayed well above T_g for several seconds, enough for the crystallization to take place, as the XRD spectrum in the first inset of

Figure 4.17 shows. For the slightly larger copper mold in the second casting trial (ring 2), some small sharp peaks superimposed the two broad maxima of the amorphous matrix, indicating a small volume fraction of crystals. The cooling curves of the second casting trial show that the temperature did not rise above T_g at the position of the thermocouples (positions as indicated in Figure 4.16). Inside the mold probably higher temperatures occurred during casting, initializing the crystallization onset. With a copper mold mass m_{Cu} of 88 g, which corresponds to a m_{Cu}/m_{melt}-ratio of 5.5, a completely XRD-amorphous sample was cast in the third casting trial.

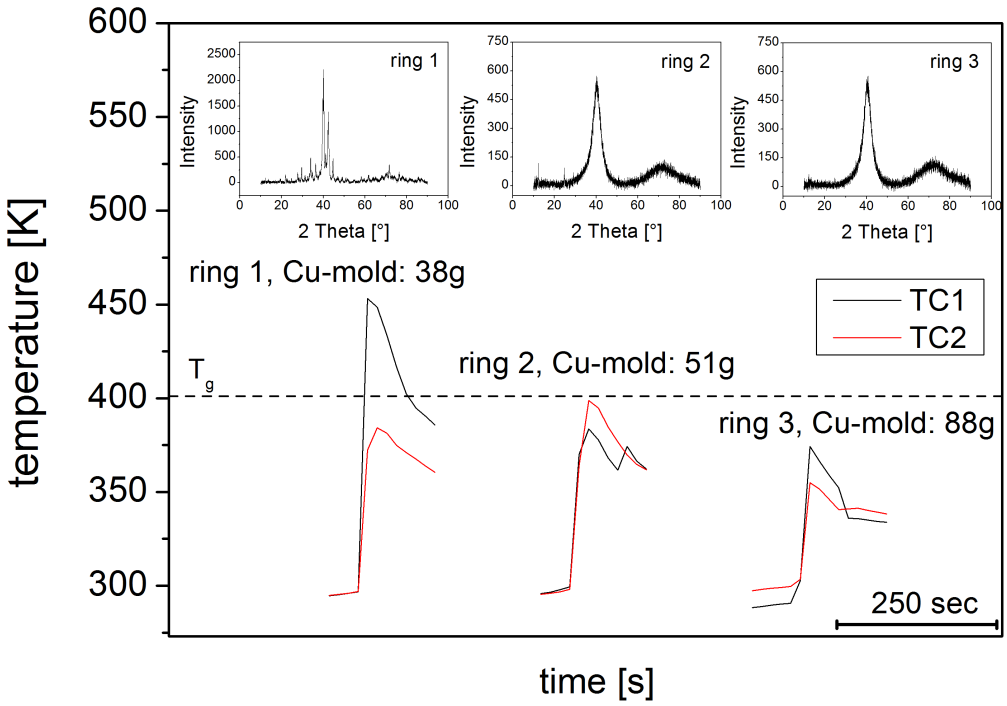

Figure 4.17: Cooling curves determined with 2 thermocouples (TC) on the outside of the respective copper molds (position of the thermocouples as indicated in Figure 4.16 (a)). The weight of each copper mold is indicated in the plot. XRD spectra indicate that for a casting of 16 g melt at 1073 K (800 °C) casting temperature, 88 g copper mold weight is sufficient for amorphous solidification.

Figure 4.18 shows examples of jewelry items cast with the new casting method. The high form filling combined with fast cooling is a result of the employed centrifugal casting. Geometries as in Figure 4.18 (b) are only castable with lost mold casting methods. A patent for this casting method was filed by the author of the present work and three co-workers

in 2013 under the numbers DE 10 2013 009 975.7 A1 and WO2014198380A1 [5].

(a) simple ring (b) cage ring

Figure 4.18: Casting into lost metal molds: cast products; (a) simple ring shape (polished); (b) complex cage ring with sprue after removal of the copper mold by etching. after [13, 14, 15].

4.1.5 Thermoplastic Forming of $Au_{49}Ag_{5.5}Pd_{2.3}Cu_{26.9}Si_{16.3}$

For the thermoplastic forming of bulk samples, the granules were tested as a feedstock material. At a forming temperature between 423 and 443 K (150 - 170°C) the granules were pressed together to form a small cup-shaped bulk sample. Due to an interruption of the cooling cycle, the sample crystallized inside the TPF device. The brittle crystalline sample cracked during disassembly, one of the fractured parts is shown in Figure 4.19 (a). A metallographic cross-section was done with the cross-section plane as indicated in Figure 4.19 (a). An overview of the sample in cross-section is given in Figure 4.19 (b).

The boundary between two former granules can still be determined from images taken in the SEM, see the arrows in Figure 4.20 (a) and magnifications of the boundary in (b) and (c). About 50 % of the boundary shows a perfect bonding between the former granules. Residual SiO_2 from the granule surface probably prevents a 100 % bonding of the granules. During the thermoplastic forming process, the granule surfaces are strained, and the superficial SiO_2 brakes up, resulting in island-like SiO_2 and "fresh" pristine surface areas of $Au_{49}Ag_{5.5}Pd_{2.3}Cu_{26.9}Si_{16.3}$, where atomic bonding can take place. A similar behavior was observed by Chen et al. [51] for a $Zr_{35}Ti_{30}Cu_{7.5}Be_{27.5}$.

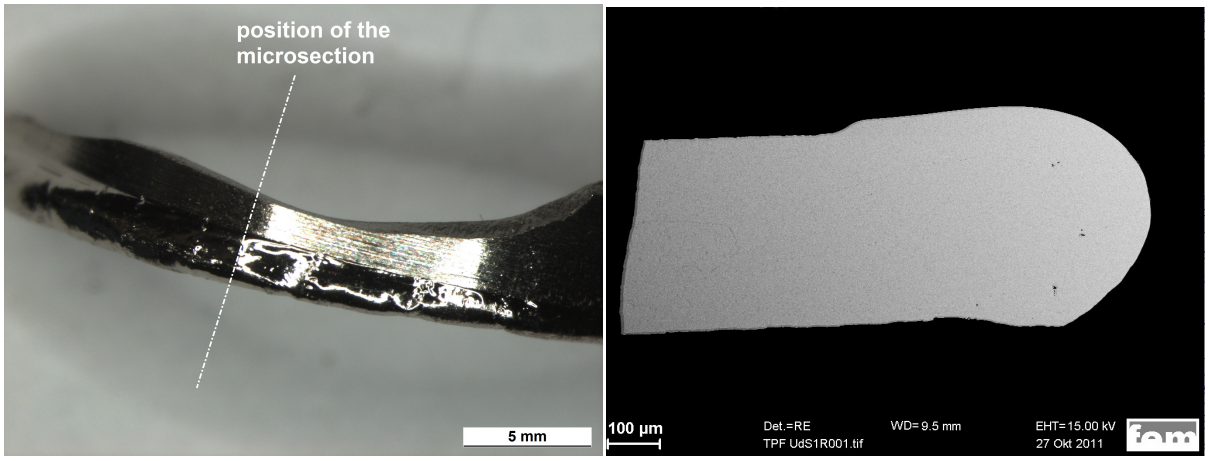

(a) Thermoplastically formed specimen (b) Cross-section of (a)

Figure 4.19: Cross-section through a thermoplastically formed specimen. Granules were used as feedstock for the thermoplastic forming process. The specimen crystallized due to a cooling problem after the forming procedure and therefore broke into several parts during the disassembling from the TPF-insert-device. The position of the microsection in (b) is indicated by the dotted line in (a).

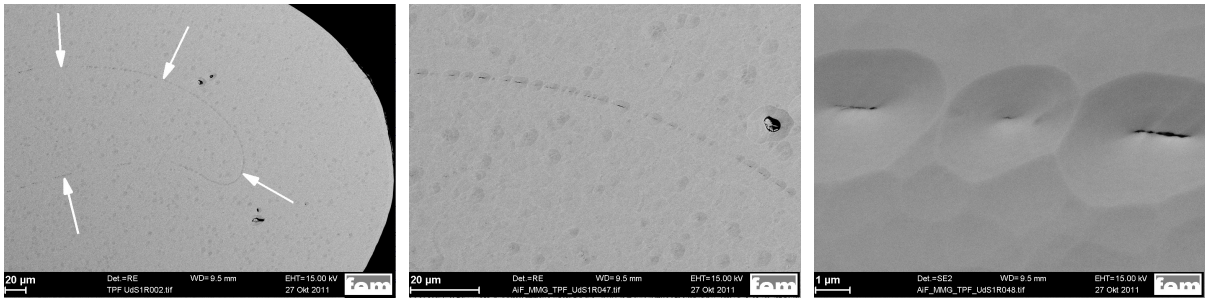

(a) Overview of the interface between 2 former granules (b) Detail of (a) (c) Detail of (b)

Figure 4.20: Former granule boundaries can only be determined at high magnification in the SEM after an ion-milling procedure. About 50% of the interface between former granule surfaces is bonded. Imperfections in the bonding interface are probably due to residual SiO_2 on the granule surfaces.

4.2 Alloy Development

Several glass-forming gold-based alloys are reported in the literature. Though $Au_{49}Ag_{5.5}Pd_{2.3}Cu_{26.9}Si_{16.3}$ is considered to be the best gold-based glass-forming composition, other alloy compositions are promising for applications in jewelry, watchmaking and technical parts as well. In the present work, especially alloys introduced by Zhang et al. [6] were investigated in terms of casting performance and tarnish resistance in comparison to $Au_{49}Ag_{5.5}Pd_{2.3}Cu_{26.9}Si_{16.3}$. Already at the beginning of the study, a pronounced discoloring of several samples was observed, which emphasized the necessity to develop of a tarnish-resistant alloy. The following sections show the first results of the ongoing alloy development that is based on the findings of the present work, starting with an overview of all the compositions investigated in the present work.

4.2.1 Composition Overview

The compositions of every alloy developed and investigated during the present work along with alloy compositions taken from literature are listed in table 4.3.

Alloys 19 to 29 were derived from isopleth sections in the respective alloy systems calculated using ThermoCalc®. Casting alloy 19 to 29 into plates of 1 mm thickness resulted in crystalline samples.

To investigate the influence of certain elements on the overall corrosion performance, micro-alloying of a sixth component to the mother alloy composition of $Au_{49}Ag_{5.5}Pd_{2.3}Cu_{26.9}Si_{16.3}$ in the range between 1 and 3 at.% was carried out. As the non precious elements copper and silicon dominate the tarnishing process, the additional elements were introduced as a substitution for either copper or silicon, depending on the nature of the sixth element. Metallic alloying elements were chosen as a substitution for part of the copper, whereas germanium was used to substitute 1 and 3 at% silicon, respectively. Table 4.4 gives a more detailed overview of the micro-alloyed compositions.

Small amounts of additional elements can already have an impact on the glass-forming ability. XRD scans showed that crystallization had taken place to some extent for alloys 7, 10 and 13. Hence, the critical casting thickness d_c for these new alloys is reduced below 2 mm or 1 mm, respectively. Substituting 1 at.% silicon with germanium resulted in an XRD amorphous alloy, whereas substituting 3 at.% silicon with germanium caused crystallization to start.

Table 4.3: Tabular overview of the alloys produced and investigated in the present study. The first 5 compositions were introduced by Schroers and Zhang et al. (see the respective references). The other compositions in this overview are new compositions developed during the present work.

Alloy No.	Composition [at%]	Composition [wt%]	Reference
1	$Au_{49}Ag_{5.5}Pd_{2.3}Cu_{26.9}Si_{16.3}$	$Au_{76}Ag_{4.7}Pd_{1.9}Cu_{13.5}Si_{3.6}$	[1]
2	$Au_{50}Ag_{7.5}Cu_{25.5}Si_{17}$	$Au_{77.21}Ag_{6.34}Cu_{12.7}Si_{3.74}$	[6]
3	$Au_{60}Ag_{7.5}Cu_{15.5}Si_{17}$	$Au_{83.88}Ag_{5.74}Cu_{6.99}Si_{3.39}$	[6]
4	$Au_{65}Ag_{7.5}Cu_{10.5}Si_{17}$	$Au_{86.76}Ag_{5.48}Cu_{4.52}Si_{3.24}$	[6]
5	$Au_{70}Ag_{7.5}Cu_{5.5}Si_{17}$	$Au_{89.39}Ag_{5.25}Cu_{2.27}Si_{3.1}$	[6]
6	$Au_{49}Ag_{5.5}Pd_{2.3}Cu_{25.9}Si_{16.3}Al_1$	$Au_{76.5}Ag_{4.7}Pd_{1.94}Cu_{13}Si_{3.6}Al_{0.2}$	this study
7	$Au_{49}Ag_{5.5}Pd_{2.3}Cu_{24.9}Si_{16.3}Al_2$	$Au_{76.7}Ag_{4.71}Pd_{1.95}Cu_{12.6}Si_{3.64}Al_{0.43}$	this study
8	$Au_{49}Ag_{5.5}Pd_{2.3}Cu_{25.9}Sn_1Si_{16.3}$	$Au_{75.92}Ag_{4.67}Pd_{1.93}Cu_{12.95}Sn_{0.93}Si_{3.6}$	this study
9	$Au_{49}Ag_{5.5}Pd_{2.3}Cu_{25.9}Ga_1Si_{16.3}$	$Au_{76.22}Ag_{4.68}Pd_{1.93}Cu_{13}Ga_{0.55}Si_{3.62}$	this study
10	$Au_{49}Ag_{5.5}Pd_{2.3}Cu_{25.9}Fe_1Si_{16.3}$	$Au_{76.30}Ag_{4.69}Pd_{1.94}Cu_{13.01}Fe_{0.44}Si_{3.62}$	this study
11	$Au_{49}Ag_{5.5}Pd_{2.3}Cu_{25.9}Cr_1Si_{16.3}$	$Au_{76.30}Ag_{4.69}Pd_{1.94}Cu_{13.01}Cr_{0.44}Si_{3.62}$	this study
12	$Au_{49}Ag_{5.5}Pd_{2.3}Cu_{26.9}Ge_1Si_{15.3}$	$Au_{75.99}Ag_{4.67}Pd_{1.93}Cu_{13.46}Ge_{0.57}Si_{3.38}$	this study
13	$Au_{49}Ag_{5.5}Pd_{2.3}Cu_{26.9}Ge_3Si_{13.3}$	$Au_{75.46}Ag_{4.64}Pd_{1.91}Cu_{13.37}Ge_{1.7}Si_{2.92}$	this study
14	$Au_{60}Ag_{5.5}Pd_2Cu_{15.5}Si_{17}$	$Au_{83.9}Ag_{4.2}Pd_{1.5}Cu_7Si_{3.4}$	this study
15	$Au_{65}Ag_{5.5}Pd_2Cu_{10.5}Si_{17}$	$Au_{86.8}Ag_4Pd_{1.4}Cu_{4.5}Si_{3.2}$	this study
16	$Au_{70}Ag_{5.5}Pd_2Cu_{5.5}Si_{17}$	$Au_{89.4}Ag_{3.9}Pd_{1.4}Cu_{2.3}Si_{3.1}$	this study
17	$Au_{50.85}Ag_{5.7}Cu_{27.9}Si_{15.53}$	$Au_{78}Ag_{4.79}Cu_{13.81}Si_{3.4}$	this study
18	$Au_{75}Ag_{5.5}Cu_{2.5}Si_{17}$	$Au_{92.32}Ag_{3.71}Cu_{0.99}Si_{2.98}$	this study
19	$Au_{76.5}Sb_{10}Si_{13.5}$	$Au_{90.42}Sb_{7.31}Si_{2.28}$	this study
20	$Au_{55}Sb_5Ag_{7.5}Cu_{15.5}Si_{17}$	$Au_{79}Sb_{4.44}Ag_{5.9}Cu_{7.18}Si_{3.48}$	this study
21	$Au_{52.5}Sb_{7.5}Ag_{7.5}Cu_{15.5}Si_{17}$	$Au_{76.45}Sb_{6.75}Ag_{5.98}Cu_{7.28}Si_{3.53}$	this study
22	$Au_{75.2}Ga_{9.3}Si_{15.5}$	$Au_{93.18}Ga_{4.08}Si_{2.74}$	this study
23	$Au_{70.2}Ag_5Ga_{9.3}Si_{15.5}$	$Au_{90.12}Ag_{3.28}Ga_{3.95}Si_{2.65}$	this study
24	$Au_{70.2}Cu_5Ga_{9.3}Si_{15.5}$	$Au_{91.36}Cu_{1.96}Ga_4Si_{2.69}$	this study
25	$Au_{65.2}Ag_{10}Ga_{9.3}Si_{15.5}$	$Au_{85.59}Ag_{7.19}Ga_{4.32}Si_{2.9}$	this study
26	$Au_{65.2}Cu_{10}Ga_{9.3}Si_{15.5}$	$Au_{88.19}Cu_{4.36}Ga_{4.45}Si_{2.99}$	this study
27	$Au_{65.2}Ag_5Cu_5Ga_{9.3}Si_{15.5}$	$Au_{86.87}Ag_{3.65}Cu_{2.15}Ga_{4.39}Si_{2.95}$	this study
28	$Au_{52.11}Ag_{7.52}Cu_{15.57}Ga_{9.3}Si_{15.5}$	$Au_{78.06}Ag_{6.17}Cu_{7.53}Ga_{4.93}Si_{3.31}$	this study
29	$Au_{48.26}Ag_{4.7}Pd_2Cu_{31.9}Si_{13.14}$	$Au_{75.31}Ag_{4.02}Pd_{1.69}Cu_{16.06}Si_{2.92}$	this study

Table 4.4: Systematic micro-alloying of $Au_{49}Ag_{5.5}Pd_{2.3}Cu_{26.9}Si_{16.3}$. The casts were carried out employing massive copper molds with plate geometry, the smallest dimension d_{cast} varying between 1 and 2 mm thickness, and applying centrifugal casting

Composition at%	Au	Ag	Pd	Cu	Si	Al	Sn	Ga	Fe	Cr	Ge	d_{cast}
Au-BMG1	49	5.5	2.3	26.9	16.3							2 mm
6	49	5.5	2.3	25.9	16.3	1						2 mm
7	49	5.5	2.3	24.9	16.3	2						2 mm
8	49	5.5	2.3	25.9	16.3		1					1 mm
9	49	5.5	2.3	25.9	16.3			1				1 mm
10	49	5.5	2.3	25.9	16.3				1			1 mm
11	49	5.5	2.3	25.9	16.3					1		1 mm
12	49	5.5	2.3	26.9	15.3						1	1 mm
13	49	5.5	2.3	26.9	13.3						3	1 mm

4.2.2 Colorimetric Characterization of Gold-based Amorphous Alloys

The initial "as-polished" color of the glass-formers investigated in the present work was determined according to the standard tests described in Section 3.3.1. As an indicator for their suitability as a white gold jewelry alloy, the YI values are listed below (table 4.2.2). All YI values are below 19 and are thus within the premium white gold regime.

Table 4.5: All documented YI values are mean values of several measurements (a minimum of 3 per composition).

Alloy No.	Composition in at%	Cu/Si	Au/Si	YI as-polished
1	$Au_{49}Ag_{5.5}Pd_{2.3}Cu_{26.9}Si_{16.3}$	1.65	3	17.8
2	$Au_{50}Ag_{7.5}Cu_{25.5}Si_{17}$	1.5	2.94	14.74
3	$Au_{60}Ag_{7.5}Cu_{15.5}Si_{17}$	0.9	3.53	16.09
4	$Au_{65}Ag_{7.5}Cu_{10.5}Si_{17}$	0.6	3.82	18.01
6	$Au_{49}Ag_{5.5}Pd_{2.3}Cu_{25.9}Si_{16.3}Al_1$	1.6	3	15.01
7	$Au_{49}Ag_{5.5}Pd_{2.3}Cu_{24.9}Si_{16.3}Al_2$	1.53	3	16.11
8	$Au_{49}Ag_{5.5}Pd_{2.3}Cu_{25.9}Si_{16.3}Sn_1$	1.6	3	15.22
9	$Au_{49}Ag_{5.5}Pd_{2.3}Cu_{25.9}Si_{16.3}Ga_1$	1.6	3	14.99
10	$Au_{49}Ag_{5.5}Pd_{2.3}Cu_{25.9}Si_{16.3}Fe_1$	1.6	3	16.16
11	$Au_{49}Ag_{5.5}Pd_{2.3}Cu_{25.9}Si_{16.3}Cr_1$	1.6	3	18.94
12	$Au_{49}Ag_{5.5}Pd_{2.3}Cu_{26.9}Si_{15.3}Ge_1$	1.76	3.2	15.3
13	$Au_{49}Ag_{5.5}Pd_{2.3}Cu_{26.9}Si_{13.3}Ge_3$	2	3.7	16.55
14	$Au_{60}Ag_{5.5}Pd_2Cu_{15.5}Si_{17}$	0.9	3.53	17.28
15	$Au_{65}Ag_{5.5}Pd_2Cu_{10.5}Si_{17}$	0.6	3.82	17.77

4.2.3 Calorimetric Characterization of New Alloy Compositions

Table 4.6 lists the characteristic temperatures like T_g, T_x, T_m and T_l that were determined using differential scanning calorimetry DSC during up-scans with 20 K/min in Ar flux. For the crystalline compositions, only the melting temperature T_m and the liquidus temperatures T_{l1} and T_{l2} are reported. Secondary liquidus temperatures T_{l2} occur, if residual crystalline portions of the material melt at higher temperatures than the primary liquidus temperature, causing a second signal in the DSC scan.

Figure 4.21 shows the DSC scans for (a) the compositions $Au_{50}Ag_{7.5}Cu_{25.5}Si_{17}$, $Au_{60}Ag_{7.5}Cu_{15.5}Si_{17}$ and $Au_{70}Ag_{7.5}Cu_{5.5}Si_{17}$ taken from [6] and (b) the compositions $Au_{60}Ag_{5.5}Pd_2Cu_{15.5}Si_{17}$ and $Au_{65}Ag_{5.5}Pd_2Cu_{10.5}Si_{17}$, which were developed as part of the present work. The idea was to re-introduce palladium into the composition similar to $Au_{49}Ag_{5.5}Pd_{2.3}Cu_{26.9}Si_{16.3}$, because palladium was observed to be beneficial for the critical casting thickness in this system by Lohwongwatana [104].

The DSC scans of the micro-alloyed compositions developed in the present work $Au_{49}Ag_{5.5}Pd_{2.3}Cu_{25.9}Si_{16.3}Al_1$, $Au_{49}Ag_{5.5}Pd_{2.3}Cu_{24.9}Si_{16.3}Al_2$, $Au_{49}Ag_{5.5}Pd_{2.3}Cu_{25.9}Cr_1Si_{16.3}$, $Au_{49}Ag_{5.5}Pd_{2.3}Cu_{26.9}Ge_1Si_{15.3}$ and $Au_{49}Ag_{5.5}Pd_{2.3}Cu_{26.9}Ge_3Si_{13.3}$ are shwown in Figure 4.22.

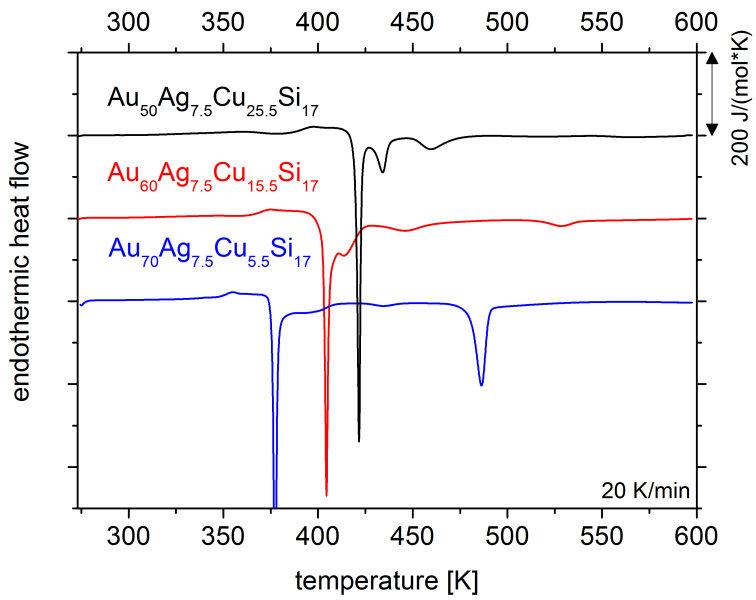

(a)

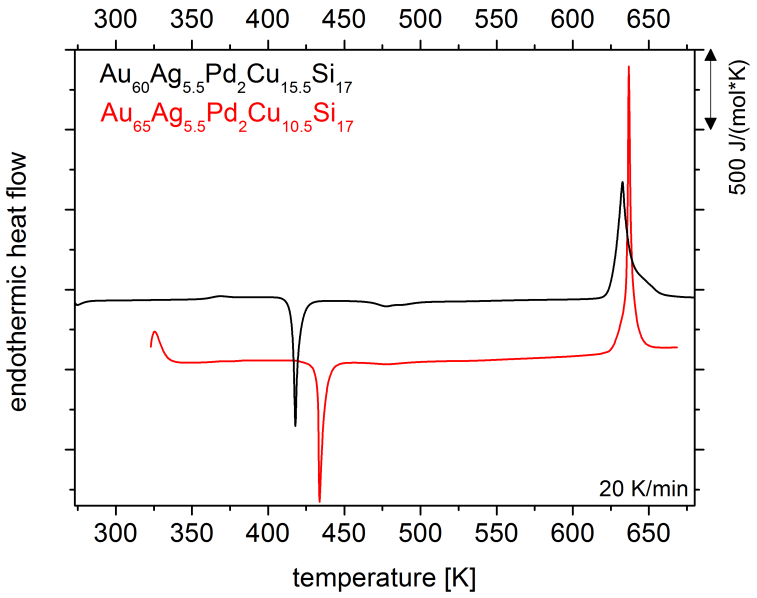

(b)

Figure 4.21: DSC scans of (a) compositions taken from [6] (alloys 2, 3 and 5) and (b) similar compositions with 2 at% palladium as a substitution for silver developed in the present work (alloys 14 and 15). The heating rate was 20 K/min.

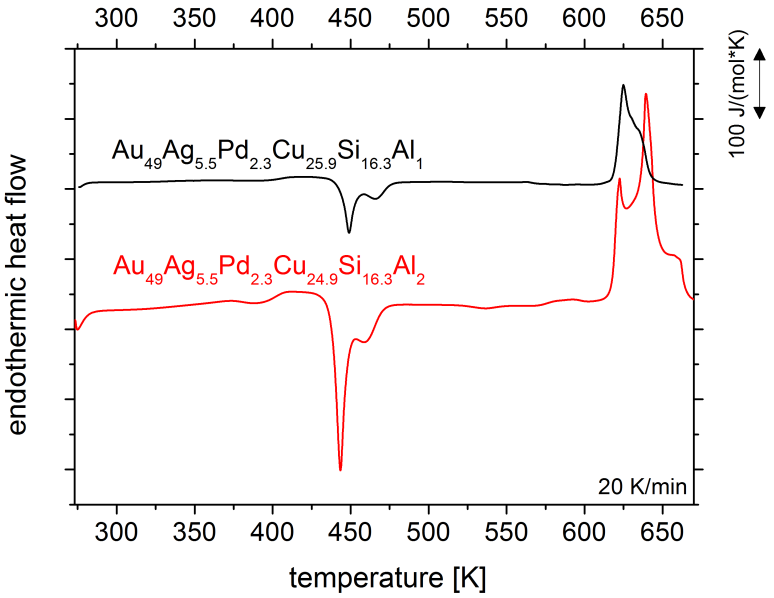

(a)

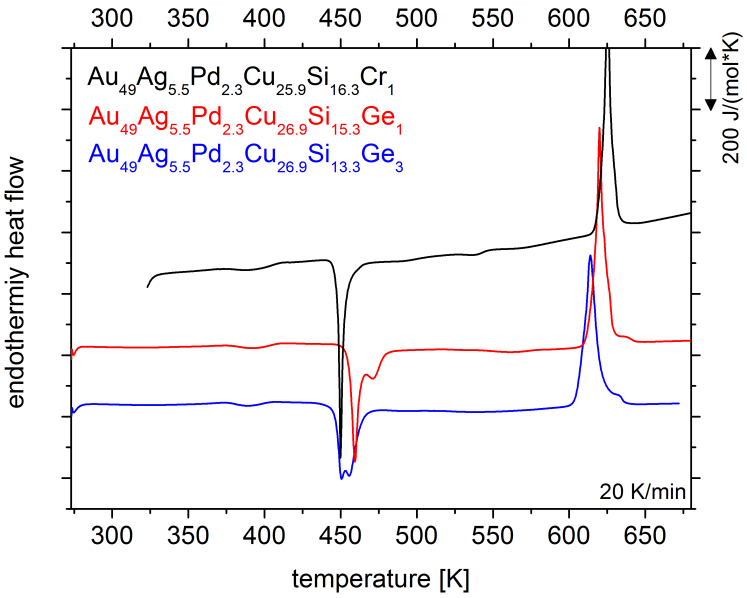

(b)

Figure 4.22: DSC scans of some of the micro-alloyed compositions. (a) shows the scans of the alloys with 1 and 2 at% aluminum substitution for copper (alloys 6 and 7) and (b) the scans of the alloys with a 1 at% chrome substitution for copper and a 1 and 3 at% substitution of germanium for silicon (alloys 11-13).

Figure 4.23 shows DSC scans of the alloys $Au_{50.85}Ag_{5.7}Cu_{27.9}Si_{15.53}$ and $Au_{75}Ag_{5.5}Cu_{2.5}$

Si_{17}. The first alloy composition was measured as the matrix composition of a partially crystalline sample of $Au_{49}Ag_{5.5}Pd_{2.3}Cu_{26.9}Si_{16.3}$. The scope of this cast was to find a composition even more stable against crystallization than the mother alloy Au-BMG1 by casting the exact composition that remained as amorphous matrix even after the onset of crystallization. Unfortunately, this matrix compositions proved to be partially crystalline already at 1 mm casting thickness. The latter composition $Au_{75}Ag_{5.5}Cu_{2.5}Si_{17}$ was developed as a continuation in the composition line of [6] towards a higher gold content. The purpose was to find a bulk metallic glass composition with 22k gold. This composition proved to be crystalline at a casting thickness of 2 mm. The exothermic peaks in the DSC scan are either a crystallization signal, which would mean that the sample was indeed partially amorphous, or it is the phase transformation of a metastable phase formed during rapid cooling to a stable crystal phase.

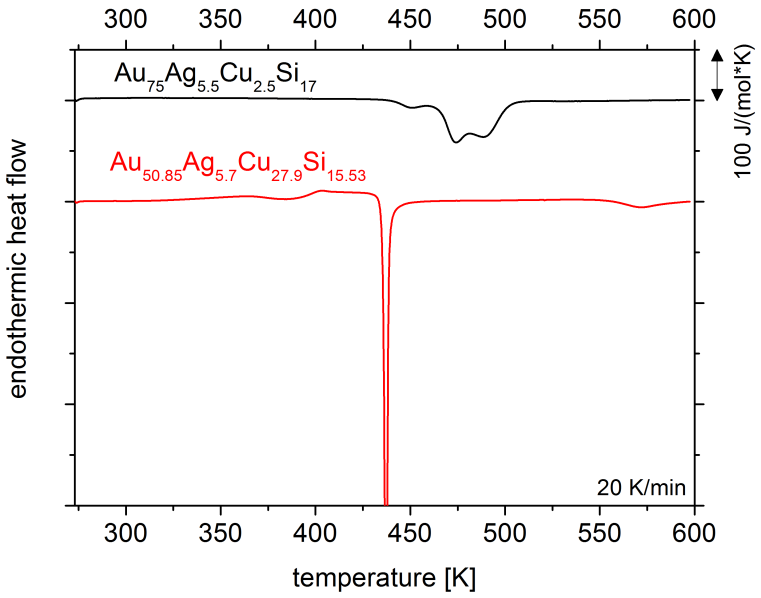

Figure 4.23: DSC Scans of the alloys $Au_{50.85}Ag_{5.7}Cu_{27.9}Si_{15.53}$ (alloy 17) and $Au_{75}Ag_{5.5}Cu_{2.5}Si_{17}$(alloy 18).

The Au-Ga-(Cu-Ag)-Si and the Au-Sb-(Cu-Ag)-Si system were explored systematically, testing several sample compositions according to the isopleth sections derived from thermocalc calculations (not shown here). No bulk amorphous solidifying composition has been found in these systems so far. The DSC scans were thus only analyzed to determine the melting and liquidus temperatures. Figure 4.24 shows the DSC scans for the chosen compositions in (a) the Au-Ag-Ga-Si system and (b) in the Au-Ga-Si and the Au-Cu-Ga-Si system.

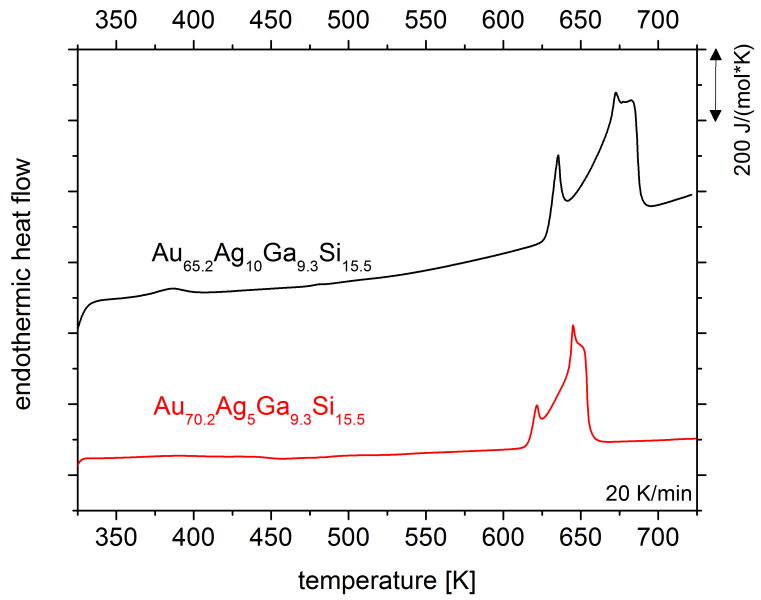

(a)

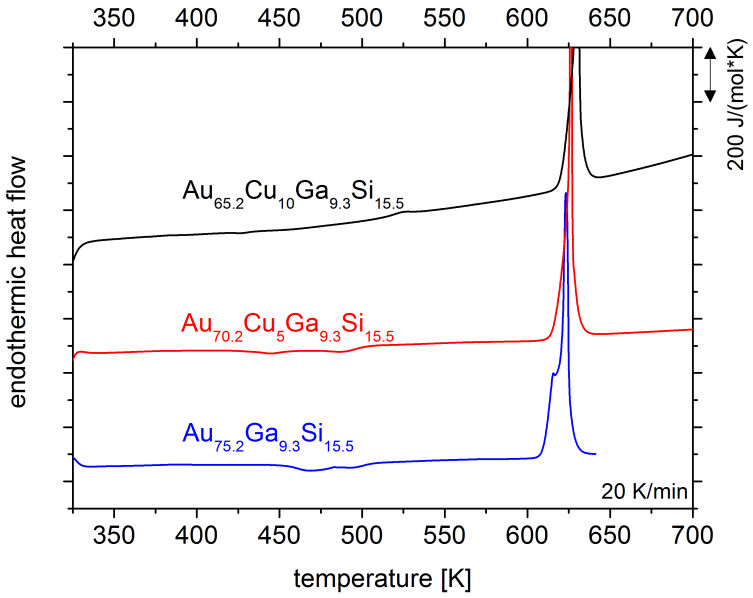

(b)

Figure 4.24: DSC scans of the compositions in (a) the Au-Ag-Ga-Si system (alloys 23 and 25) and (b) in the Au-Ga-Si and the Au-Cu-Ga-Si system (alloys 22, 24 and 26).

Figure 4.25 shows the DSC scans for the chosen compositions in (a) the Au-Ag-Cu-Ga-Si system and (b) in the Au-Sb-Si and the Au-Cu-Ag-Sb-Si system.

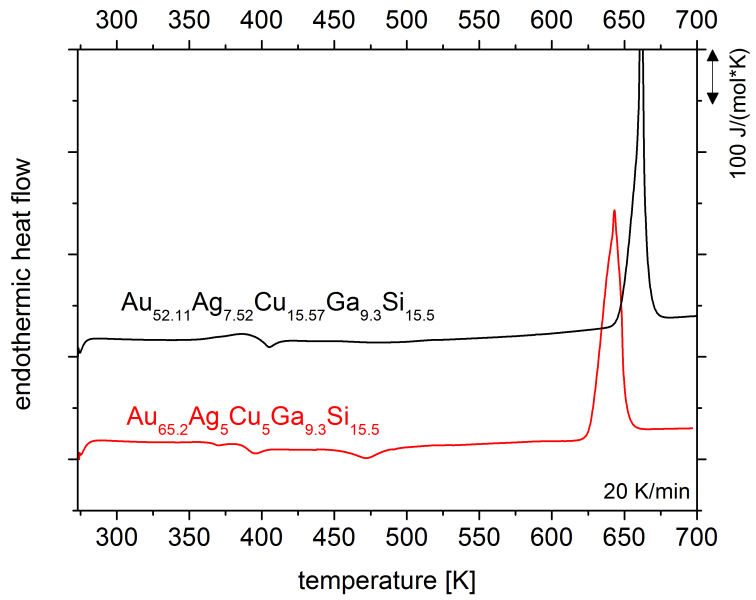

(a)

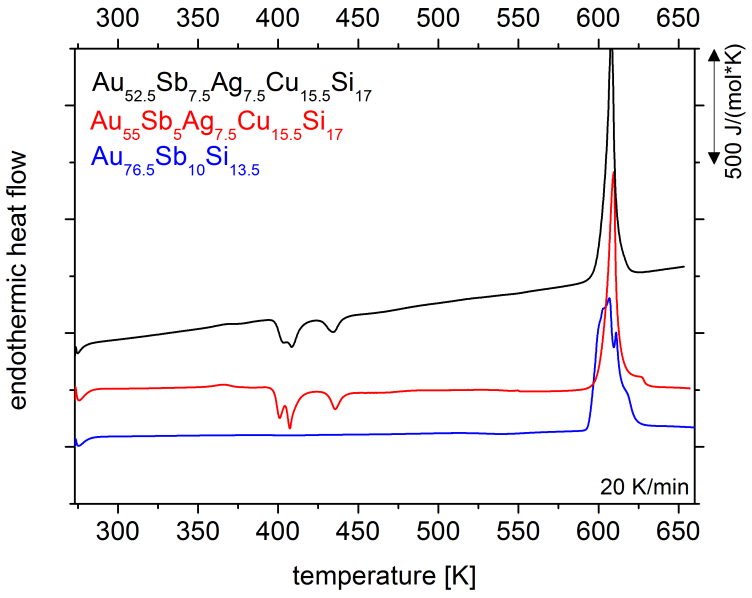

(b)

Figure 4.25: DSC scans of the compositions in (a) the Au-Ag-Cu-Ga-Si system (alloys 27 and 28) and (b) in the Au-Sb-Si and the Au-Cu-Ag-Sb-Si system (alloys 19, 20 and 21).

Table 4.6 shows an overview on the temperature values derived from the DSC scans.

Table 4.6: Overview of the characteristic temperatures derived from the DSC analysis. Red figures are the values taken from publications of Schroers et al. [1], Pogatscher et al. [105] and Zhang et al. [6]. All other values were determined during the present study.

alloy [at.%]	$T_{g,onset}$ [K]	$T_{g,end}$ [K]	T_{x1} [K]	T_{x2} [K]	T_{x3} [K]	T_m [K]	T_{l1} [K]	T_{l2} [K]
$Au_{49}Ag_{5.5}Pd_{2.3}Cu_{26.9}Si_{16.3}$	401		459			618	644	
$Au_{50}Ag_{7.5}Cu_{25.5}Si_{17}$	385/377	396	419/422	423	450		652	
$Au_{60}Ag_{7.5}Cu_{15.5}Si_{17}$	364/359	374	403/403	411	435		670	
$Au_{65}Ag_{7.5}Cu_{10.5}Si_{17}$	342		392				678	
$Au_{70}Ag_{7.5}Cu_{5.5}Si_{17}$	348/339	355	376/375	426	481		680	
$Au_{49}Ag_{5.5}Pd_{2.3}Cu_{25.9}Si_{16.3}Al_1$	393	413	441	455		619	643	666
$Au_{49}Ag_{5.5}Pd_{2.3}Cu_{24.9}Si_{16.3}Al_2$	394	408	436	451		618	627	
$Au_{49}Ag_{5.5}Pd_{2.3}Cu_{25.9}Cr_1Si_{16.3}$	394	414	448	519?		618	633	
$Au_{49}Ag_{5.5}Pd_{2.3}Cu_{26.9}Ge_1Si_{15.3}$	396	408	455	466		612	629	645
$Au_{49}Ag_{5.5}Pd_{2.3}Cu_{26.9}Ge_3Si_{13.3}$	392	405	446	453		605	627	637
$Au_{60}Ag_{5.5}Pd_2Cu_{15.5}Si_{17}$	368		468			626	647	
$Au_{65}Ag_{5.5}Pd_2Cu_{10.5}Si_{17}$	357	367	415	465		625	659	
$Au_{50.85}Ag_{5.7}Cu_{27.9}Si_{15.53}$	385	402	435					
$Au_{76.5}Sb_{10}Si_{13.5}$						595	614	623
$Au_{55}Sb_5Ag_{7.5}Cu_{15.5}Si_{17}$						601	614	629
$Au_{52.5}Sb_{7.5}Ag_{7.5}Cu_{15.5}Si_{17}$						600	613	
$Au_{75.2}Ga_{9.3}Si_{15.5}$						610	625	
$Au_{70.2}Ag_5Ga_{9.3}Si_{15.5}$						616	656	
$Au_{70.2}Cu_5Ga_{9.3}Si_{15.5}$						616	632	
$Au_{65.2}Ag_{10}Ga_{9.3}Si_{15.5}$						628	689	
$Au_{65.2}Cu_{10}Ga_{9.3}Si_{15.5}$						621	636	
$Au_{65.2}Ag_5Cu_5Ga_{9.3}Si_{15.5}$						626	652	
$Au_{52.11}Ag_{7.52}Cu_{15.57}Ga_{9.3}Si_{15.5}$						647	668	

4.3 Tarnishing Mechanism of Amorphous $Au_{49}Ag_{5.5}Pd_{2.3}Cu_{26.9}Si_{16.3}$

Amorphous granules and plates were subjected to different environmental conditions with different aggressiveness in terms of corrosion attack. The corroded samples were characterized using SEM, FIB, STEM and TEM technology after the tests, and the development of the color change was quantified throughout the test period by determining the CIELab color coordinates. Rates for the oxidation progress were then determined for different temperatures. For the quantification of the development of a yellow color, the Yellowness Index was plotted against the exposure time. For any other color change, the ΔE (color change) values were plotted. Finally Auger and XPS analyzes were applied on several tarnished sample surfaces. The following subsections show the results of these investigations. An overview on the various individual samples, their respective compositions, and the tests they were subjected to is given in the previous Chapter 3 "Methods" (Table 3.3).

4.3.1 Tarnishing Behavior at Different Temperatures and Atmospheres

The rapid tarnishing of this 18k gold alloy is unexpected at room temperature. Gold alloys with high caratage usually show a distinctly high resistance against corrosion attacks, hence their application in decorative products like jewelry and watches.

To investigate the influence of different temperatures below T_g, samples of the amorphous $Au_{49}Ag_{5.5}Pd_{2.3}Cu_{26.9}Si_{16.3}$ were stored under controlled testing conditions at 255 K (-18°C), at room temperature, body temperature 310 K (37°C), and at the elevated temperature 348 K (75°C), which is approx. 50 K below T_g. The influence of the surrounding atmosphere was additionally investigated by applying vacuum (at RT) and an Ar-flux treatment (348 K). For detailed information on the test procedure see Chapter 3, Section 3.2.1.

4.3.1.1 Tarnishing of Amorphous Granules

As-cast granules of $Au_{49}Ag_{5.5}Pd_{2.3}Cu_{26.9}Si_{16.3}$ have been observed to retain their initial premium white color over months during which they were stored at room temperature in the laboratory without any precaution. SEM investigations on as-cast granules showed a thin SiO_2 layer on the sample surface, which is presumably responsible for the prohibited tarnishing of the granules. To evaluate this assumption, a portion of granules was etched with hydrofluoric acid (HF). HF is known to remove SiO_2 very effectively [106]. An SEM analysis confirmed that native[1] SiO_2 layers on Au-BMG granules can be completely removed from the surface by HF treatment. This is shown in Figure 4.26.

[1] native means the formation of oxides on cast products or granules during solidification in contrast to artificial surface alterations after solidification like corrosion products or coatings

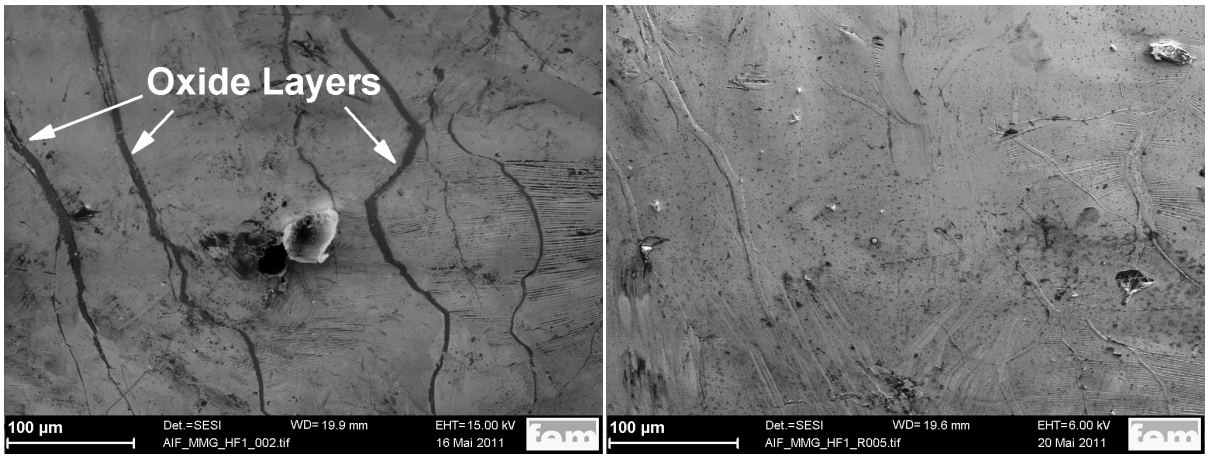

(a) as-cast (b) after HF treatment

Figure 4.26: SEM images of (a) an as-cast granule surface and (b) a similar location after etching with HF. The dark SiO_2 islands are completely removed by the HF treatment.

Figure 4.27 shows the as-cast granules (sample 1 and 2) and the etched granules (sample 3) after storage for different time periods at room temperature and at 348 K (75 °C), respectively. Even after two years storage time, almost no color change can be observed for sample 1 while sample 3, which was etched prior to the aging treatment at 348 K, already shows a distinct discoloring after 7 days and very severe tarnishing after further 30 days of storage. The native superficial SiO_2 largely improves the tarnishing behavior of granules. Even at elevated temperatures, after 7 days no color change can be observed on sample 2 in as-cast condition. A longer test period of 37 days in total causes a color change on sample 2, as well. However, the color change is not as intense as on etched granules (sample 3).

Some granules did not completely separate before they solidified, resulting in a necking between two connected spheres. In the necking between individual spheres, the SiO_2 layer is thicker than on the surface of the spheres and additionally geometrically protected from abrasion. This can be attributed to a stretching and a contraction, respectively, of the melt surface. Figure 4.28 illustrates this development of the native silica during granule formation.

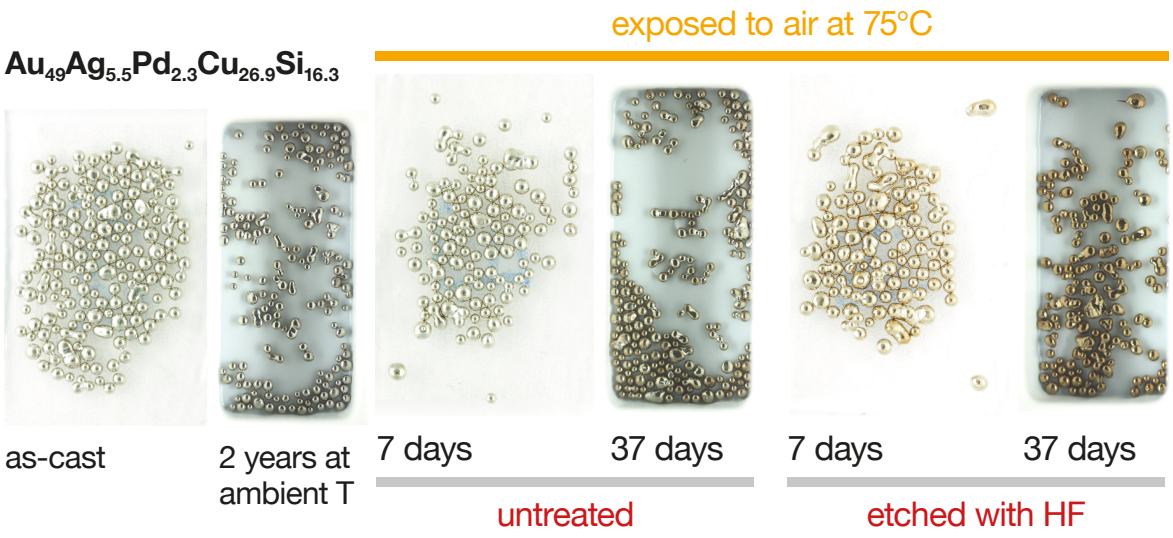

(a) sample 1 (b) sample 2 (c) sample 3

Figure 4.27: Granules in as-cast condition and after a heat treatment at 348 K in etched and unetched condition; reprinted from [3].

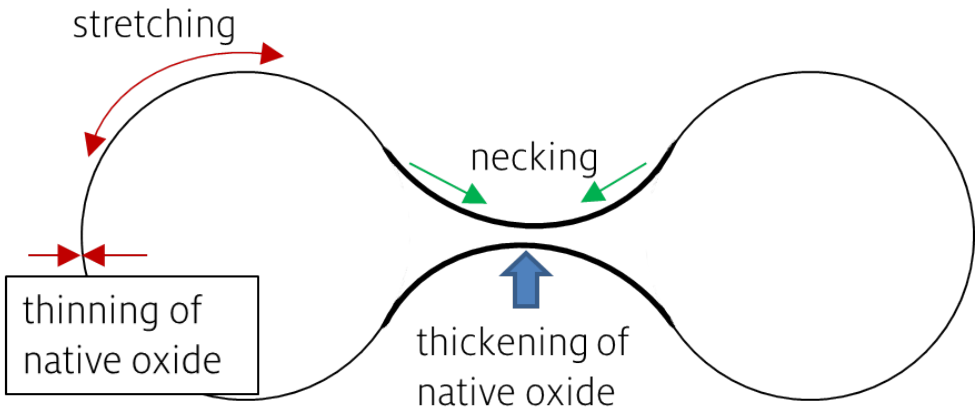

Figure 4.28: Sketch of the silica development on granules in the necking and in the bulging of two connected granules. The stretching causes a thinning effect, while the necking causes a thickening effect, resulting in a thicker silica layer and hence protection in the necking.

The slight discoloring of as-cast granules at room temperature after a time period of 2 years can probably be attributed to a mechanical abrasion of the SiO_2 layer caused by the relative movement of granules in close contact. Figure 4.29 shows detailed images of magnified granules (samples 1 to 3) after the respective aging treatments.

The thicker layers in the necking areas on sample 1 and 2 are still protective at elevated temperatures and after prolonged aging times as can be observed in Figure 4.29 (a) and (b). This can probably be attributed both to the larger SiO_2-thickness as well as to the geometric protection against abrasion in the less exposed necking area. Hence, in the necking no color change takes place and the respective surface areas remain white. Once the protective SiO_2 is removed completely by an HF etching, a uniform color tarnishing can proceed as shown in Figure 4.29 (c) on sample 3.

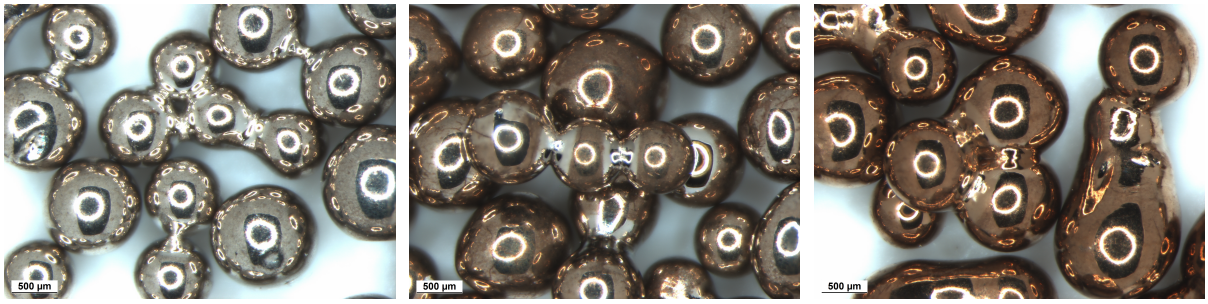

(a) Sample 1, as cast, 2 years RT (b) Sample 2, as cast, 37 days at 348 K (c) Sample 3, HF etched, 37 days at 348 K

Figure 4.29: Granules after different heat treatments: (a) a slight discoloring is observable on the spheres but not in the necking; (b) a clear discoloring is visible on the spheres but not in the necking; (c) a uniform color change took place on the entire sample surface including the necking.

4.3.1.2 Investigation of the Effect of Tarnishing on the Micro Structure of Plate-Shaped Samples

The first attempt to quantify the development of a superficial tarnishing layer was performed on an old sample (sample 4) that was not stored under controlled conditions, but was cast, polished, and subsequently handled with bare hands [3]. This sample is the remaining part of a larger cast plate of geometry $2 \times 10 \times 30$ mm that was cut into several smaller plates for various investigations. The results of these investigations have been published in [4]. The sample was initially not intended to be used for an investigation of the tarnishing mechanism, hence the undefined storage conditions, which give a semi-realistic picture of a commercial product storage condition. After approximately 30 months storage time, the sample showed severe discoloring towards yellow as can be observed in Figure 4.30.

Figure 4.30: Sample 4 after approx. 30 months in lab air. The sample was polished on one side and not cleaned. The sample surface shows a distinct tarnishing toward yellow.

A FIB lamella was prepared cutting normally to the corroded surface. The sample surface area from which the lamella was obtained had been polished prior to the storage period. The lamella was then investigated with a high resolution SEM equipped with a field emission cathode in STEM mode. As is indicated in Figure 4.31 (a), three regions can be determined starting from the outer surface. Layer 1 shows a lighter gray than layer 2. Both layers have a thickness between 20 and 30 nm. The matrix region is indicated with number 3. Above layer 1, the platinum coating originating from the sample preparation is visible.

Layer 1 was found to be enriched in copper and sulfur by a qualitative EDX analysis with a Cu/S ratio of 2/1 in at.%. This ratio fits a formation of Cu_2S sulfide on the surface. Sample 4 was additionally sent to an external laboratory for an AES spectroscopy. The resulting concentration profiles for gold, copper, silicon, palladium, silver, oxygen and sulfur are shown in Figure 4.31 (b). Region 1 is enriched in copper and sulfur, supporting the findings of the EDX analysis. Gold is generally depleted in region 1 but has a higher concentration within the first few nm in the surface, while silicon, palladium, and silver are depleted towards the surface. In the second layer, silicon and oxygen are enriched. The overall concentration of the alloying elements reach the nominal matrix composition in region 3. This was again determined by a qualitative EDX analysis.

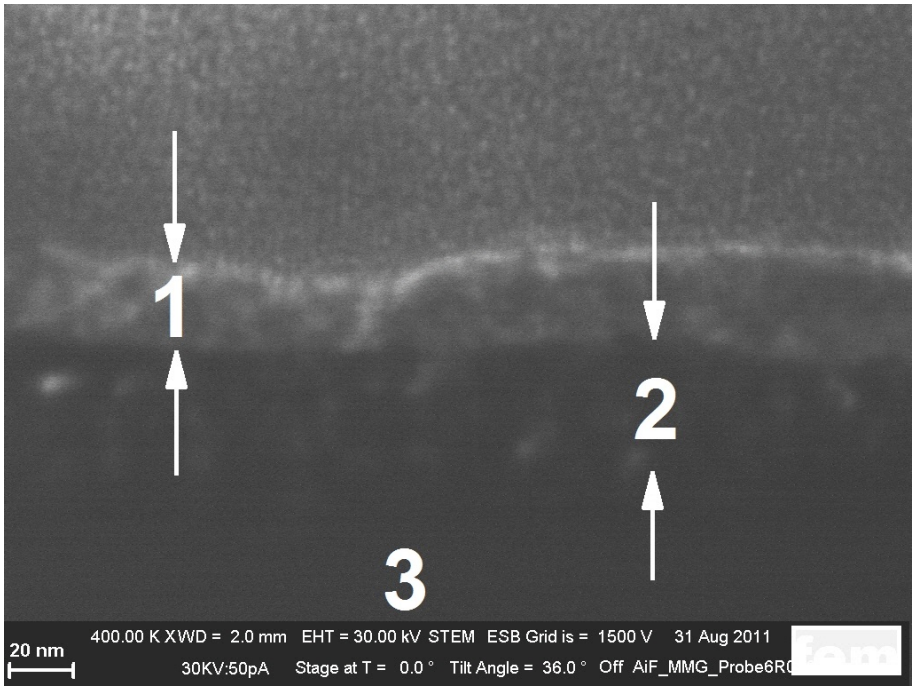

(a) STEM image of FIB lamella

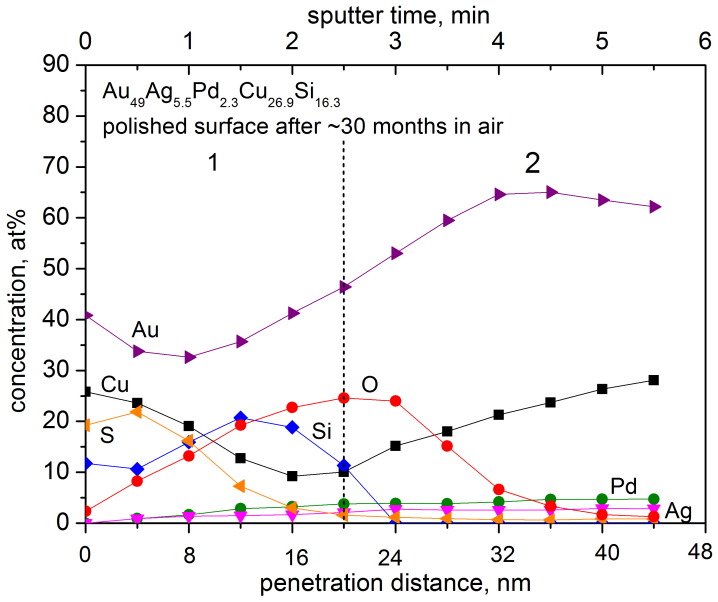

(b) Auger profile

Figure 4.31: (a) superficial corrosion attack on sample 4 after undefined storage at RT for ≈ 30 months. The sample was polished and handled with bare hands to cut samples for various investigations and then stored uncleaned in a plastic sample bag in lab air. Image reprinted from [3] (b) An enrichment in copper and sulfur within a surface layer of approximately 20 nm (1) was detected according to the AES profile. Palladium, silicon, gold, and silver are depleted in layer (1). In a second layer (2), silicon and oxygen are enriched, and copper has a depletion zone, published in an earlier version in [3].

The undefined storage conditions of sample 4 allow only a phenomenal interpretation of the results. For a more distinguished analysis, a test under controlled environmental conditions was set up and plate-shaped samples were prepared.

All plate-shaped samples were ground and polished to mirror finishing according to the standard grinding and polishing procedure of Section 3.1.4 prior to testing. Some of the samples showed pores on the cast surface that were probably caused by air pockets trapped by the liquid melt in the copper mold during casting. Those pores remained on the surface after the grinding and polishing procedure, because they lay several μm beneath the overall surface level and were therefore not affected by the surface finishing.

Figure 4.32 shows an example of a specimen with a residual cast pore. This sample (sample no. 5) was stored at 348 K in air. The image in Figure 4.32 shows a photograph that was taken after 4 days storage time. Sample 5 shows a very distinct discoloring at the polished part of the surface in contrast to the surface of the pore with as-cast surface condition, which still has the initial white gold color.

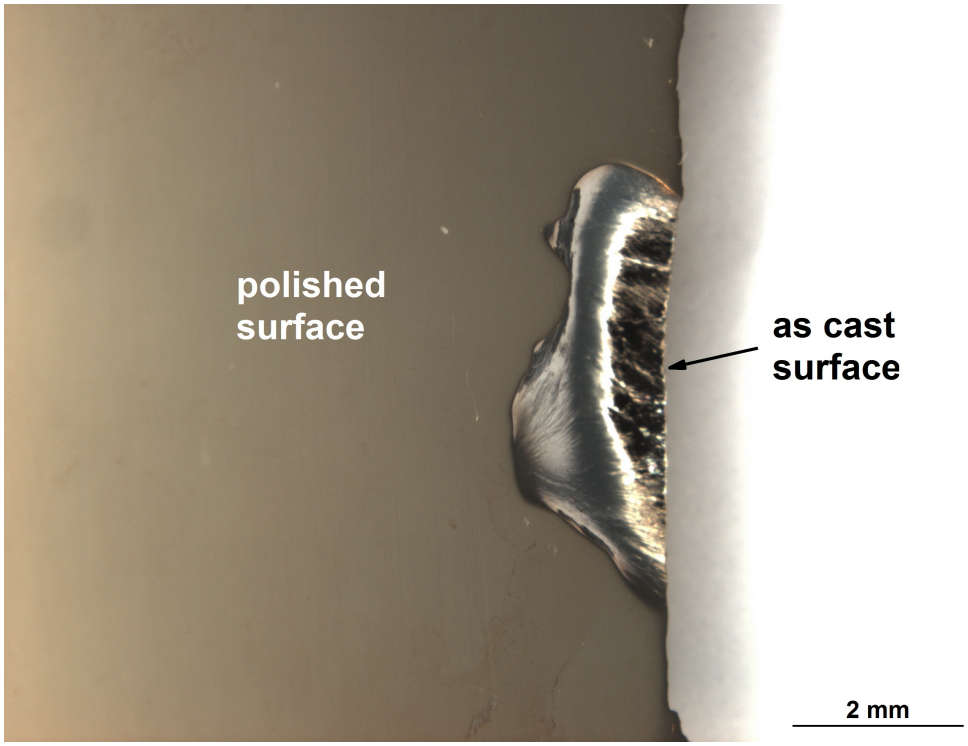

Figure 4.32: Sample 5 after 4 days at 348 K in air. The polished surface area is massively tarnished, while the surface of a cast pore is still white; previously published in [4].

After a total aging time of 131 days, FIB lamellae were prepared in the tarnished area and in the pore area as shown in Figure 4.33. In Figure 4.33 (a), the effect of the tarnishing process on the micro structure in the surface is clearly visible. Starting from the surface, dark corrosion products grow into the matrix material. The length of these corrosion products varies and reaches up to 100 nm. The dark features grow in branches into

the bulk matrix material. On top of these features, a dark surface layer can be seen. In areas where the dark branches grow noticeably deeper into the matrix the dark top layer forms cone-shaped protrusions.

In comparison, the STEM image of the pore lamella with the as-cast surface condition shows no corrosion attack. Only a very thin dark layer of few nanometer thickness is visible, and the matrix is unaffected by the heat treatment as can be seen in Figure 4.33 (b). On these STEM-lamellae, EDX mappings were performed (Figures 4.34 and 4.35). The distribution of copper, silicon, and oxygen for each lamella is plotted. In the lamella from the polished and corroded surface region, the branches are enriched in oxygen and silicon while they are depleted in copper. These branches can thus be interpreted as SiO_2 branches growing into the matrix material. On top of the silicon and oxygen-enriched branches, copper and oxygen are enriched in the dark surface layer in Figure 4.33(a).

A similar EDX mapping was carried out on the lamella taken from the pore region of sample 5, representing an as-cast surface. In a layer of a few nanometer thickness, silicon and oxygen are enriched as shown in Figure 4.35. Similar to the granules, the pore surface seems to be covered with a protective native SiO_2 layer that was formed during casting. This surface layer is able to prevent tarnishing for at least 131 days of observation time at an elevated temperature.

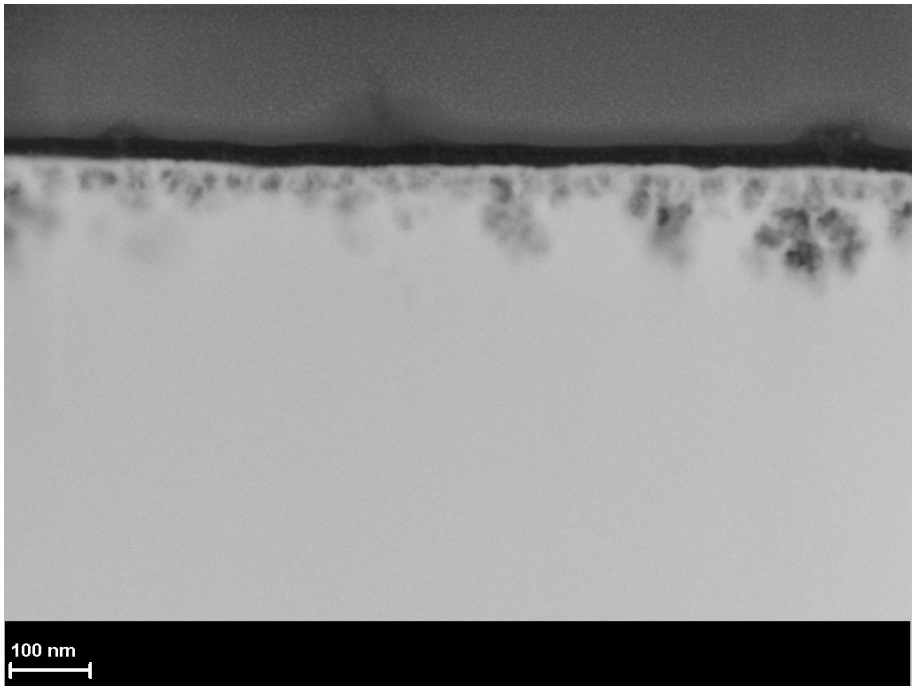

(a) polished and corroded surface area

(b) as cast surface in a pore

Figure 4.33: STEM images of FIB cuts after 131 days of storage at 348 K, cut perpendicularly to the surface of sample 5 from Figure 4.32. (a) was taken from the polished area, (b) was taken from the as-cast surface in the pore; published in an earlier version in [4].

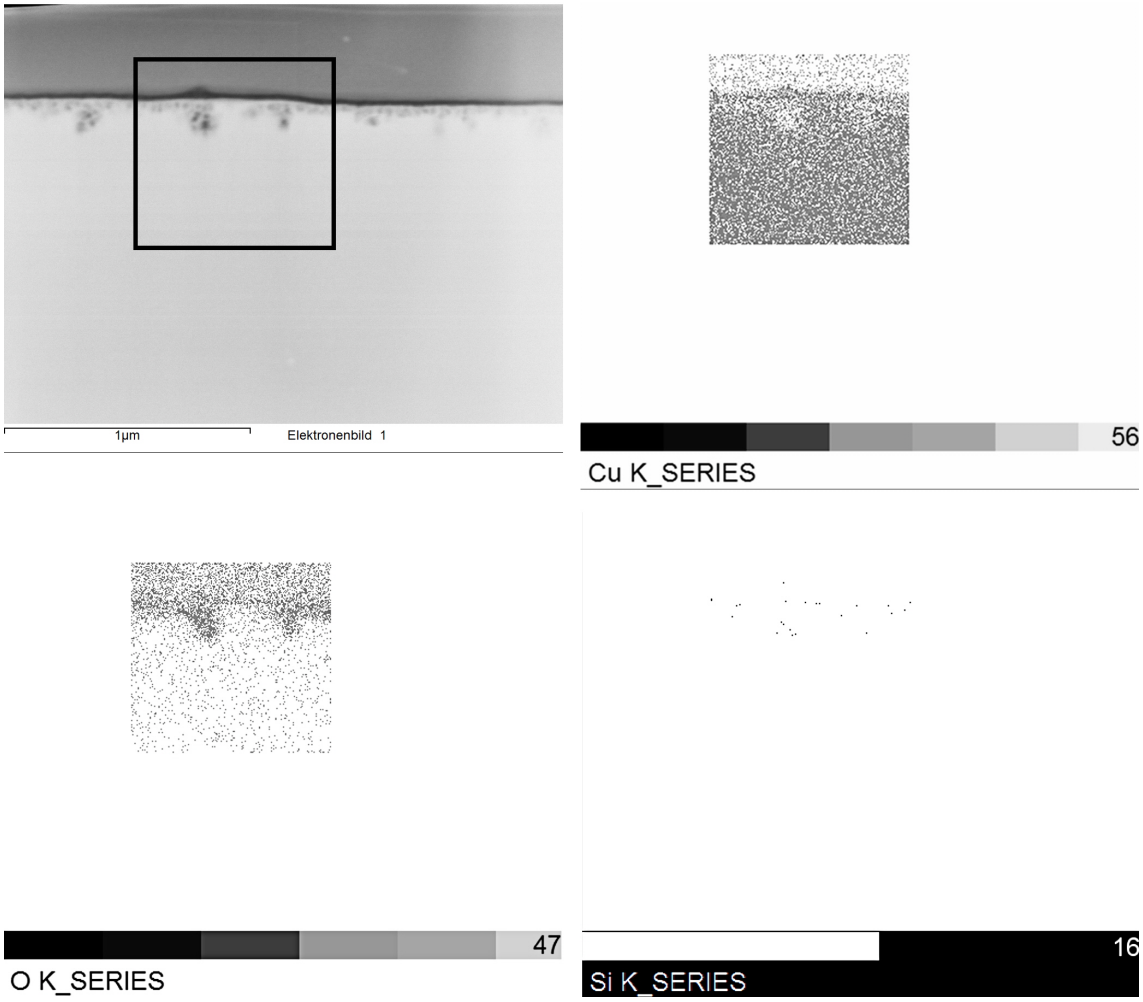

Figure 4.34: EDX Mapping of a FIB lamella cut perpendicularly to the corroded surface area of sample 5 after a total storage time of 131 days at 348 K in air. The top surface layer is enriched in copper and oxygen; the branched structure below is enriched in silicon and oxygen; published in an earlier version in [4].

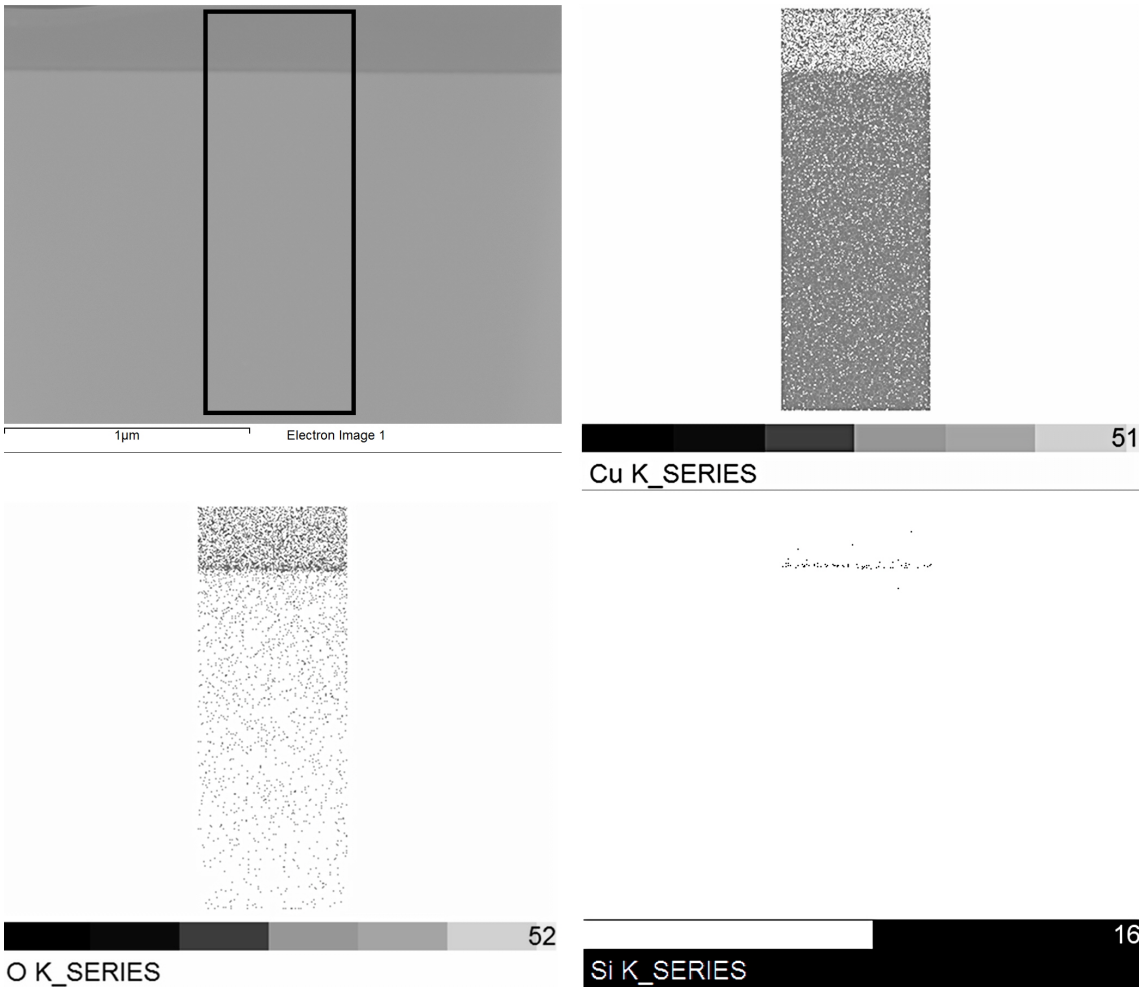

Figure 4.35: EDX Mapping of a FIB lamella cut perpendicularly to the cast pore surface of sample 5 after 131 days of storage at 348 K. In a scale of a few nanometers thickness, an enrichment in silicon and oxygen was proven. This native SiO_2 skin prevents the corrosion attack; hence the absence of the branched structure and the Cu_2O Scale; published in an earlier version in [4].

The corrosion attack on polished surfaces is not homogeneous. At randomly distributed positions, the SiO_2 grows distinctly deeper into the matrix paired with a cone-shaped protrusion of the Cu_2O scale on top. This finding could be reproduced in several tarnishing experiments. Figure 4.36 (a) shows a FIB cut through an exceptionally large corrosion cone on the surface of sample 6, which was kept at 348 K for a total aging time of 327 days. The SiO_2 grows in a dense branching morphology as shown in figure 2.6 (a) in contrast to a dendritic growth as in figure 2.6 (b). They grow up to 1.15 μm into the bulk material. The surrounding corrosion attack has a SiO_2 branch growth length of only 100 - 350 nm. On top of the large SiO_2 branches, the cone was analyzed by EDX to be enriched in copper and oxygen, probably Cu_2O. Smaller cones are randomly distributed on the entire sample surface. Several cones were analyzed with EDX, proving an enrichment in copper

and oxygen in the smaller cones as well as on the sample surface between the cones.

An SEM image of the corrosion pit at a higher magnification recorded with BSD detector is shown in Figure 4.36 (b). The Cu_2O pit and the SiO_2 branches are illustrated in a darker coloring than the bulk material, which is typical for oxidized material in back-scatter electron SEM images. Spherical brighter inclusions can be seen above the former sample surface level in the cut through the large protrusion. The brighter color indicates that these inclusions may be unoxidized material, but they were too small to be analyzed by EDX. The sample volume interacting with the electron beam is an order of magnitude larger than the volume of these spheres.

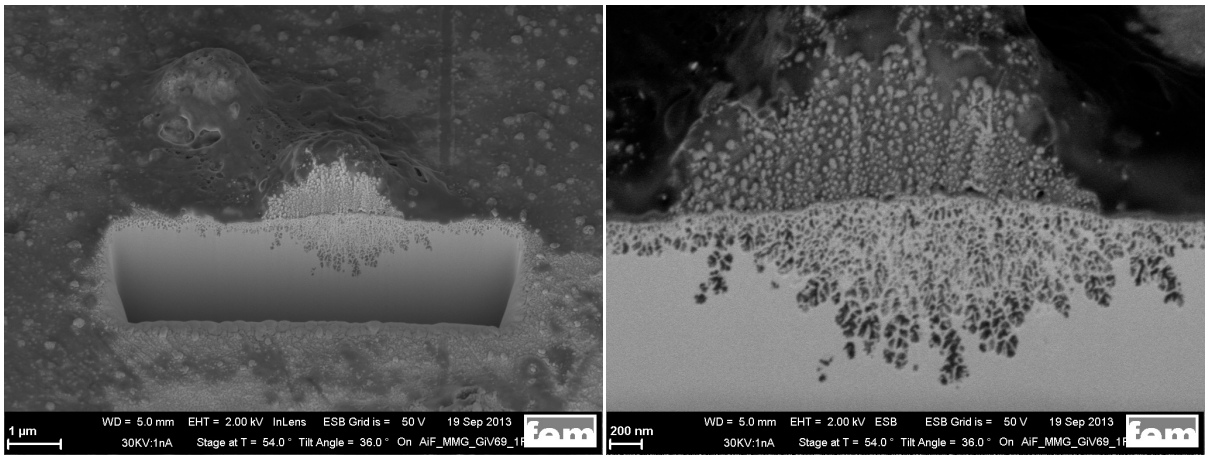

(a) SE Detector (b) BSD Detector

Figure 4.36: SEM images of a FIB cut through a large corrosion pit on the surface of sample 6 after an aging treatment for 327 days in air at 348 K. More images of this pit were published in [4].

In a later test, run for 365 days in laboratory air at 348 K, sample 7 with the composition $Au_{49}Ag_{5.5}Pd_{2.3}Cu_{26.9}Si_{16.3}$ was investigated. On the surface of this sample for the first time in the present study, bright islands were found as indicated in figure 4.37 (a). A FIB cut was performed at the position indicated in Figure 4.37 (b).

Figure 4.38 shows the FIB cut, that includes the section of the bright island and several dark islands or cones on the surfaces. EDX analyzes were carried out in the bright island and the large dark cone shown in Figure 4.38 (b). This analyzes indicate an enrichment of copper and gold but not of oxygen in the bright island and an enrichment of copper and oxygen in the dark island, consistent with the EDX results of the Cu_2O corrosion products found on the other samples. The islands are positioned above the former surface level of sample 7. The copper and gold enriched bright island is located between silica branches while the Cu_2O cone is found on top of particularly large silica branches, similar to the observations made on the samples above.

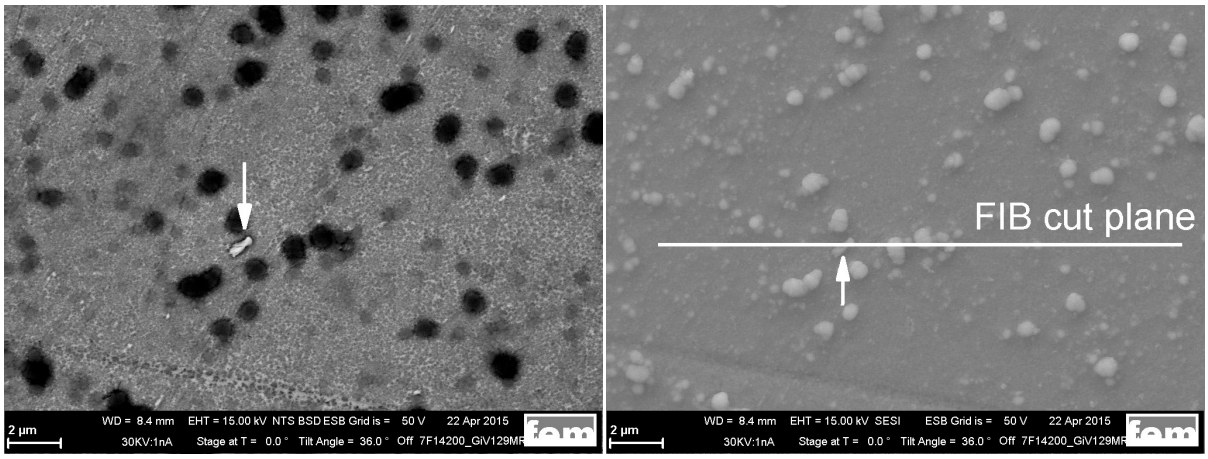

(a) BSD Detector (b) SESI Detector

Figure 4.37: SEM images of the surface of sample 7. (a) A bright island is visible on the surface after storage at 348 k in air for 365 days. A FIB cut was performed at the location indicated in (b).

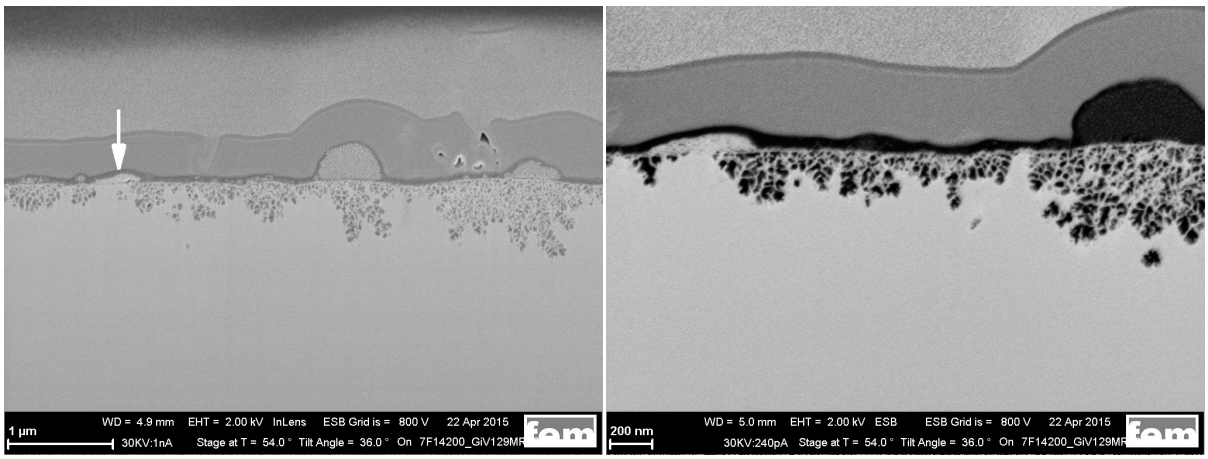

(a) InLens Detector (b) ESB Detector

Figure 4.38: SEM images of the the FIB cut along the plane indicated in Figure 4.37 (b) of sample 7 after storage at 348 k in air for 365 days. (a) The bright island indicated with a white arrow is positioned between two larger silica branch clusters. The darker islands in the back scatter electron image (b) are positioned above silica branches.

4.3.1.3 XPS Study on Samples Aged in Air

For a better understanding of the chemical composition in the tarnished surface layers, XPS studies were carried out on three samples. Two of those samples had been kept at 348 K in air for different aging times, 23 days (sample 8) and 327 days for sample 6 of Figure

4.36, respectively. The third sample (sample no. 9) had been stored at room temperature in a desiccator filled with air for 593 days. The samples had been ground and polished to mirror finish on one side prior to the storage test. The XPS analysis was carried out on the polished side of the samples after the test. For the XPS analysis, the sample surface was sputtered away stepwise. In the sputtered area some material from the surface is removed and the underlying matrix material is observable. This observable matrix area represents the last sputter step and hence the last data point in the concentration profile.

Figure 4.39 shows SEM images of sample 8 after the XPS analysis. Image (a) shows the surface *outside* the sputtered area that is representative for the original tarnished surface. Figure 4.39 (b) shows the surface *inside* the sputtered area that is representative for the material at the level of the final sputter step. Both images were taken with the back-scattering electron detector (RE-detector). The dark islands on the surface in image 4.39 (a) correspond to areas in which a high concentration of copper and oxygen in comparison to the surrounding surface areas was found according to qualitative EDX analysis. In Figure 4.39 (b), the bulk material in the sputtered zone is shown. For an estimated sputter rate of 4.56 nm/min, and a total sputter time of 5500 s, this view resembles the bulk material at a level approx. 420 nm beneath the original surface of sample 8. The bulk material is shown in an overall light gray coloring with some minor dark inclusions. These darker inclusions correspond again to an enrichment in oxygen, but not in copper. Instead an enrichment in silicon is detected by EDX analysis along with the enrichment in oxygen in comparison to the brighter surrounding matrix material.

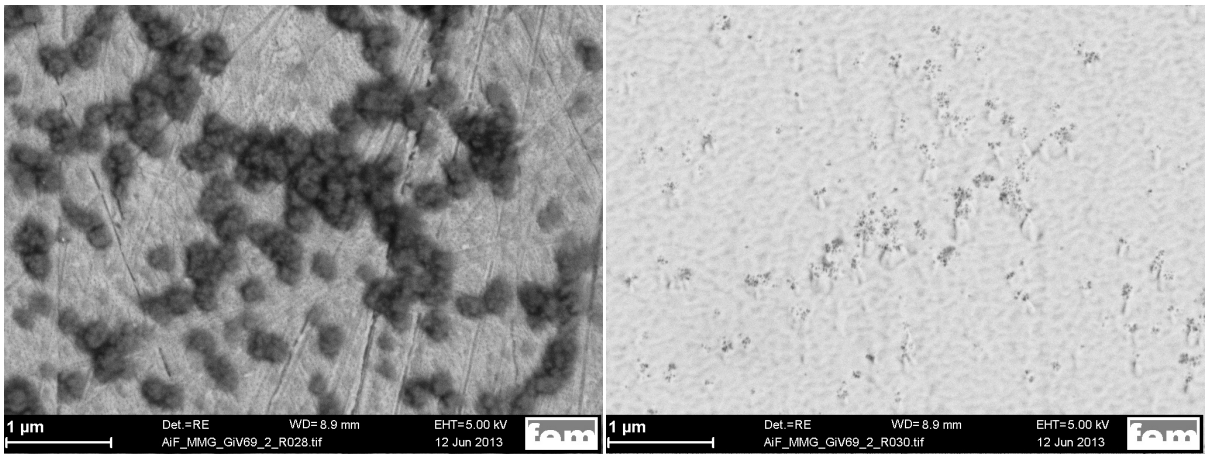

(a) outside the sputtered zone (b) within the sputtered zone

Figure 4.39: SEM image of a polished surface of sample 8 after an aging treatment for 23 days in air at 348 K after the XPS analysis. The dark islands in the left image correspond to areas in which a high concentration of Cu and O was measured by EDX analysis. The dark phases in the right image correspond to areas in which a high concentration of Si and O was measured by EDX analysis.

After longer aging times, the corrosion attack is more pronounced. Figure 4.40 shows

the images of sample 6, which was stored for 327 days at 348 K in air, after the XPS investigation. The copper/oxygen islands become larger and more densely distributed as shown in Figure 4.40 (a). In the sputtered area of Figure 4.40 (b), the difference is even more distinct. The matrix is characterized by a dense distribution of dark inclusions enriched in silicon and oxygen. The sputtering was carried out for 4040 s in this case, corresponding to a depth of ≈ 300 nm beneath the original sample surface level prior to sputtering.

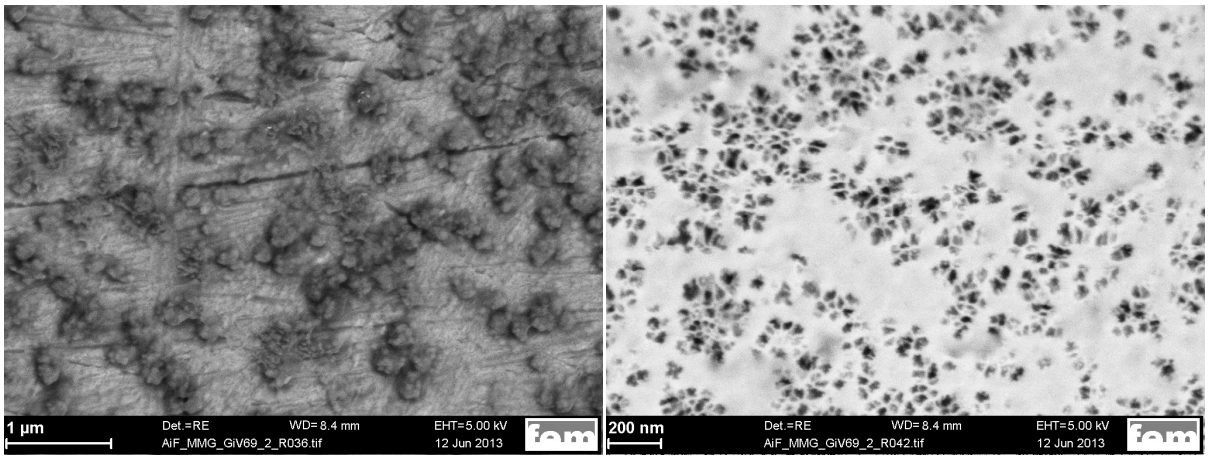

(a) outside the sputtered zone (b) within the sputtered zone

Figure 4.40: SEM image of a polished surface of sample 6 after an aging treatment for 327 days in air at 348 K after the XPS analysis. The dark islands in the left image (a) correspond to areas in which a high concentration of Cu and O was measured by EDX analysis. The dark phases in the right image (b) correspond to areas in which a high concentration of Si and O was measured by EDX analysis.

At room temperature, approx. 50 K beneath the tests at the elevated temperature of 348 K, the corrosion attack is distinctly less pronounced even after very long aging times. Figure 4.41 shows the surfaces of sample 9 after an aging period of 593 days and after the XPS analysis. Only few islands with an enrichment in copper and oxygen are visible on the non-sputtered surface. Different brightnesses on the surrounding surface areas indicate some less thick tarnishing layers. In the sputtered area, a uniform bright matrix material is visible. The variations in the brightness of the back-scatter electron image (left half of Figure 4.41 (b)) are due to the topographical roughness resulting from local differences in the sputtering effect and not to differences in the chemical composition, e.g. local oxygen enrichment. The topographical unevenness of the surface can be observed in the secondary electron (SE) image in the right half of Figure 4.41 (b).

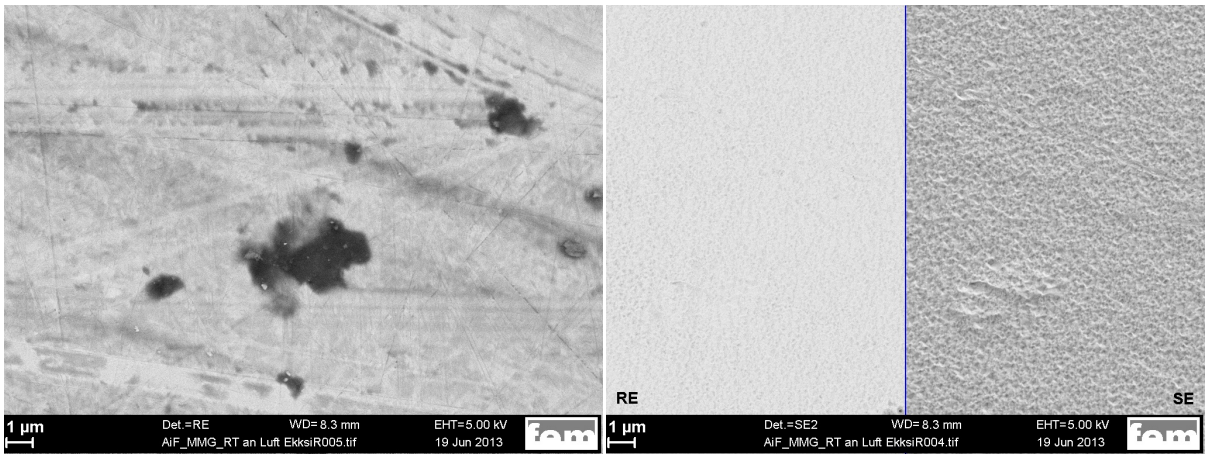

(a) outside the sputtered zone (b) within the sputtered zone

Figure 4.41: SEM image of a polished surface of sample 9 after an aging treatment for 593 days in air at room temperature after the XPS analysis. The sample was stored in a desiccator, i.e. in dry air. The dark island in the left image (a) corresponds to an area in which a high concentration of Cu and O was measured by EDX analysis. The sputtered surface in (b) shows a homogeneous one-phase matrix. Different brightnesses in the back-scatter image (RE) can be attributed to the topology of the sample surface caused by the sputtering, as can be seen in the secondary electron image (SE, right half of (b)).

The percentage of the dark Cu_2O islands in the respective SEM images of sample 6 and 8 was evaluated using a software for image analysis. The evaluated area is colored green in the SEM images of Figure 4.42. The Cu_2O islands are randomly distributed over the entire surface areas. The distribution is especially heterogeneous with sample 8, which was stored for 23 days at 348 K. Within the analyzed surface area, the Cu_2O islands cover between 5.8 % and 34.94 % of the sample. Sample 6, stored for 327 days at 348 K, is covered by Cu_2O islands at 40.62 % of the analyzed surface. On sample 9, only few islands like in Figure 4.41 were found and the majority of the sample is only covered by a thin Cu_2O flash. Hence, the investigated area is non-representative and was not included in the analysis.

The percentage of the copper oxide islands on the analyzed surface area is too heterogeneously distributed to yield data for the quantification of the tarnishing rate.

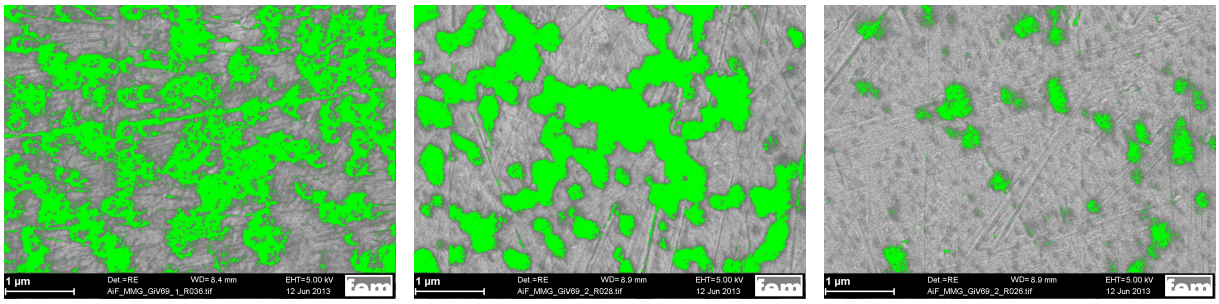

(a) Sample 6, 327 days, 348 K (b) Sample 8, 23 days, 348 K (c) Sample 8, 23 days, 348 K

Figure 4.42: (a) Cu_2O islands cover 40.62 % of the surface in the investigated area. (b) and (c): On sample 8, a heterogeneous distribution of the islands was observed, varying between 34.94 % and 5.8 % in the analyzed surface area.

Figure 4.43 (a) shows the FIB lamella cut through the surface of sample 8 after an aging treatment for 23 days, while Figure 4.43 (b) shows the corresponding XPS profile of this sample. The palladium concentration is not shown in the profile due to a possible overlap with the gold peaks. The XPS profile reveals a copper enrichment in a very thin superficial layer of few nm thickness, followed by an enrichment in silicon in a much thicker layer of approx. 50 nm thickness. Beneath the silicon-enriched zone, a small peak in the copper concentration is visible before the overall matrix composition is reached [4].

If the oxygen distribution is taken into account the ratio of Cu/O and Si/O, respectively, indicates that the thin top layer is probably Cu_2O followed by a SiO_2 layer. The ratio of Cu to O is almost 2 at its peak value, and in the silicon-enriched layer, the silicon to oxygen ratio is close to 0.5. The fact that the measured ratios stay slightly beneath the stoichiometric ratio of the proposed oxides can be explained by the morphology of the oxide-layer. Due to the branching morphology, the XPS profile shows not only the silicon oxide but also the surrounding matrix, and the top copper oxide layer is too thin to be measured alone, so some of the silica is probably being measured as well. The small copper peak beneath the silicon-enriched layer does not correspond to a similar peak in the oxygen content. In fact, at this location the oxygen content seems to be slightly depleted in comparison to the adjacent data points, indicating that the copper is probably elementary and not in its oxide form. Directly underneath the Cu_2O surface layer, the gold is depleted along with an enrichment of silicon. This can be seen in the Au/Si profile in Figure 4.44 (b) [4].

The copper profile shows a depletion even below the main silica branches. The copper concentration is rising for $\approx$ 4500 s until it reaches a level at which it stays constant (not shown here). This corresponds to a distance of 342 nm to the original sample surface.

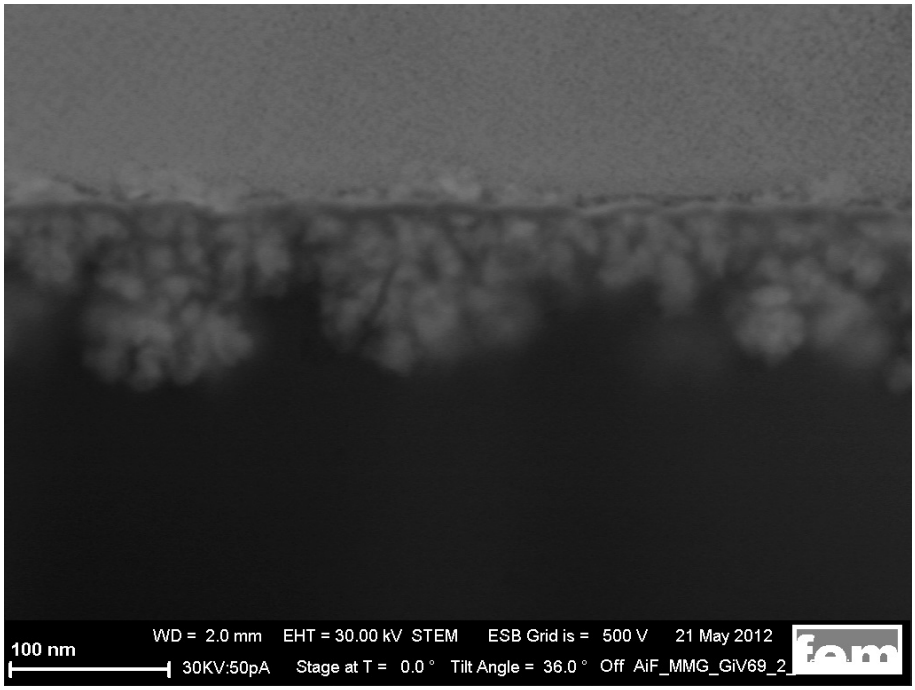

(a) STEM image of FIB lamella

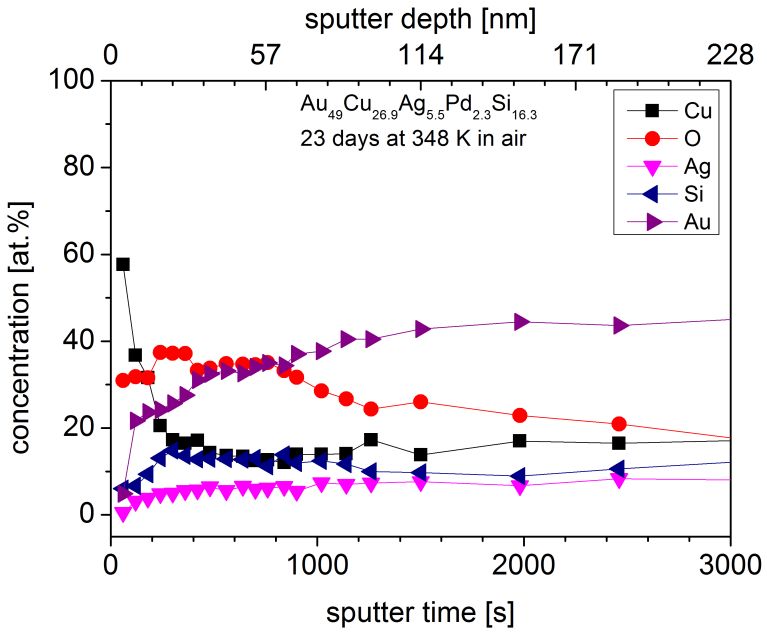

(b) XPS profile

Figure 4.43: STEM image and corresponding XPS profiles of Au, Cu, O, Si and Ag of sample 8 after polishing and aging treatment for 23 days in air at 348 K. The sputter rate was estimated to be 4.56 nm/min; published in an earlier version in [4].

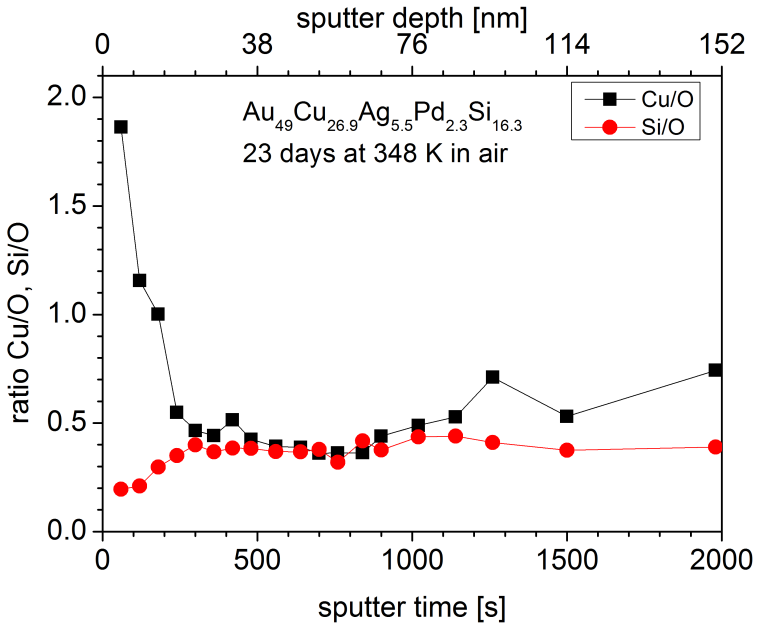

(a) Cu/O and Si/O

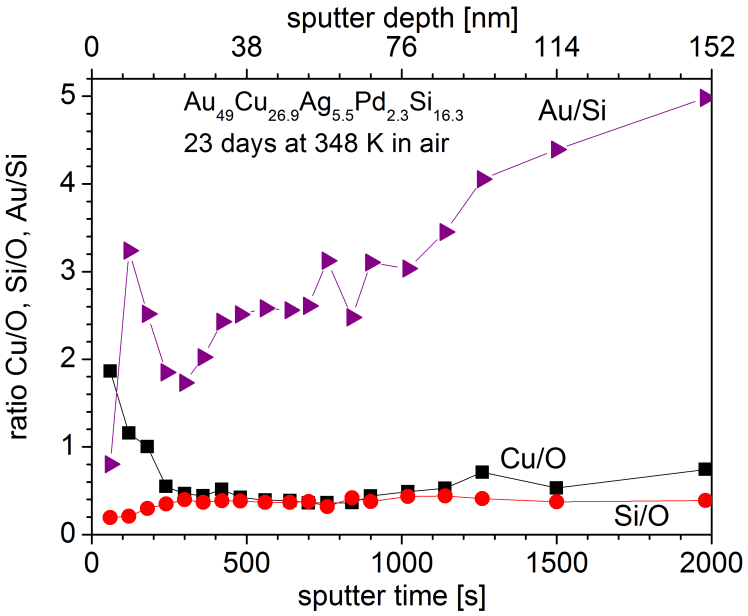

(b) Cu/O, Si/O and Au/O

Figure 4.44: Ratios of copper and silicon to oxygen and of gold to silicon depending on the distance to the sample surface for sample 8. The sputter rate was estimated to be 4.56 nm/min; published in an earlier version in [4].

The element concentration profiles are different for sample 6 (Figure 4.45). The oxygen concentration for this sample stays at approx. 40 at% for the entire analysis. The supposed

matrix composition of $Au_{49}Ag_{5.5}Pd_{2.3}Cu_{26.9}Si_{16.3}$ at.% is never reached during this analysis, probably because the analysis stayed within the silicon oxide layer of the heavily corroded surface. This assumption is supported by the findings of the aforementioned SEM analysis of Figure 4.40, which showed a high amount of oxide particles distributed in the matrix material. The concentration of silver stays at approx. 5 at% throughout the entire profile, while gold is slightly depleted towards the sample surface. The largest effect can be observed for the copper and silicon distribution. Copper is enriched in a thin surface layer, while in the same location silicon is depleted, very similar to the top layer in sample 8 in Figure 4.43. Beneath this top layer, the concentration of silicon is distinctly higher than that of copper (almost twice as high), while the nominal concentration of silicon is much lower than that of copper for $Au_{49}Ag_{5.5}Pd_{2.3}Cu_{26.9}Si_{16.3}$. This can probably be attributed to an enrichment of silicon in the SiO_2-branches and a depletion of copper due to the diffusion of copper to the sample surface where it forms Cu_2O.

Despite the much longer aging period, the surface alteration due to the corrosion process is not as distinct in sample 9, which was stored at room temperature, shown in Figures 4.41 and 4.46, approx. 50 K below the temperature at which samples 6 and 8 were stored. The oxygen enrichment is very pronounced on the surface but does not reach very deep into the matrix. Silicon, gold and silver are depleted towards the surface. In the case of silicon, this depletion is followed by an enrichment, similar to the preceding XPS analyzes of samples 6 and 8. Copper is the only element that stays approx. at the same level.

The high concentration of oxygen on the surface of approx. 75 at% contorts the concentration profiles of the other alloying elements to lower values. As soon as the oxygen content is subtracted from the plot and the other elements concentrations rescaled to a total of 100 at%, the copper and silicon enrichment towards the surface is visible, while the silver and gold content is still depleted as shown in Figure 4.46 (b). This again indicates the oxidation of the non-noble elements copper and silicon in the surface and near-surface regions through the tarnishing procedure.

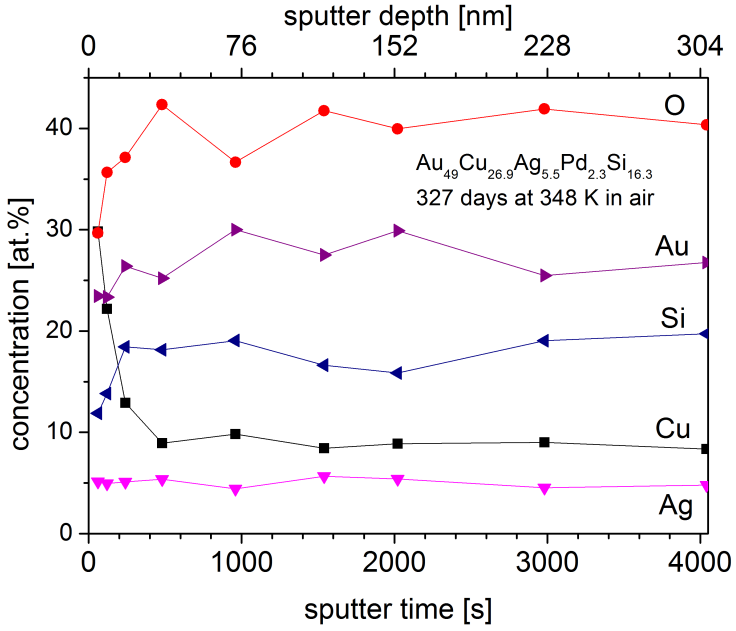

(a) XPS concentration profile

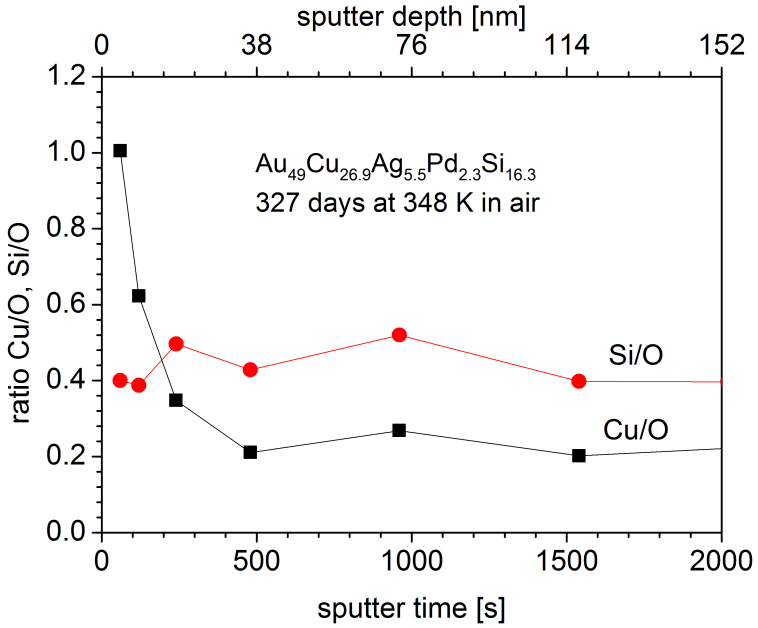

(b) Cu/O and Si/O ratios

Figure 4.45: (a) XPS profiles of Au, Cu, O, Si and Ag and (b) ratios of copper and silicon to oxygen of a polished surface of sample 6 after storage for 327 days in air at 348 K. The sputter rate was estimated to be 4.56 nm/min.

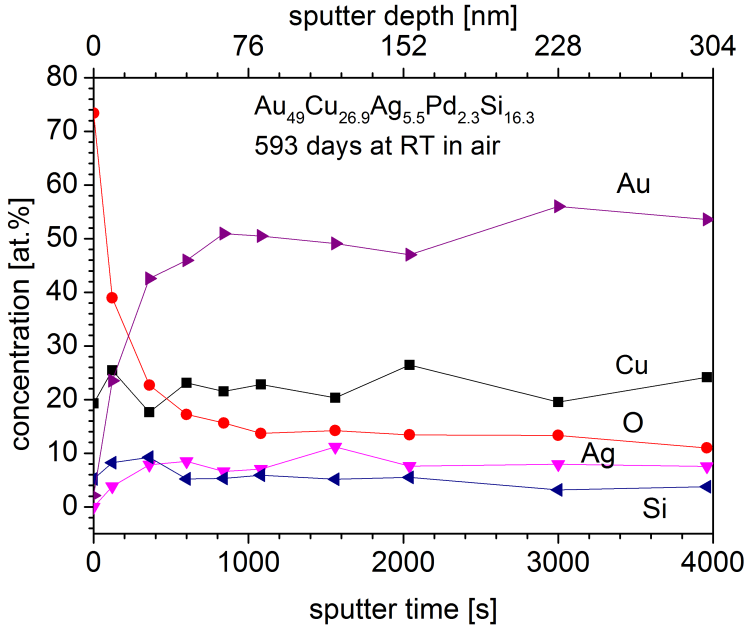

(a) XPS concentration profile

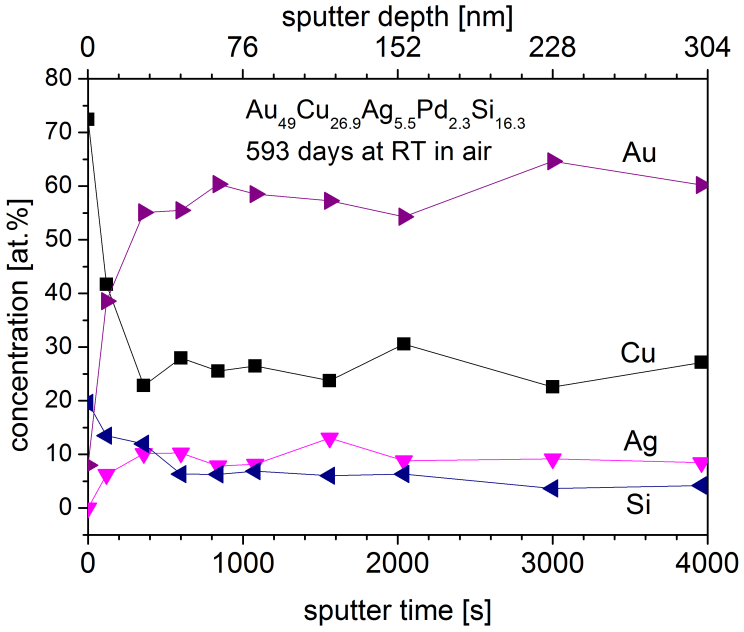

(b) scaled XPS concentration profile without oxygen

Figure 4.46: XPS profiles of Au, Cu, Ag and Si with (a) and without (b) oxygen of a polished surface of sample 9 after a storage for 593 days in air at room temperature. The sputter rate was estimated to be 4.56 nm/min; specimen shown in 4.41.

4.3.1.4 Colorimetric Study of the Tarnishing Rate

Freshly polished samples of $Au_{49}Ag_{5.5}Pd_{2.3}Cu_{26.9}Si_{16.3}$ have Yellowness Index (YI) values between 15 and 17. The YI value increases during exposure to air or corrosive environments. The influence of temperature and different atmospheres on the rate at which the YI increases was monitored during the exposure time. This can be used as a parameter for the quantification of the tarnishing rate. Figure 4.47 (a) shows the development of the YI at different temperatures in laboratory air for exposure times of up to 131 days. After circa one month of exposure at 348 K, the color change for the $Au_{49}Ag_{5.5}Pd_{2.3}Cu_{26.9}Si_{16.3}$ (solid square) reaches the detection limit (i.e. YI $>$ 90), and after that point the color change appears to have a slower rate, which is nonrepresentative. Thus, these values were excluded from the graphs in Figure 4.47. Each symbol in Figure 4.47 (a) corresponds to the average value of three individual color detections. A quick overview of the aging treatment for each sample is given in table 3.3. At temperatures above room temperature, the YI changes rapidly. At body temperature (310 K), already after a few days, off-white values are reached. This means that the color change is already noticeable with bare eyes. The change is even more drastic at 348 K. Already after 3 days, off-white colors are reached (see also Figure 5.6 and the image of sample 5 after 4 days at 348 K in laboratory air 4.32). A sample kept at room temperature in the air-conditioned laboratory stays approx. two months within the premium and standard white region, while a sample kept in the freezer remains premium white over a period of several months [4].

Figure 4.47 (b) shows the influence of humidity at 310 K and RT, argon flux at 348 K and evacuation at RT on the tarnishing rate of amorphous $Au_{49}Ag_{5.5}Pd_{2.3}Cu_{26.9}Si_{16.3}$, i.e. the rate at which the YI increases. The tarnishing rate increases as the atmosphere gets more aggressive. At room temperature (open symbols), three samples were observed. Sample 9, which was already shown in the previous section in the XPS analysis, was kept in dry air in a desiccator at room temperature, and the tarnishing rate is slightly better than for sample 10, which was stored in an air-conditioned laboratory. Sample 11 was stored in vacuum with a pressure below 10^{-5} hPa and was only in contact with air when it was taken to the test apparatus for the YI determination. Sample 11 tarnished at a similar rate as sample 12, which was aged in a freezer at 255 K. Two samples (13 and 14) have been air-treated in a furnace located in a non-air-conditioned laboratory at 310 K, represented by open crossed symbols in Figure 4.47. During the isothermal test of sample 14, represented by crossed circles labelled ”humid”, the furnace hosted at the same time a sweat analysis immersion testing apparatus and thus the atmosphere in the furnace was more ”humid” and corrosive than when sample 13 was aged at 310 K. Two aging treatments at 348 K, represented in Figure 4.47 (b) by closed symbols, were performed. Sample 5 was aged in a furnace placed in a not-air-conditioned laboratory at 348 K and sample 15 was kept under a constant argon flux of approximately 50 ml/min [4].

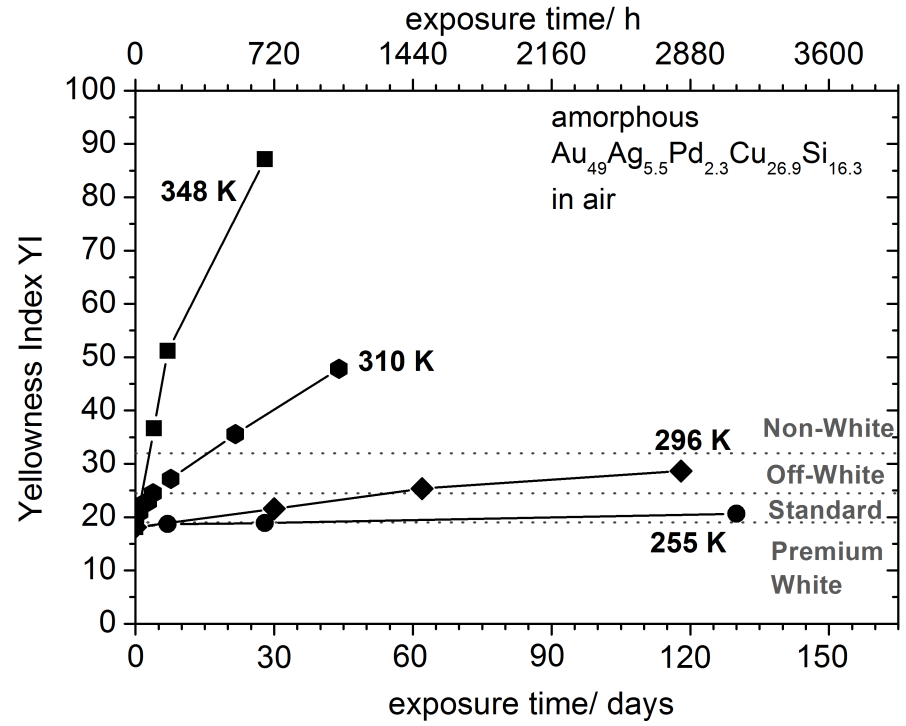

(a) In dry air

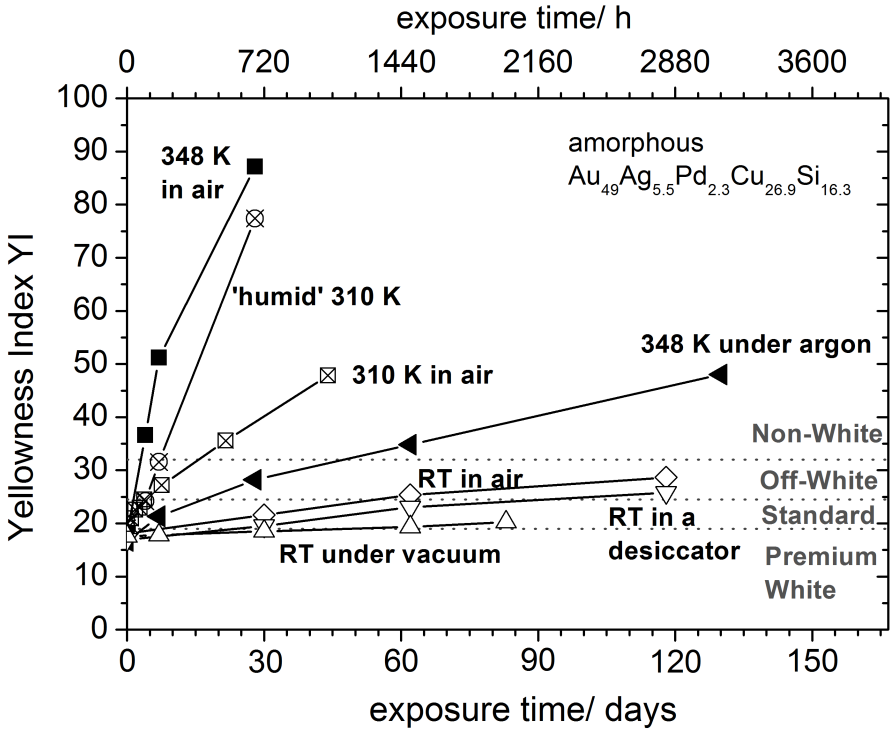

(b) Influence of humidity, evacuation, and Ar flux

Figure 4.47: Development of the Yellowness Index of amorphous $Au_{49}Ag_{5.5}Pd_{2.3}Cu_{26.9}Si_{16.3}$ for different temperatures and different atmospheres. All samples were still X-Ray amorphous after the exposure, figures published in an earlier version in [4].

The samples of $Au_{49}Ag_{5.5}Pd_{2.3}Cu_{26.9}Si_{16.3}$ remained amorphous throughout the entire observed time period, as is shown for the samples aged at 348 K in air in Figure 4.48.

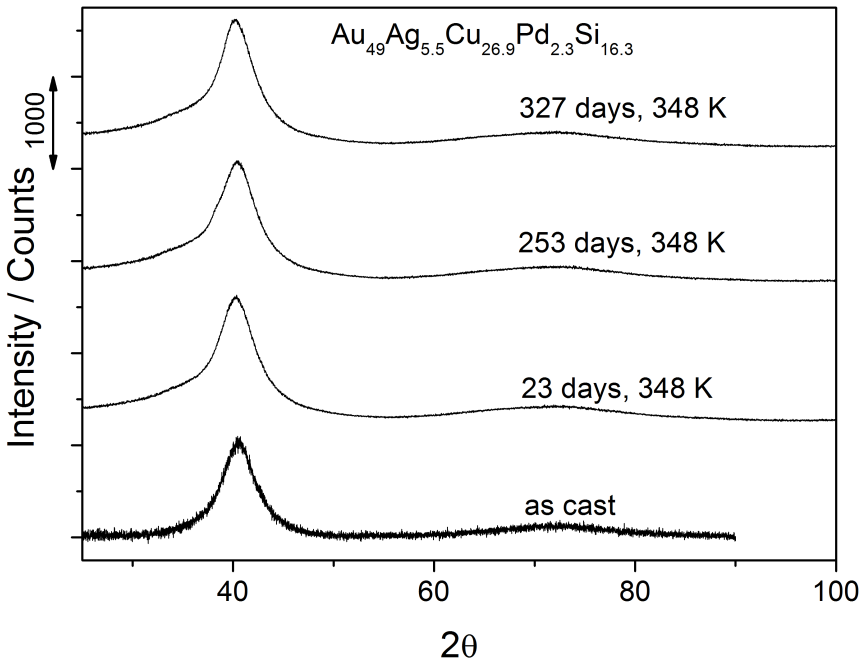

Figure 4.48: XRD scans of $Au_{49}Ag_{5.5}Pd_{2.3}Cu_{26.9}Si_{16.3}$ after different aging times at 348 K analyzed on the polished (and corroded) surfaces. No crystallization was observed within the experimental time period.

4.3.2 Tarnishing Behavior in Artificial Sweat and Artificial Saliva Immersion Test

The immersion test in artificial body fluids was performed on two samples for the artificial sweat test and on four samples for the artificial saliva test. For each test solution, one representative sample is presented in the macro images of Figures 4.49 and 4.50.

Figure 4.49 shows the ground samples 16 and 17 of $Au_{49}Ag_{5.5}Pd_{2.3}Cu_{26.9}Si_{16.3}$ prior to the tests in simulated body fluids, artificial sweat and artificial saliva, respectively, and Figure 4.50 shows the same samples after 7 days of immersion testing at 310 K. Some residual cast pores were present on the sample surfaces after the grinding procedure. Such cast pores are usually caused by air pockets trapped in the copper mold cavity. After the test, the samples surfaces showed a red coloring with the exception of the cast pores, which retained their white color similar to samples aged in air shown in Figure 4.32.

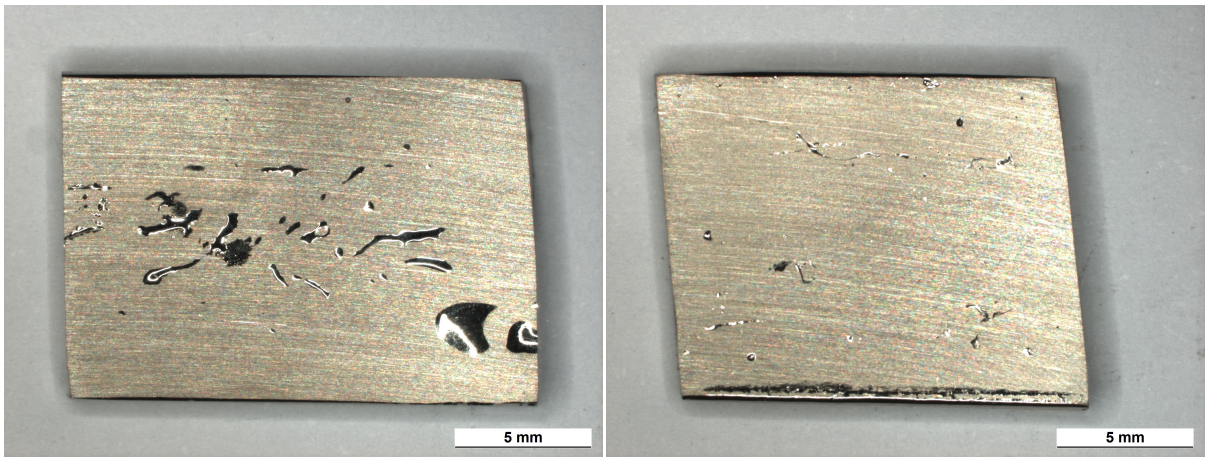

(a) Sample 16 prior to artificial sweat test (b) Sample 17 prior to artificial saliva test

Figure 4.49: Samples 16 and 17 prior to the test in simulated body fluids. The sample surface of each sample was ground for the test. Some cast pores with the original as-cast surface remained (previously published in [13, 14, 15]).

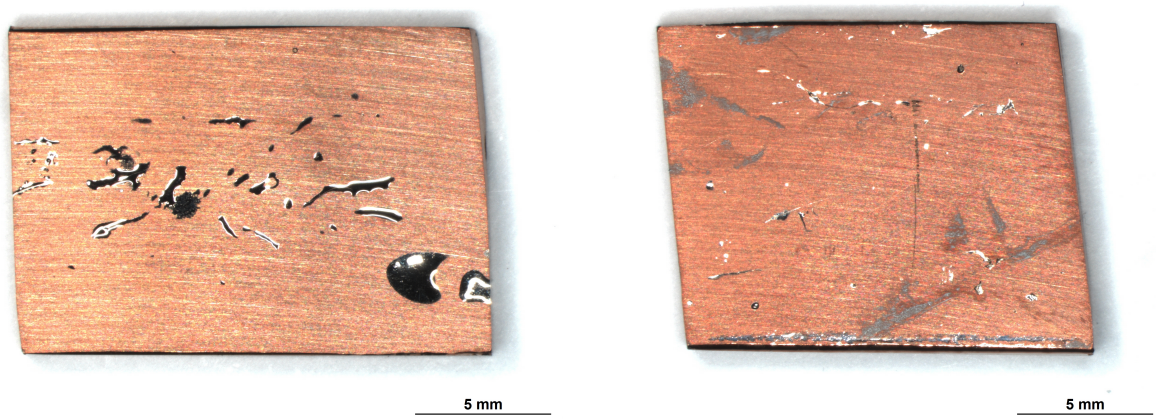

(a) Sample 16 after artificial sweat test (b) Sample 17 after artificial saliva test

Figure 4.50: Samples 16 and 17 after a test in simulated body fluids at 310 K for 7 days (previously published in [13, 14, 15]).

The test solutions were analyzed after the test. The concentrations of the dissolved elements are plotted in Figure 4.51 giving mean values for two samples in artificial sweat and four samples in artificial saliva, respectively. A comparatively high amount of copper was found dissolved in the test solution, especially in the case of the artificial saliva test. A small amount of silicon was also detected. The concentration of the noble elements gold, silver, and palladium was below the detection limit of 0.05 $\mu g/cm^2$.

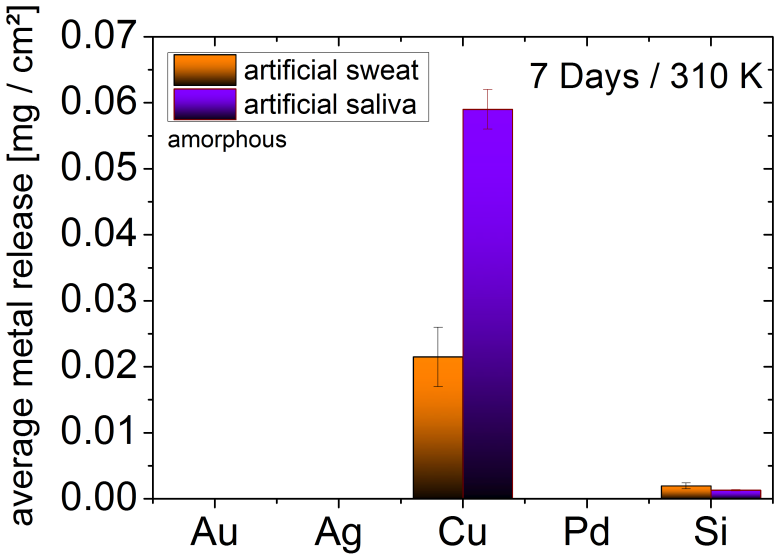

Figure 4.51: Metal and silicon release into the test solutions after 7 days at 310 K in artificial sweat giving the mean value for two samples, and artificial saliva giving the mean value of four samples. The artificial saliva test results in a higher amount of free corrosion in comparison to the artificial sweat test. Alloy composition: $Au_{49}Ag_{5.5}Pd_{2.3}Cu_{26.9}Si_{16.3}$.

Macroscopic photos of the cast pores are shown in Figure 4.52. The pore retained the initial white color of the as cast $Au_{49}Ag_{5.5}Pd_{2.3}Cu_{26.9}Si_{16.3}$ alloy, except for several locations where the cast pore shows thin scratches. The cast pores lie below the surface level, hence the sanding procedure did not affect the complete cast pore but only some random locations where the surface was scratched. Here the surface developed a red coloring as well.

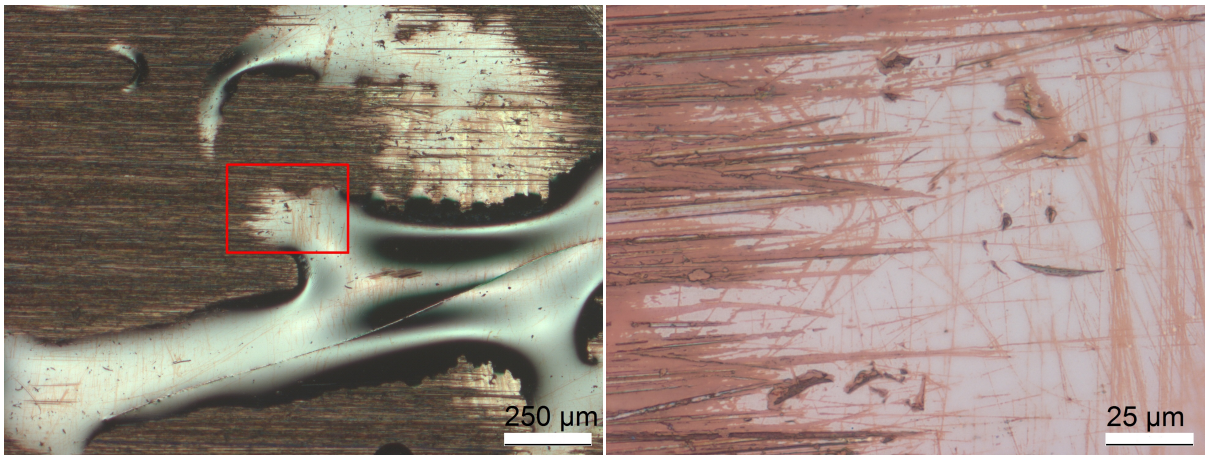

(a) Sample 16 - overview (b) Sample 16 - detail of (a)

Figure 4.52: Surface of sample 16 after 7 days in artificial sweat at 310 K. The pore area stays white while the ground areas of the sample turn red. In locations where the pore surface was scratched the surface develops a red coloring as well; previously published in [13, 14].

Figure 4.53 shows an EDX mapping of a boundary between the smooth surface of a cast pore and the ground (and corroded) sample surface. The ground area is depleted in copper and enriched in oxygen compared to the non-corroded pore surface. The depletion in copper within the corroded surface areas can be explained by a superficial loss of copper to the test solution as shown in Figure 4.51.

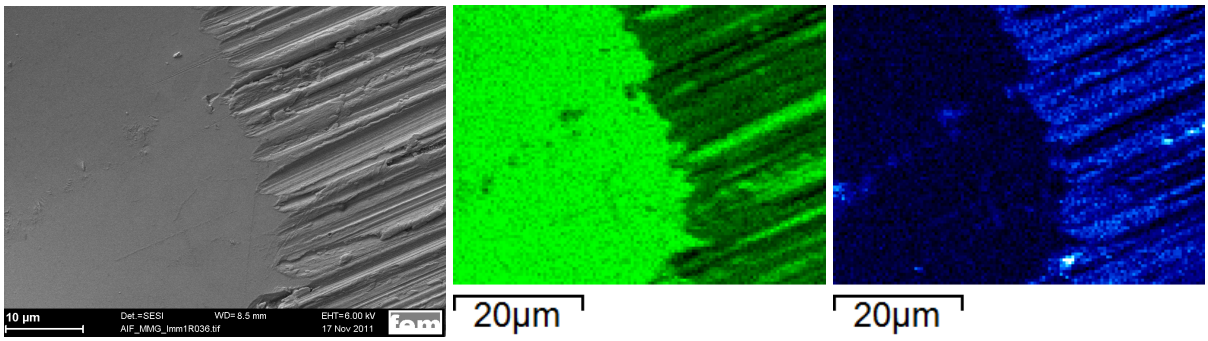

(a) REM image of the pore boundary (b) EDX mapping of the copper content (c) EDX mapping of the oxygen content

Figure 4.53: Pore boundary on the surface of sample 16 after the test in artificial sweat at 310 K for 7 days. Light green and light blue color, respectively, indicates a high concentration of copper and oxygen, respectively; previously published in [13, 14, 15].

The pore surface was analyzed in an SEM investigation. Figure 4.54 (a) shows an overview of several scratches in the as-cast surface and 4.54 (b) a magnification of sev-

eral scratches. Cone-shaped extrusions follow the the scratches in the pore region. Figure 4.55 shows these cone-shaped extrusions at a higher magnification.

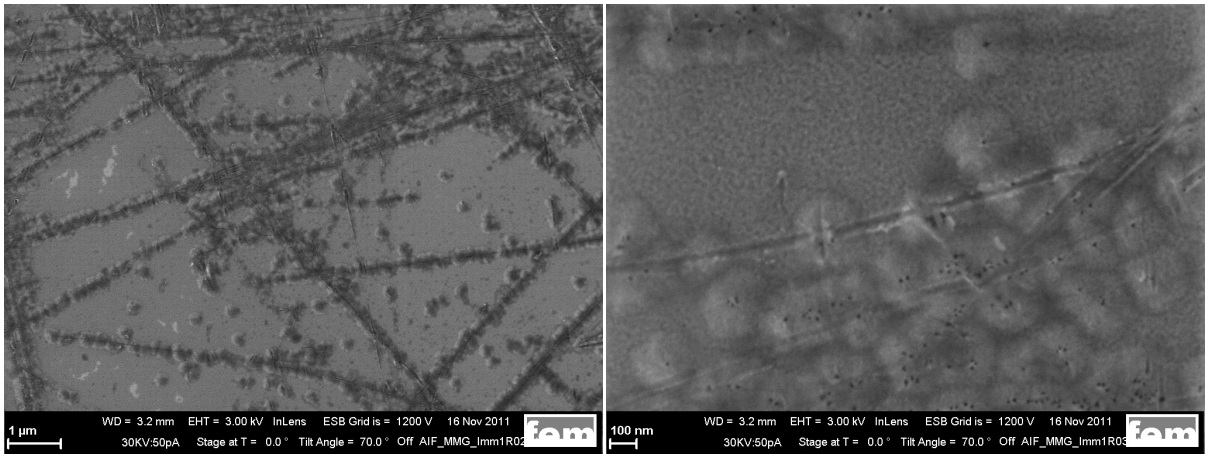

(a) SEM image of a cast pore - overview (b) SEM image of a cast pore - detail of (a)

Figure 4.54: Surface of a pore area on sample 16 after the test in artificial sweat. The pore area is scratched, and the scratches appear dark in the SEM overview image (a) (previously published in [3]). In the detailed image, bulging is visible at the scratches due to a volume increase caused by the localized corrosion (b).

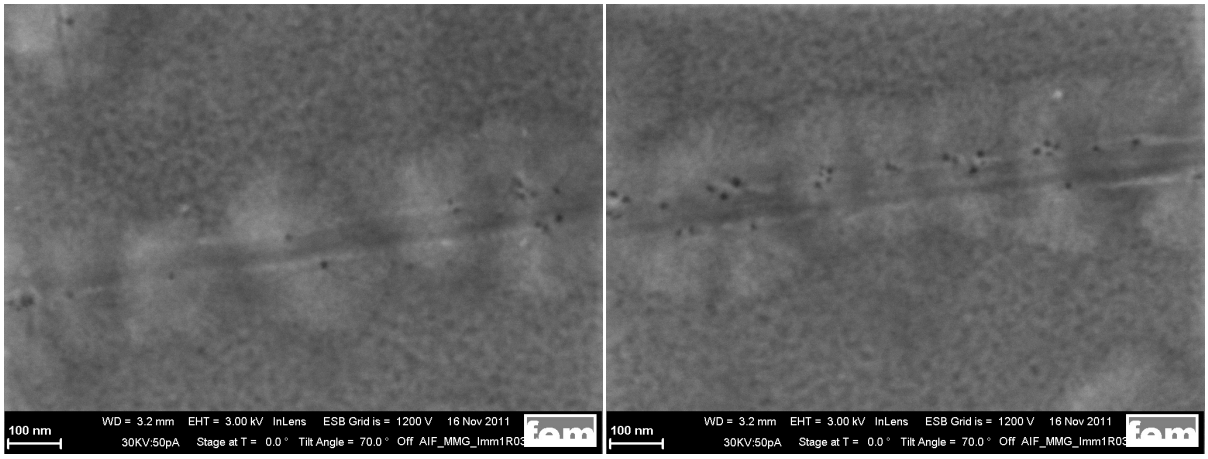

Figure 4.55: Details of Figure 4.54.

A FIB lamella was cut perpendicularly to the pore surface cross-sectioning two parallel scratches, as shown in Figure 3.12 in Section 3.3.4. One of the scratches is a single scratch (Figure 4.56(a)), and the other one actually consists of a double scratch, which means two very narrow scratches next to each other only circa 100 nm apart (Figure 4.56(b)).

The corrosion products grow fan-shaped into the matrix material, starting from the surface defects caused by the scratches (Figure 4.56). The corrosion products grow in a dense branching morphology (DBM) as described in Section 2.6. Since the EDX mapping of the pore surface shows a clear enrichment in oxygen in scratched locations, the corrosion products are probably oxide branches. The growth of oxide branches into the amorphous matrix seems to be related to the branched features formed during aging in air. Only the origin is localized at the surface defects, in this case scratches, in the as-cast pore surface, and the corrosion products grow fan-shaped into the amorphous matrix. The formation of these oxide branches causes a volume increase, hence the bulging of the surface and the cone-shaped extrusions along the scratches that were observed by the SEM investigation in topview of Figure 4.55.

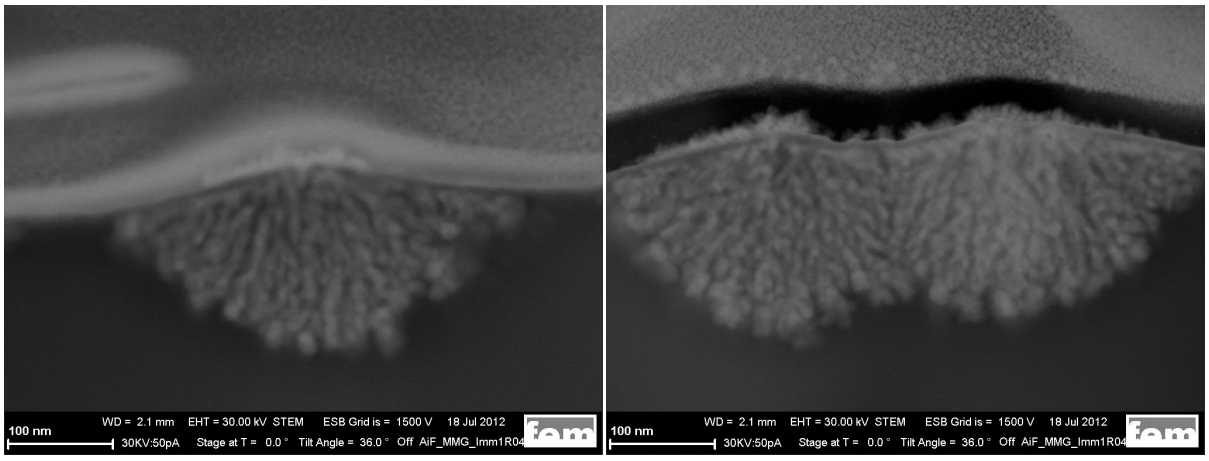

(a) Single scratch (b) Double scratch

Figure 4.56: STEM images of the scratches. Starting from the surface defects caused by the scratches, the corrosion products grow in fan shape into the matrix material, thereby causing a volume increase that results in a cone-shaped surface extrusion; previously published in an earlier version in [3].

4.3.3 TEM investigation

The TEM micrograph of Figure 4.57 (a) shows the cross section of the surface of the polished amorphous $Au_{49}Ag_{5.5}Pd_{2.3}Cu_{26.9}Si_{16.3}$ sample no. 8 after air annealing for 23 days at 348 K. Circles in (a) indicate the locations where electron-beam-diffraction patterns were obtained. Detailed TEM-images of these locations are shown in Figure 4.57 (b) for the matrix and (c) for a branching feature. The corresponding diffraction patterns are shown in Figure 4.58 (a) and (b).

The branched features were found to be amorphous (see bright contrast regions in Figure 4.58 (b)). The TEM analysis did not find detectable traces of sulphur in agreement with the dry conditions in the furnace, due to the lack of a constant flux of air. In addition, in

the TEM analyses, the Cu-oxidation products (detected by XPS) were not detected with certainty [4].

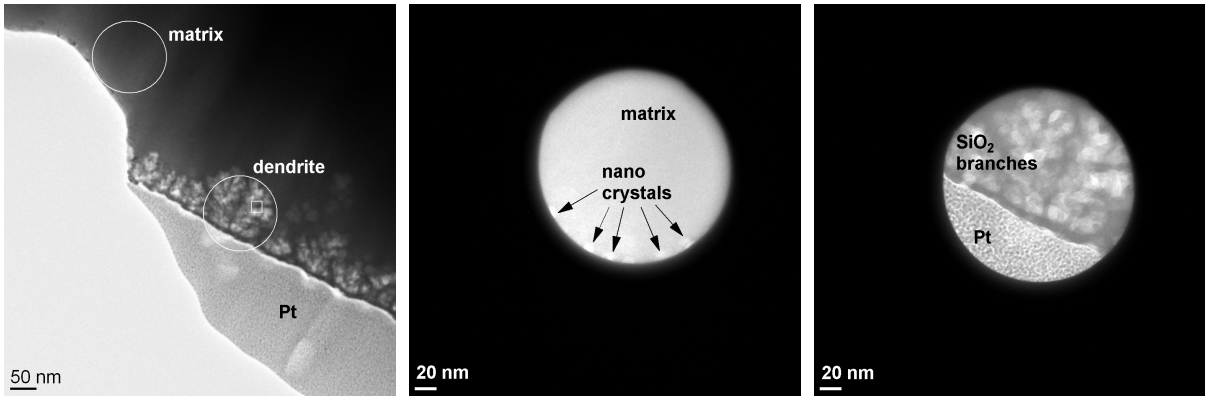

(a) TEM image

(b) Detail of matrix with nano-crystals

(c) Detail of SiO_2 branch

Figure 4.57: TEM images of the FIB lamella of sample 8 from Figure 4.43. (a) TEM-image of the surface region. The platinum coating was partially removed by the gallium ion milling, and the matrix is exposed. Here, the corroded surface part is milled away. (b) and (c) show magnified images of the areas inside the circles of image (a). (b) at the location where the gallium ion beam has reached the matrix the formation of nano-sized crystals can be observed. (c) the silica branches start from the sample surface and grow into the matrix material. Below the sample surface, the platinum protection layer of the FIB preparation is visible. Published in an earlier version in [4].

In Figure 4.58 (c), a high magnification of the SiO_2 branch of Figure 4.57 (c) is shown. The localization of this magnified image is indicated with the small white rectangle in Figure 4.57 (a). The interface between the metallic matrix is shown in dark contrast, while the silica branches are shown in bright contrast. The fringes of the branches show patterns that indicate long range order, namely crystallinity. Beside the amorphous rings, the electron diffractions of the matrix and the dendrite, in Figure 4.58 (a) and (b), respectively, show some crystalline reflections that can be assigned to nano-crystalline gold. Some other reflections that are difficult to assign are present. One possible structure that could give these reflections is the Cu_3Au intermetallic compound [4].

The FIB lamella of sample 16, a cross section of a corrosion zone at a scratch in an as-cast location, was analyzed in the TEM as well (Figure 4.58. No detectable traces of sulfur nor any copper oxidation products on the surface could be found, since they were dissolved and detected in the chemical analysis of the test solution shown in the plot of Figure 4.51. Superimposing the amorphous rings, the TEM electron diffractions of the silica branches beneath the scratch in Figure 4.58 again show reflections attributed to nano-crystalline gold and probably Cu_3Au, similar to the findings of the TEM investigation of sample 8 [4].

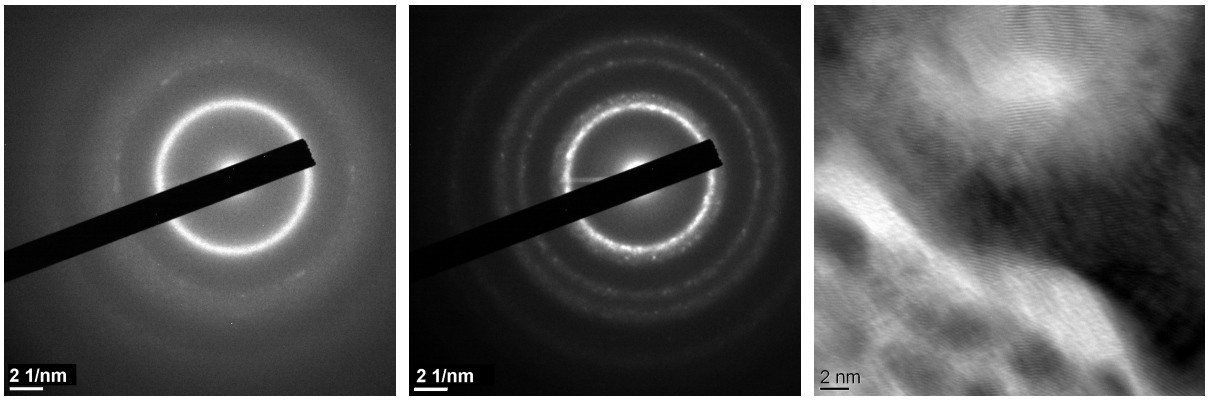

(a) Electron diffraction pattern matrix (b) Electron diffraction pattern SiO_2 branch (c) Detail of SiO_2 branch from Figure 4.57 (c)

Figure 4.58: (a) and (b) Electron diffraction patterns taken from the positions within the circles in Figure 4.57 (a) and a magnified image of the bright SiO_2 branches in image (c). The bright reflections in the diffraction patterns of (a) and (b) indicate the presence of crystals. The positions of the reflections are in good accordance to crystalline Au and maybe Cu_3Au precipitates. In the magnified image (c), crystalline fringes between SiO_2 branches can be observed. Published in an earlier version in [4].

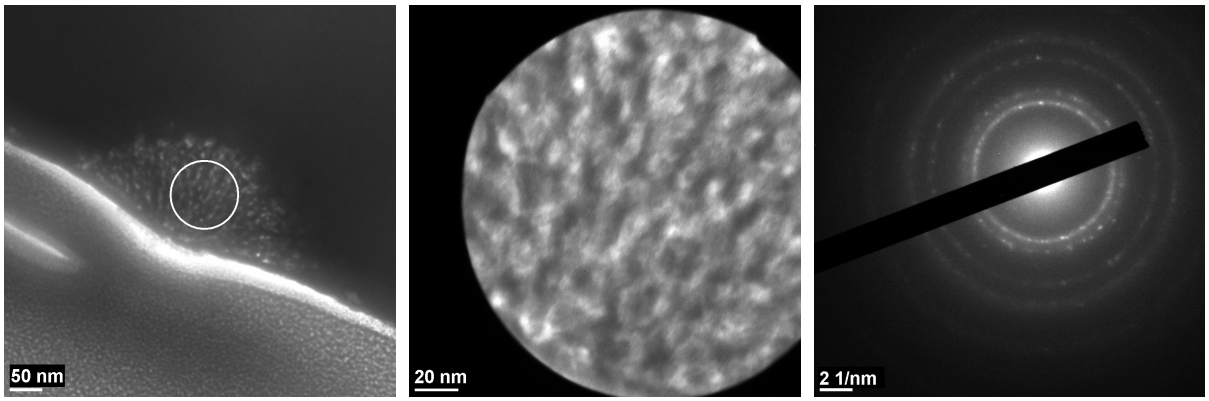

(a) TEM image (b) Detail of SiO_2 branch from (a) (c) Electron diffraction pattern SiO_2 branch

Figure 4.59: TEM investigation of the corrosion attack in artificial sweat on sample 16, same location as in Figure 4.56 (a). The circle indicates the location where the magnified image of the SiO_2 branching (b) and the electron diffraction pattern (c) were taken. Published in an earlier version in [3].

4.4 Tarnishing Behavior as a Function of Alloy Composition

4.4.1 Tarnishing Behavior in Air

In Figure 4.60 (a) the color change of four different compositions is plotted against the exposure time to air at 348 K. The sample of composition $Au_{49}Ag_{5.5}Pd_{2.3}Cu_{26.9}Si_{16.3}$ is the sample no. 6, which was already presented in the microstructure and XPS analysis in Sections 4.3.1.2 and 4.3.1.3. The samples were placed in the furnace at the same time and therefore experienced the same conditions to ensure similar testing conditions [4].

Each symbol in Figure 4.60 (a) corresponds to the average value of three individual color detections. After circa one month of exposure, the color change for the $Au_{49}Ag_{5.5}Pd_{2.3}Cu_{26.9}Si_{16.3}$ (solid square) reaches the detection limit (i.e. YI > 90) and after that point the color change appears to have a distinctly slower rate that is nonrepresentative. Therefore, these values have been excluded from the graph in Figure 4.60. Each specimen was analyzed by X-ray diffraction after 327 days of aging treatment at 348 K in laboratory air. The corresponding XRD patterns are shown in Figure 4.60 (b) [4].

$Au_{49}Ag_{5.5}Pd_{2.3}Cu_{26.9}Si_{16.3}$ (sample 6) and $Au_{49}Ag_{5.5}Pd_{2.3}Cu_{25.9}Si_{16.3}Al_1$ (sample 18) were still amorphous whereas the $Au_{60}Ag_{5.5}Pd_2Cu_{15.5}Si_{17}$ (sample 19) and the $Au_{50}Ag_{7.5}Cu_{25.5}Si_{17}$ (sample 20) crystallized at some point during the treatment. The tarnishing rate of $Au_{49}Ag_{5.5}Pd_{2.3}Cu_{26.9}Si_{16.3}$ (solid squares in Figure 4.60 (a)) is drastically slowed down by either reducing the Cu/Si ratio or by micro-alloying aluminum. For example for the BMG with composition $Au_{60}Ag_{5.5}Pd_2Cu_{15.5}Si_{17}$ (solid circles in Figure 4.60 (a)), after 3 weeks of air exposure, the color change is only 50 % of that for $Au_{49}Ag_{5.5}Pd_{2.3}Cu_{26.9}Si_{16.3}$. The color change rate of $Au_{49}Ag_{5.5}Pd_{2.3}Cu_{25.9}Si_{16.3}Al_1$ (star symbols) is remarkably low. It is reduced by at least 75% over the same time of exposure compared to $Au_{49}Ag_{5.5}Pd_{2.3}Cu_{26.9}Si_{16.3}$ (square symbols). The matrix of $Au_{49}Ag_{5.5}Pd_{2.3}Cu_{25.9}Si_{16.3}Al_1$ has retained its amorphous structure similarly to the mother-alloy (see Figure 4.60 (b)). The palladium-free $Au_{50}Ag_{7.5}Cu_{25.5}Si_{17}$ (open triangles) has Cu/Si and Au/Si ratios very similar to those of $Au_{49}Ag_{5.5}Pd_{2.3}Cu_{26.9}Si_{16.3}$ (see Table 4.3). Nevertheless, the removal of palladium seems to improve the tarnishing resistance. However, $Au_{50}Ag_{7.5}Cu_{25.5}Si_{17}$ crystallized during the 1 year heat treatment at 348 K (see Figure 4.60 (b))[4].

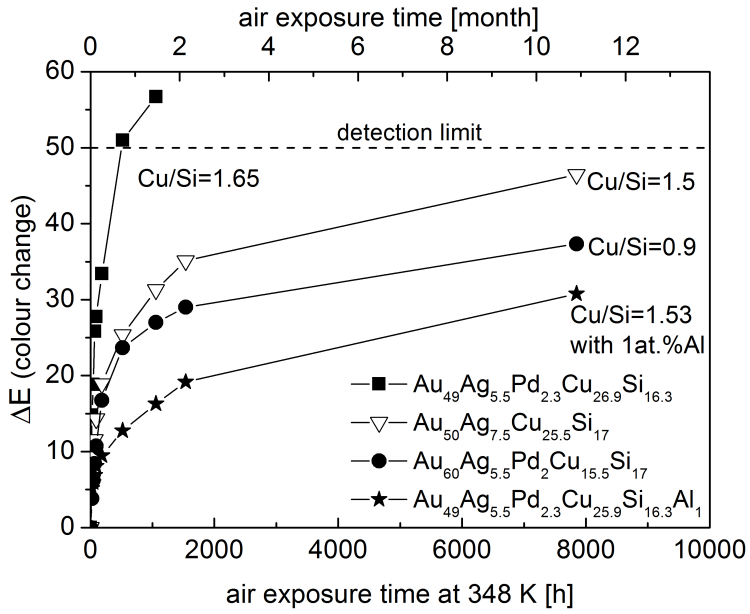

(a) Development of the color change

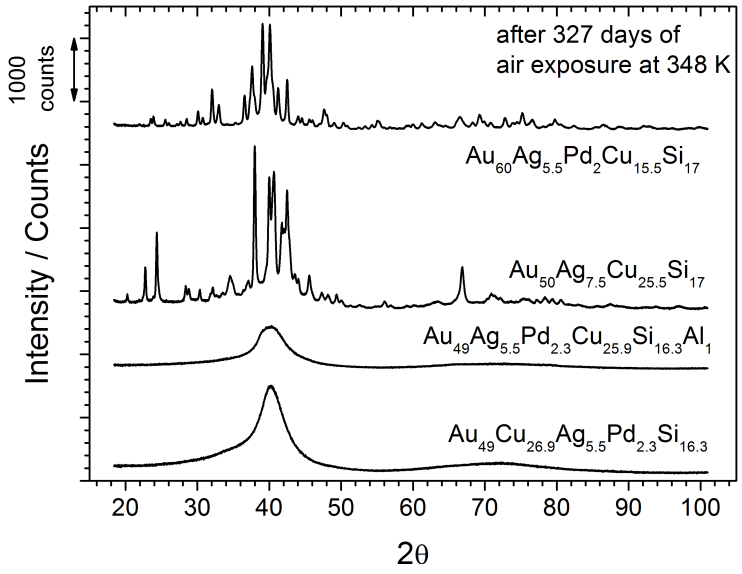

(b) XRD spectra after 327 days

Figure 4.60: (a) The color change for $Au_{49}Ag_{5.5}Pd_{2.3}Cu_{26.9}Si_{16.3}$, $Au_{49}Ag_{5.5}Pd_{2.3}Cu_{25.9}Si_{16.3}Al_1$, $Au_{60}Ag_{5.5}Cu_{15.5}Si_{17}Pd_2$, and $Au_{50}Ag_{7.5}Cu_{25.5}Si_{17}$ BMG compositions detected during a 348 K heat treatment in air. (b) The XRD patterns corresponding to each specimen are shown in (a) at the end of the exposure (327 days). Prior to the exposure, the samples were confirmed to be X-ray amorphous. Published in an earlier version in [4].

Figure 4.61 shows the development of the YI during exposure to laboratory air at 348 K for up to 253 days for $Au_{49}Ag_{5.5}Pd_{2.3}Cu_{26.9}Si_{16.3}$ (sample 27) and micro-alloyed variations of this alloy (samples 21 to 26 according to Table 3.3). The rate of the YI increase is significantly lower than for similar experiments shown in previous sections, for example in Figure 4.47. This is a result of the storage condition in this particular setup. These samples were stored in quartz test tubes rather than ceramic crucibles, allowing less air circulation to the sample surface and therefore reducing the available amount of oxygen on the sample surface. The setup is sketched in Figure 3.7 in Chapter 3.

Surprisingly, almost every micro-addition deteriorates the tarnishing performance with the exception of the substitution of 1 % copper by gallium represented by green circles in Figure 4.61.

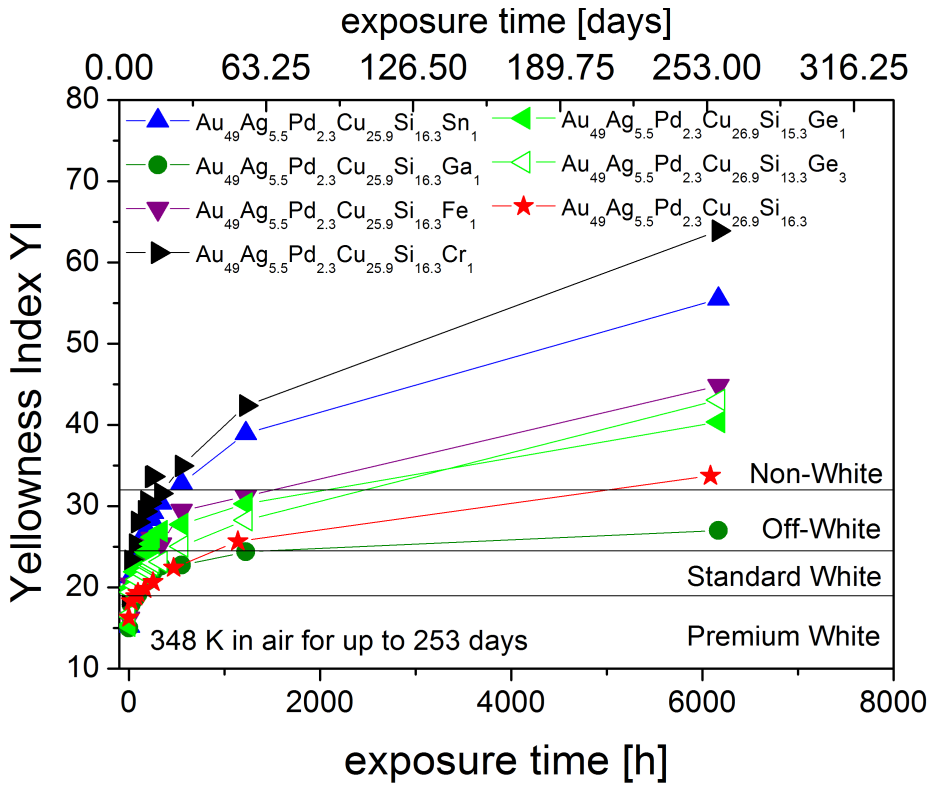

Figure 4.61: The YI development for $Au_{49}Ag_{5.5}Pd_{2.3}Cu_{26.9}Si_{16.3}$ and microalloyed variations with 1 to 3 at% of Fe, Cr, Sn, Ga, and Ge detected during a 348 K heat treatment in air.

4.4.2 Tarnishing Behavior in Sulfide Dip Test

For the sulfide dip test, alloy compositions according to Table 4.7 were chosen. Figure 4.62 shows the polished samples in the epoxy resin after the 7 days sulfide dip test. A clear difference in the test performance is visible already with bare eyes. The smaller the Cu/Si ratio, the better the tarnish resistance becomes.

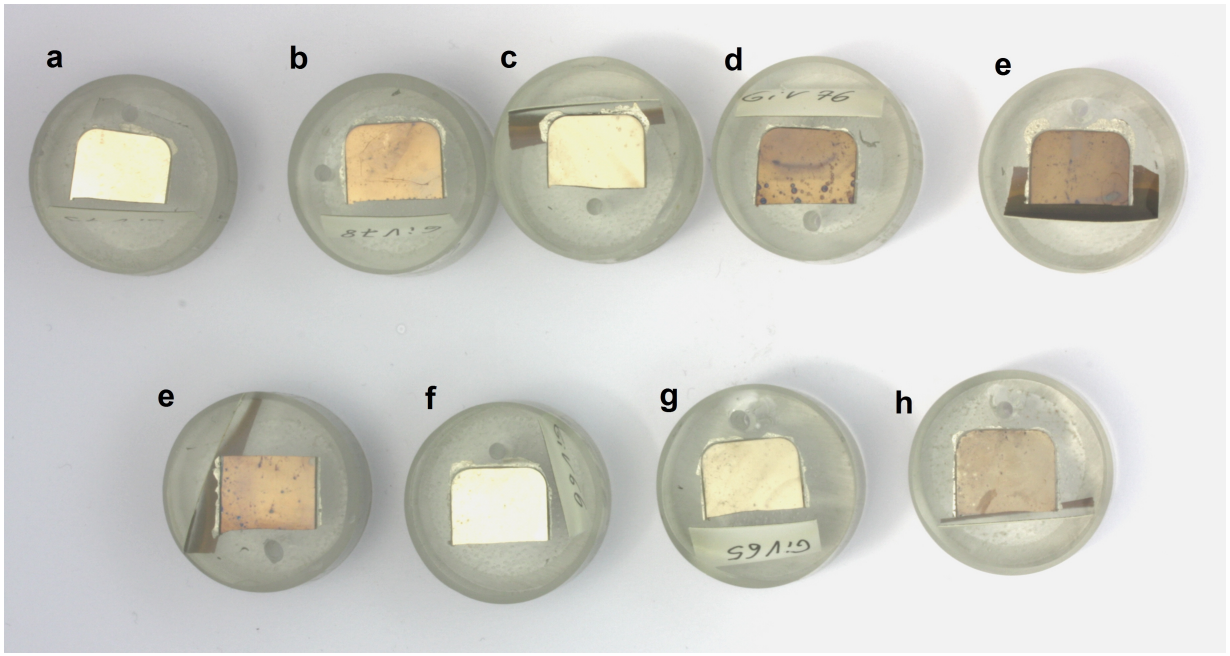

Figure 4.62: Development of the color change in a 7-days sulfide dip test.

Table 4.7: Compositions and ratio of copper to silicon for the samples shown in Figures 4.62 and 4.63.

Label	Sample No.	Alloy No.	Composition at%	Ratio Cu/Si
a	Sample 28	Alloy No. 15	$Au_{65}Ag_{5.5}Pd_2Cu_{10.5}Si_{17}$	0.6
b	Sample 29	Alloy No. 7	$Au_{49}Ag_{5.5}Pd_{2.3}Cu_{24.9}Si_{16.3}Al_2$	1.5
c	Sample 30	Alloy No. 14	$Au_{60}Ag_{5.5}Pd_2Cu_{15.5}Si_{17}$	0.9
d	Sample 31	Alloy No. 6	$Au_{49}Ag_{5.5}Pd_{2.3}Cu_{25.9}Si_{16.3}Al_1$	1.6
e	Sample 32 & 33	Au-BMG1	$Au_{49}Ag_{5.5}Pd_{2.3}Cu_{26.9}Si_{16.3}$	1.65
f	Sample 34	Alloy No. 4	$Au_{65}Ag_{7.5}Cu_{10.5}Si_{17}$	0.6
g	Sample 35	Alloy No. 3	$Au_{60}Ag_{7.5}Cu_{15.5}Si_{17}$	0.9
h	Sample 36	Alloy No. 2	$Au_{50}Ag_{7.5}Cu_{25.5}Si_{17}$	1.5

To quantify the tarnishing rate, in this case the color change ΔE rather than the Yellowness Index was chosen as a parameter to quantify the development of the tarnishing during the experiment since the color of these tarnished samples has red, blue, and gray color components (Figure 4.62). The plot of ΔE in Figure 4.63 shows a clear tendency towards a better tarnish resistance with decreasing Cu/Si ratio.

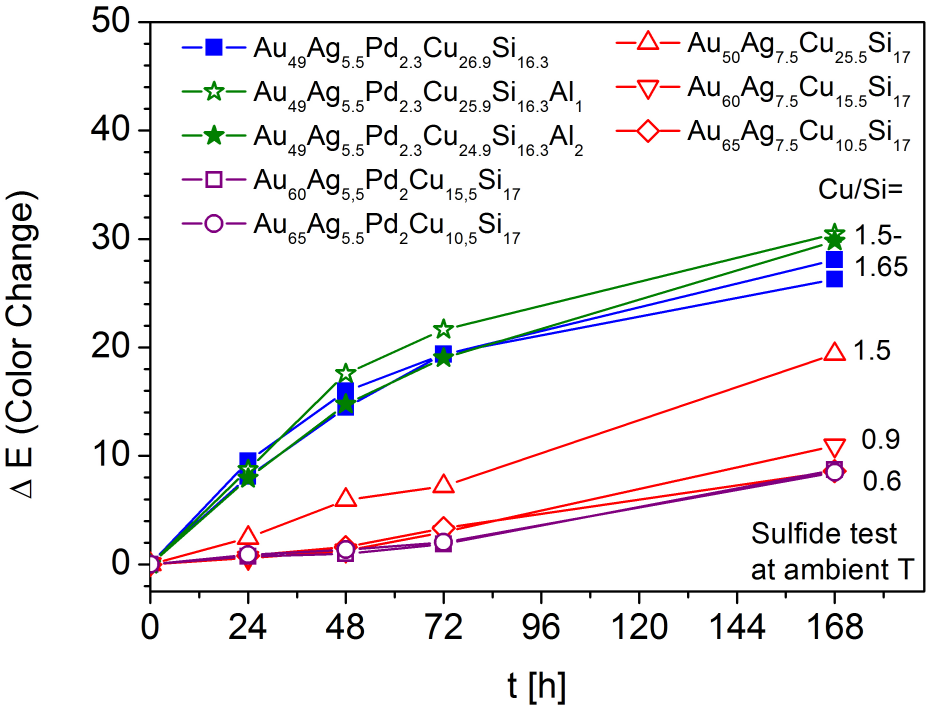

Figure 4.63: Development of the color change ΔE in a 7-days sulfide standard test as a function of immersion time for each studied Au-based BMG composition, published in an earlier version in [4].

4.5 Tarnishing Behavior of Amorphous versus Crystalline State

Crystalline samples were generally found to change their color less rapidly than the amorphous samples despite having the same nominal alloy composition $Au_{49}Ag_{5.5}Pd_{2.3}Cu_{26.9}Si_{16.3}$. Figure 4.64 shows the YI plot for an aging treatment at 348 K in laboratory air. Crystallization of sample 37 was performed using furnace cooling, i.e. applying a slow cooling rate by letting the sample cool from the melt inside the furnace rather than quenching it in a copper mold. Sample 38 was crystallized starting from a solid amorphous condition, re-heating it above T_g and then isothermally crystallizing it. The slow furnace cooling allows a near equilibrium final phase constitution. The latter crystallization technique in the super-cooled-liquid temperature regime results in the formation of small crystals at nano- to micro-scale, hence the sample is denoted as "nano-crystalline" These procedures have been described in Section 3.1.3 in more detail.

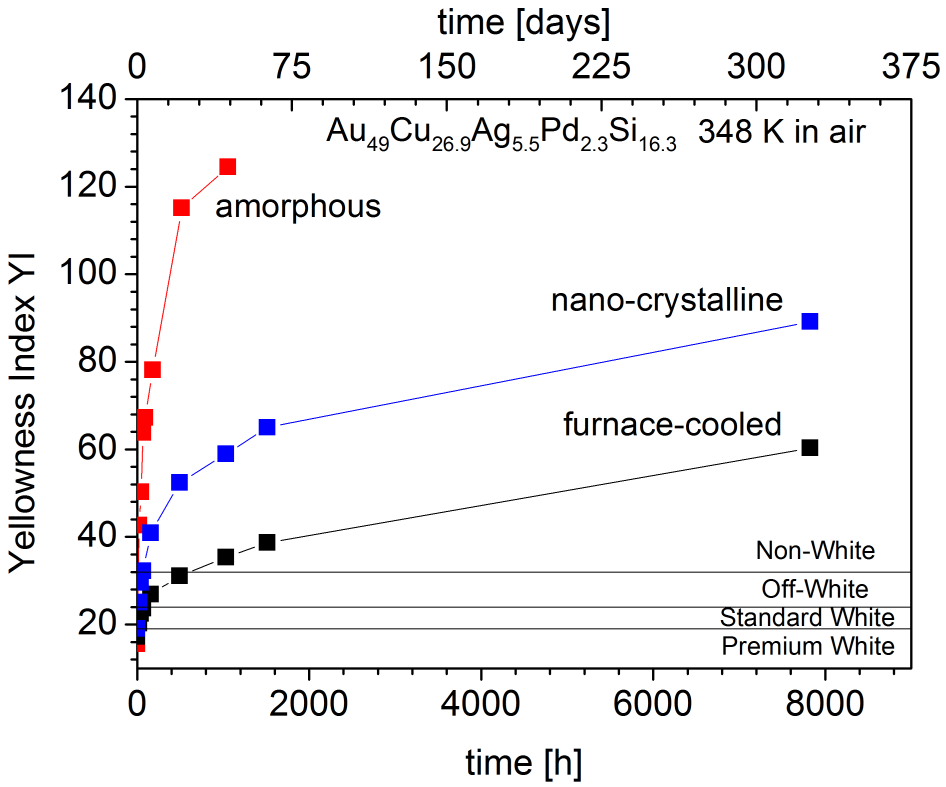

Figure 4.64: Yellowness Index development for amorphous (sample no. 6) and crystalline $Au_{49}Ag_{5.5}Pd_{2.3}Cu_{26.9}Si_{16.3}$ for an aging treatment at 348 K in laboratory air. The furnace-cooled sample is sample no. 37. The nano-crystalline sample is sample no. 38.

Photographs of the crystalline samples after the aging treatment are shown in Figure 4.65. The samples have attained a dark yellow/brown color. The furnace cooled sample has formed much larger crystals than the iso-thermally aged sample. The crystals of the former sample can be observed in the macro-image without distinct magnification. During the slow cooling, diffusion at high temperatures is easier, resulting in easy formation and growth of crystals compared to the much slower kinetics of crystallization between T_g and T_X.

The large dendritic or star-shaped gold-rich crystals of sample 37 in Figure 4.65 (a) have a bright yellow color while the surrounding material is distinctly darker. This probably results in an underestimation of the YI in Figure 4.64, because the color analysis gives an average value of the YI within an analyzed circle area of 6 mm diameter. The nano-crystalline sample 38 has a more uniform appearance. No individual crystals can be observed at this magnification.

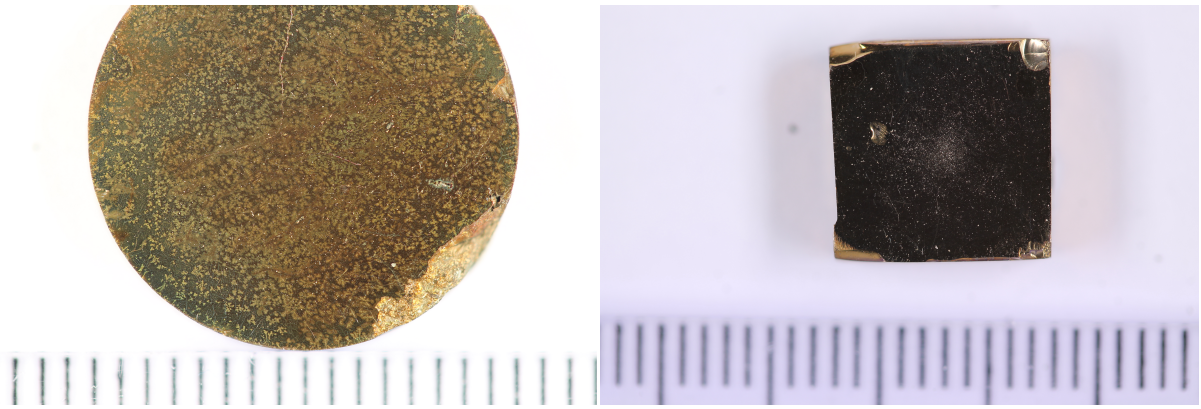

(a) Sample 37, furnace-cooled specimen (b) Sample 38, nano-crystalline specimen

Figure 4.65: Images of an equilibrium crystallized (furnace-cooled) sample (no. 37) and a nano-crystallized sample (no. 38) of $Au_{49}Ag_{5.5}Pd_{2.3}Cu_{26.9}Si_{16.3}$ after the aging treatment for 327 days in air at 348 K. The slow cooling in the furnace results in larger crystals that can be observed with bare eyes. The gold-rich dendritic (star-shaped) crystals are distinctly brighter than the surrounding corroded surface.

A better understanding of the corrosion attack on crystalline samples can be derived from an investigation of their microstructure. Figure 4.66 shows SEM images of the cross sections of sample 37. The images were taken at the tarnished surface regions of the samples. Different phases can be distinguished by different brightnesses in the image. A semi-quantitative EDX analysis of the phases visible in Figure 4.66 (b) revealed that the bright crystal in the center of the image has a distinctly higher concentration of gold and silver than the surrounding material. The silver content was measured to be more than three times as high as in the nominal composition. At the same time copper is clearly depleted to less than a third of the nominal composition and silicon was not detected at all.

Figure 4.66 (b) shows a magnified detail of (a). There is a pronounced selective corrosion at phases that have a low gold content and a high copper content in comparison to the star-shaped gold- and silver rich-phase. This corrosion attack is visible as a dark and structured fringe towards the surface. The fringe was to small to be analyzed via EDX.

Figure 4.67 shows further details of the same cross section. The selective corrosion is clearly visible. The corrosion affects darker crystals, i.e. phases with less noble content, to a much larger extent than the brighter crystals, which have a higher content of noble elements and less copper content. The morphology of the corrosion attack seems to be related to the morphology that was observed in the studies on amorphous material, but it appears to have a finer structure. The magnification in the cross section is very limited in comparison to a FIB lamella, and the structure could not be determined with certainty yet.

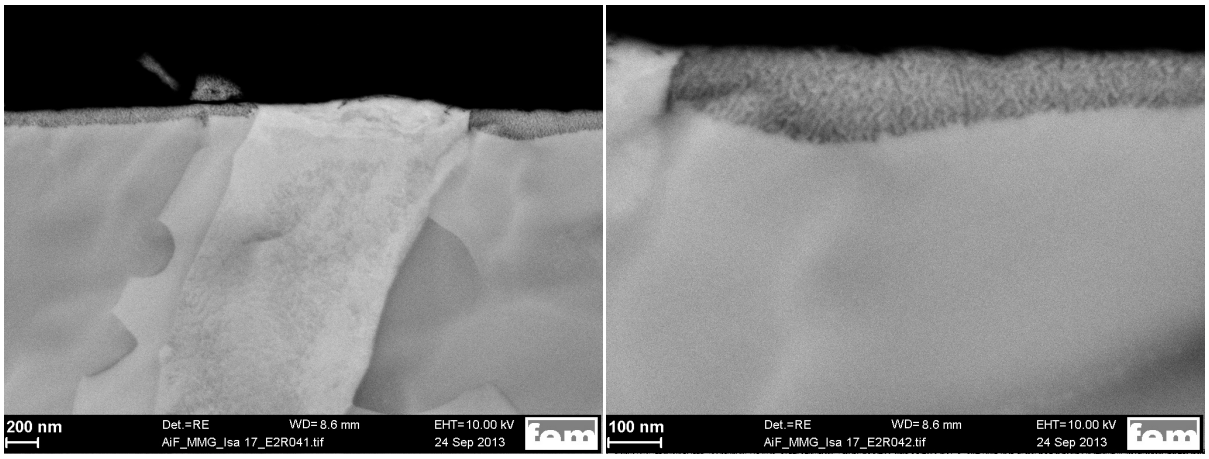

(a) Sample 37, furnace-cooled specimen (b) Sample 37, furnace-cooled specimen

Figure 4.66: SEM images of the cross section of sample 37 shown in 4.65 cut perpendicularly to the surface.

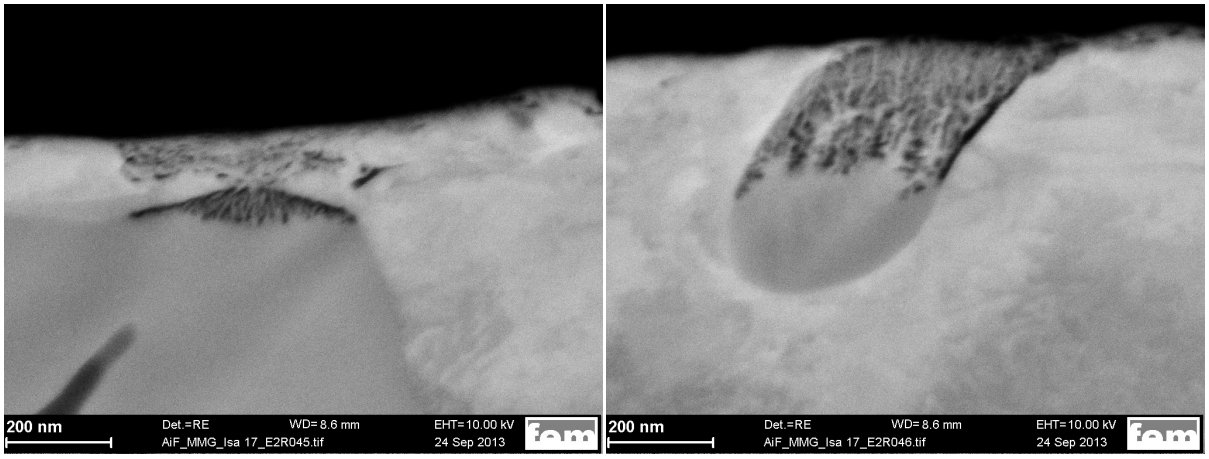

(a) Sample 37, furnace-cooled specimen (b) Sample 37, furnace-cooled specimen

Figure 4.67: SEM images of the cross section of sample 37 shown in 4.65 cut perpendicularly to the surface.

The nano-crystalline sample consists of different phases as well. The backscatter images in Figure 4.68 show the distribution of heavier and lighter phases in the sample. Again, a selective corrosion clearly has taken place. It affects preferentially the darker plotted grains of the sample. The deepest advance of the corrosion can be observed along the grain boundaries between noble and less noble crystals, affecting almost exclusively the less noble crystals. In contrast to the findings derived from the YI plot in Figure 4.64, sample 38 is much less corroded than sample 37 in terms of a visible corrosion attack on the microstructure.

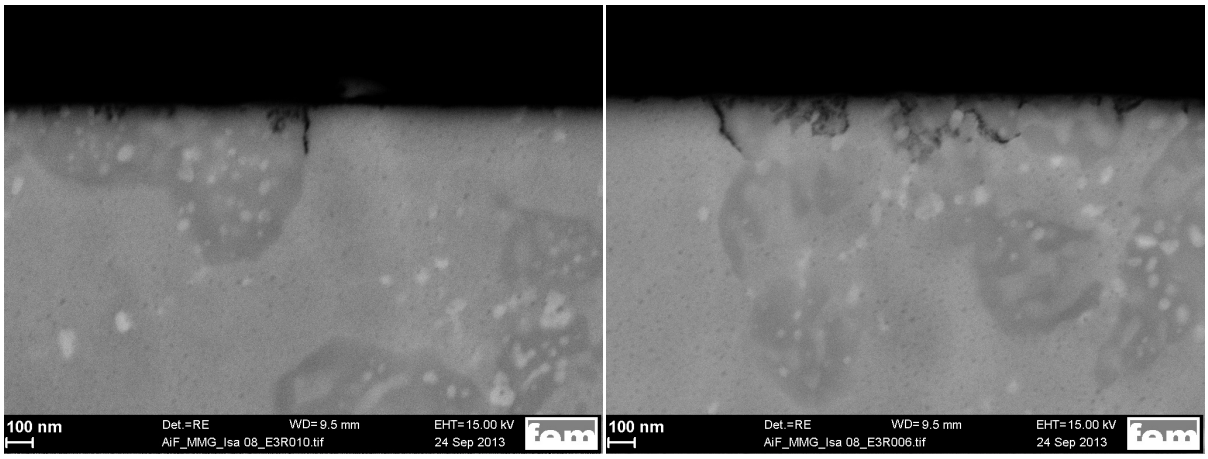

(a) Sample 38, nano-crystalline specimen (b) Sample 38, nano-crystalline specimen

Figure 4.68: SEM images of the cross section of sample 38 shown in 4.65 cut perpendicularly to the surface.

A comparative study on amorphous and crystalline samples of $Au_{49}Ag_{5.5}Pd_{2.3}Cu_{26.9}Si_{16.3}$ versus typical crystalline jewelry alloys and sterling silver Ag 925 and 935 has been carried out in artificial saliva according to standard test DIN EN 10271. Table 4.8 lists the compositions that were investigated in this test and the respective concentrations of copper, silicon and silver found in the test solutions after the test. The precious metals gold, palladium and platinum could not be detected. The detection limit of the test is 0.05 mg/l, which equals 0.05 $\mu g/cm^2$ for this setup.

As a benchmark for comparison, two samples of amorphous Au-BMG1 (samples 39 and 40) were included in the study. The highest amount of ion release into the artificial saliva test solution was observed for the silver alloys (samples 45 and 46). The copper concentration in the test solution was up to one order of magnitude higher than for the amorphous $Au_{49}Ag_{5.5}Pd_{2.3}Cu_{26.9}Si_{16.3}$. It was significantly higher for the 925 sterling silver than for the 935 sterling silver. The latter alloy has only one mass percent, equaling 1.5 atom percent, less copper, yet the metal release is reduced by more than a third. Aside from the silver alloys, the amorphous samples 39 and 40 show the largest loss of alloying elements, namely copper and silicon, to the test solution. Crystallization of the sample material results in a reduction of the copper release to less then a quarter of the amount of released copper, and the silicon concentration is approximately reduced by a half.

Interestingly, the copper release of a conventional crystalline 18k white gold (sample 42) is two orders of magnitude lower than for the crystalline sample 41 of $Au_{49}Ag_{5.5}Pd_{2.3}Cu_{26.9}Si_{16.3}$. It stays at the same level for the 14k sample 43 and for the platinum alloy (sample 44). Both conventional jewelry gold alloys (18k and 14k) have a very similar copper content.

Figure 4.69 shows the bar plot of the release into the test solution in log scale and a photo of the samples after the test. The difference of the tarnishing effect is clearly visible.

Table 4.8: Tabular overview of the samples used in the artificial saliva test.

No.	Alloy	Cu $[\frac{\mu g}{cm^2}]$	Si $[\frac{\mu g}{cm^2}]$	Ag $[\frac{\mu g}{cm^2}]$
39/40	$Au_{49}Ag_{5.5}Pd_{2.3}Cu_{26.9}Si_{16.3}$ at.% $Au_{76}Ag_{4.7}Pd_{1.9}Cu_{13.5}Si_{3.6}$ wt.%	59±3	1.3	< 0.05
41*	$Au_{49}Ag_{5.5}Pd_{2.3}Cu_{26.9}Si_{16.3}$ at.% $Au_{76}Ag_{4.7}Pd_{1.9}Cu_{13.5}Si_{3.6}$ wt.%	13	0.6	< 0.05
42	$Au_{56.9}Pd_{22.4}Cu_{13.9}Zn_{6.8}$ at.% $Au_{75.1}Pd_{16}Cu_{5.9}Zn_3$ wt.%	0.18		< 0.05
43	$Au_{40.8}Ag_{23.5}Pd_{20.6}Cu_{13}Zn_{2.1}$ at.% $Au_{58.5}Ag_{18.5}Pd_{16}Cu_6Zn_1$ wt.%	0.16		0.25
44	$Pt_{88.66}Cu_{11.34}$ at.% $Pt_{96}Cu_4$ wt.%	0.16		< 0.05
45	$Ag_{87.9}Cu_{12.1}$ at.% $Ag_{92.5}Cu_{7.5}$ wt.%	566		< 0.05
46	$Ag_{89.45}Cu_{10.55}$ at.% $Ag_{93.5}Cu_{6.5}$ wt.%	328		< 0.05

* Sample crystallized according to the third crystallization procedure of Section 3.1.3 i.e. casting of an amorphous sample and subsequent aging at 523 K (250 °C) for 1 h.

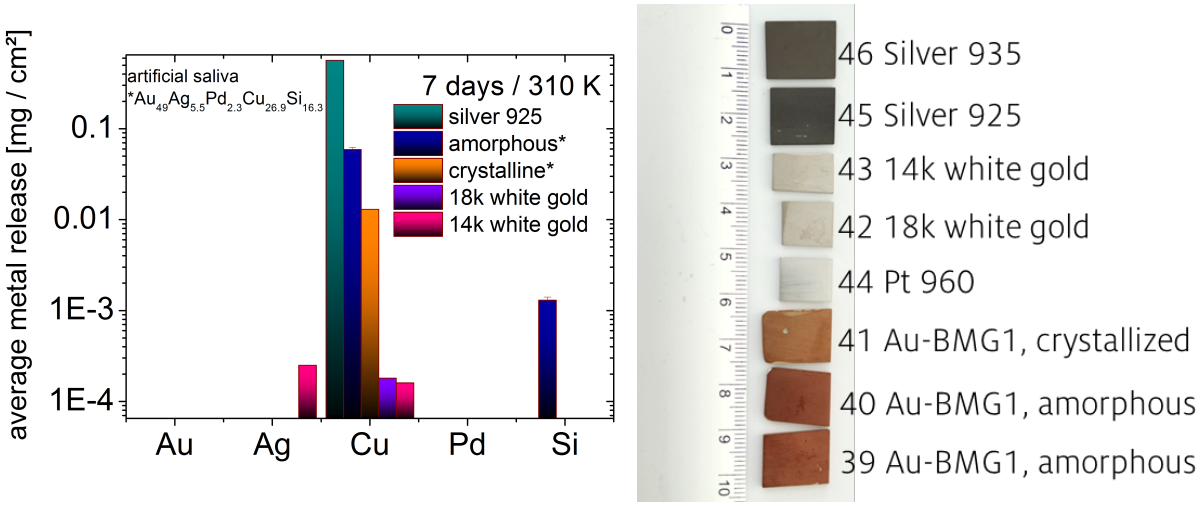

(a) Metal release

(b) Samples after test

Figure 4.69: (a) bar plot of the metal ion release into the test solution according to Table 4.8 starting from the detection limit of 0.05 mg; (b) photographs of the samples after the artificial saliva test.

5 Discussion

Parts of the discussion that are presented here have been published in an earlier version by the author of the present work and co-workers [4, 13, 14, 15, 3].

5.1 Processing

5.1.1 Melting

Critical for successful casting in the Au-Cu-Pd-Ag-Si system is to avoid the formation of Pd-Si precipitates. This is an observation both made during this research work as well as described in literature [11]. It can be successfully prohibited by either

- pre-alloying silicon and palladium in separate pre-alloys, which can then be alloyed in a second melting step

  or

- by placing silicon and palladium separately inside the crucible and placing all the other elements in between, resulting in a one step casting process.

For the present work, only commercially available casting equipment that is used in industrial jewelry production was employed. Compared to high-vacuum laboratory conditions, in industrial casting equipment still a fairly high amount of residual oxygen is expected to be left inside the casting device after the evacuation of the device and subsequent fluxing with argon, the process gas. A direct result of this residual oxygen is the observed native SiO_2 skin on as-cast surfaces as described in Section 4.3.1.2. Still, the comparatively high oxygen content, which is usually posing problems in zirconium based systems [107, 108, 109], seems to have no harming effect on the casting in gold-based systems.

Repeated casting experiments have shown that once the final composition has been prepared, the alloy can be remelted and recast at least 12 times in a row into a rod shape of 5 mm diameter with no negative effect on the amorphous solidification [76]. The high repeatability of subsequent castings into 5 mm rods is unexpected as one of the best bulk metallic glass-formers for commercial use, Vit.1, has been reported to achieve a maximum of 7 subsequent casting repetitions at a casting thickness of less than its d_c before the material has to be recycled [110].

The critical casting thickness of $Au_{49}Ag_{5.5}Pd_{2.3}Cu_{26.9}Si_{16.3}$ has earlier been reported to be 5 mm [1] but it was now found to be at least 6 mm [76]. The casting experiments on

repeatability were carried out with rod shaped casting geometries with 5 mm diameter. This is close to the critical casting thickness, hence this repeatability is extraordinary good, especially when the applied casting procedure in the study, tilt casting [76], is taken into account. Tilt casting can easily be applied in an industrial jewelry casting process. However, the atmosphere is usually not very clean since the oxygen is not titanium gettered. Additionally, the form filling and hence the cooling rate is reduced in comparison to suction casting.

This high repeatability under industrial casting conditions is a crucial property for the commercial use of the alloy, since repeated melting and casting steps are to be expected during typical jewelry processing and recycling of the material is a significant cost factor.

5.1.2 Processing of a Semi-finished Product

In the laboratory setup used for the present work, oxidation of the granules cannot be completely avoided. This does not affect the amorphous state of the granules and poses no problem for remelting and recasting of the material, meanwhile providing protection from the tarnishing. The oxide layer formation can probably be largely reduced in a setup with a designated granulation chamber that can be evacuated and purged with an inert gas.

During the studies on thermoplastic forming described in Section 4.1.5, the native oxide layer proved to be detrimental for a 100% bonding between individual granules. The native oxide layer can easily be removed by a treatment with hydrofluoric acid as shown in Section 4.3.1.1. It can be expected that once the native oxide layer is removed, complete bonding of granules by thermoplastic forming can be achieved. It has yet to be quantified to which extent, if any, residual SiO_2 in the joining zone harms the performance of the joined part.

In view of the commercial application of this material class, the granules are an ideal semi-finished product that provides an easy-to-portion supply of the target composition. Applying granules as semi-finished products reduces the production efforts as the weighing of 4 to 5 individual elements for each cast can be a source of failure and impreciseness and it is time-consuming. Producing a large amount of material with the final alloy composition in an easy and fast manner is advantageous for industrial processing.

5.1.3 Casting

5.1.3.1 Crystallization Effects during Casting

The existence of a thin superficial layer in the range of 10 to 80 μm enriched in nano-crystals on cast samples of $Au_{49}Ag_{5.5}Pd_{2.3}Cu_{26.9}Si_{16.3}$ has been reported before by Ketov et al. [89]. Heterogeneous nucleation as well as high shear rates at the copper mold may trigger the formation of small, nanometer-sized crystals. The often observed partial yellowish color of freshly cast products [89] may be attributed to these crystals. The surface layer can easily be removed by a standard polishing procedure, which is usually applied in any case for most precious metal applications. This superficial layer probably poses no problems for the overall performance of small technical parts if it is not removed, as long as the bulk material

beneath is amorphous. A chemical reaction of the melt with the copper mold, however, could only be observed at the sprue, i.e. the location where the maximum temperature in the mold-system can be expected to last the longest.

The crystallization in cast products not only superficially but distributed over the whole cross-section (see Figure 4.11) despite a casting thickness significantly below the critical casting thickness was observed in centrifugal casting of $Au_{60}Ag_{7.5}Cu_{15.5}Si_{17}$ and to a lesser extent of $Au_{49}Ag_{5.5}Pd_{2.3}Cu_{26.9}Si_{16.3}$ (see Section 4.1.3). While the crystallization phenomenon in the center of the sample may be attributed to delayed cooling in the center, the material volumes in close distance to the copper mold should experience a sufficiently high cooling rate for amorphous solidification.

This type of crystallization has been observed before in the Au-BMG system [111] and has been discussed as a phenomenon called "shear thinning". Crystallization was found to be triggered by large strain rates during solidification. Lohwongwatana et al. studied the strain-rate-induced crystallization behavior of $Au_{49}Ag_{5.5}Pd_{2.3}Cu_{26.9}Si_{16.3}$ and found that no fully amorphous splat-cooled samples could be produced despite the more than sufficiently high cooling rates in the range of 10^6 to 10^8 K/s. In contrast to this, casting into copper molds results in fully amorphous samples of up to 6 mm in diameter [76]. The critical cooling rate for this alloy has recently been reported to be in the order of 600 K/s [105], much lower than cooling rates occurring in splat cooling. One possible explanation for the crystallization at given high strain rates during solidification was introduced by the authors of [111], who suggested a phase separation and thus formation of regions within the melt in which the chemical composition is outside the metallic glass-forming window, at least for the applied cooling rates. To date, the actual underlying mechanism is still unknown.

5.1.3.2 Development of a New Casting Technique

The newly developed casting technique presented in Section 4.1.4 introduces the use of the traditional wax molding procedure to the field of bulk metallic glass casting. It combines investment casting with copper-mold casting and thereby provides a solution to the problem of the insufficient cooling rate of the investment material used in conventional jewelry casting processes.

In 2006, investment casting of bulk metallic glasses was patented by Peker and Kim [93] despite the fact that they never successfully applied the process (see Section 2.8). The new casting technique introduced here, employing lost copper molds, solves the problem posed by Peker and Kim [93]. In investment casting, the investment is actually designed to do the direct opposite to fast cooling. Usually, the objective during investment casting is to keep the melt at a high temperature as long as possible, because this is crucial for a good form filling. For the filling of complex cavities, the investment may even be heated prior to casting to achieve this goal [112]. Hence, it is not surprising that casts with conventional investment material have so far been unsuccessful in terms of amorphous solidification. Applying lost copper molds with a certain minimum copper mass (see Section 4.1.4) supplies the sufficient cooling rate for amorphous solidification.

The advantage of lost copper molds over re-usable copper molds is the possibility to

realize geometries that cannot be cast using dividable copper molds. Wax prototypes can furthermore easily be shaped very individually, providing the opportunity of a low cost production of very unique designs.

5.1.4 Thermoplastic Forming

The thermoplastic joining of granule material was successfully applied for $Au_{49}Ag_{5.5}Pd_{2.3}Cu_{26.9}Si_{16.3}$. Due to the native SiO_2 surface layer, the bonding succeeded only on approx. 50 % of the interface area. With the oxide layer intact, the process can be compared to the joining of zirconium-based reactive bulk metallic glasses, which quickly develop an oxide layer in air when processed at elevated temperatures. This was reported by Chen et al. in [51]. The forming process results in a stretching of the granules surface, and the rather brittle oxide layer is forced to break up due to its low plastic deformability and reveals the pristine matrix material below. This pristine material can then diffuse and form a metallic bond in the spacing between the SiO_2 islands. For the precious-metals-based bulk metallic glasses, the formation of a fresh oxide layer that prevents a metallic bonding during the TPF process is negligible. Once the native oxide layer on the surface is etched away, a 100 % joining is expected to be feasible.

5.2 Tarnishing Behavior

5.2.1 Native Oxide Formation during Solidification

In the present work faster tarnishing kinetics on polished surfaces were observed, as well as on scratched locations on as-cast samples or HF-etched granule surfaces. This can probably be attributed to the lack or removal of a protective silica surface layer. Distinctly slower tarnishing kinetics were observed on as-cast surfaces that oxidized during the solidification - namely surfaces at air pockets as in Figures 4.32 and 4.33 or surfaces of untreated granules like in Figure 4.27 (a) and (b). It is important to notice that the silicon oxide layer that has been formed at high temperatures during the solidification acts as a protective coating, in contrast to the amorphous SiO_2 that forms on solid surfaces at low temperatures on polished glassy specimens during the tarnishing process [4].

It was observed that dense SiO_2-like coatings possess excellent barrier effects against tarnishing of silver artifacts [113]. The protective effectiveness of the coating acts against the diffusion of water and other (gaseous) aggressive agents present in the environment and prevents them from coming into contact with the pristine metal surface. The formation of amorphous silica or silicides is also the probable reason responsible for the good oxidation resistance of alloys containing high amounts of silicon. It is well known that vitreous well-adhering scales of silica or of silicides (e.g. $MoSi_2$, $TiSi_2$) are highly protective. Ionic diffusion through those scales is very slow. Fukumoto et al. [114] reported that also the hot corrosion resistance of stainless steels has been significantly improved by the surface alloying of silicon, due to the formation of protective SiO_2, which would resist basic or

acidic dissolution in molten salts during electrolysis in fused Na_2SO_4. The formation of the protective SiO_2 film is considered to be the result of the oxidation of the silicon-enriched surface layer of molten material during the solidification process [4].

Indeed, in the present work SiO_2 films a few nm thick were observed on the surface of cast specimens at air-pockets or on the surface of granules (having a thickness of a few nm to ≈ 100 nm in some locations), which were exposed to air during free dropping (Figure 4.8), and not on the surface of specimens that solidified in contact with copper cavities and/or under high vacuum or high-purity argon flux. This effect was also observed by Battezzati and co-workers on the surface of amorphous $Au_{49}Ag_{5.5}Pd_{2.3}Cu_{26.9}Si_{16.3}$ melt spun ribbons. There, XPS analysis proved that the formation of SiO_2 occurs only on the air side surface and not on the copper wheel side surface [87, 78] [4].

The enrichment of silicon, and therefore its oxidation, on the surface of molten $Au_{49}Ag_{5.5}Pd_{2.3}Cu_{26.9}Si_{16.3}$ may be attributed to liquid silicon having a lower surface tension than liquid gold. Recently the evidence of a silicon-enriched surface layer of 2.5 nm thickness was reported by Shpyrko et al. on the $Au_{81}Si_{19}$ eutectic formed at the eutectic temperature of 636 K (363 °C) [88, 115]. The composition of the surface layer was found to be approximately 70 at.% Si [88]. Similarly, surface crystallization of presumably Si-enriched phases was detected in liquid eutectic Au-Si, in liquid $Au_{77}Ge_{14}Si_9$, and in liquid $Au_{49}Ag_{5.5}Pd_{2.3}Cu_{26.9}Si_{16.3}$ [88, 116, 117]. The surface crystallization was shown by observing melting of ordered surface-structures detected for these systems at temperatures much higher than the liquidus temperature (approx. 1073 to 1173 K) [117, 118]. It was also reported that $Au_{49}Ag_{5.5}Pd_{2.3}Cu_{26.9}Si_{16.3}$ metallic glass requires significant pressure for filling cavities below 100 nm in lateral dimension at temperatures between 773 and 973 K due to an antiwetting behavior on quartz [119], which can be considered an indication of its surface crystallization according to reference [119] [4].

5.2.2 Dense Branching Morphology of the SiO_2 Branches

A FIB tomography was carried out for one of the particularly larger pits on sample 6 after an aging treatment for 327 days in air at 348 K to determine the growth patterns of the internal SiO_2 branches. Figure 5.1 shows the 3D image of this tomography. They start out to be of small and capillary character and seem randomly distributed. Deeper into the matrix, some of the branches coarsen and grow deeper while they also broaden. Other branches disappear in favor of the larger SiO_2 branches, a process that can be referred to as Ostwald ripening. The reason for the coarsening effect is the reduction of the surface free energy due to the development of particles with larger radii [120, 121].

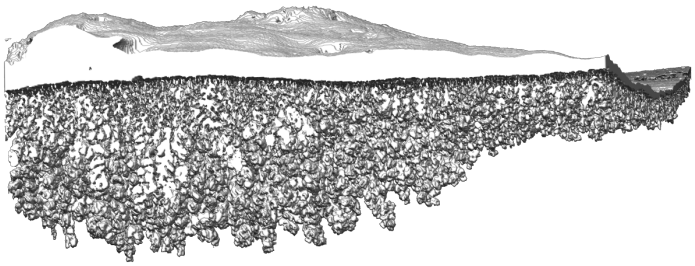

(a)

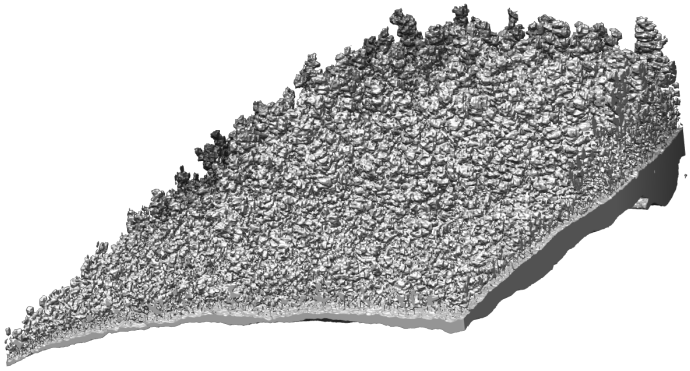

(b)

Figure 5.1: 3D reconstruction obtained by FIB tomography of a corrosion pit with especially pronounced dense branching of SiO_2 into the matrix material on sample 6 after an aging treatment for 327 days in air at 348 K.

Figure 5.2 shows the 3D reconstruction of one distinctly large SiO_2 branch. It is clearly visible that the SiO_2 grows into connected branches starting from the surface rather than individual spherical SiO_2 islands inside the matrix.

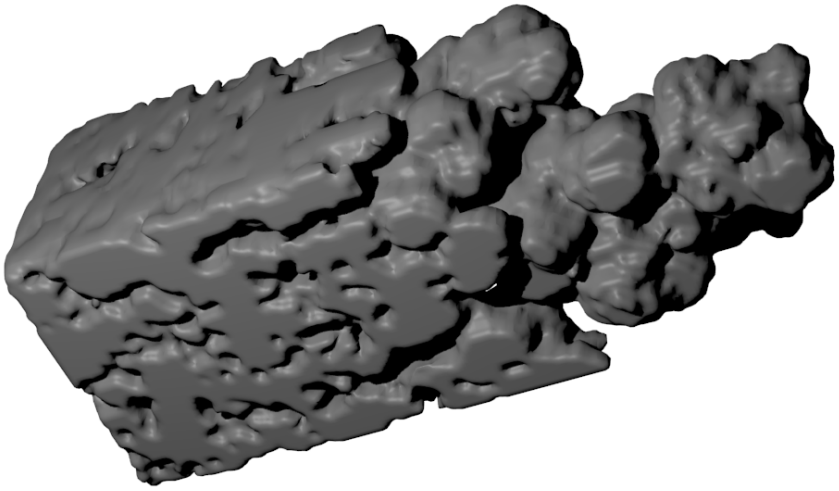

Figure 5.2: Detailed view of the branching morphology of a SiO_2 branch of sample 6 after an aging treatment for 327 days in air at 348 K. 3D reconstruction of a FIB tomography.

In the case of the silica branches observed in this study, an amorphous solid phase grows into another amorphous solid phase driven by the oxidation of the silicon in the alloy by oxygen from the gas phase in contact with the sample surface. Crystallographic growth directions or anisotropy in the bulk phase such as constitutional undercooling during solidification of a liquid play no role in this process, hence the anisotropy required for the formation of dendrites is not present (see also Section 2.6).

According to [83], protrusions that are formed in Hele-Shaw cells at the interface between a more and a less viscous liquid are most likely caused by Mullins-Sekerka instability leading to a pressure gradient that is largest at the protrusions. The Hele-Shaw cell experiments describe the displacement of a viscous liquid by another, less-viscous liquid or gas. While the liquid/liquid interface may have more similarities to the amorphous/amorphous interface in the gold BMG than the liquid-solid transition during dendrite formation, there are still differences between the Hele-Shaw dense branching and the silica branch growth in the present work. The silica branches grow by the formation of SiO_2 at the expense of silicon from the bulk. No external pressure gradient can be accounted for this growth pattern. It is more likely that the availability of the reactants plays a crucial role in the stabilization of the protrusions, since the tips advancing farther into the bulk material have a better access to the silicon of the amorphous matrix.

5.2.3 The Role of Copper and Gold Partitioning during Silicon Oxidation

The present work shows the experimental evidence that the tarnishing mechanism is controlled by the internal oxidation of silicon, which is linked in some way to an enhanced

out-diffusion of copper and gold and an enhanced oxidation of copper on the surface. It is important to notice that this happens rapidly even at ambient temperature. Amorphous SiO_2 was found to form on polished surfaces as well (see Figure 4.58 (c)). Just underneath, a silicon-depleted (gold-enriched) zone is found (see Figure 4.44), and more internally glassy silica branching features nucleate at low partial pressure of oxygen within the sub-surface matrix. Kelton and Spaepen reported that Pd-Si metallic glasses have a native surface layer of SiO_2 and saw the evidence of a release of elemental palladium into the matrix [122]. Similarly, in the analyzed Au-Ag-(Pd)-Cu-Si BMGs, during the oxidation of silicon, the adjacent matrix gets depleted in silicon and enriched in the other elements. The fast color change of polished surfaces from white to yellow gold colors can probably be attributed to the surface partitioning of gold and copper as amorphous silica underneath is colorless and transparent to light. When elemental gold and copper are released out of the matrix during the formation of SiO_2, they can diffuse out extremely fast. The diffusivity of gold in bulk Au-Si eutectic is, indeed, one order of magnitude faster than in pure gold at the same temperature [123, 124][4].

Gold is also well known to have a strong tendency for surface granulation, and this has been detected in bulk metallic glasses as well. The nano-crystallization of gold particles as a result of air oxidation of zirconium-based BMGs was reported by Köster and co-workers [125]. Recent work performed on melt spun ribbons by Battezzati and co-workers on the dealloying of $Au_{49}Ag_{5.5}Pd_{2.3}Cu_{26.9}Si_{16.3}$ in artificial sweat [86] and on the Au-Cu-Ti-Si BMG system [78] has found experimental evidence of nano-crystalline gold particles left on top of dealloyed ribbons. Zhang et al. assumes in [6] that an atomic gold-enrichted surface layer could form on the amorphous Au-Ag-Cu-Si samples, which would even provide some protection against corrosion.

In the present work, gold nano-particles were detected on the surface of air-exposed specimens. On sample 6, the bright contrast nano-particles dispersed on the surface of Figure 4.36 (a) could be attributed only to Cu_2O, while the smaller granular particles of bright contrast were too small for an EDX analysis. Evidence that they might form during the tarnishing in air was first found in the TEM electron diffraction patterns (Figure 4.58 (b)) in the matrix adjacent to the SiO_2 features. Since a nano-crystallization processes may take place during the FIB-lamellae sample preparation as in Figure 4.57 (b), it cannot be concluded with certainty that the gold nano-crystallization in this case is an oxidation-induced process. EDX results on sample 7 of Figure 4.38 indicate the formation of islands of clustered elemental copper and gold nanoparticles after exposure to air at 348 K for 1 year at locations, where reduced sub-surface silica branching was observed. This island can clearly be distinguished from the Cu_2O protrusions observed above clusters of particularly large SiO_2 branches.

At longer times of exposure, the tarnishing to orange and brown colors may be discussed in terms of copper partitioning, out diffusion and its subsequent corrosion on the surface [4].

An abnormal surface oxidation of silicon at room temperature has been reported to occur in the presence of copper [126, 127, 128]. First, Harper et al. proposed the possibility of the following reactions [126]:

$$3Cu + Si \longrightarrow Cu_3Si \tag{5.1}$$

and

$$Cu_3Si + 2O \longrightarrow SiO_2 + 3Cu_{elemental} \tag{5.2}$$

with the intermediate formation of Cu_3Si as catalyst for the SiO_2 formation.

After copper ion implantation, on pure silicon, the copper was found diffusing through the silicon dioxide surface layer even at room temperature and the silicon oxide growth was found to depend on the amount of copper present at the moving Si/SiO_2 interface [127]. It was proposed that copper is essential for the dissociation of oxygen on the silicon surface, by forming Cu_2O according to the reaction

$$4Cu + 2O \longrightarrow 2Cu_2O \tag{5.3}$$

Moreover, copper oxide is known to be reduced by the presence of Si to form SiO_2 and elemental copper, following the reaction

$$2Cu_2O + Si \longrightarrow 4Cu + SiO_2 \tag{5.4}$$

This can be attributed to the very negative driving force for formation of SiO_2 in comparison to Cu_2O [129][4].

According to the proposed chemical reactions of equations 5.2 and 5.4, elemental copper is released (partitioned), and SiO_2 is formed by oxidation. The partitioning of elemental copper in the surroundings is even enhanced by the glassy nature of the matrix, due to weak atomic interactions in the amorphous material, as discussed later in Section 5.2.9. Once copper is partitioned (dealloyed) from the glassy matrix, it can become highly mobile even at room temperature and can diffuse to the surface very rapidly. In fact, as a consequence of its small ionic radius, copper is known to have relatively weak interactions with the other atoms, especially with the metalloid silicon as reported in reference [130][4].

The internal oxidation of silicon was observed here to occur exclusively underneath polished surfaces (see Figure 4.33). The formation of similar SiO_2 dendrite-like features was reported in Cu-Si alloys only for high temperatures of 923 to 1273 K (650-1000 °C) [131, 132, 133]. They are formed as a result of the internal oxidation of silicon and are observed in various Cu-Si crystalline structures: in polycrystalline alloys [131], in the bulk of single crystals [132], and along the grain boundary of bicrystals [133]. In this system, SiO_2 structures form in dense branching morphology (DBM) in a glassy Au-Cu-Si-based matrix at much lower temperatures, ambient to 348 K. At these low temperatures fast atomic diffusivities in the glassy matrix can be expected because, in addition to the arguments discussed in Section 5.2.9, they scale with the low T_g (401 K) rather than with the high melting point of the Cu-Si crystalline alloys, 1073 K or higher [4].

The nucleation and growth of the glassy silica features appear to be controlled by the supply of oxygen and the partitioning of copper. The largest DBM formations appear to grow faster at locations underneath porous cone-shaped Cu_2O products like for example

in Figure 4.36. The reduction of the Cu_2O to elemental copper due to the oxidation of silicon leads to a self-supporting reaction circle that can account for locations of maximum growth of both oxides. The morphology of the silica features is best described as "dense branching morphology" according to the 3D reconstruction of Figure 5.2 and based on the findings from literature shown in Section 2.6. This was expected considering the amorphous structure that supports isotropic growth like a liquid. Similar silica features seem to grow from the surface of crystallized samples. However, the features are finer and grow selectively in the less noble phases (see Figure 4.67) [4].

Similar observations were reported by Hinode and co-workers in [128]. The oxidation of silicon occurs abnormally at room temperature in the presence of copper. Reference [128] shows that areas of a silicon substrate covered with very thin or cone-like copper-islands oxidized fast, forming SiO_2 films of $\approx$ 100 nm thickness. Areas covered with a thick and uniform non-island-like copper-rich film did not oxidize that fast [4].

The supply of oxygen through the copper oxide layer controls the silicon oxidation process. The presence of a copper silicide, such as Cu_3Si, was found in [128] to be not necessarily needed for oxidation in contrast to what was reported earlier in [126]. Copper atoms were detected at the SiO_2/Si interface and identified not as silicide but as body-centred, cubic-structured copper several atom layers thick. In the amorphous $Au_{49}Ag_{5.5}Pd_{2.3}Cu_{26.9}Si_{16.3}$ alloy oxidized at 348 K for almost a year as illustrated in Figure 4.36, the internal SiO_2 formation reaches a depth of approximately 1.15 μm under cone-shaped Cu_2O products and only 0.1-0.3 μm at other locations [4].

In Figure 4.44 the detected XPS concentration values are plotted by using the ratio of copper and silicon to oxygen, as well as the ratio Au/Si. This way the gold enrichment (and silicon depletion) underneath the Cu_2O scale is very evident (at 100 s) as well as the presence of a copper enrichment at the front tip of the growing SiO_2 particle (at 1250 s) and between its branches (e.g. at 400 s). Other evidence that the formation of internal SiO_2 involves a considerable partitioning of elemental gold and elemental copper is the formation of gold nano-particles and copper-rich intermetallic in the surrounding matrix (see TEM images of Figures 4.57, 4.58 and 4.59) [3, 4]. Islands rich in gold and copper were found on a sample stored in air at 348 K for one year (see Figure 4.38, suggesting formation of clusters of elemental copper and gold nano-crystals on the surface.

Figure 5.3 sketches the proposed tarnishing mechanism of amorphous $Au_{49}Ag_{5.5}Pd_{2.3}Cu_{26.9}Si_{16.3}$. The native SiO_2 (a) acts as a diffusion barrier and protects the metal matrix underneath from tarnishing effects. (b) once the native silica is removed, the pristine metal matrix is accessible for oxygen. (c) the partitioning of elemental copper from the glassy matrix triggers the formation of a superficial SiO_2 layer. (d) the elemental copper can diffuse through the SiO_2 very fast and once it reaches the surface, it is itself oxidized (compare Equation 5.3). (e) Cu_2O on the surface can be reduced to elemental copper by the silicon from the alloy contributing to the SiO_2 growth and leaving elemental copper on the surface that can be oxidized again (Equation 5.4). The self-supporting reaction cycle contributes to the formation of the cone shaped Cu_2O formations on the surface. The SiO_2 growth into the matrix supports the out diffusion of elemental copper and gold. (f) shows an actual image of SiO_2 branching into the matrix, the SiO_2 superficial layer, an island of

clustered gold and copper between subsurface silica branches and the Cu_2O scale with a cone shaped extrusion at a position of a particularly large SiO_2 branch [4].

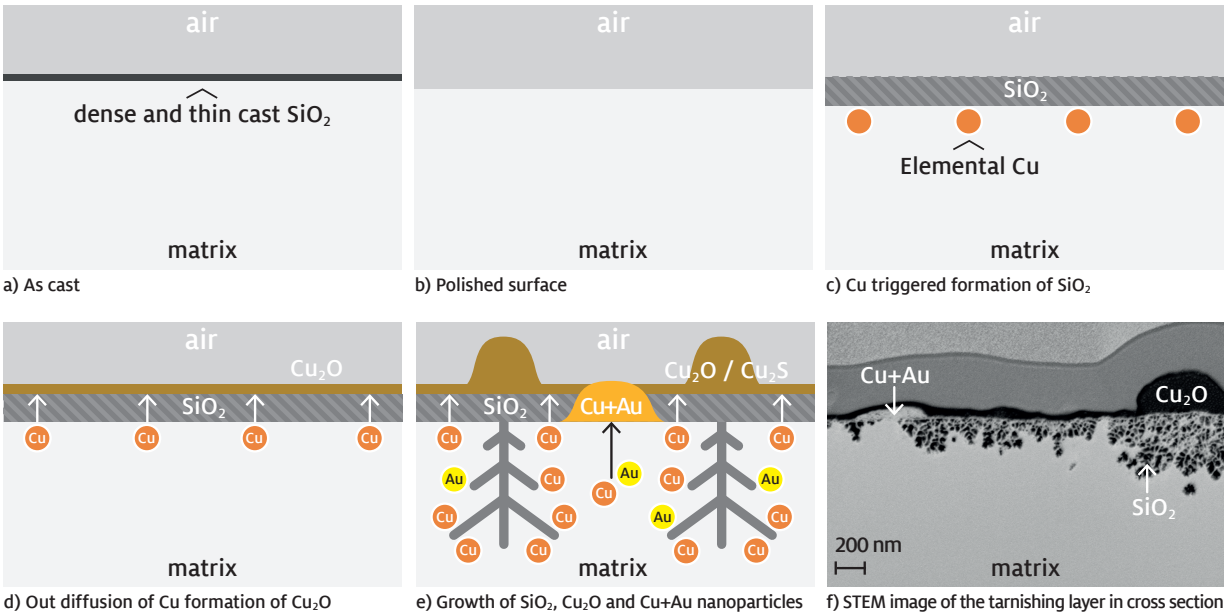

Figure 5.3: Schematic drawing of the mechanism behind the tarnishing process: a) surface of the sample with a thin and dense native SiO_2 layer; b) pristine metal surface after the removal of the native SiO_2; c) partitioning of elemental copper, which triggers the oxidation of silicon at the surface; d) diffusion of the elemental copper to the surface where it can react with oxygen itself according to Equation 5.3; e) Cu_2O can be reduced to copper by elemental silicon, which is itself oxidized leading to a growth of the SiO_2 into the matrix and to further diffusion of elemental copper and gold to the surface; f) actual STEM image of a cross section showing the SiO_2 branching, the island of elemental copper and gold, the Cu_2O top layer, and the cone-shaped Cu_2O islands at locations of maximum SiO_2 growth. Published in an earlier version in [3].

5.2.4 Kinetics of SiO_2 Branch Growth versus Out-diffusion of Copper

The tarnishing seems to be controlled by diffusion. From the microstructure investigation, the lengths of silica branches are known for certain aging times at 348 K. Assuming a diffusion controlled corrosion process, the oxide scale thickness and the storage time should be correlated according to the following equation 5.5 [81, 134]:

$$x = \sqrt{D * t} \tag{5.5}$$

which gives a diffusion coefficient of:

$$D = \frac{x^2}{t} \tag{5.6}$$

The microstructure of sample 6 is best documented by FIB investigations in the present work and allows an estimation of the diffusion coef]ficient by evaluating the branch sizes both for particularly large branches underneath large corrosion pits and for the uniform branch growth between corrosion pits.

For the large silica dendrites of sample 6, a maximum length of 1.15 μm was determined after a total storage of 327 days. Between the more prominent corrosion pits with remarkably long silica branches, smaller branches were observed with a more uniform growth of 100 to 350 nm length. Hence, a maximum diffusion coefficient for the large silica branches can be estimated as follows:

$$D_{sample6,max} = \frac{(1.15\mu m)^2}{327 days} \tag{5.7}$$

$$D_{sample6,max} = \frac{1.3225 * 10^{-8} cm^2}{28252800 s} = 4.7 * 10^{-16} cm^2/s \tag{5.8}$$

Calculating the diffusion coefficient for the 350 nm growth length of the more uniform average branches between the distinctly large branches gives:

$$D_{sample6,uniform} = \frac{1.225 * 10^{-9} cm^2}{28252800 s} = 4.3 * 10^{-17} cm^2/s \tag{5.9}$$

This is one order of magnitude below $D_{sample6,max}$.

Sample 8 was stored only 23 days at 348 K and developed silica branches of up to $\approx$ 100 nm length as shown in Figure 4.43 (a). A development of distinctly large corrosion pits as for sample 6 was not observed for sample 8. Applying equation 5.6 for the data of the uniformly growing silica branches gives:

$$D_{sample8,uniform} = \frac{1 * 10^{-10} cm^2}{1987200 s} = 5.0 * 10^{-17} cm^2/s \tag{5.10}$$

This is in very good agreement with the uniform silica growth *between* the larger corrosion cones of sample 6. Hence, the uniform growth of silica branches at a given temperature of 348 K may be driven by a diffusion process with a diffusion coefficient of $\approx$ 4-5 $*10^{-17} cm^2/s$, while the large corrosion pits grow with a diffusion coefficient that is one order of magnitude larger.

For the formation of Cu_2O on top of the silica branches, a similar consideration can be made. In order to form the oxide, a supply of copper from the substrate has to be given. The copper has to diffuse from the bulk to the surface to form the CuO_2 on the surface, thus the diffusion length correspond rather to the copper depletion zone than to only the copper-oxide layer thickness.

Analyzing the data of the XPS analysis of sample 8, a depletion of the copper even farther into the matrix than the tips of the main silica branches was observed in the plot of Figure 4.43 (b). The copper was found to reach a constant concentration only after 4500 s sputter time, corresponding to a sputter depth of 342 nm beneath the original surface. Since the silica branches only go as deep as $\approx$ 100 nm, the copper depletion zone

seems to extend three times as deep. Hence, for the copper out diffusion scenario, a similar estimation as for the silica branches can be made that gives the following result:

$$D_{sample8,Cudepl.} = \frac{1.17 \times 10^{-9} cm^2}{1987200 s} = 5.9 * 10^{-16} cm^2/s \tag{5.11}$$

In summary, assuming a diffusion controlled tarnishing rate and estimating the diffusion coefficient from the relationship $D = \frac{x^2}{t}$ yields the values listed in table 5.1.

Table 5.1: Table of the estimated diffusion coefficients for silica branch growth and for the Cu_2O-layer development at 348 K.

	D estimated [cm^2/s]
Sample 6, large branch	$4.7 * 10^{-16}$
Sample 6, uniform branches	$4.3 * 10^{-17}$
Sample 8, uniform branches	$5.0 * 10^{-17}$
Sample 8, Cu depletion	$5.9 * 10^{-16}$

The growth of the silica branches into the amorphous matrix starts at the unprotected sample surface. STEM and TEM images suggest, that at first small features are built that later grow inward forming a DBM morphology with larger and at the same time fewer features. The fresh oxygen supply for the silica formation has to be provided from the air in contact with the sample surface. The amount of oxygen dissolved in the metal matrix is negligible in terms of silica growth as was shown in the experiments on samples kept in argon flux and in vacuum. The oxygen has to diffuse to the tip of the silica branches in order to form fresh SiO_2. Let us assume, that the diffusion of fresh oxygen takes place through the silica that is already in place:

The review [135] summarizes various data of oxygen diffusion through silica. Unfortunately, only high temperature data between 1223 and 1351 K (950 °C and 1078 °C) seem to be available of oxygen diffusion through *amorphous* silica. An overview of the values shown in [135] is given in Figure 5.4 (b). With a known activation energy Q and the temperature independent material constant for diffusion D_0, the diffusion coefficient at a certain temperature can be calculated as follows [81]:

$$D = D_0 \exp \frac{-Q}{RT} \tag{5.12}$$

For the oxygen diffusion through amorphous silica between 1223 and 1353 K, the following Arrhenius equation was derived:

$$D = 2.7 * 10^{-4} * \frac{cm^2}{s} \exp \frac{-113000 \frac{J}{mol}}{RT} \tag{5.13}$$

Resulting in $D_{1351} = 1.154 * 10^{-8}$ and $D_{1223} \frac{cm^2}{s} = 4.02653 * 10^{-9} \frac{cm^2}{s}$ (note that the results in Figure 5.4 (b) are given in $\frac{m^2}{s}$). Calculating D from equation 5.13 for 348 K yields 2.948

$* 10^{-21} \frac{cm^2}{s}$, a value that is far from the estimations for the silica branch growth made above. However, extrapolating equation 5.13 to very low temperature values is probably not accurate, since the activation energy may be different at lower temperatures. Diffusion data for silicon diffusion in gold are not available [136].

According to [137], the diffusion coefficient of copper in gold is 1.29 $*10^{-13}$ cm^2/s at 423 K (150 °C), 3.61 $*10^{-14}$ cm^2/s at 398 K (125 °C) and 6.41 $*10^{-15}$ cm^2/s at 373 K (100 °C) as in figure 5.4 (a). Judging from these values, the copper diffusion in gold should be in the order of $1.07 * 10^{-15}$ cm^2/s at 348 K, as was determined by a linear fit of the experimental values in the plot of the logarithmic values in Figure 5.4 (a). This lies in the same range as the diffusion coefficient derived from the estimation for the copper depletion above (Table 5.1).

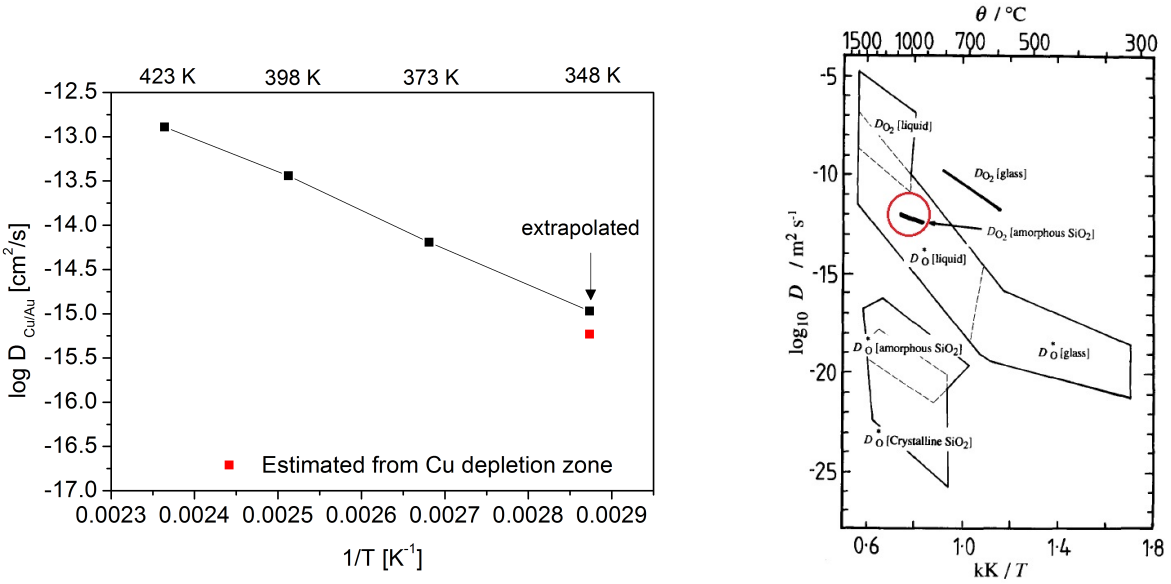

(a) Low temperature diffusion of copper in gold

(b) Data for oxygen diffusion through silica

Figure 5.4: (a) Diffusion coefficients for copper in gold according to [137] and the extrapolated value for 348 K (75 °C) together with $D_{sample8,Cudepl.}$ of equation 5.11. (b) Diffusion coefficient data for oxygen in SiO_2 reprinted from [135] .

Judging from the available data for oxygen diffusion through amorphous silica, the tarnishing seems not mainly driven by diffusion of oxygen into the silica branches. A much better correlation was found for the copper out diffusion and the formation of Cu_2O on the surface. Since the diffusivity of copper may differ significantly in crystalline gold from the amorphous $Au_{49}Ag_{5.5}Pd_{2.3}Cu_{26.9}Si_{16.3}$, this estimation can really only give an approximation of the order of magnitude at which the diffusion may take place.

The diffusion coefficient for copper in gold may even change over the tarnishing progress. The XPS profiles showed distinct fluctuations in the gold content in the tarnished region.

Chemical composition can have a huge impact on the diffusion behavior of copper in gold. Matano [138, 139] investigated the diffusion of the nickel-gold system depending on the gold content. Copper is chemically very similar to nickel and is expected to behave qualitatively in the same way. Matano [138] found a steep rise in the diffusion coefficient above 60 at.% gold (Figure 5.5) at 1173 K (900 °C). The variation of diffusivity in metals was observed to change considerably greater with the composition than it is usually observed in gases. In the case of tarnishing in $Au_{49}Ag_{5.5}Pd_{2.3}Cu_{26.9}Si_{16.3}$, the fluctuations of the gold content in the tarnishing zone may change the diffusivity considerably and even further promote an out-diffusion of copper when the gold content locally exceeds 60 at.%.

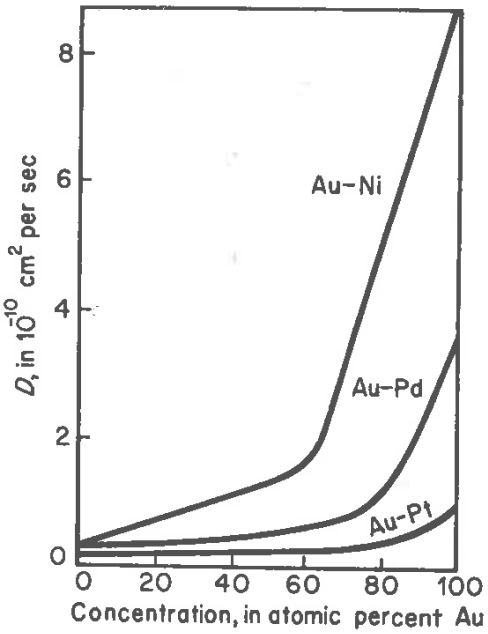

Figure 5.5: Variation of the diffusion coefficient (D) with composition at 1173 K, reprinted from [139, 85].

5.2.5 The Colorimetric Study

According to Henderson et al. [97], Yellowness Index values as low as the ones reported in the present work are to be considered among the lowest values ever detected on premium white gold alloys. This means that, according to the definition given in Chapter 3, among white gold alloys the studied glassy compositions possess very small aberrations from a perfect white color towards a yellow color [4].

The YI of the amorphous $Au_{49}Ag_{5.5}Pd_{2.3}Cu_{26.9}Si_{16.3}$ alloy was previously reported to be 25.3, an intermediate value between standard white to off-white gold color [11]. The value of reference [11], however, was not measured immediately after polishing but after

a non-protective storage period. In Figure 4.47, a value of 25.3 indeed corresponds to a tarnishing after air exposure for circa 60 days at RT. Only when kept in the freezer (circle symbols in Figure 4.47), the rate of the YI variation is very slow. In Figure 5.6 the time that is necessary to reach off-white gold colors (24.5 YI) is plotted as a function of temperature when the amorphous $Au_{49}Ag_{5.5}Pd_{2.3}Cu_{26.9}Si_{16.3}$ specimen is simply exposed to air atmospheres. This figure shows that the white gold regime exists only a short time for this BMG alloy. For example, at room temperature, the polished surface of this composition tarnishes to off-white gold values after only 2 months of air exposure. The samples kept at higher temperatures are so intensively tarnished that the YI reaches off-scale values after 2 months of storage [4].

Rate constants k_{lin} for the initial tarnishing reaction were obtained by applying a linear rate dependency (valid in first approximation) to the data of Figure 4.47.

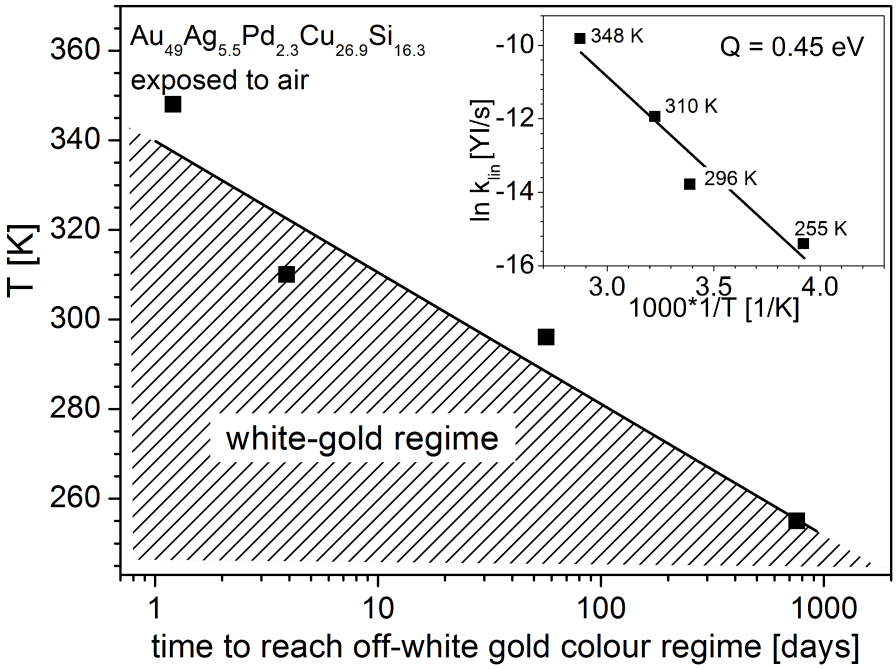

Figure 5.6: Time till off-white values for the Yellowness Index are reached in air obtained for $Au_{49}Ag_{5.5}Pd_{2.3}Cu_{26.9}Si_{16.3}$ at different temperatures; published in an earlier version in [4].

The ln of the linear rate constants k_{lin} for the tarnishing in air are plotted in the inset of Figure 5.6 against the inverse temperature. The slope of these data points in a logaraithmic plot over the inverse temperature can be used to estimate an activation energy by applying an arrhenius equation:

$$k_{lin} = k_0 \exp -\frac{Q}{RT} \tag{5.14}$$

k_{lin} is the rate of YI development per second, k_0 represents a pre-exponential factor. Q is the activation energy for the tarnishing process. R is the universal gas constant and T is the temperature in Kelvin.

Equation 5.14 can also be written as:

$$\ln k_{lin} = \ln k_0 - \frac{Q}{RT} \tag{5.15}$$

The ln k_lin values plotted in Figure 5.6 yield a slope m_k. Treating equation 5.15 as a linear equation for the linear fit shown in the inset of Figure 5.6 gives:

$$Q = -m_k * R = 44.480 \frac{kJ}{mol} \tag{5.16}$$

This results in an activation Energy Q of 44.480 $\frac{kJ}{mol}$ or ≈ 0.45 eV, respectively. This is a typical average value for a corrosion mechanism that includes more than one oxidation mechanism. In comparison, the thermal activation energy for Cu+ diffusing into Cu_2S is 0.3 eV and that for Cu+ diffusing throughout Cu_2O is 1.8 eV. For Si_2O the thermal activation energy of formation is 0.7-0.8 eV [140] [4].

5.2.6 Formation of Cu_2O versus Cu_2S and the Role of the Cu/Si and Au/Si Ratios

The results of the present work show that the aggressiveness of the environment plays an important role in the tarnishing effect (see Figure 4.47). An as-cast BMG plate with composition $Au_{49}Ag_{5.5}Pd_{2.3}Cu_{26.9}Si_{16.3}$ built an Cu_2S (Cu(I) sulfide) corrosion scale on the surface after two years of being exposed to air, wet environments and to human pollutions. In the XPS concentration profiles (Figures 4.44, 4.45 and 4.46) derived from samples aged under controlled conditions in a furnace, the external corrosion scale is Cu_2O and not Cu_2S (ratio Cu/O ≈ 2 in Figure 4.44). This is attributed to the fact that the air in the furnace was not highly polluted with H_2S gases and the contact to sweat was avoided altogether by consistently handling the specimens with gloves [4].

In terms of Cu_2O versus Cu_2S formation, the relative humidity of the atmosphere has to be taken into account. In [141], the nucleation rate of Cu_2O on a pure copper surface is reported to be stimulated at high relative humidity and, the average Cu_2O thickness is increased by a factor of 48, when relative air humidity increases from 40% to 80%. In the case of Cu_2S, along with a gas-period the mechanism of formation involves also an aqueous-period, which could have been the case with $Au_{49}Ag_{5.5}Pd_{2.3}Cu_{26.9}Si_{16.3}$ in contact to human sweat [3]. In the present work, a standard 7-day sulfide formation test was performed on most of the presented gold-based BMG alloy compositions. The color change ΔE caused by the formation of the tarnishing layer was detected during the test and plotted in Figure 4.63 [4].

The rate of the color change of the $Au_{49}Ag_{5.5}Pd_{2.3}Cu_{26.9}Si_{16.3}$ decreases along with the reduction of the Cu/Si content in the alloy. For example for the BMG with composition $Au_{60}Ag_{5.5}Pd_2Cu_{15.5}Si_{17}$ (circles in Figure 4.60 (a)), after 3 weeks of air exposure the color

change is only 50 % of that for the $Au_{49}Ag_{5.5}Pd_{2.3}Cu_{26.9}Si_{16.3}$. It is remarkable that the rate can be drastically slowed down by reducing the Cu/Si ratio independently of the exposure, as shown in Figure 4.60 (a) and Figure 4.63. When the data of Figure 4.60 (a) are plotted as double logarithmic (see Figure 5.7), the tarnishing rate appears to change behavior as the Cu/Si ratio is decreased and the Au/Si ratio is increased. For example, the $Au_{49}Ag_{5.5}Pd_{2.3}Cu_{26.9}Si_{16.3}$ (squares) and the $Au_{50}Ag_{7.5}Cu_{25.5}Si_{17}$ (open triangles) follow a fast pure parabolic rate, and the $Au_{60}Ag_{5.5}Pd_2Cu_{15.5}Si_{17}$ (circles) shows a more passivating pure logarithmic behavior. The logarithmic law was proven by a linear fitting of the log(ΔE) values versus log(time). Based on this observation, it is expected that the tarnishing of $Au_{49}Ag_{5.5}Pd_{2.3}Cu_{26.9}Si_{16.3}$ BMGs can be brought to acceptable rates and the long term white gold stability region can be prolonged by several orders of magnitude, if the nominal Cu/Si and/or the Si/Au ratios in the alloy are in some way drastically reduced [4].

In Figure 5.7, $Au_{49}Ag_{5.5}Pd_{2.3}Cu_{26.9}Si_{16.3}$ and the palladium-free $Au_{50}Ag_{7.5}Cu_{25.5}Si_{17}$ change the mode of their tarnishing behavior from a pure parabolic to a slower rate at long exposure times. In the case of $Au_{49}Ag_{5.5}Pd_{2.3}Cu_{26.9}Si_{16.3}$ (squares) this is an apparent effect due to the achievement of the detection limit of log(ΔE)=1.7 (for ΔE = 50). For $Au_{50}Ag_{7.5}Cu_{25.5}Si_{17}$ (open triangles), this is an indication of crystallization during the heat treatment at this point (as shown in Figure 4.60 (b)). This alloy has a lower T_g of 377 K (104 °C) and therefore faster bulk kinetics than $Au_{49}Ag_{5.5}Pd_{2.3}Cu_{26.9}Si_{16.3}$ could be expected. Despite this expectation, its parabolic tarnishing behavior (before it crystallizes) is slower than the parabolic tarnishing rate of $Au_{49}Ag_{5.5}Pd_{2.3}Cu_{26.9}Si_{16.3}$ [4].

The aluminum-containing alloy $Au_{49}Ag_{5.5}Pd_{2.3}Cu_{25.9}Si_{16.3}Al_1$ (stars) follows a cubic rate law which could be attributed to a mixture between logarithmic and parabolic behavior. It is very stable and it is still x-ray amorphous after almost a year at 348 K (Figure 4.60 (b)) [4].

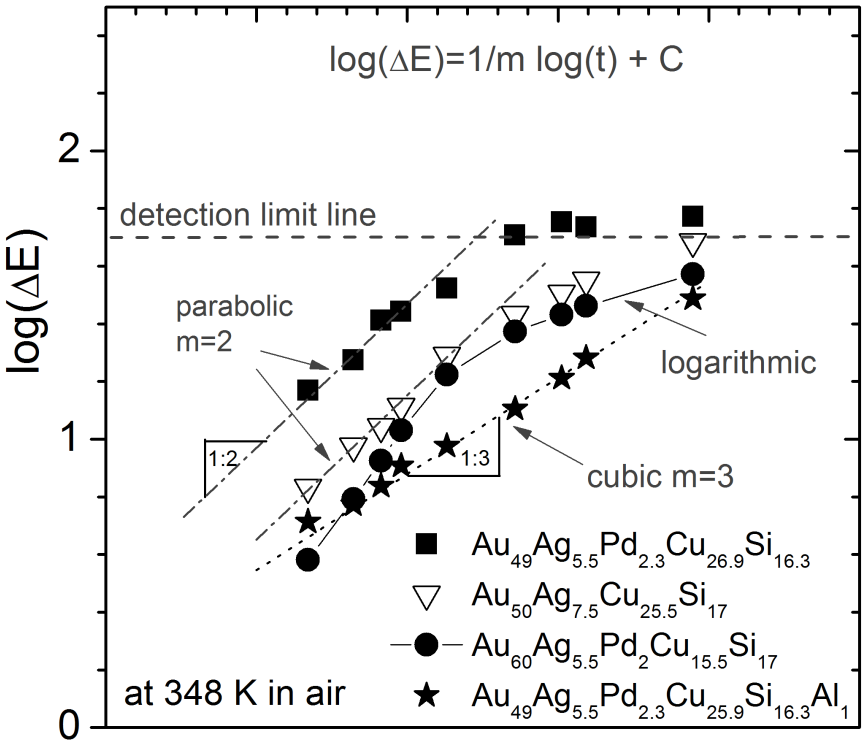

Figure 5.7: Double logarithmic plot for the ΔE development at 348 K in air for different alloy compositions; published in an earlier version in [4].

5.2.7 The Role of Palladium and Silver

The palladium-free $Au_{50}Ag_{7.5}Cu_{25.5}Si_{17}$ has Cu/Si and Au/Si atomic ratios very similar to those of the $Au_{49}Ag_{5.5}Pd_{2.3}Cu_{26.9}Si_{16.3}$. The removal of palladium increases the silver content. This palladium-free BMG has a lower T_g and therefore faster bulk kinetics in the glassy matrix could be expected. Still, the tarnishing rate is half the rate of $Au_{49}Ag_{5.5}Pd_{2.3}Cu_{26.9}Si_{16.3}$ even before the $Au_{50}Ag_{7.5}Cu_{25.5}Si_{17}$ crystallizes (see Figure 4.60 (a) and Figure 4.62). Crystalline Au-Cu-Ag alloys show the opposite trend. For example, Suoninen et al. [142] showed experimental evidence that small additions of palladium to dental crystalline Au-Ag-Cu alloys played an important role in essentially reducing the thickness of the sulfide scale on surfaces of samples treated in aqueous Na_2S solutions. The palladium did not enrich in the sulfide phase, in contrast to silver, but was found enriched below the sulfide scale [4].

The mechanism for the impeding tarnishing effects was assumed to be a decrease in diffusion of silver from the bulk alloy to the surface due to the palladium enrichment layer. Similarly Lang et al. found that when palladium is added to dental Au-Ag-Cu, a drastic reduction in the degree of tarnishing is observed [143]. There, an atomic ratio of Pd/Au

of 1/12 (which is the ratio in $Au_{49}Ag_{5.5}Pd_{2.3}Cu_{26.9}Si_{16.3}$) is usually enough to cause the largest reduction of the degree of tarnishing, and Hattori et al. [144] observed a tarnishing-inhibiting effect by the addition of palladium to low gold content (about 20 mass %) alloys. They also observed a detrimental impact of silver additions on the tarnishing resistance, as silver has a low sulfidation resitance [4].

The opposite trend for palladium addition is observed in the present work and could indicate that the tarnishing mechanism in the case of bulk metallic glass alloys is surface controlled, rather than bulk-diffusion-controlled as is the case for crystalline alloys [4].

5.2.8 The Role of Aluminum

The addition of 1 at.% aluminum and thereby reduction of the copper content by 1 at.% to $Au_{49}Ag_{5.5}Pd_{2.3}Cu_{26.9}Si_{16.3}$ seems to be able to drastically reduce (by 2/3) the tarnishing rate when the alloy is exposed to air at elevated temperatures and therefore dry conditions in the laboratory furnace (see Figure 4.60 (a)) and to follow a slower cubic law in comparison to the mother alloy as is indicated in the double logarithmic plot of Figure 5.7. It is interesting to note that aluminum in as-cast Zr-Ni-Cu-Al-Nb based BMG has been detected in its oxidized state, even in the bulk amorphous matrix by XPS analyzes [108]. The other elements were found in bulk in their metallic state. Therefore, it cannot be argued that the much higher affinity to oxygen of aluminum can compete with silicon to form a passivating oxide on the as-polished surfaces, since the aluminum is probably already in its oxidized state after casting. The role of aluminum in the apparent slower tarnishing rate is, therefore, not yet fully understood [4].

The alloy with 1 at.% aluminum did not show any improvement with respect to the mother alloy in terms of color change reduction during the sulfide test (Figure 4.62) when Cu_2S products are involved. This could also be an effect caused by dealloying and the occurrence of loss of some corrosion products to the liquid test solution [4].

5.2.9 The Role of the Glassy Matrix versus Crystalline State

The most important finding of the present work is the observation that the large amount of copper (up to $\approx$ 27 at.%) and silicon ($\approx$ 16 at.%) alloyed to gold to form a glassy structure is the major contributing factor to the fast tarnishing kinetics observed at low temperatures on the studied Au-Ag-(Pd)-Cu-Si BMGs [4].

In the glassy structure, despite of short- or medium-range ordering phenomena, atomic positions are random. The lack of grain boundaries and the chemical homogeneity are often held responsible for an expected better corrosion and oxidation resistance of the glassy structure with respect to crystalline alloys. However, it has been shown that amorphous alloys can have worse oxidation resistance than their crystalline counterparts [145]. In crystalline alloys, grain boundaries, interphase boundaries, and other defects such as dislocations are known to act as fast diffusion paths and as reactive heterogeneous sites on the surface. The assumption that the lack of these defects alone would slow down diffusion and consequently oxidation or corrosion processes is an oversimplification. It is based on

the assumption that diffusion in metallic glasses is comparable in nature and kinetics to volume diffusion in crystals. However, diffusion in metallic glasses is sharply different from vacancy-mediated diffusion in most crystalline metals. During the diffusion process, a certain amount of frozen-in 'free volume', or 'quasivacancies' according to Faupel in reference [146], serve as diffusion vehicles until they have healed during an annealing process. The diffusion process, in the order of one atomic displacement, involves thermally activated, highly collective atomic motions of 10 to 20 atoms in a chainlike manner [146] [4].

To complete the picture, the interatomic interactions between the constituents have to be taken into consideration. In the metal-metalloid glass system Au-Ag-(Pd)-Cu-Si-(Me), the interactions between the metallic elements and the metalloid (silicon) are weaker than the (already weak) metal-metalloid interactions in the crystal. In general, the interatomic energy potential in the glass is much shallower in shape than in the crystal state, and therefore the bond strength is weaker in the glass than in the crystalline structure. This is also reflected in the smaller elastic modulus of the glass compared to the crystalline counterparts. It implies a certain facility of the metastable glassy matrix to local atomic rearrangements, which can lead to easy partitioning and dealloying processes. At the studied concentrations, i.e. close to the Au-Si eutectic concentration, a homogeneous single phase crystal structure cannot thermodynamically exist in equilibrium. Due to its extremely low solubility in gold, the silicon would precipitate out at this overall concentration, since intermetallic compounds do not thermodynamically exist in the Au-Si system. In the solidification process, the random atomic structure of the liquid is frozen during the glass formation and a metastable homogenous phase is formed. In contrast, the crystalline counterpart is not homogeneous. In fact, the equilibrium crystalline state at the nominal composition of the alloy is a multiphase structure made of pure silicon, gold-rich solid solution and other intermetallic phases of three constituents rich in gold, in palladium, and in the less noble copper. [57]. This crystalline mixture is therefore already decomposed and cannot be compared to the homogeneous glassy matrix in terms of diffusivity and surface reactivity [4].

According to the artificial saliva test, the crystalline silver-based alloys show an extraordinarily poor performance. The fast and distinct tarnishing of silver artifacts is based on the formation of dark Ag_2S on the surface of silver alloys [147]. Despite its poor tarnishing resistance, silver is still very common as a low-priced jewelry alloy, because the tarnishing layer wears off during continuous usage, revealing the white native color of the metal. The yellow tarnishing layer on gold-based BMG, on the other hand, does not wear off as was shown in a 52 days wearing test (Figure 1.1).

The YI plot in Figure 4.64 shows a more prominent discoloring for the nano-crystalline sample (sample 38) than for the furnace-cooled sample (sample 37). In contrast to this finding, the investigation of the microstructure revealed that the corrosion attack on the nano-crystalline sample is much less pronounced than for the furnace-cooled sample. The very large crystals in the furnace-cooled sample result in a much more heterogeneous discoloring for sample 37 in comparison to the homogeneous appearance of sample 38. The large bright gold-rich crystals in sample 37 seem to compromise the YI analysis and lead to an underestimation of the tarnishing in the color analysis.

Corrosion attack on crystalline material is highly selective in $Au_{49}Ag_{5.5}Pd_{2.3}Cu_{26.9}Si_{16.3}$. The less noble crystals experience a much more significant corrosion than the more noble crystals. This is a common observation in crystalline materials and has lead to the assumption that the amorphous counterpart of a certain alloy composition is generally less susceptible to corrosion than the crystalline version. This has been attributed to the homogeneity of the amorphous phase, the lack of grain boundaries, dislocations and other defects that can trigger a corrosion attack, and to the formation of a more homogeneous passivation film on the BMG surface [16]. In fact, the first two effects could clearly be observed for the corrosion attack on samples 37 and 38. More noble and less noble crystals in close contact create a local cell that accelerates the corrosion of the less noble crystal. This is even more pronounced at grain boundaries or similar surface irregularities [148].

Still, the overall corrosion performance of the crystalline sample material is significantly better than that of the amorphous samples. This is also supported by the findings of the artificial saliva test, where only a quarter of the amount of copper that was dissolved into the test solution from amorphous samples was detected for the crystalline samples of the same alloy composition. The detrimental influence of inhomogeneity and surface defects is somehow outweighed by the amorphous structure. The corrosion mechanism of $Au_{49}Ag_{5.5}Pd_{2.3}Cu_{26.9}Si_{16.3}$ is driven by the out-diffusion of copper and gold and the diffusion of oxygen into the bulk material where SiO_2 is formed and, as stated before, the diffusion of the elements participating in the tarnishing process is much easier in the amorphous state than in the crystalline state.

Thus, the tarnishing process observed in crystalline state is kinetically slowed down in comparison to the amorphous state. This appears to be in contradiction with the findings of Rizzi et al. [87] who observed a slightly better corrosion behavior for the amorphous sample material than for the crystalline samples of the composition $Au_{49}Ag_{5.5}Pd_{2.3}Cu_{26.9}Si_{16.3}$. The corrosion behavior was characterized by an immersion test in artificial sweat (see also Section 2.7). The different results of the study of Rizzi et al. and the findings of the present work can be explained by the nature of the sample material. While in the work presented by Rizzi et al. the crystalline samples were cut from a larger lump and subsequently polished, the amorphous sample material was taken from melt-spun ribbons without a polishing or etching treatment. The silica on the air side surface probably prohibited the out-diffusion of copper into the test solution, leading to a better tarnishing behavior for the amorphous ribbons in comparison to the polished crystalline sample material.

Though the findings of the present work show a significantly better corrosion resistance of the crystalline counterparts to the respective amorphous BMG samples, the crystalline condition is not suitable for application since the crystalline counterparts of the gold-based BMG are mechanically unstable and susceptible to brittle failure. The nano-crystalline condition is thermodynamically unstable and is susceptible to grain growth under the influence of time and temperature.

The detrimental combination of silicon and copper in the nominal composition of $Au_{49}Ag_{5.5}Pd_{2.3}Cu_{26.9}Si_{16.3}$ is not found in conventional gold-based jewelry alloys. The typical jewelry alloys presented in Section 4.5 have no silicon as a constituent element; hence, the oxidation of silicon and the interaction with elemental copper, which is the driving force

behind the tarnishing mechanism in the Au-Cu-(Pd)-Ag-Si system, does not take place. This results in drastically higher tarnish resistance for the conventional crystalline jewelry alloys presented in the present work.

6 Conclusions

Parts of the conclusions that are presented here have been published in an earlier version by the author of the present work and co-workers [4, 3].

The processing of Au-based amorphous metals gains increasing interest in jewelry industry. The high hardness and the as-cast premium white gold color are attractive properties for decorative applications. The thermoplastic formability is considered a potential low-cost processing alternative to casting. The present work has found the Au-based alloys and especially the alloy $Au_{49}Ag_{5.5}Pd_{2.3}Cu_{26.9}Si_{16.3}$ to be easily processed and insensitive to non- and low-protective atmospheres during granulation, casting, and thermoplastic forming. Apart from the detrimental tarnishing behavior, the investigated alloys are suitable for the casting of amorphous jewelry items. The central conclusions derived from the present work are:

- Granules as a semi-finished product can be easily portioned and used as feedstock for casting and thermoplastic forming. For the latter processing routine, it might be advantageous to remove the superficial SiO_2, for example by employing an HF-etching, prior to the thermoplastic forming process.

- $Au_{49}Ag_{5.5}Pd_{2.3}Cu_{26.9}Si_{16.3}$ can be cast in at least 12 consecutive casting steps without the necessity for an intermediate recycling step. Thus, a manufacturer can use the same material multiple times.

- Despite the fast cooling mandatory for the production of amorphous products, a very good form filling can be achieved using centrifugal casting. Due to the high strain rates during solidification when centrifugal casting is applied, shear thinning may cause a premature crystallization. The actual strain rate depends on the geometry of the cast product, hence the possibility of premature crystallization has to be checked for each new design in cast trials or in a casting simulation.

- The combination of electroforming on wax models, centrifugal casting, and subsequent removal of the copper mold allows the casting of jewelry items very similar to classic investment casting. The wax models can be used in either process, hence the design of the wax part does not have to be varied in order to cast amorphous parts. The copper mold thickness can be estimated by employing equation 4.4. This casting procedure is a new invention by the author of the present work and co-workers, and a patent was filed under no. DE 10 2013 009 975.7 A1 and WO2014198380A1 [5].

The main obstacle on the way to a successful application of this alloy class is the fast tarnishing of unprotected metal surfaces. Hence the central objective of the present work

was to find the underlying mechanism that causes this unexpected fast tarnishing. The following conclusions can be derived from the results of the present work:

- As shown in the schematics of figure 5.3, a native SiO_2 layer has been detected on as-cast surfaces that solidified in contact to air, like at air-pockets, or surfaces of granules. This layer seems to be so dense that it acts as a diffusion barrier limiting the supply of oxygen; in general those surfaces experience minimal tarnishing [4].

- When the native silica coating-like layer is removed or damaged, the thin amorphous silica layer that forms on the surface of the bulk metallic glass at temperatures below T_g does not act as a diffusion barrier or coating like the native SiO_2 layer that forms during solidification at high temperatures [4].

- Gold and copper are released in the matrix as elements during the silicon oxidation and diffuse out to the surface through the thin SiO_2 surface layer. The color change at the beginning of exposure towards yellow and red, respectively, can probably be attributed to these gold and copper particles. At longer times of exposure, copper-rich corrosion scales have been experimentally observed [4].

- When the surface of a sample has been polished prior to exposure, the glassy matrix underneath the copper-rich scale appears destabilized and triggers the internal nucleation of amorphous SiO_2 structures that grow inwards in a dense branching morphology. This internal oxidation, which occurs at low temperatures (RT to 348 K) at low partial pressure of oxygen, is linked to the partitioning of the other elements in the surrounding matrix, and, therefore, enhances the out-diffusion of gold and copper. Gold forms nano-crystalline particles and may be left behind on the surface during dealloying in wet environments [78]. Copper can react on the surface and form scales or even cone-shaped products of Cu_2O and Cu_2S, depending on the exposure [4].

- The removal of the palladium from the alloy and the increase of silver content in the glass seem to impede the tarnishing, in contrast to known crystalline alloys. The microaddition of aluminum slows the tarnishing of the glassy alloy down when the product is in contact to air. The addition of aluminum does not help when the product is kept in wet conditions, especially because the passivating products may be etched away or dissolved in a liquid environment [4].

- Engineering the Cu/Si ratio resulted in first positive developments in the tarnishing rates and is therefore considered as one of the main factors contributing to a suppression of the tarnishing behavior[3].

- The exceptionally low T_g of Au-based amorphous alloys results in relatively fast room temperature kinetics. The effect of these fast kinetics becomes obvious when sample material is stored at 255 K. In this case the tarnishing rate is slowed down significantly. Developing an alloy with a T_g at least 50 K higher than that of $Au_{49}Ag_{5.5}Pd_{2.3}$

$Cu_{26.9}Si_{16.3}$ can probably slow the room temperature tarnishing down to rates similar to those experienced with the samples stored in a freezer. This means a T_g of 451 K (178 °C) or higher would be desirable.

The next logic step is to use these findings for the development of a tarnish-resistant gold-based amorphous metal alloy. First steps have been carried out during the duration of the present work, but there is still a lot work on alloy development to be done. Possible next steps towards suppressing the tarnishing process are therefore addressed in the next chapter "Future Work".

7 Future Work

The alloy development in new alloy systems introducing further alloying elements as a possible substitution for copper with the scope to improve the tarnishing behavior did not result in the discovery of new bulk-metallic-glass-forming compositions yet. This does not mean that there are no bulk-metallic-glass-forming compositions or composition ranges in those systems. In 3 to 6 component systems, there are too many possible alloy compositions to investigate them in a study like this. Ding et al. estimate that for ternary systems ca. 600, for quaternary systems ca. 2000 and for quinary systems ca. 6000 individual alloys can be considered possible glass formers [149]. Considering the huge impact even small deviations of the composition can have on the glass-forming ability, a thorough systematic study has to be carried out testing compositions in concentration ranges with small intermediate steps. Additionally, the samples that were cast in the Au-Ga-Si and Au-Sb-Si system so far had a thickness of 1 mm. Glass formers with d_c lower than 1 mm remain undetected by this approach.

Alloy improvement studies in the Au-Cu-(Pd)-Ag-Si-(X) system showed that engineering the Cu/Si ratio can significantly slow down the rate at which gold-based amorphous alloys tarnish. Understanding the interaction between copper and silicon built during the duration of this study is the key to future alloy development towards tarnish-free gold-based bulk metallic glasses.

The next steps towards the development of a tarnish-resistant gold-based alloy are:

- Increasing of T_g to slow down room temperature kinetics, if possible by 50 K or more
- Engineering of the Cu/Si ratio. The lower the ratio, the lower the tarnishing rate is expected to be
- Partial or total substitution of copper by a sixth element or more elements
- Systematic investigation of alternative alloy systems with reduced content of copper and/or silicon to find new amorphous solidifying compositions

A restriction for the development of gold-based BMG is the necessity to limit the gold content to specific caratages as in Table 2.3. The 9k compositions are usually found in the lower price range products due to their low precious metal content. The introduction of amorphous metals is expected to take place in a rather high-price market due to their novelty and expected higher processing costs in the first years after introduction. The 22k alternative is probably too limiting for an alloy development, as only 8.4 mass % of

alloying elements can be added. This leaves 18k and 14k as target compositions for the alloy development for jewelry.

The native SiO_2 surface layer was observed to grant good protection from tarnishing effects. Over a total time span of 3 years, several sample surface areas covered by the native oxide layer did not show any signs of tarnishing. Unfortunately, a native oxide layer was only found on surfaces that solidified freely in contact to at least some amount of oxygen. Sample surfaces in contact to the copper mold during solidification lacked a protective native oxide layer. Thus, the native silica formation alone is not a sufficient tarnish protection. Subsequent machining, grinding, and polishing would compromise this layer anyway.

Future work will aim at introducing a transparent protective surface layer on final decorative products. This means that the protective surface layer is applied on final products after solidification and subsequent finishing procedures, e.g. cutting, grinding, or polishing. Installing a protective transparent surface layer at this stage (in the solid state) requires a coating procedure, because the formation of protective native SiO_2 is probably restricted to the solidification procedure. A dense SiO_2 protective coating is only formed at high temperatures from the silicon-enriched surface region in the melt. Low temperature silicon oxidation was found to form SiO_2 in branching morphology growing into the matrix in contrast to the formation of a dense surface layer.

A coating procedure that is capable of introducing a transparent protective layer onto the pristine metal surface after finishing should be able to prevent tarnishing of the gold-based BMGs. This is already a state-of-the-art procedure to prohibit the tarnishing of valuable silver artifacts [147, 150, 151, 113], yet it is usually only applied for artifacts on display that are not in use. Since jewelry in use is subjected to wear, transparent coatings are usually destroyed by abrasion, since they are supposed to be very thin to prohibit interference and similar effects that adulterate the native color of the artifact. Once the protective transparent coating is compromised, for example scratched or worn off, localized tarnishing can take place, which is even more obvious on the background of the still protected native white silver surroundings. Based on the findings for protective coatings on silver artifacts and the results of the present work on gold BMG, protective transparent coatings to prohibit tarnishing are very promising. The wear behavior has to be analyzed, since abrasion of the respective coating leads to very obvious localized discoloring as observed on scratched pore surfaces in the artificial sweat test (Figure 4.52).

An alternative to transparent coatings could be the application of a decorative metallic coating. It is in fact very common to apply a rhodium coating on white gold jewelry, since even the "whitest" gold alloys still have a distinctly higher YI than pure rhodium, which is 6.8 [97]. In this case, the native surface of the BMG would be covered, leaving the high as-cast strength and resilience along with the thermoplastic formability as an advantage in comparison to conventional jewelry alloys. Still, even thick metallic coatings can be worn off, leaving the unprotected BMG surface to tarnish. As protective coatings, transparent as well as non-transparent, are prone to abrasion-related defects, coatings as prohibitors of tarnishing are seen as less advantageous as soon as the respective item is in active usage. The development of a tarnish-resistant alloy is therefore preferable.

Nomenclature

List of Abbreviations

at.%	Atom percent
BMG	Bulk metallic glass
BN	Boron nitride
BSD	Backscattered electron detector
BSE	Backscattered electron
CAD	Computer-aided design
CCT	Continous-cooling-transformation
DBM	Dense Branching Morphology
EBID	Electron-beam-induced depositon
EBSD	Electron backscatter diffraction
EDX	Energy-dispersive X-ray micro-analysis
EDXRF	Energy-dispersive X-ray fluorescence
EsB	Energy-selective backscatter
FEPA	Federation of European producers of abrasives
FIB	Focused ion beam
GDOES	Glow discharge optical emission spectroscopy
GFA	Glass-forming ability
GMO	General moving objects
HCl	Hydrocloric acid

HF	Hydrofluoric acid
HV	Vickers hardness
IBID	Ion beam induced deposition
ICP-OES	Inductively coupled plasma optical emission spectroscopy
k	Karat (en)
kt	Karat (de)
MEMS	Micro-electro-mechanical systems
NEMS	Nano-electro-mechanical systems
PE	Primary electron
PM	Precious metal
RE	Rückstreuelektronendetektor
RES	Rapid etching system
rpm	Rounds per minute
SDD	Silicon drift detector
SE	Secondary electron
SEM	Scanning electron microscopy
STEM	Scanning transmission electron microscopy
TC	Thermocouple
TEM	Transmission electron microscopy
TPF	Thermoplastic forming
TTT	Time-temperature-transition
wt.%	Weight percent
XPS	X-ray photoelectron spectroscopy
XRD	X-ray diffraction
YI	Yellowness Index
Z	Atomic number

List of Symbols

ΔE	Color change	
ΔH_f	Enthalpy of fusion	J
ΔQ	Heat change	J
ΔQ_{Cu}	Heat change in the copper mold	J
ΔQ_{melt}	Heat change in the melt	J
ΔS_f	Entropy of fusion	$\frac{J}{K}$
ΔT	T_x-T_g	K
ϵ_{el}	Elastic strain	%
η	Viscosity	$\frac{N}{m^2}s$
ν	Poissons's ratio	
σ	Stress	$\frac{N}{mm^2}$
$\widetilde{k_p}$	$\frac{1}{2}k_p$	
c	Heat capacity	$\frac{J}{K}$
c_p	Specific heat capacity at constant pressure	$\frac{J}{kg \cdot K}$
D	Diffusion coefficient	$\frac{cm^2}{s}$
d_c	Critical casting thickness	mm
d_{cast}	Thickness of the casting	mm
E	Young's modulus	$\frac{N}{mm^2}$
E_{el}	Elastic energy	$\frac{N}{mm^2}$
G	Gibbs free energy	J
$G_{crystal}$	Gibbs free energy of a crystal	J
G_{glass}	Gibbs free energy of a BMG	J
H	Enthalpy	J
k_0	Pre-exponential factor	$\frac{YI}{s}$

k_{lin}	Rate of YI development per second	$\frac{YI}{s}$
L	Length	m
m	Mass	kg
m_k	Slope	K
m_{Cu}	Copper mass	kg
m_{melt}	Mass of the melt	kg
P	Pressure	$\frac{N}{m^2}$
Q	Activation energy	$\frac{J}{mol}$
Q	Activation energy	eV or $\frac{kgm^2}{s^2}$
R	Universal gas constant	$8.314\frac{J}{mol*K}$
R_c	Critical cooling rate	$\frac{K}{s}$
R_m	Yield strength	$\frac{N}{m^2}$
R_{cool}	Cooling rate	$\frac{K}{s}$
RT	Room temperature	K
S	Entropy	$\frac{J}{K}$
T	Temperature	K
t	Time	s
T_l	Liquidus temperature	K
T_M	Melting temperature	K
T_x	Crystallization temperature	K
T_{cast}	Casting temperature	K
T_{end}	Equilibrium temperature	K
T_g	Glass transition temperature	K
$t_{x,onset}$	Time till onset of crystallization	s
v	Velocity	$\frac{m}{s}$
k_l	Linear rate constant	

k_p	Parabolic rate constant
k_{log}	Logarithmic rate constant
Y	Corrosion parameter

Bibliography

[1] J. Schroers, B. Lohwongwatana, W. L. Johnson, and A. Peker. Gold based bulk metallic glass. *Applied Physics Letters*, 87(6):061912–1 – 061912–3, 2005.

[2] Jan Schroers, Boonrat Lohwongwatana, William L. Johnson, and Atakan Peker. Precious bulk metallic glasses for jewelry applications. *Materials Science and Engineering: A*, 449-451:235 – 238, 2007. Proceedings of the 12th International Conference on Rapidly Quenched & Metastable Materials.

[3] Miriam Eisenbart, Ulrich E. Klotz, Ralf Busch, and Isabella Gallino. On the abnormal room temperature tarnishing of an 18 karat gold bulk metallic glass alloy. *Journal of Alloys and Compounds*, 615, Supplement 1(0):S118 – S122, 2014.

[4] M. Eisenbart, U. E. Klotz, R. Busch, and I. Gallino. A colourimetric study of the tarnishing of gold-based bulk metallic glasses. *Corrosion Science*, 85:258 – 269, 2014.

[5] M. Eisenbart, U.E. Klotz, A. Pfund, and A. Zielonka. Verfahren zum Giessen eines Gegenstands aus metallischem Glas, December 18 2014. WO Patent App. PCT/EP2014/001,418.

[6] W. Zhang, H. Guo, M.W. Chen, Y. Saotome, C.L. Qin, and A. Inoue. New Au-based bulk glassy alloys with ultralow glass transition temperature. *Scripta Materialial*, 61(7):744 – 747, 2009.

[7] G. Fiore and L. Battezzati. Developing Au-based amorphous alloys. *Reviews on Advanced Materials Science*, 18(2):190 – 192, 2008.

[8] Shuo-Hong Wang and Tsung-Shune Chin. Tin-modified gold-based bulk metallic glasses. *Gold Bulletin*, 45:3 – 8, 2012.

[9] Boonrat Lohwongwatana. Liquidmetal - hard 18k and .850 pt alloys that can be processed like plastics or blown like glass. In Eddie Bell, editor, *Proceedings of the twenty-first Santa Fe Symposium in Albuquerque, New Mexico*, pages 289 – 303, 2007.

[10] J. Schroers. Processing of bulk metallic glass. *Advanced Materials*, 22:1566 – 1597, 2010.

[11] S. Mozgovoy, J. Heinrich, U.E. Klotz, and R. Busch. Investigation of mechanical, corrosion and optical properties of an 18 carat Au-Cu-Si-Ag-Pd bulk metallic glass. *Intermetallics*, 18(12):2289 – 2291, 2010.

[12] Christopher W. Corti. What is a white gold? Progress on the issues. In *The Santa Fe Symposium*, pages 103 – 120, 2005.

[13] M. Eisenbart U. E. Klotz. Gold-based bulk metallic glasses: Hard like steel, moldable like plastics. In *Proceedings of the Jewelry Technology Forum*, 2014.

[14] M. Eisenbart U. E. Klotz. Gold-based bulk metallic glasses: Hard like steel, moldable like plastics. In *Proceedings of the Twenty-Seventh Santa Fe Symposium in Albuquerque, New Mexico*, pages 221 – 236, 2013.

[15] U. E. Klotz M. Eisenbart. Herstellungs- und Anwendungsmöglichkeiten massiver metallischer Gläser auf Edelmetallbasis. In *Pforzheimer Werkstofftag*, pages 101 – 115, 2013.

[16] C. Suryanarayana and A. Inoue. *Bulk Metallic Glasses*. CRC Press, 2011.

[17] H. Beck, J.L. Cote, P. Duwez, T. Egami, H.-J. Güntherodt, J. Hafner, U. Herold, W.L-Johnson, U. Köster, A.P. Malozemoff, L. Meisel, and J. Wong. *Glassy Metals I - Iconic Structure, Eletronic Transport, and Crystallization*. Springer-Verlag, 1981.

[18] Mingwei Chen. A brief overview of bulk metallic glasses. *NPG Asia Mater*, 3:82 – 90, 2011.

[19] Jun. W. Klement, R. H. Willens, and P. Duwez. Non-crystalline structure in solidified gold-silicon alloys. *nature*, 187:869 – 870, 1960.

[20] M.F. Ashby and A.L. Greer. Metallic glasses as structural materials. *Scripta Materialia*, 54(3):321 – 326, 2006. Viewpoint set no: 37. On mechanical behavior of metallic glasses.

[21] Nobuyuki Nishiyama, Kana Takenaka, Haruko Miura, Noriko Saidoh, Yuqiao Zeng, and Akihisa Inoue. The world's biggest glassy alloy ever made. *Intermetallics*, 30(0):19 – 24, 2012. Bulk Metallic Glasse VIII.

[22] A. Lindsay Greer. Metallic glasses... on the threshold. *Materials Today*, 12(1-2):14 – 22, 2009.

[23] A. R. Yavari, J. J. Lewandowski, and J. Eckert. Mechanical properties of bulk metallic glasses. *MRS Bulletin*, 32(8):635 – 638, 2007.

[24] Z. Evenson, S. E. Naleway, S. Wei, O. Gross, J. J. Kruzic, I. Gallino, W. Possart, M. Stommel, and R. Busch. β relaxation and low-temperature aging in a Au-based bulk metallic glass: From elastic properties to atomic-scale structure. *Physical Review B*, 89:174204, 2014.

[25] Jan Schroers, Tranquoc Nguyen, Sean O'Keeffe, and Amish Desai. Thermoplastic forming of bulk metallic glass–applications for MEMS and microstructure fabrication. *Materials Science and Engineering: A*, 449-451:898 – 902, 2007. Proceedings of the 12th International Conference on Rapidly Quenched & Metastable Materials.

[26] A. Inoue, X.M. Wang, and W. Zhang. Developments and applications of bulk metallic glasses. *Reviews on Advanced Materials Science*, 18(1):1 – 9, 2008.

[27] P. Sharma, N. Kaushik, H. Kimura, Y. Saotome, and A. Inoue. Nano-fabrication with metallic glass - an exotic material for nano-electromechanical systems. *Nanotechnology*, 18(3), 2007.

[28] Yasunori Saotome, Kenichi Imai, Shigeo Shioda, Susumu Shimizu, Tao Zhang, and Akihisa Inoue. The micro-nanoformability of Pt-based metallic glass and the nanoforming of three-dimensional structures. *Intermetallics*, 10(11-12):1241 – 1247, 2002.

[29] Y. Saotome, Y. Fukuda, I. Yamaguchi, and A. Inoue. Superplastic nanoforming of optical components of Pt-based metallic glass. *Journal of Alloys and Compounds*, 434-435:97 – 101, 2007. Proceedings of the 12th International Symposium on Metastable and Nano-Materials (ISMANAM-2005).

[30] Mark Telford. The case for bulk metallic glass. *Materials Today*, 7(3):36 – 43, 2004.

[31] Jan Schroers and William L. Johnson. Ductile bulk metallic glass. *Phys. Rev. Lett.*, 93(25):255506, Dec 2004.

[32] Mingwei Chen, Akihisa Inoue, Wei Zhang, and Toshio Sakurai. Extraordinary plasticity of ductile bulk metallic glasses. *Phys. Rev. Lett.*, 96:245502, Jun 2006.

[33] Maximilien E. Launey and Robert O. Ritchie. On the fracture toughness of advanced materials. *Advanced Materials*, 21(20):2103 – 2110, 2009.

[34] B. Yang, J. Wadsworth, and T.-G. Nieh. Thermal activation in Au-based bulk metallic glass characterized by high-temperature nanoindentation. *Applied Physics Letters*, 90(6):061911–1 – 061911–3, 2007.

[35] M.E. Launey, R. Busch, and J.J. Kruzic. Effects of free volume changes and residual stresses on the fatigue and fracture behavior of a Zr-Ti-Ni-Cu-Be bulk metallic glass. *Acta Materialia*, 56(3):500 – 510, 2008.

[36] Z.F. Zhang, H. Zhang, B. L. Shen, A. Inoue, and J. Eckert. Shear fracture and fragmentation mechanisms of bulk metallic glasses. *Philosophical Magazine Letters*, 86(10):643 – 650, 2006.

[37] Bing Yang, Laura Riester, and T.G. Nieh. Strain hardening and recovery in a bulk metallic glass under nanoindentation. *Scripta Materialia*, 54(7):1277 – 1280, 2006.

[38] Prashant Wadhwa, Jochen Heinrich, and Ralf Busch. Processing of copper fiber-reinforced $Zr_{41.2}Ti_{13.8}Cu_{12.5}Ni_{10.0}Be_{22.5}$ bulk metallic glass composites. *Scripta Materialia*, 56(1):73 – 76, 2007.

[39] M. Heilmaier and J. Eckert. The synthesis and properties of Zr-based metallic glasses and glass-matrix composites. *JOM Journal of the Minerals, Metals and Materials Society*, 52:43 – 47, 2000.

[40] C. Douglas, Hofmann, Jin-Yoo Suh, Aaron Wiest, Gang Duan, Mary-Laura Lind, Marios D. Demetriou, and William L. Johnson. Designing metallic glass matrix composites with high toughness and tensile ductility. *nature*, 451:1085 – 1090, 2008.

[41] S.V. Madge, D.V. Louzguine-Luzgin, J.J. Lewandowski, and A.L. Greer. Toughness, extrinsic effects and poisson's ratio of bulk metallic glasses. *Acta Materialia*, 60(12):4800 – 4809, 2012.

[42] J.J. Lewandowski, M. Shazly, and A. Shamimi Nouri. Intrinsic and extrinsic toughening of metallic glasses. *Scripta Materialia*, 54(3):337 – 341, 2006.

[43] Marios D. Demetriou, Maximilien E. Launey, Glenn Garrett, Joseph P. Schramm, Douglas C. Hofmann, William L. Johnson, and Robert O. Ritchie. A damage-tolerant glass. *Nature Materials*, 10:123 – 128, 2011.

[44] A. Lindsay Greer. Damage tolerance at a price. *Nature Materials*, 10:88 – 89, February 2011.

[45] R. Busch, E. Bakke, and W. L. Johnson. Viscosity of the supercooled liquid and relaxation at the glass transition of the $Zr_{46.75}Ti_{8.25}Cu_{7.5}Ni_{10}Be_{27.5}$ bulk metallic glass forming alloy. *Acta Materialia*, 46(13):4725 – 4732, 1998.

[46] Livio Battezzati, Alberto Castellero, and Paola. On the glass transition in metallic melts. *Journal of Non-Crystalline Solids*, 353(32-40):3318 – 3326, 2007. Liquid and Amorphous Metals XII - Proceedings of the 12th International Conference on Liquid and Amorphous Metals.

[47] Jan Schroers. On the formability of bulk metallic glass in its supercooled liquid state. *Acta Materialia*, 56(3):471 – 478, 2008.

[48] Jan Schroers. The superplastic forming of bulk metallic glasses. *JOM Journal of the Minerals, Metals and Materials Society*, 57:35 – 39, 2005.

[49] Jan Schroers and William L. Johnson. Highly processable bulk metallic glass-forming alloys in the Pt-Co-Ni-Cu-P system. *Applied Physics Letters*, 84:3666 – 3668, 2004.

[50] Douglas Hofmann, Henry Kozachkov, Hesham Khalifa, Joseph Schramm, Marios Demetriou, Kenneth Vecchio, and William Johnson. Semi-solid induction forging of metallic glass matrix composites. *JOM Journal of the Minerals, Metals and Materials Society*, 61:11 – 17, 2009.

[51] Wen Chen, Ze Liu, and Jan Schroers. Joining of bulk metallic glasses in air. *Acta Materialia*, 62(0):49 – 57, 2014.

[52] Robert Martinez, Golden Kumar, and Jan Schroers. Hot rolling of bulk metallic glass in its supercooled liquid region. *Scripta Materialia*, 59(2):187 – 190, 2008.

[53] Jan Schroers, Quoc Pham, Atakan Peker, Neil Paton, and Richard V. Curtis. Blow molding of bulk metallic glass. *Scripta Materialia*, 57(4):341 – 344, 2007.

[54] Golden Kumar, Amish Desai, and Jan Schroers. Bulk metallic glass: The smaller the better. *Advanced Materials*, 23(4):461 – 476, 2011.

[55] Theodore Waniuk, Jan Schroers, and William L. Johnson. Timescales of crystallization and viscous flow of the bulk glass-forming Zr-Ti-Ni-Cu-Be alloys. *Phys. Rev. B*, 67:184203, May 2003.

[56] C.W. Tang, Y.C. Chang, T.T. Wu, J.C. Huang, and C.T. Pan. Micro-forming of $Au_{49}Ag_{5.5}Pd_{2.3}Cu_{26.9}Si_{16.3}$ metallic glasses in supercooled region. *Advanced Materials Research*, 47-50:266 – 269, 2008.

[57] Gianluca Fiore, Paola Rizzi, and Livio Battezzati. Phase constitution and glass formation in an Au-based alloy. *Journal of Alloys and Compounds*, 509, Supplement 1(0):S166 – S169, 2011. XVII International Symposium on Metastable, Amorphous and Nanostructured Materials.

[58] N. Paton J. Schroers. Amorphous metal alloys form like plastics. *Advanced Materials & Processes*, 61:61 – 63, 2006.

[59] Günter Beck, Hans-Herrmann Beyer, Wolfgang Gerhartz, Jürgen Haußelt, and Ulrike Zimmer. *Edelmetalltaschenbuch*. Degussa Frankfurt am Main, 1967.

[60] David Turnbull. Under what conditions can a glass be formed. *Contemp. Phys.*, 10:473 – 488, 1969.

[61] R. Busch, J. Schroers, and W. H. Wang. Thermodynamics and kinetics of bulk metallic glass. *MRS Bulletin*, 32(8):620 – 623, 2007.

[62] A. Inoue and A. Takeuchi. Recent development and application products of bulk glassy alloys. *Acta Materialia*, 59(6):2243 – 2267, 2011.

[63] Jörg F. Löffler. Bulk metallic glasses. *Intermetallics*, 11(6):529 – 540, 2003.

[64] Y. Li, S. J. Poon, G. J. Shiflet, J. Xu, D. H. Kim, and J. F. Löffler. Formation of bulk metallic glasses and their composites. *MRS Bulletin*, 32(08):624 – 628, 2007.

[65] S. Mukherjee, J. Schroers, Z. Zhou, W. L. Johnson, and W. K. Rhim. Viscosity and specific volume of bulk metallic glass-forming alloys and their correlation with glass forming ability. *Acta Materialia*, 52(12):3689 – 3695, 2004.

[66] D.B. Miracle. The efficient cluster packing model - an atomic structural model for metallic glasses. *Acta Materialia*, 54(16):4317 – 4336, 2006.

[67] Marios D. Demetriou, Michael Floyd, Chase Crewdson, Joseph P. Schramm, Glenn Garrett, and William L. Johnson. Liquid-like platinum-rich glasses. *Scripta Materialia*, 65(9):799 – 802, 2011.

[68] *Measured at fem Research Instiute Precious Metals + Metals Chemistry.*

[69] Mark Grimwade. *Introduction to precious metals - Metallurgy for jewelers and silversmiths.* Brynmorgen Press, 2009.

[70] C.J. Lee, Y.H. Lai, C.W. Tang, J.C. Huang, and J.S.C. Jang. Mechanical behavior of Au-based metallic glass in micro-sacle at ambient and elevated temperatures. *Materials Transactions*, 50(12):2795 – 2800, 2009.

[71] T.W. Tang, Y.C. Chang, J.C. Huang, Q. Gao, J.S.C. Jang, and Chi Y.A. Tsao. On thermomechanical properties of Au-Ag-Pd-Cu-Si bulk metallic glass. *Materials Chemistry and Physics*, 116(2-3):569 – 572, 2009.

[72] G. Raykhtsaum. Age hardenable gold alloys. In *The Santa Fe Symposium on Jewelry Manufacturing Technology, pages 343 ff.*, 2009.

[73] Jingbei Liu, Yanhui Liu, Pan Gong, Yanglin Li, KimberlyM. Moore, Ellen Scanley, Fred Walker, ChristineC. Broadbridge, and Jan Schroers. Combinatorial exploration of color in gold-based alloys. *Gold Bulletin*, pages 1–8, 2015.

[74] C. Corti. The role of hardness in jewelry alloys. In *Proceedings of the Twenty-Seventh Santa Fe Symposium in Albuquerque, New Mexico*, pages 103 – 120, 2008.

[75] J. Schroers and A. Peker. Au-base bulk solidifying amorphous alloys, April 27 2006. WO Patent App. PCT/US2005/038,171.

[76] Lisa-Yvonn Schmitt. Bachelorthesis, Untersuchung der Prozessierbarkeit des metallischen Massivglases $Au_{49}Ag_{5.5}Pd_{2.3}Cu_{26.9}Si_{16.3}$ und dessen strukturelle Relaxation, 2013.

[77] *Technical Chart of the Legor-Group.*

[78] Federico Scaglione, Annett Gebert, and Livio Battezzati. Dealloying of an Au-based amorphous alloy. *Intermetallics*, 18:2338 – 2342, 2010.

[79] Federico Scaglione, Paola Rizzi, and Livio Battezzati. De-alloying kinetics of an Au-based amorphous alloys. *Journal of Alloys and Compounds*, 536, Supplement 1(0):S60 – S64, 2012. Materials, ISMANAM-2011 (26th June to July 1st 2011).

[80] A.S. Khanna. *Logarithmic Rate Equations.* ASM International, 2002.

[81] D.A. Porter, K.E. Easterling, and M. Sherif. *Phase Transformations in Metals and Alloys, Third Edition (Revised Reprint)*. Taylor & Francis, 2009.

[82] E. Ben-Jacob, G. Deutscher, P. Garik, Nigel D. Goldenfeld, and Y. Lareah. Formation of a dense branching morphology in interfacial growth. *Phys. Rev. Lett.*, 57:1903 – 1906, Oct 1986.

[83] Eshel Ben-Jacob and Peter Garik. The formation of patterns in non-equilibrium growth. *Nature*, 343(6258):523 – 530, 1990.

[84] E. Ben-Jacob, P. Garik, and D. Grier. Interfacial pattern formation far from equilibrium. *Superlattices and Microstructures*, 3(6):599 – 615, 1987.

[85] Robert E. Reed-Hill. *Physical Metallurgy Principles*. PWS-KENT Publishing Company, 1994.

[86] S. Kaciulis, A. Mezzi, G. Fiore, I. Ichim, L. Battezzati, and P. Rizzi. XPS study of gold-based metallic glass. *Surface and Interface Analysis*, 42(6-7):597 – 600, 2010.

[87] Paola Rizzi, Ingrid Corazzari, Gianluca Fiore, Ivana Fenoglio, Bice Fubini, Saulius Kaciulis, and Livio Battezzati. Ion release and tarnishing behavior of Au and Pd based amorphous alloys in artificial sweat. *Corrosion Science*, 77(0):135 – 142, 2013.

[88] Oleg G. Shpyrko, Reinhard Streitel, Venkatachalapathy S. K. Balagurusamy, Alexei Y. Grigoriev, Moshe Deutsch, Benjamin M. Ocko, Mati Meron, Binhua Lin, and Peter S. Pershan. Surface crystallization in a liquid AuSi alloy. *Science*, 313(5783):77 – 80, 2006.

[89] S.V. Ketov, N. Chen, A. Caron, A. Inoue, and D.V. Louzguine-Luzgin. Structural features and high quasi-static strain rate sensitivity of $Au_{49}Ag_{5.5}Pd_{2.3}Cu_{26.9}Si_{16.3}$ bulk metallic glass. *Applied Physics Letters*, 101(24):241905, 2012.

[90] J. Jahn. Effektive Fertigungsmöglichkeiten für Kleinteile. *Wirtschaftsjournal*, 10:1, 2008.

[91] J. Jahn. Bemerkenswerte Entwicklungen - Neue Technologien zur schnellen Herstellung von Feingussteilen aus Stahl in kleinen Stückzahlen. *Giesserei-Erfahrungsaustausch*, 10:35 – 38, 2008.

[92] M. Lätchen. Fertigung von Feinguß-Prototypen aus Titan und Aluminium. *Gussprodukte 2000*, pages 245 – 246, 2000.

[93] A. Peker and C.P. Kim. Patent; investment casting of bulk-solidifying amorphous alloys, 2006.

[94] Horst Czichos and Manfred Hennecke, editors. *HÜTTE – Das Ingenieurwissen*. Springer, Berlin, 34 edition, 2012.

[95] Z. Ali-Abassi and N. Kanani. *Kupferschichten: Abscheidung, Eigenschaften, Anwendungen ; mit 73 Tabellen*. Schriftenreihe Galvanotechnik und Oberflächenbehandlung. Leuze, 2000.

[96] Ksenia Sinitsyna. Herstellung von Kupfergussformen durch Galvanoformung für das Giessen von massiven metallischen Gläsern auf Edelmetallbasis. Bachelorthesis, Hochschule für Technik und Wirtschaft Aalen, 2012.

[97] Steven Henderson and Dippal Manchanda. White gold alloys: Colour measurement and grading. *Gold Bulletin*, 38:55 – 67, 2005.

[98] D.P. Agarwal and G. Raykhtsaum. Color technology for jewelry alloy applications. In *Proceedings of the Second Santa Fe Symposium, 1988, Santa Fe, New Mexico*, 1988.

[99] Peter Fritz Schmidt. *Praxis der Rasterelektronenmikroskopie und Mikrobereichsanalyse*. expert-Verlag, 1994.

[100] Jonathan England, Michael W. Phaneuf, Alexandre Laquerre, Andrew Smith, and Russell Gwilliam. Ion beam assisted crystallization of amorphous silicon layers using high current density gallium beams. *Nuclear Instruments and Methods in Physics Research Section B: Beam Interactions with Materials and Atoms*, 272(0):409 – 413, 2012.

[101] Thaddeus B. Massalski, editor. *Binary Alloy Phase Digrams - Volume 2*. William W. Scott, Jr., 1986.

[102] Gonzalo Vazquez, Estrella Alvarez, and Jose M. Navaza. Surface tension of alcohol water + water from 20 to 50 °C. *Journal of Chemical & Engineering Data*, 40(3):611 – 614, 1995.

[103] Private communication with the chair of metallic materials, Saarland University.

[104] Boonrat Lohwongwatana. *Development, characterization, and applications of gold and platinum bulk metallic glasses*. PhD thesis, California Institute of Technology, 2007.

[105] S. Pogatscher, P. J. Uggowitzer, and J. F. Löffler. In-situ probing of metallic glass formation and crystallization upon heating and cooling via fast differential scanning calorimetry. *Applied Physics Letters*, 104(25):251908, 2014.

[106] D. Martin Knotter. Etching mechanism of vitreous silicon dioxide in HF-based solutions. *Journal of the American Chemical Society*, 122(18):4345 – 4351, 2000.

[107] J Heinrich and B. Busch, R.and Nonnenmacher. Processing of a bulk metallic glass forming alloy based on industrial grade Zr. *Intermetallics*, 25:1 – 4, 2012.

[108] Jochen Heinrich, Ralf Busch, Frank Müller, Samuel Grandthyll, and Stefan Hüfner. Role of aluminum as an oxygen-scavenger in zirconium based bulk metallic glasses. *Applied Physics Letters*, 100(7):071909, 2012.

[109] Jochen Heinrich. *Massivglasbildende metallische Legierungen als Konstruktionswerkstoff - Materialoptimierung und Technologieentwicklung zur Herstellung und Verarbeitung.* PhD thesis, Universität des Saarlandes, 2012.

[110] Jan Schroers, private communications.

[111] Boonrat Lohwongwatana, Jan Schroers, and William L. Johnson. Strain rate induced crystallization in bulk metallic glass-forming liquid. *Phys. Rev. Lett.*, 96(7):075503, Feb 2006.

[112] U. E. Klotz and T. Drago. The role of process parameters in platium casting. In *Proceeding of the twenty-fourth Santa Fe Symposium in Albuquerque, New Mexico*, volume 24, pages 287 – 326, 2010.

[113] E. Angelini, S. Grassini, G. M. Ingo, D. Mombello, F. Fracassi, and F Palumbo. Surface analysis of SiO_2-like high-barrier thin films for protection of silver artefacts. *Surface and Interface Analysis*, 42(6-7):666 – 670, 2010.

[114] Michihisa Fukumoto, Chiharu Tachikawame, Yuuki Matsuzaka, and Motoi Hara. Formation of Si diffusion layer on stainless steels and their high temperature corrosion resistance in molten salt. *Corrosion Science*, 56(0):105 – 113, 2012.

[115] Oleg G. Shpyrko, Reinhard Streitel, Venkatachalapathy S. K. Balagurusamy, Alexei Yu. Grigoriev, Moshe Deutsch, Benjamin M. Ocko, Mati Meron, Binhua Lin, and Peter S. Pershan. Crystalline surface phases of the liquid Au-Si eutectic alloy. *Phys. Rev. B*, 76:245436, Dec 2007.

[116] S. Mechler, E. Yahel, P. S. Pershan, M. Meron, and B. Lin. Crystalline monolayer surface of liquid Au-Cu-Si-Ag-Pd: Metallic glass former. *Applied Physics Letters*, 98:251915–1 – 251915–3, 2011.

[117] L. Bischoff, J. Teichert, Th. Ganetsos, and G.L.R. Mair. Temperature dependence of the electric characteristics of liquid metal alloy ion sources. *Journal of Physics D: Applied Physics*, 33(6):692 – 695, 2000.

[118] L. Bischoff, G.L.R. Mair, C.J. Aidinis, C.A. Londos, C. Akhmadaliev, and Th. Ganetsos. A $Au_{82}Si_{18}$ liquid metal field-ion emitter for the production of Si ions: fundamental properties and mechanisms. *Ultramicroscopy*, 100:1 – 7, 2004.

[119] Shiyan Ding, Jian Kong, and Jan Schroers. Wetting of bulk metallic glass forming liquids on metals and ceramics. *Journal of Applied Physics*, 110:043508–1 – 043508–6, 2011.

[120] P. Kofstad. *High Temperature Corrosion*. Elsevier applied science publishers Ltd., 1988.

[121] Carl Wagner. Theorie der Alterung von Niederschlägen durch Umlösen (Ostwald-Reifung). *Zeitschrift für Elektrochemie, Berichte der Bunsengesellschaft für physikalische Chemie*, 65(7-8):581 – 591, 1961.

[122] K.F. Kelton and F. Spaepen. A study of the devitrification of $Pd_{82}Si_{18}$ over a wide temperature range. *Acta Metallurgica*, 33(3):455 – 464, 1985.

[123] A. Pasturel, Emre S. Tasci, Marcel H. F. Sluiter, and N. Jakse. Structural and dynamic evolution in liquid Au-Si eutectic alloy by *ab initio* molecular dynamics. *Phys. Rev. B*, 81:140202, Apr 2010.

[124] A. Bruson and M. Gerl. Diffusion coefficient of ^{195}Au in the liquid $Au_{0.81}Si_{0.19}$ alloy. *Journal of Applied Physics*, 53(5):3616 – 3619, 1982.

[125] Lioba Jastrow, Uwe Köster, and Monika Meuris. Catastrophic oxidation of Zr-TM (noble metals) glasses. *Materials Science and Engineering: A*, 375-377(0):440 – 443, 2004. Eleventh International Conference on Rapidly Quenched and Metastable Materials.

[126] J.M.E. Harper, A. Charai, L. Stolt, F.M. d'Heurle, and P.M. Fryer. Room temperature oxidation of silicon catalyzed by Cu_3Si. *MRS Proceedings*, 187:2519 – 2521, 1 1990.

[127] T. L. Alford, E. J. Jaquez, N. David Theodore, S. W. Russell, M. Diale, D. Adams, and Simone Anders. Influence of interfacial copper on the room temperature oxidation of silicon. *Journal of Applied Physics*, 79(4):2074 – 2078, 1996.

[128] Kenji Hinode, Ken'ichi Takeda, and Seiichi Kondo. Abnormal room-temperature oxidation of silicon in the presence of copper. *Journal of Vacuum Science & Technology A: Vacuum, Surfaces, and Films*, 20(5):1653 – 1658, 2002.

[129] I. Gallino, M.E. Kassner, and R. Busch. Oxidation and corrosion of highly alloyed Cu-Fe-Ni as inert anode material for aluminum electrowinning in as-cast and homogenized conditions. *Corrosion Science*, 63(0):293 – 303, 2012.

[130] Andrei A. Istratov and Eicke R. Weber. Physics of copper in silicon. *Journal of The Electrochemical Society*, 149(1):G21 – G30, 2002.

[131] P. Bolsaitis and M. Kahlweit. The internal oxidation of Cu-Si alloys. *Acta Metallurgica*, 15:765 – 772, 1967.

[132] S.K. Bhattacharyya and K.C. Russell. Coarsening kinetics of silica in copper. *Metallurgical Transactions A*, 7(3):453 – 462, 1976.

[133] Hisashi Sato, Ibuki Ota, Toshiyuki Fujii, Susumu Onaka, and Masaharu Kato. Morphological evolution of grain-boundary SiO_2 in internally oxidized Cu-Si bicrystals. *Materials Transactions*, 45(3):818 – 823, 2004.

[134] Adolf Fick. Über Diffusion. *Poggendorffs Annalen der Physik und Chemie*, 94:59 – 86, 1855.

[135] M.A. Lamkin, F.L. Riley, and R.J. Fordham. Oxygen mobility in silicon dioxide and silicate glasses a review. *Journal of the European Ceramic Society*, 10(5):347 – 367, 1992.

[136] Dmitri V. Louzguine-Luzgin, Ichiro Seki, Sergey V. Ketov, Larissa V. Louzguina-Luzgina, Vladislav I. Polkin, Na Chen, Hans Fecht, Alexander N. Vasiliev, and Hitoshi Kawaji. Glass-transition process in an Au-based metallic glass. *Journal of Non-Crystalline Solids*, 419(0):12 – 15, 2015.

[137] H. G. Tompkins and M. R. Pinnel. Low-temperature diffusion of copper through gold. *Journal of Applied Physics*, 47:3804 – 3812, 1976.

[138] Chujiro Matano. On the relation between the diffusion-coefficients and concentrations of solid metals (the nickel-copper system). *Japanese Journal of Physics*, 8:109, 1933.

[139] Chujiro Matano. On the relation between the diffusion coefficients and concentrations of the Au-Pt, Au-Pd and Au-Ni systems. *Proceedings of the Physico-Mathematical Society of Japan*, 15:405 – 406, 1933.

[140] B. E. Deal and A. S. Grove. General relationship for the thermal oxidation of silicon. *Journal of Applied Physics*, 36(12):3770 – 3778, 1965.

[141] T.T.M. Tran, C. Fiaud, and E.M.M. Sutter. Oxide and sulphide layers on copper exposed to H_2S containing moist air. *Corrosion Science*, 47(7):1724 – 1737, 2005.

[142] M. Ohta, M. Nakagawa, and S. Matsuya. Effect of palladium addition on the tarnishing of dental gold alloys. *Journal of Materials Science: Materials in Medicine*, 1:140 – 145, 1990.

[143] B. R. Lang, S. H. Bernier, Z. Giday, and K. Asgar. Tarnish and corrosion of noble metal alloys. *The Journal of Prosthetic Dentistry*, 48:245 – 252, 1982.

[144] Michihiko Matsumoto Masayuki Hattori, Teruhiko Tokizaki and Yutaka Oda. Corrosion properties of Ag-Au-Cu-Pd system alloys containing indium. *The Bulletin of Tokyo Dental College*, 51(1):7 – 13, 2010.

[145] D. Zander, U. Köster, and V. Khare. Transformation in hydrogenated Zr-Cu-Ni-Al quasicrystals. *MRS Online Proceedings Library*, 643, 1 2000.

[146] Franz Faupel and Klaus Rätzke. Diffusion in metallic glasses and supercooled melts. In Paul Heitjans and Jörg Kärger, editors, *Diffusion in Condensed Matter*, pages 249–282. Springer Berlin Heidelberg, 2005.

[147] L. Paussa, L. Guzman, E. Marin, N. Isomaki, and L. Fedrizzi. Protection of silver surfaces against tarnishing by means of alumina/titania-nanolayers. *Surface and Coatings Technology*, 206(5):976 – 980, 2011.

[148] Erhard Hornbogen. *Werkstoffe*. Springer, 2002.

[149] S. Ding, J. Gregoire, J.J. Vlassak, and J. Schroers. Solidification of Au-Cu-Si alloys investigated by a combinatorial approach. *Journal of Applied Physics*, 111:114901–1 – 114901–6, 2012.

[150] Sabrina Grassini, Emma Angelini, Yangwu Mao, Jelica Novakovic, and Panayota Vassiliou. Aesthetic coatings for silver based alloys with improved protection efficiency. *Progress in Organic Coatings*, 72(1-2):131 – 137, 2011.

[151] M.C. Bernard, E. Dauvergne, M. Evesque, M. Keddam, and H. Takenouti. Reduction of silver tarnishing and protection against subsequent corrosion. *Corrosion Science*, 47(3):663 – 679, 2005. Corrosion, Electrodeposition and Surface treatment of the 54th Annual Meeting of the ISE.

List of Figures

Copyright Permissions

Several figures in this work have been reprinted with permission granted through the copyright clearance center.

Figure	Reference	License Number
2.6	[55]	3727671015614
2.7	[57]	3726080456112
2.6	[83]	3726100532940
4.1	[101]	3726590330776
4.27, 4.31 (a), 4.54 (a)	[3]	3726070253868
5.4 (b)	[135]	3726090628161
4.32	[4]	3730060695228

List of Tables